UNIVERSITY OF SOUTHAMPTON

Faculty of Engineering and Physical Sciences

National Centre for Advanced Tribology at Southampton (nCATS)

Rain Erosion Protection for Fan Blades

by

Dina Ma

Thesis for the degree of Doctor of Philosophy

2018

UNIVERSITY OF SOUTHAMPTON

Abstract

Faculty of Engineering and Physical Sciences

National Centre for Advanced Tribology at Southampton (nCATS)

Rain Erosion Protection for Fan Blades

by Dina Ma

Rain erosion, or water droplet erosion (WDE), of turbofan blades arises problems in the aeronautics community. The phenomenon changes the profiles on fan blade leading edges, affecting the aerodynamic performance that subsequently leads to a significant efficiency drop for the aircraft engine. A potential risk of blade flutter is also raised consequently. Hence, this research work aims to identify the damage mechanisms induced by water droplet erosion on Ti6Al4V turbofan blade in order to ultimately improve the performance with potential coating techniques.

Studies on WDE are restricted to laboratory testing with simplified conditions and samples. Hence, this work will be the first to demonstrate real-life WDE damage on turbofan blades during their 'complicated' in-service conditions. Intergranular fracture is observed at the tip of the leading edges, which is induced due to anisotropic behaviour of α grains under high impact pressure and stress waves during early WDE stages. The roughened surface features then interact with lateral outflow jetting, forming cracks. Material removal then takes place in the forms of tunnelling and upheaval of the overlying materials under the effect of hydraulic penetration. Vibratory CE apparatus is employed to replicate the predominant damage induced by WDE on fan blade, so that it can be used as a screening process to predict the performance of the coated systems. A systematic test plan is adopted to cross-check the damage generated by CE with actual damage on the fan blade leading edge, as well as the WDE damage generated on Ti6Al4V base material using whirling-arm rig to ensure the relevance of the work to the application. Correlation between the damage mechanisms of CE and WDE are identified as similar damage mechanisms are involved in both processes, especially during the incubation period. Exposed grain boundaries are observed due to the displacement of α grains under dynamic loading induced by CE and WDE during incubation period. The effect of crystal orientation on CE and WDE performance is identified as certain grains show greater resistance better than others.

For the second stage of the work, a series of coatings are proposed and tested under CE to evaluate their potentials for WDE application. As a result, the Hardide CVD-W/WC T1200 coating, Hardide CVD-W/WC LT coatings, HIPIMS deposited CrAlYN/CrN nanoscale multilayer C1 coating and HIPIMS deposited CrAlYN/CrN nanoscale multilayer C2 coating are selected. In-depth understanding on the coating damage mechanisms are established by

correlating the coating performance with microstructure, crystallographic texture, interface design, deposition conditions and mechanical properties for the first time. In both Hardide and HIPIMS coating systems, a beneficial crystalline texture is identified that better resists to CE. For Hardide W/WC coating, the damage tends to initiate at the grain boundaries of the exposed surfaces. While in the case of the HIPIMS deposited multilayer coatings, the primary damage mechanism is believed to be the cracks formed at the substrate/interlayer interface. The nanoscale multilayer structure greatly extends the coating lifetime with crack deflection mechanisms at the interfaces between the nanolayers. Therefore, it is found that the coating performance under dynamic compressive loadings cannot be predicted with simple H/E approaches. However, combining the H/E ratios with the factors of microstructure, crystal orientations and nano-layered systems might further facilitate the understanding of coating performances.

Ultimately, WDE testing using the whirling arm rig with 500 μm droplets at 300 $m \cdot s^{-1}$ impact velocity of the screened coating specimens is attempted to validate their potentials for rain erosion protection of fan blade leading edge. However, the results are considered not representative due to a fault with the test rig.

Nomenclature

AFM: Atomic Force Microscope

BCC: Cody Centred Cubic

BEI: Backscattering Electron Imaging

CE: Cavitation Erosion

CNT: Carbon NanoTube

CVD: Chemical Vapour Deposition

DB: Daimler Benz

DB-SPF: Diffusion Bonding Super Plastic Forming

EBSD: Electron Backscatter Diffraction

EDS: Energy Dispersive x-ray Spectroscopy

FEG: Field Emission Gun

FIB: Focussed Ion Beam

FOD: Foreign Object Damage

HCP: Hexagonal Closed Packed

HIPIMS: High Power Impulse Magnetron Sputtering

HP: High Pressure

HVOF: High Velocity Oxy-Fuel

IP: Intermediate Pressure

LCF: Low Cycle Fatigue

LP: Low Pressure

LPB: Low Plasticity Burnishing

LSP: Laser Shock Peening

MDE: Mean Depth of Erosion

MSP: Metallic Shot Peening

MUD: Multiples of Uniform Density

NCD: NanoCrystalline Diamond

NPL: National Physical Laboratory

PVD: Physical Vapour Deposition

SEI: Secondary Electron Imaging

SEM: Scanning Electron Microscope

SPE: Solid Particle Erosion

SPE: Solid Particle Erosion

TEM: Transmission Electron Microscopy

VAR: Vacuum Arc Re-melting

WDE: Water Droplet Erosion

XRD: X-Ray Diffraction

Table of Contents

List of Figures

List of Tables

Declaration of Authorship

I, Dina Ma declare that this thesis and the work presented in it are my own and has been generated by me as the result of my own original research.

Rain erosion protection for fan blades.

I confirm that:

This work was done wholly or mainly while in candidature for a research degree at this University;

Where any part of this thesis has previously been submitted for a degree or any other qualification at this University or any other institution, this has been clearly stated;

Where I have consulted the published work of others, this is always clearly attributed;

Where I have quoted from the work of others, the source is always given. With the exception of such quotations, this thesis is entirely my own work;

I have acknowledged all main sources of help;

Where the thesis is based on work done by myself jointly with others, I have made clear exactly what was done by others and what I have contributed myself;

None of this work has been published before submission.

Signed:

Date:

Acknowledgements

I would like to express my sincere gratitude and appreciation to my supervisors Professor Robert Wood and Dr Terry Harvey for their time, suggestions, supports and encouragements since I started my PhD project at University of Southampton. My sincere thanks also goes to Dr Richard Wellman and Rolls Royce aeroengine for the sponsorship and technical advices for this project. I would also like to acknowledge the great support from our collaborator Professor Papken Hovsepian and Professor Arutiun Ehiasarian from National HIPIMS Technology Centre at Sheffield Hallam University.

I would like to thank my colleagues Pedro, Andreu, Heather, Jahnabi and Behrad for their help on building my skills on experimental techniques. I have also appreciated the valuable discussions with Charlie, who is working on the theoretical side of my research topic. Many thanks also go to Damian, Stuart and Oliver from EDMC workshop, who helped me with the preparation of the test rig setup.

Special mentioning of Andreu Laborda Cabo, my loving and supportive husband, who encouraged and motivated me through my PhD time, lifted me up when I hit low point of my research and life. I appreciate all the love, supports and care from my loving in-laws. I am also grateful to our new furry family member, Bartal, who brought loads of joy and comfort to my long and tough journey of writing.

Last but not least, special love and gratitude goes to my mother Kalima, father Omarkhan, grandmother Kulgun and brother Yetay, for all of the sacrifices that they have made on my behalf. I would never have been able to stand at this point of my life without their unwavering love, endless supports and devoted encouragements. I love you all and I am so grateful to be part of this wonderful family.

Chapter 1.
Introduction

1.1 Background

In nature, rain erosion is seen when the raindrops hit the surface of the Earth, as well as the raindrops accumulate and flow in the forms of small streams. This phenomenon leads to the formation of rills and gullies. Rain erosion, or water droplet erosion (WDE), was observed on the exterior of high-speed military aircraft shortly after World War II [1]. It induced progressive loss of original material from a solid surface due to continuous impingements of water droplets. Actual flight tests in order to determine the severity of rain erosion were carried out by the United States Air Force and Cornell Aeronautical Laboratory in 1927 [2]. It was found that the aluminium leading edges of wings and the glass reinforced plastic nose radome are particularly susceptible to degradation induced by rain droplets impingements, and both components exhibited serious erosion after exposure to rainfall of moderate intensity at flight speeds approaching 223 $m \cdot s^{-1}$ (500 mph). The subject was extensively investigated from the early 1950s to the 1960s [1-12]. Researchers have established a variety of theories to understand the damage mechanisms of rain erosion, particularly on rain erosion at 223 $m \cdot s^{-1}$ with droplets of 2 mm diameters (typical mean diameter for rain droplets) [3–6]. However, due to the shift of interest after wartime, the amount of research effort on rain erosion was drastically reduced.

Recent attention toward WDE has been generated in various industrial applications. For example, deterioration of compressor efficiency in the power generation industry due to WDE was induced by over-sprayed droplets during inlet fog cooling process. Severe WDE was encountered at the leading edge of steam turbine blades during operation. Rain erosion at the leading edge of wind turbine blades has also been found to result in severe performance degradation. Finally, rain erosion of aeroengine fan blades, which is the core of current study that has not been covered by any past literature, but now found to be affecting engine efficiency.

This project focuses on the rain erosion of turbofan blades, which arises problems in aeronautics community since the changes of leading edge profiles affect aerodynamic performance of the turbofan blades. In order to improve the engine efficiency, the rotation speed and the diameter of turbofan blades is increased. Hence, this pushes the tip velocity to exceed supersonic speed, which leads to severe WDE damage. Additionally, the tendency of material debris removed during rain erosion to attach to the surfaces of the turbofan high-pressure (HP) stage blades further reducing engine efficiency is concerned.

1.2 Project aims and objectives

This project is sponsored by Rolls-Royce to primarily address rain erosion at the leading edge of Ti6Al4V turbofan blades. The phenomenon results in a decrease of overall aeroengine

efficiency and high fuel burn. Furthermore, it can potentially lead to blade flutter. Therefore, this project aims to identify the damage mechanisms induced by rain droplets at Ti6Al4V turbofan blade leading edge in order to replicate the predominant damage on Ti6Al4V base material through laboratory testing. It also aims to apply surface engineering techniques to improve the performance of Ti6Al4V base material.

The objectives of the project are then set as follows:

(1) Identify the rain erosion degradation mechanisms of Ti6Al4V turbofan blades.
(2) Use vibratory cavitation erosion (CE) testing to generate the predominant rain erosion damage on Ti6Al4V base material.
(3) Verify the correlation of the damage mechanisms between WDE and CE on Ti6Al4V.
(4) Following a comprehensive understanding of WDE damage mechanisms and location on turbofan blades, propose applicable coating solutions.
(5) Use vibratory CE testing to screen the proposed coating solutions.
(6) Investigate the coating performance and failure mechanisms under CE.
(7) Validate the performance of the CE screened coatings under WDE testing and propose understandings on damage mechanisms.

1.3 Thesis layout

The thesis is composed of 10 chapters and it is structured as follows: Chapter 1 gives a brief introduction to the background, aim and objectives of the project. Thesis layout is also included in this chapter. Chapter 2 is literature review on Ti6Al4V turbofan blade material, damage mechanisms of WDE, as well as, means for prevention. A review paper based on Chapter 2 will be submitted to the Journal of *Surface Topography: Metrology and Properties*. Chapter 3 demonstrates the experimental methodologies and techniques applied. Chapter 4 presents the results and discussions based on the forensic analysis of the ex-service turbofan blades. Past studies of WDE are restricted to laboratory testing with simplified conditions and samples. Hence, this will be the first study to demonstrate real-life WDE damage on real turbofan blades during their 'complicated' in-service conditions. A manuscript based on this chapter has been submitted to the *Wear* Journal on 1st September 2018. Chapter 5 characterises the correlation between the damage mechanisms of WDE and CE on Ti6Al4V base material. It validates the employment of CE as a screening process for WDE application. Additionally, the experimental results are compared to the damage mechanisms detected on the ex-service fan blades. Chapter 6 discusses the CE performance of CVD W/WC coatings. A presentation based on part of this work has been showcased in *73rd STLE (Society of Tribologists and Lubrication Engineers) Annual Meeting and Exhibition* in Minneapolis, USA. A manuscript based on this chapter will be submitted to the Journal of *Materials and Design*. Chapter 7 describes the CE performance of HIPIMS nanoscale multilayer coatings. A manuscript based on this chapter has been submitted to the Journal of *Alloy and Compounds* on 16th November 2018. Chapter 8 shows the WDE test results of the best performing coatings under CE screen tests. Chapter 9 concludes the thesis. Chapter 10 details the plan for future work.

Chapter 2.
Literature Review

The word "erosion" from the Greek "erodere" is defined as surface destruction and material removal by external mechanical forces. The three main forces that cause erosion are water, wind and ice. These forces are mainly in the forms of multiple impacts generated by dynamic impingements of a liquid on a solid surface (cavitation erosion and water droplet erosion) or of a solid on another solid surface (solid particle erosion).

In this study, rain erosion of turbofan blades is concerned. It creates problems in the aeronautics community as the rain erosion affects aerodynamic performance of turbofan blades that subsequently leads to significant efficiency drop for the aircraft engine. This chapter covers a literature review on two main subjects. Firstly, a brief introduction of the turbofan engine is given with respect to its function, structure and the materials used. It demonstrates the essential role played by the component studied in the current project: the Ti6Al4V fan blades. The common failure modes of turbofan blades encountered during in-service condition are then reviewed, leading to the main concern of the project: rain droplet erosion. The second subject focuses on delivering a state-of-the-art review of water droplet erosion (WDE), including its damage mechanisms, driving parameters, test methods and finally solutions that have been applied in past studies.

2.1 Turbofan engine

Modern airliners mostly use turbofan engines due to the benefits of high thrust and good fuel efficiency as against propellers. A turbofan engine is generally composed of four sections, which are the fan, the compressor, the combustor and the turbine, as shown in Fig. 2.1. At the very front of the engine, a fan helps to increase the flow of the ambient air into the compressor. The compressor pressurises the air flowing through the engine before it enters the combustion chamber, where the air is mixed with fuel, ignited and burnt. The last stage is the turbine, which is the component that extracts work from the high-pressure, hot gases exiting the combustion system and provides power for the compressor stages and auxiliary engine systems.

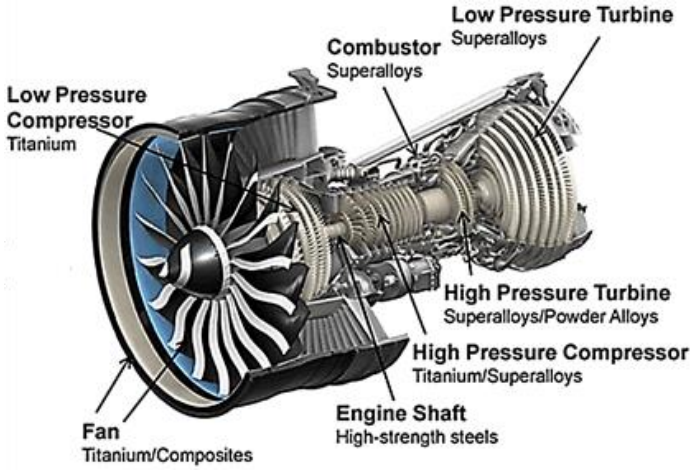

Fig. 2.1 Schematic illustrating the structure of Rolls-Royce turbofan engine [13].

2.1.1 Material used in Rolls-Royce turbofan engine.

Employment of a range of lightweight, high-strength, corrosion resistant and thermally stable materials are vital to the success of any turbofan engine. The intake fan at the front of the engine must be able to avoid fracture when birds and other debris are sucked into the engine and struck its blades; it is thus predominantly made of titanium alloy. Additionally, composite fan blades with titanium shielding at the leading edge have been applied for some of the turbofan engines, as shown in Fig. 2.1. This combination will also be utilised for future ultra-fan design. The compressor components are also made from titanium, and the combustor components are typically made of nickel superalloys.

2.1.2 Turbofan blades (Ti6Al4V, Grade 5 alloy)

This project focuses on improving rain erosion resistance of Ti6Al4V turbofan blades, the crucial components that produce 75% of the engine thrust [13]. The biggest Rolls-Royce engines have a fan diameter of 3 metres and can shift up to 1.2 tonnes of air per second, thus increasing efficiency [13]. As the ambient air enters the engine, most of the air that passes through the fan travels around the core of the engine (the centre of the engine where the compressor, combustor, turbine, and exhaust nozzle are located.), which is called the bypass air. The bypass air is then accelerated out of the back of the engine by the fan thereby creating thrust [14–16].

The turbofan blades see temperatures from - 50°C (at cruise altitude) to 40°C [14]. The components should be able to last for 80 million km (10,000 flights) and perform sufficient flexibility and damage tolerance to operate through wind, rain, hail, snow and the occasional bird impacts [16]. In this instance, Ti6Al4V Grade 5 alloy is widely used in manufacturing the turbofan blades. It meets the mechanical requirements stipulated above and with the maximum strength to weight ratio (a combination of high strength and low density) possible [16]. Commercially available titanium alloys are graded according to the quantity of interstitial elements that primarily affect their physical properties. Grade 5 titanium, which is Ti6Al4V alloy is the most commonly used of all titanium alloys. The chemical composition limits and mechanical properties of Ti6Al4V alloy is listed in Table 2.1 and Table 2.2, respectively. This high-strength alloy can work at cryogenic temperatures to about 427°C [17].

Table 2.1 Chemical composition limits of Ti6Al4V alloy [18]

Element	Ti	C	Fe	N	Al	O	V	H	Y	Other
Weight%	balance	0.08	0.03	0.05	5.5-6.75	0.20	3.5-4.5	0.015	0.005	0.40

Table 2.2 Mechanical properties of Ti6Al4V alloy [18]

Density	Yield strength	Compressive Yield Strength	Tensile strength	Fracture Toughness	Rockwell hardness	Young's modulus
4.4 g/cc	860 MPa	970 MPa	1060-1330 MPa	75 MPa-$m^{½}$	30-39 HRC	100-145 GPa

The typical microstructure of Ti6Al4V alloy consists of primary α_p grains and secondary α_s embedded in β matrix, as shown in Fig. 2.2. Aluminium acts as the alpha stabilizer and vanadium as the beta stabilizer [19] in Ti6Al4V alloy. The shape of each phase various with the manufacturing process, for instance, Fig. 2.2 (a) shows the microstructure of Ti6Al4V alloy with globular primary α phase after cross-rolling process, while in Fig. 2.2 (b) the primary α phase elongates due to forging processes.

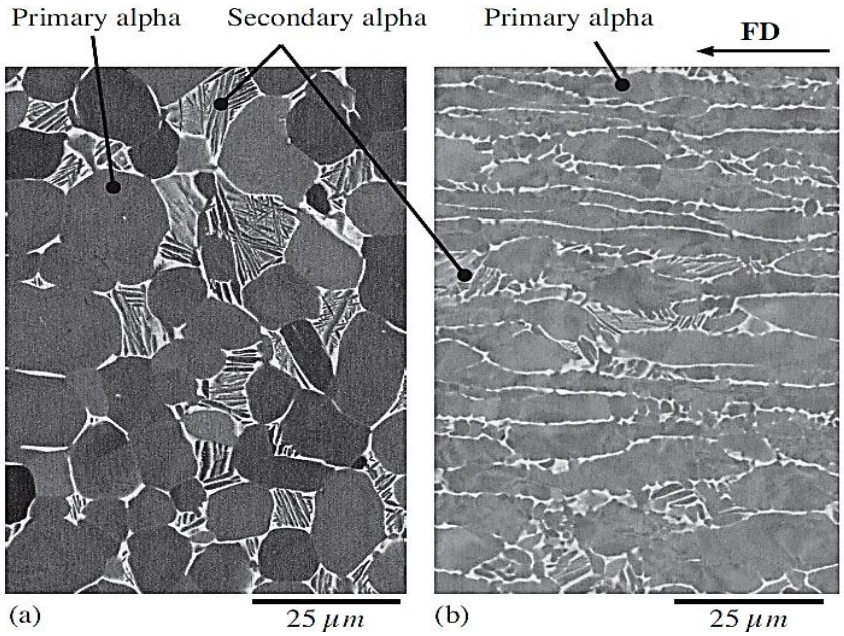

Fig. 2.2 SEM images of Ti6Al4V alloys under various manufacturing processes: (a) cross-rolled Ti6Al4V plate; (b) forged Ti6Al4V bar [13]

The α-phase in Ti6Al4V alloys have hexagonal close packed (hcp) structures, and the β-matrix has a body-centred cubic (bcc) crystal structure. The anisotropic mechanical properties of Ti6Al4V alloy is dominated by the anisotropy of α-phase [20]. Fig. 2.3 shows the crystallographic orientations of hard and soft grains in an hcp structured polycrystalline material. Soft oriented grains are those that are favourably oriented for easy slip whereas hard grains are not. It has been proposed that failure in α+β Titanium alloys was related to the high plastic anisotropy of titanium, which give rise to undesirable hard/soft grain interactions. The presence of macronzones can magifiy such an effect. In titanium alloys, slip systems include <11-20>, <11-23> directions, the basal {0001}, prismatic {10-10} and pyramidal planes [21].

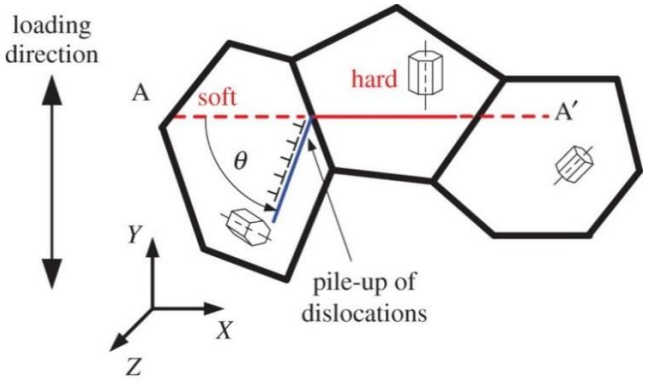

Fig. 2.3 Rogue grain combination [20].

Turbofan blades are produced by vacuum arc re-melting (VAR) [22]. During the VAR process, the metal drops fall into a water-cooled copper mould. Re-melting is operated with minimal superheating; segregation is thus minimized, producing a fine grain structure [23]. The Rolls-Royce Trent engines use hollow Ti6Al4V fan blades with an internal Warren-girder structure (as shown in Fig. 2.4) manufactured using diffusion bonding super plastic forming (DB-SPF) process to achieve strength, stiffness and robustness at low weight [24]. This unique Warren-girder structure of the fan blades offers a significant weight saving (50%) over the solid blade alternatives, reducing the engine's specific fuel consumption, resulting in cost saving and reduced emissions (CO_2 footprint) for the airlines [25].

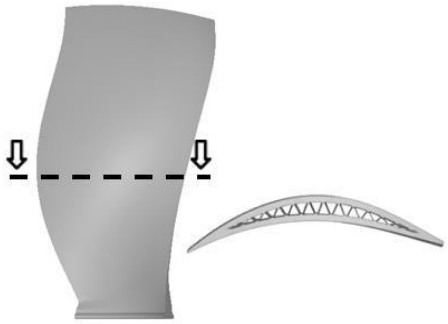

Fig. 2.4 Schematic of the Rolls-Royce hollowed fan blade structure [24].

2.1.3 Common deterioration mechanisms of turbofan blades.

Turbofan blades suffer from various damage induced by impacts from debris of aircraft parts or external objects, such as volcanic ash, bird strikes or harsh weather conditions (rain, fog or hail). Failures of turbofan blades can affect the thrust generation and eventually resulting in the efficiency drop of the aeroengine [15,16,26].

i. Foreign object damage (FOD)

Foreign-object damage (FOD) induced by hard body (such as stones) impacting primarily on the fan blades results in immediate blade fracture or damage from stress-raising notches [27,28] or cracks [29]. The most common in-flight FOD is caused by bird strikes and turbofan engines experience more severe FOD incidents on the ground than in-flight condition. In a recent study on Ti6Al4V alloy [29], where FOD was simulated by high-velocity impacts of steel shot on a flat surface, reduction of fatigue strength was detected due to plastic deformation induced by crater formation. The principal effect of FOD on fatigue life reduction was associated with inducing microcracks in the pile-up of material around the impact crater rim, which is considered as preferred sites for the premature initiation of fatigue cracks.

ii. Solid particle erosion (SPE)

Turbomachines, such as gas turbine engines, centrifugal and axial compressors, are often operated in hostile environments that result in a significant amount of ingestion of fine particles [30]. The actual flight environment is complicated by the probability that a combination of rain

and solid particles is present. Aeroengine operating in dusty environments are subject to ingestion of erodent particles leading to solid particle erosion (SPE) of blades and a permanent drop in aerodynamic performance [31]. SPE in aerospace engineering can take place when the plane takes off from a sand-covered runway or flies at high altitudes encountering hail, sand or volcanic ash.

iii. Water droplet erosion (WDE)

The focus of current study is rain erosion, or WDE, of turbofan blades, which is of growing interest to aeronautics community in recent years. It induces progressive material loss at the leading edge of turbofan blades under repetitive water droplet impingements [32]. Thus, over time the leading edge is roughened and the profile is changed. The process shortens the chord lengths of the blades, so that the gap between the trailing edges and the fan casing increases. This phenomenon leads directly to the loss of thrust and a decline in engine performance. WDE is also commonly seen in steam turbine and wind turbine blades, as shown in Fig. 2.5. More details on WDE will be discussed in the following sections.

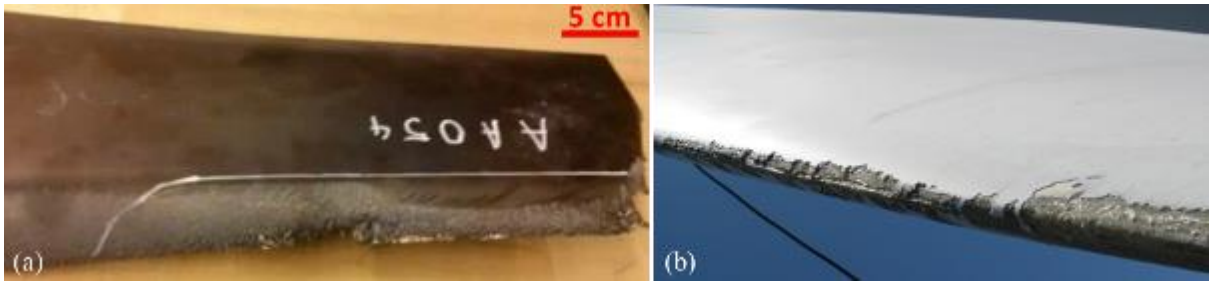

Fig. 2.5 Water droplet erosion at the leading edge: of the steam turbine blade [33]; (b) wind turbine blade [34].

2.2 Damage mechanisms of WDE

WDE is a time dependant process, it exhibits several erosion rate-time patterns [35], as shown in Fig. 2.6. The first stage is the incubation period, in which there is no measurable erosion damage; the erosion rate then increases to its maximum and remains constant at its maximum value in the maximum erosion rate stage; thirdly is the deceleration stage, in which the erosion rate starts to decline. There is a fourth terminal stage suggested, in which the erosion rate stays constant again but for a smaller value. The nominal incubation period and maximum erosion rate are determined by drawing a straight line that best fits the maximum erosion rate stage of the WDE curve [35]. The interception of the straight line with the x-axis (the exposure time) is the nominal incubation period and the slope of the straight line is the maximum erosion rate, as illustrated in Fig. 2.6 (a). In most practical situations, the first three stages of WDE are of main concern. For coating applications, the improvements of material performance are expected to extend the incubation period [35,36].

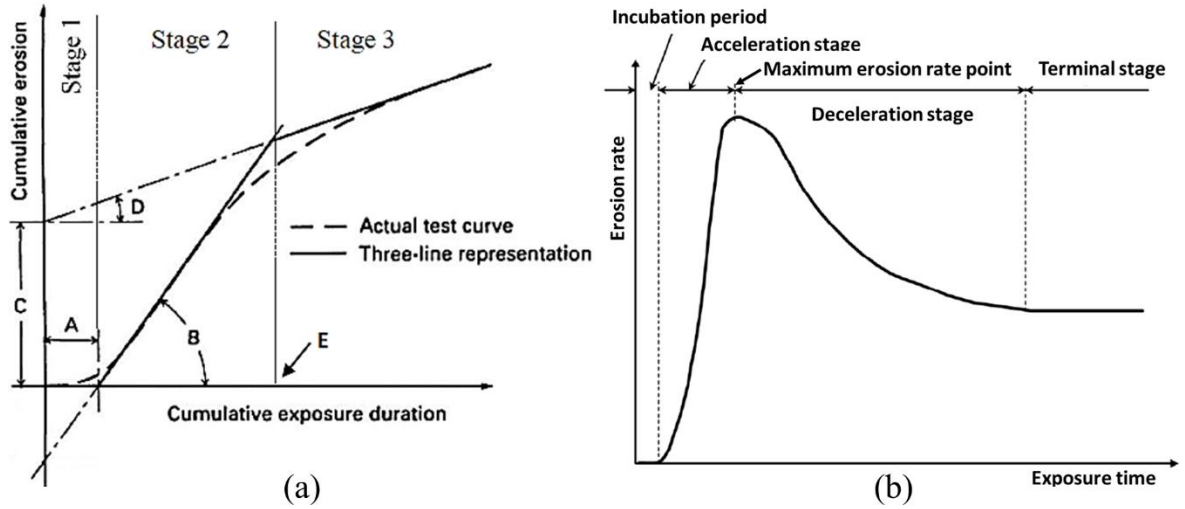

Fig. 2.6 (a) Typical WDE curve with characterization of the nominal incubation period and the maximum erosion rate [35]; (b) erosion rate versus exposure time curve during WDE process [35].

WDE damage is predominantly caused by two main factors: (1) water-hammer pressure and (2) the radial outflow (lateral jetting) along the surface at high speed [31,32,45–54,37,55–63,38–44]. Water-hammer pressure drives the damage mechanisms during the incubation period, while those of the advanced stages are governed by lateral outflow jetting.

2.2.1 Incubation period

The concept of water-hammer pressure was firstly raised by Cook in 1928 [56]. It generates high pressure and stress waves as a result of the collision of high-velocity water droplets with the target solid surface, coupled with the compressibility of water droplet. The initial stage of water droplet impact on a solid surface is shown schematically in Fig. 2.7.

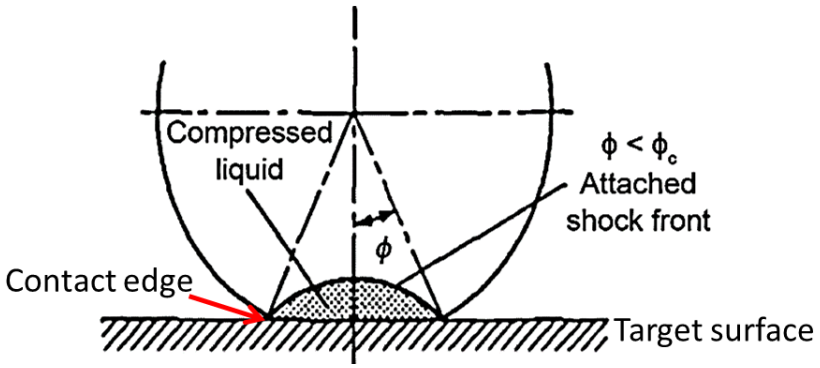

Fig. 2.7 Initial stage of impact between a water droplet and a solid target [63–65], where φ_c is the critical contact angle.

Heymann [53] proposed a theoretical model to modify the magnitude of the water-hammer pressure in consideration of the formation of the shock wave generated during droplet impingements, as presented in Equation 1.

$$P = \rho CV[2 + (2k - 1)\frac{V}{C}] \qquad \textbf{Equation 1}$$

where $\boldsymbol{\rho}$ is the density of the water; C is the shock wave velocity in the liquid, which is 1463 $m \cdot s^{-1}$ for water; V is the liquid impact velocity; and k is a constant dependant on the liquid within the droplet and the corresponding value for water is 2.

The duration of the water-hammer pressure was introduced by Bowden and Field [57], as shown in Equation 2.

$$\Delta\tau = \frac{3rV}{2(C + kV)^2} \qquad \textbf{Equation 2}$$

The radius of the contact area at which the lateral outflow jetting commences [36] can be interpreted as follows:

$$Xc = \frac{rV}{C + kV} \qquad \textbf{Equation 3}$$

where *r* represents the curvature of the radius of the water droplet front.

Under the application of dynamic pressures, stress waves are generated upon impingements of water droplets within the solid. It is revealed that most of the damage induced during incubation period occurred within fractions of a microsecond. This is due to the stress waves generated and propagated into the material, causing the initiation of microcracks [32,52,54,63]. Elastic wave theory of solids [66] states that under an impulse loading, a compression and a shear wave are generated in the solid bulk; a Rayleigh surface wave is generated on the surface. As the compression wave propagates along the solid material, the shear wave is formed. The Rayleigh surface wave propagates radially on the surface. These stress waves can interact with microstructural features within the material and with each other [67]. As the stress waves propagate along the solid material, stress wave reflection and reinforcement can occur due to the mismatch of acoustic impedance, leading to formation of tensile stress [68].

The microstructure of exposed surface drives the material response during incubation period of WDE [39,69–72]. The pre-existing microstructural features, such as grain and interphase boundaries, are seen as the preferential sites for damage initiation under water droplet impacts [39,67,69–72]. The first detectable evidence of damage induced during the incubation period appears in the form of micron-size depressions on the surface, as shown in Fig. 2.8. This is attributed to the extreme pressures that can be of the order of GPa for high-speed impact. Additionally, Thomas and Brunton [73] have identified the occurrence of "grain tilting" during incubation period. The terminology refers to the change in the grain orientation caused by the water droplet impacts, which leads to visibility of grain boundaries on the exposed surface. This effect was also reported by Kamkar et al. [69] in the WDE study of Ti6Al4Al tested with 460 µm droplets at 350 $m \cdot s^{-1}$. Formation of slip bands around the tilted grains and intergranular damage was developed during the incubation period, as shown in Fig. 2.9. Moreover, topographical analysis using AFM (atomic force microscope) was applied to verify the "grain-tilting" phenomenon by Huang et al [39], as shown in Fig. 2.10. The relative coordinates (distance-height coordinates) of the two adjacent reference points were extracted and the tilt angle was calculated. The results indicate that although the angles of grain tilting were very

small (the maximum observed angle of the surface being 1.6° from the horizontal), they result in steps along the grain boundary, thus the surface was slightly roughened. The same analysis has been applied by Kamkar et al. [69] on forged Ti6Al4V alloy and the same conclusion was drawn. However, the mechanism of tilting the grains during extreme short duration of loading remains uncertain and it has not been clarified. Furthermore, the effect of the macronzones observed on the surface of the forged Ti6Al4V in the latter study [69] has not been further discussed.

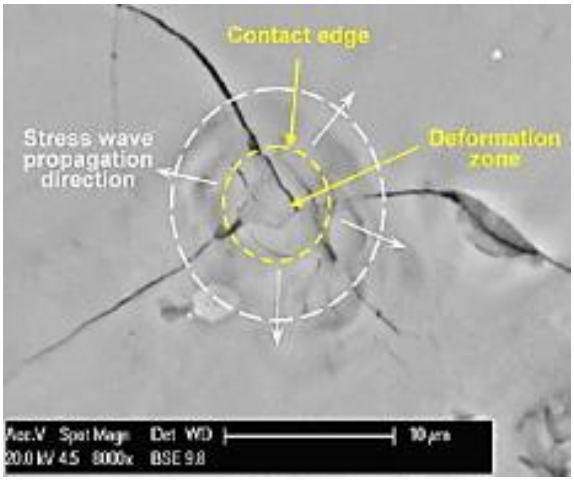

Fig. 2.8 Deformation zone and cracks observed on γ-TiAl surface at low water-hammer pressure (730 MPa) [46].

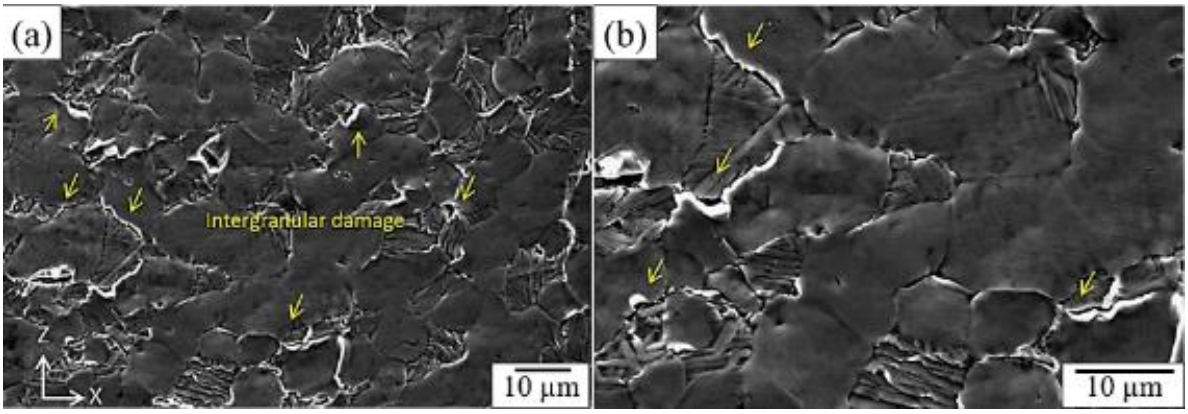

Fig. 2.9 Incubation period of Ti6Al4V surface tested with 460 µm droplets at 350 m·s^{-1} [69].

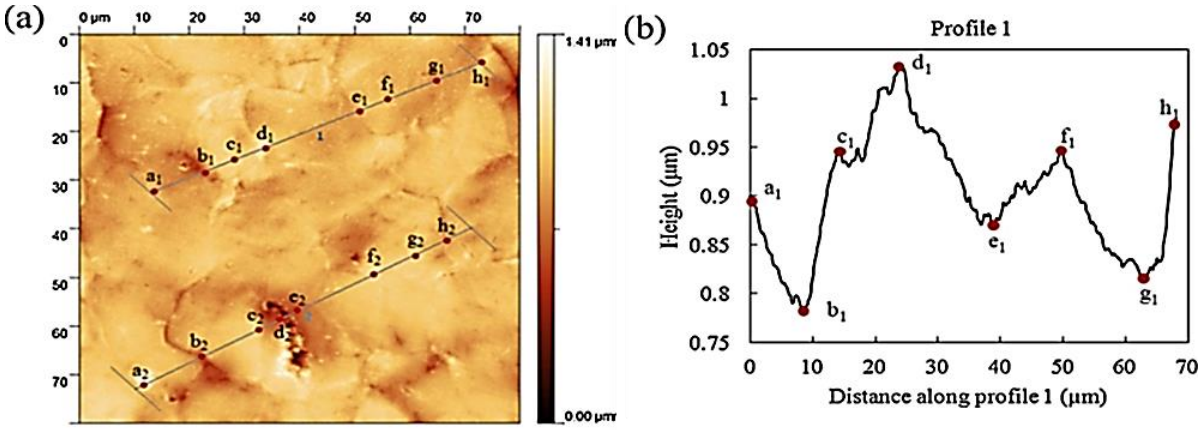

Fig. 2.10 Extracted height profiles across tilted grains from AFM height image of the Ti6Al4V surface impacted with a water-hammer pressure of 0.94 GPa at 410 m·s^{-1}: **(a)** AFM height image with indication of the extracted profiles; **(b)** extracted average height profile [39].

2.2.2 Advanced stages

After the initial stage of a water droplet impact, the high-pressure loading terminates abruptly with the onset of lateral outflow jetting across the impacted surface [12,64,65,74], as shown in Fig. 2.11 (a). This high-speed (up to 10 times greater than the impact velocity) lateral outflow jetting causes a strong shear wave in the solid material. Thomas and Brunton [73] revealed that the shear wave generated by lateral waterjet only focus at surface discontinuities. As the roughened features (such as plastic deformation, pitting and fractures) developed on the exposed surface during the incubation period, they act as stress concentrators for radial outflow, initiating cracks [12,46,75], as shown in Fig. 2.11 (b). Material removal mechanism of WDE is then dominated by the shear stress induced by lateral waterjet instead of the water-hammer pressure [73]. Additionally, lateral outflow jetting is always accompanied with hydraulic penetration. As the water being forced into the previously formed erosion pits or cracks, leading to the formation of significantly enhanced local stresses. The phenomenon opens up the existing cracks and promotes crack propagation, resulting in the most severe mode of material removal.

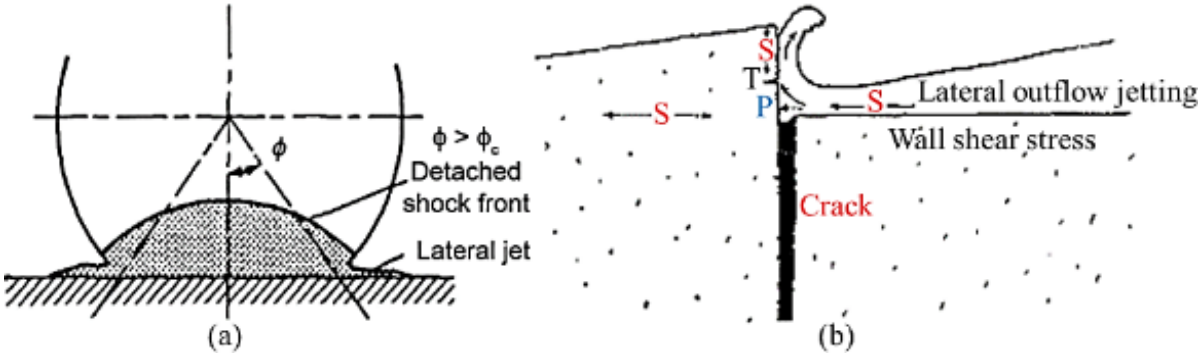

Fig. 2.11 (a) Lateral outflow jetting [64,65]; **(b)** formation of crack due to the effect of lateral outflow jetting interacts with surface asperities, where S is shear stress, T is tensile stress and P is compression [12].

The damage mechanisms of Ti6Al4V alloy at advanced stages of WDE are well established in past studies [70,71,76–78]. The microstructure of Ti6Al4V has little effect on the damage induced in the advanced stages of WDE. It is believed that the stress field developed in the advanced stages of WDE is complex due to the roughening of the surface and growth in defects, dominating the crack propagation. Fig. 2.12 shows the features observed on Ti6Al4V specimens in the advanced stages of WDE. The specimens were tested with 460 µm droplets at 350 $m \cdot s^{-1}$ impact velocity using whirling-arm rig. A material folding phenomenon, shown in Fig. 2.12 (a), has been reported by several researchers [71,78,79]. It is considered as one typical failure modes induced by the shear stress generated due to the action between lateral outflow jetting and surface asperities. Ductile failure, such as dimples are formed on the folded material, Fig. 2.12 (b). Additionally, from the transverse section of the erosion crater shown in Fig. 2.12 (c), formation of lateral cracks on the side wall is considered as further evidence of the effect of lateral outflow jetting. Higher impact velocity results in greater expansion of erosion craters [71], which was claimed to be associated with the enhanced effect of the lateral jetting. The material removal behaviour is assisted by hydraulic penetration in the advanced stage of WDE, which contributes to significant propagation of existing cracks or pits in the form of tunnelling

[71,78]. The ability of this mechanism can propagate sub-micrometre sized cracks to several millimetres [36]. The existing cracks are broadened to form tunnels and water is forced into these tunnels for the overlying material to bend upwards, eventually leading to material removal, as demonstrated in Fig. 2.12 (d), (e) and (f).

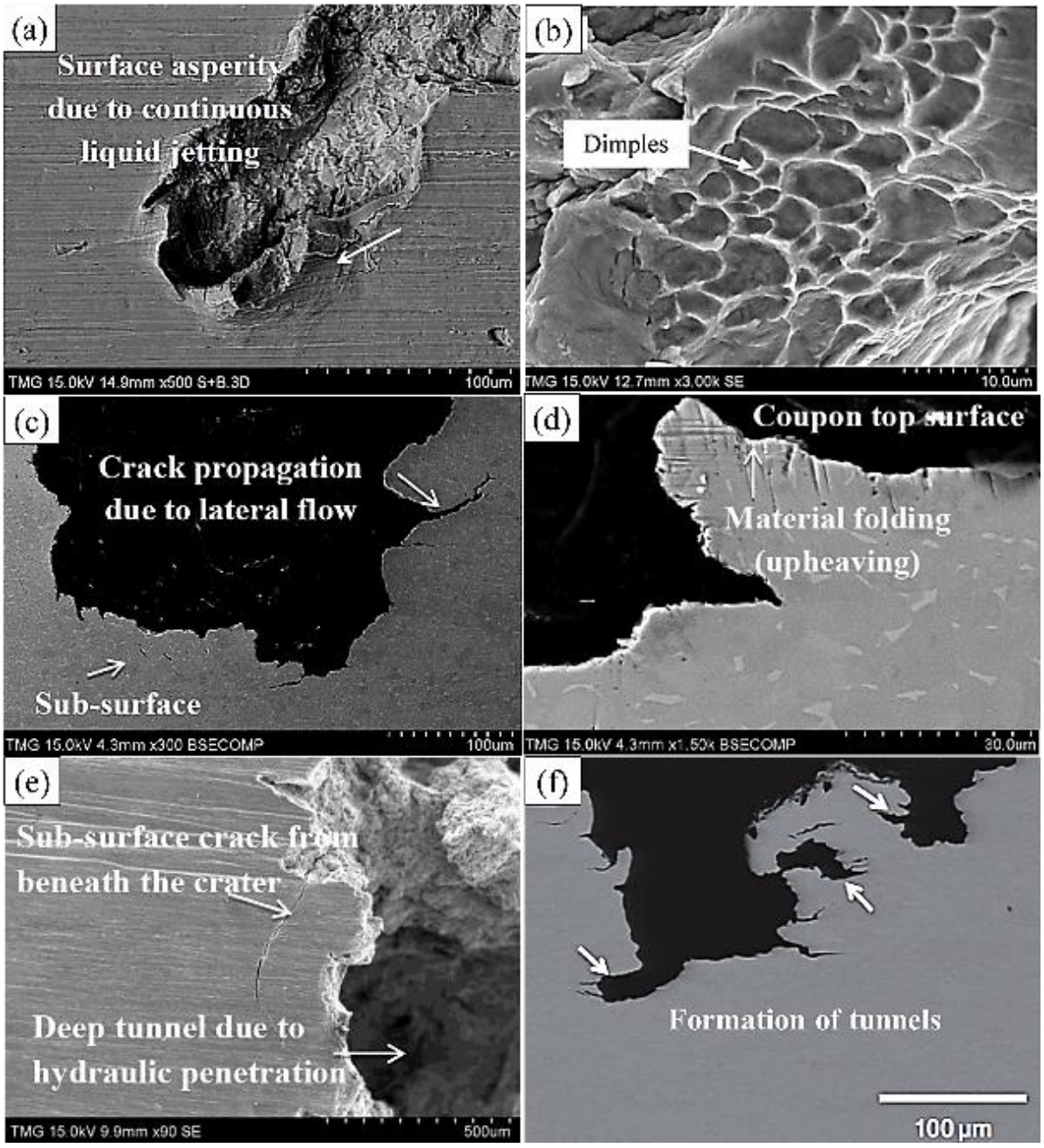

Fig. 2.12 Features of Ti6Al4V in advanced stages of WDE with 400 µm droplets at 350 m·s^{-1} impact velocity [71,78,79].

Additionally, the fracture surface of Ti6Al4V reveals the formation of striation marks inside the erosion craters in Fig. 2.13. The WDE process has been associated with fatigue process due to its cyclic nature of loading and unloading [80]. Momber et al. [81] proposed that a low-cycle fatigue (LCF) process was induced by waterjet impacts on a low-carbon steel. However, none of the attempts was universally applicable. The "fatigue" phenomenon detected during WDE is likely to have happened on a strained material, hence, classic fatigue test data is not relevant.

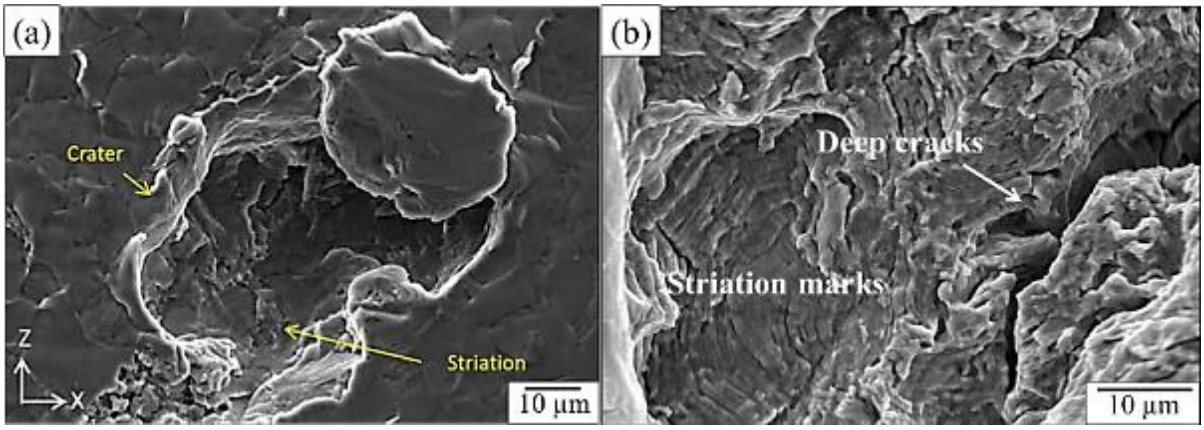

Fig. 2.13 Formation of striation marks in erosion craters formed under WDE tests with 460 μm droplets at 350 m·s^{-1} [69,79].

2.3 Factors affecting severity of WDE

In order to understand the damage mechanisms involved in WDE, a number of critical parameters must be examined:

2.3.1 Impact velocity

Impact velocity has a significantly effect on the WDE behaviour [2,70,71,82–85]. Increase in impact velocity leads to an increase in erosion rate and shorter incubation period. Erosion rate (ε̇) is empirically defined as the cumulative volume or weight loss per erosion time, and its relation between impact velocity (V) can be interpreted as:

$$\dot{\varepsilon} = V^n \qquad \textbf{Equation 4}$$

where n is a material dependent constant. The observed velocity exponents for erosion rate-impact velocity relationship is listed in Table 2.3. The values varies with the experimental conditions of WDE.

Table 2.3 The impact velocity exponent in equation (3) collected from literatures [2,70,71,82–85]

Tested materials	**Range of impact speed (m·s^{-1})**	**Testing conditions**	**Velocity exponent range (n)**
Al, Ni, 316 stainless steel, Ti6Al4V	90-250	800 μm, waterjet, rotating arm	5-7
Stainless steel, TiN coated steel, sprayed cermet coating	60-300	45 to 130 μm, water droplet, spraying water droplets on a stationary target	3-5.5
Zinc sulphide (for infrared window application)	200-350	700 to 1800 μm, water droplet (rain erosion), rotating arm	9-14
Stainless steel, Ti-6Al-4V	350-580	100-350 μm, spraying water droplet, rotating arm	3.8-5.3

Stainless steel	450-630	50 µm, water droplet, rotating arm	5
Ti6Al4V	150-350	460 µm, water droplet, rotating arm	> 9
Ti6Al4V, TiAl	200-350		7-9
			11-13

2.3.2 Impact angle

The erosion rate of WDE is at a maximum when the droplets impinging perpendicularly to the solid surface [55,58,84,86]. Ahmad et al. [84] proved this experimentally under a WDE testing condition with 90 µm droplets at 360 $m \cdot s^{-1}$ impact velocity on steel material with a rotating-disk rig. Wahl [50] stated in his work that the erosion rate approaches zero when it is less than 15°, which confirmed that the severity of the erosion damage rapidly decreased with the reduction of the impact angle.

2.3.3 Water droplet diameter

The effect of droplet shape and diameter on WDE behaviour has been investigated by researchers [55,58,86], however, it is less significant than that of impact velocity. Larger water droplets cause greater erosion damage [55]. Characterisation of water droplets was conducted prior to the WDE tests under the same testing conditions [77]. It can be seen that the shape of the droplets generated from the nozzle is not uniform, as seen in Fig. 2.14 (a). The distribution of droplets diameter lies in a bell-shape curve shown in Fig. 2.14 (b). Ahmad et al [86] conducted WDE tests on Ti6Al4V specimens at an impact speed of 488 $m \cdot s^{-1}$ using droplets range from 100 µm to 500 µm in diameter. The results show that the test conducted with 500 µm droplets has the shortest incubation period, while the one tested with 100 µm droplets has the longest incubation period, Fig. 2.15.

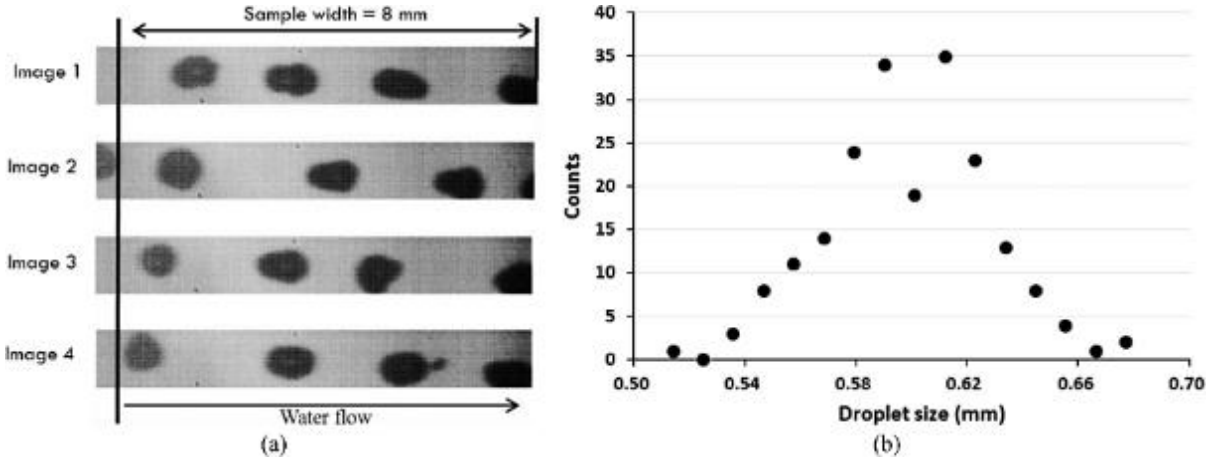

Fig. 2.14 (a) High-speed photography set-up for droplet size and shape measurements [87]; **(b)** An example of images used to study the shape of the water droplets [77].

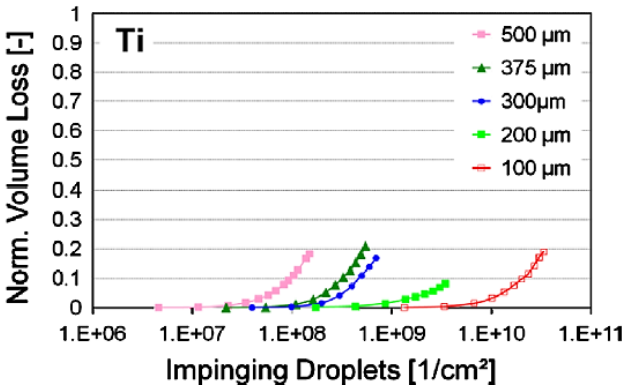

Fig. 2.15 Erosion behaviour of Ti6Al4V at different droplet sizes tested at the impact speed of 488 m·s^{-1} [86].

2.3.4 Initial surface profile of the exposed surface

It is discussed earlier that rough surface features interact with lateral outflow jetting, leading to increased erosion rate. Hence, initial surface profile of the target material plays an important role in WDE performance, especially during the incubation period [2,77]. However, little attention has been given to the early stage of the WDE research. Kirols et al. [77] studied the effect of initial surface roughness on WDE behaviour of Ti6Al4V alloy. The tests were conducted with the same droplet size (460 µm) at different impact velocities (300 m·s^{-1} and 350 m·s^{-1}, respectively) on the specimens with various surface roughness: 0.04 µm, 0.12µm and 0.30 µm. The results are shown in Fig. 2.16. It can be seen that the smooth surface prolongs the incubation period as the interaction between the surface asperities and lateral outflow jetting has been delayed.

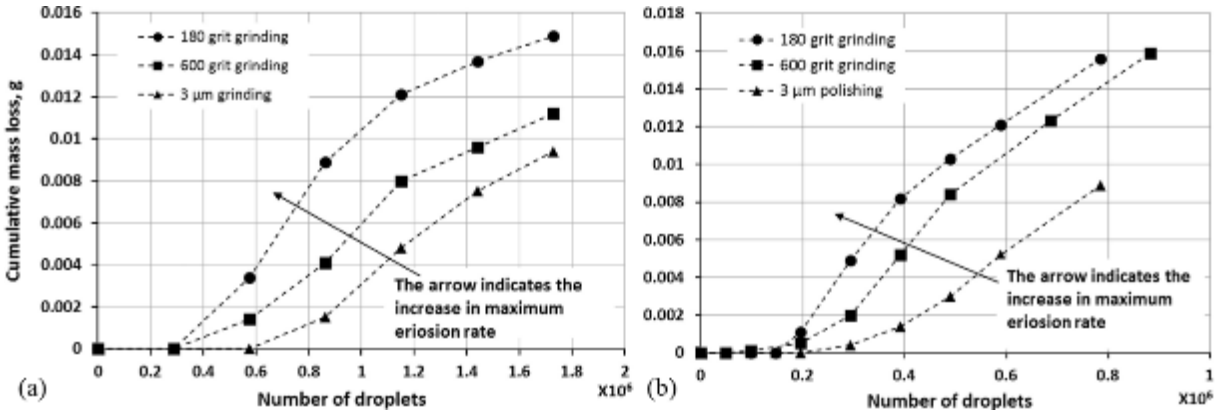

Fig. 2.16 Water droplet erosion of Ti6Al4V alloy at impact speed of (a) 300 m·s^{-1} and (b) 350 m·s^{-1} with droplet size of 460 µm for the three different surface conditions [77].

2.3.5 Geometry of the exposed surface

Little work has studied the effect of target geometry on WDE behaviour. Charles et al [88] investigated the importance of surface curvature in modelling droplet impingement on fan blades, Fig. 2.17 (a). The results suggest that the nature of WDE will be significantly affected by the curvature due to asymmetric contact stresses. Additionally, Gujba et al [89] examined

the WDE performance of the surface treated Ti6Al4V using aerofoil specimens in comparison to a flat specimen, as shown in Fig. 2.17 (b). The geometry of the specimen was found to affect the applied residual stress that later can lead to different damage mechanisms.

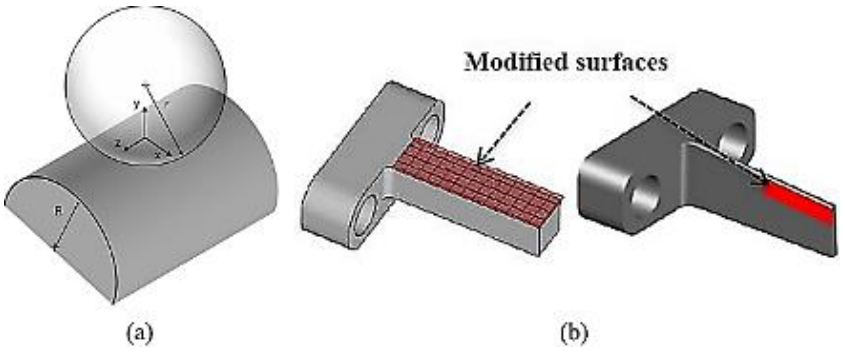

Fig. 2.17 (a) Idealised 3D geometry for droplet impingement on fan blades [88]; (b) T-shape flat and aerofoil specimens for WDE tests [89].

2.4 Test methods of WDE

2.4.1 Whirling-arm (disc) rig

Whirling-arm (disc) rig test is a standard approach for studies concerning multiple impacts, as shown in Fig. 2.18. A WDE curve that monitors the cumulative material loss with increasing test period can be plotted, which is applicable for evaluation of materials or coating resistance. The specimens are attached to the periphery of a rotating disc or arm, such that in their circular path they repeatedly pass through and impact against water jets, sprays or simulated rain drops [35]. The velocity of the specimen determines the impact velocity that can be up to 500 $m \cdot s^{-1}$. ASTM G73 [35] gives comprehensive guidelines for conducting the test and analysing the data. In addition, some of the facilities are equipped with high-speed imaging system, which enables characterization of the droplets as well as observation of the impingement process. Service experience and in-flight tests have confirmed that the whirling-arm rig test predicts the correct relative rain erosion resistance and the failure modes [5].

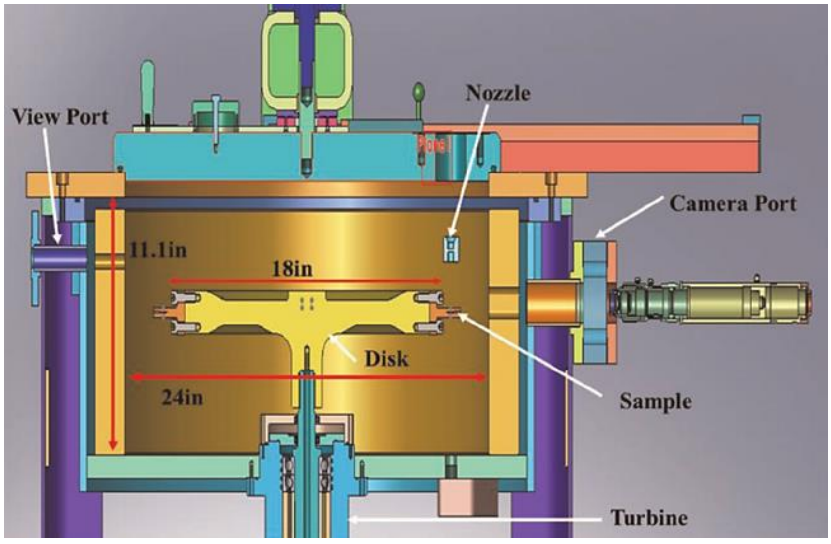

Fig. 2.18 High-speed rotating arm droplet erosion rig in Concordia University Canada [33,87,90].

2.4.2 Vibratory cavitation erosion rig

Cavitation erosion (CE) test methods such as the vibratory method has been used to screen and predict material performance for service under WDE. The results of past studies show positive correlation between WDE and CE tests [91–94]. The CE process is the explosive growth and intense collapse of bubble nuclei in a liquid when exposed to large pressure variations. Whereas water droplet impingement contains discrete water droplets, cavitation involves a continuous liquid phase with discrete vaporous bubbles or cavities. Although still debated, the nature of CE and WDE has many similarities. In fact, both processes are based on small-scale liquid/solid impacts. Many studies have shown, experimentally as well as analytically, that the asymmetrical collapse of cavitation bubbles near rigid boundaries results in high-speed re-entrant liquid jets [95–98]. These microjets penetrate the highly deformed bubbles to strike a nearby rigid boundary with a velocity up to hundreds of metre per second [99,100], generating water-hammer like impact pressure [101]. The resulting re-entrant jet has been found as a key element in pit formation on the material surface [102–104].

Additionally, under an impulsive loading generated by implosion of cavitation bubbles, stress waves are generated and propagated in the specimen. Two basic types of waves, body waves and surface waves, can be generated [105], as shown in Fig. 2.19. The body waves are the compressive wave and the shear wave, and the surface wave is the Rayleigh wave. The body waves propagate radially outward from the source along hemispherical wave fronts, and the Rayleigh wave propagates radially outward on a cylindrical wave front. The energy induced by CE can be absorbed by two parts: one is the plastic deformation on the material surface, and the other is the wave propagation and attenuation in the materials. The plastic deformation is commonly considered as the primary mode for the material to absorb the impingement energy. However, in the case of the stress waves, especially the shearing stress, are also believed to take great effects on the fracture at the initial stage of CE [106].

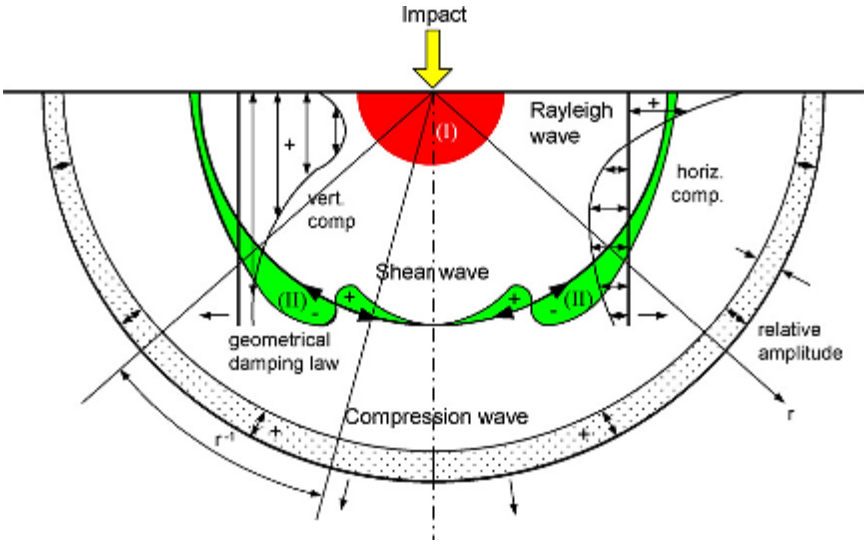

Fig. 2.19 Distribution of the stress waves in elastic half-space, and the different damage regions by the stress waves [104].

2.5 Means for combatting WDE

In order to predict WDE performance of a material, many attempts have been made to establish a simple correlation between WDE behaviour and mechanical properties. Hardness (H) was once considered to be the most reliable material property to assess the WDE resistance and it is claimed to have a linear correlation to 2.5th power of Vickers hardness number ($\propto HV^{2.5}$) [2]. However, for materials with various metallurgical structures, this simple relation does not hold. Thiruvengadam [107] was the first to propose a correlation between the CE resistance and the strain energy to fracture, but the conclusion is not applicable to a broad spectrum of materials and heat treatments. Heymann [108] demonstrated that WDE resistance is proportional to $(\sigma_u^2 E)^{2/3}$, where σ_u is the ultimate strength and E is the elasticity modulus. However, there were notable exceptions to the proposed trend. Several researchers [43,63,83,109–111] have presented the correlation between fracture toughness (K_{IC}) and WDE behaviour that brings more agreements. Fig. 2.20 shows the relation between fracture toughness and the threshold impact velocity during the WDE process for various materials. Materials with higher fracture toughness (such as diamond) tend to have higher threshold impact velocity that implies better WDE performance. Hence, it is found that developing a surface with a balanced toughness and hardness is more promising than targeting an extreme hard surface [43,63,83,109–111]. Additionally, the material variables (H, E, σ_u and K_{IC}, etc) used in the empirical models discussed above are all quasi-static derived. These values are not appropriate to use in the case of water droplet impingements, as it is a high-strain-rate loading process.

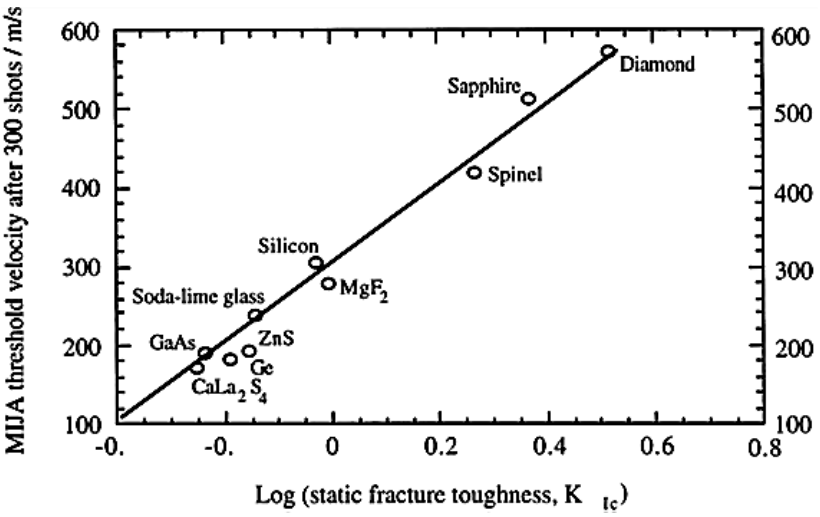

Fig. 2.20 The threshold velocity for 2 mm diameter WDE tests as a function of fracture toughness [63].

2.5.1 Surface engineering processes

Surface engineering treatments, including laser shock peening [112], ultrasonic peening [90] and ball burnishing [87], have been applied to improve WDE performance of Ti6Al4V alloy. They introduce compressive residual stress onto the surface of the material in order to retard

the crack initiation induced by tensile and shear stresses generated under droplet impingements. However, the reported results suggested that the surface engineering approaches can only be beneficial for WDE at low or moderate conditions (small droplets with low impact velocity). Researchers [79,89,90] proposed that the damage is attributed to gradient changes of the microstructure or stress state of the exposed surface through thickness introduced by surface engineering processes. Upon droplet impingements, stress waves are generated and transmitted into the material, the variation of the in-depth microstructure and stress state can affect stress wave propagation [113]. Stress wave reflection can then take place due to the mismatch of acoustic impedance. Therefore, with the repeated actions of stress wave transmissions and reflections, there will be increased potential for reinforcement of the stress waves. Tensile stress can be formed at some regions, eventually leading to brittle fracture, shown in Fig. 2.21.

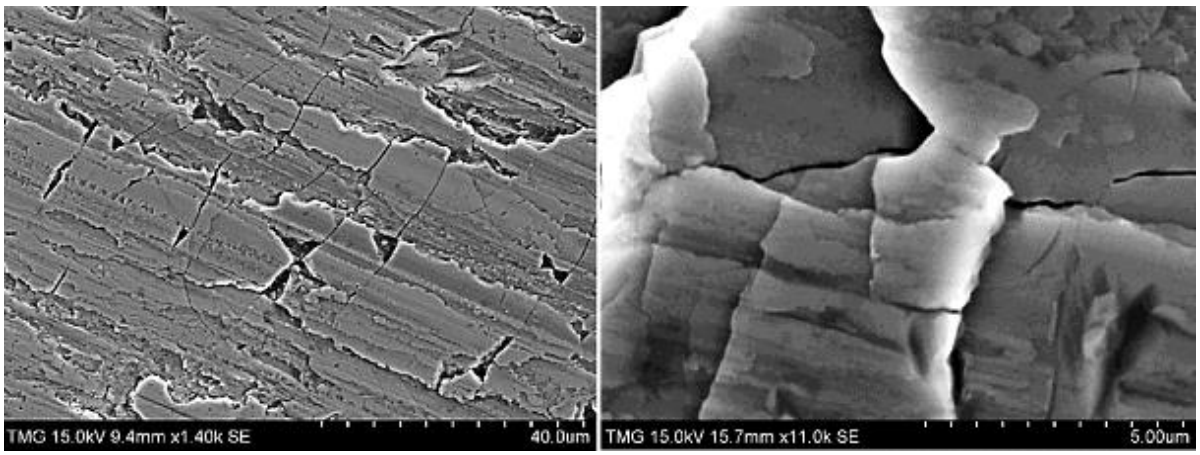

Fig. 2.21 Brittle fracture observed on ball-burnished Ti6Al4V after WDE test with 460 μm droplets at 350 $m \cdot s^{-1}$.

2.5.2 Coating approaches for WDE

Various coating approaches have been employed for WDE applications in the literature, as listed in Table 2.4. Some investigations under CE tests are also included as a general guidance in Table 2.5. The most common coating failure mode seen under WDE is induced by brittle fracture and coating delamination [37,114–116]. In comparison to the un-coated surface, the response of the coated surface to water droplet impacts can be more complicated. Stress pulses are generated and transmitted into the coated surface upon impingements. These stress waves propagate along the coating material until they encounter a structural discontinuity, such as porosity, reinforced particles or the interface between the coating and the substrate. This phenomenon results in stress reinforcement under repeated impingements, eventually leading to formation of cracks or removal of weaker elements in the coatings. Once a crack or surface asperity is formed, severe material removal mode then takes place under the joint effect of lateral outflow jetting and hydraulic penetration. Additionally, the intrinsic stresses developed during the coating manufacturing process are also a concern for coating delamination under WDE [117]. Hence, for coating applications, the primary target is to prolong the incubation period, while maintaining a smooth surface finish. Examples of selected coating systems are described in more details as follows.

Table 2.4 Review of coatings for WDE applications

Coatings	Substrates	Techniques	Thickness	Erosion Test	t_o	ER_{max}	Ref.
TiN	Stellite 6B	Ion plating	11 µm	Liquid jet, 500 µm, 380 ± 20 m·s^{-1}	0	/	[114]
	12Cr steel						
	Ti6Al4V	Laser nitriding	400 µm	Whirling disk, 200 µm, 400 m·s^{-1}	10^6 impacts	/	[37]
Ni-Al-TiC	AISI 420 martensitic stainless steel	Laser cladding	\	Water jet, 1.4 mm, 150 m·s^{-1}	60 min	0.25 mm^3/h	[118]
Ni-Al-WC						0.10 mm^3/h	
Composite coating	LY564 and Araldite/ Aradur	CNT reinforced	\	Whirling arm, 2 mm, 130 ± 20 m·s^{-1}	/	/	[119]
B2-NiTi and Ti_3Al	Ti6Al4V	Laser alloying	\	Whirling arm, 5 mm, 150 m·s^{-1}	0	0.008 mm^3/min	[120]
BP	ZnS and Ge	PACVD	\	Whirling arm, 2 mm, 211 m·s^{-1}	0	/	[121]
Ni	Cu-clad GFRP	Electro-plating	\	Water jet, 2 mm., 225 m·s^{-1}	0	/	[122]
Ni-Sic					0	/	
WC-Co	Ti6Al4V	HVOF	330 µm	Whirling disc, 460 µm, 250/300/350 m·s^{-1}	0	2.1 *10^{-5} mm^3/mm^3	[115]
					0	1.9	
					0	1.2	[115]
Ni-W	FRP	Electro-plating	34 µm	Water jet, 2 mm, 225 m·s^{-1}	/	/	[116]
Ni			30 µm		/	/	
Diamond	Silicon	CVD	4.8-10.5 µm	Multi-impact jet, 800 µm, 350 m·s^{-1}	/	/	[117]

*** t0** is incubation period; **ER_{max}** is the maximum erosion rate

Table 2.5 Review of coatings for CE applications.

Coatings	Substrates	Techniques	Erosion Test	to (min)	Thickness (µm)	Ref
CrN	X6CrNiTi18-10 steel	PVD	Cavitation tunnel	180	4	[123]
TiN				300		
CrN/CrCN				30	4.3	[124]
Ti/TiN-4				60	3.7	[125]
(NiTi/TiCN)0.5	steel		Vibratory cavitation	60	3.32	[126]
Ni- SiC	1045 carbon steel	Electroless-plating		0	/	[127]
Nanocrystalline diamond	Silicon	HF-CVD		30	1	[128]
M6-HV	Stainless steel	HVOF		15.6	134 ± 6	[129]
WC-CoCr				61.8	107 ± 12	[129]
Cr_3C_2-NiCr				0	30 - 40	
CoMoCrSi	Carbon steel	Plasma spray		0	/	[130]
FeNiCrBSiNbW	Stainless steel	Arc spray		0	230	[131]

*** t0** is incubation period

i. Nickel plating

Nickel based coatings have been a popular option for erosion applications because of the well-developed techniques and low cost of manufacturing. A variety of reinforcements have been employed in Nickel eletroplating process to improve coating properties, such as SiC particle and carbon nanotube. However, the interface between the Nickel matrix and reinforcements can act as a stress raiser during droplet impingements. This results in the removal of the reinforced particles from the matrix, leading to coating failure [122].

ii. HVOF tungsten carbide/cobalt (WC-Co) coatings

HVOF WC-Co coatings have been widely applied for solid particle erosion protection. The thickness of the coatings can reach up to hundreds of microns. Researchers intend to extend the application to droplet erosion. However, the high amount of defects (including porosity, splats and oxides) formed during the manufacturing process result in highly inhomogeneous coating structure. These defects causes stress concentrations and introduce detrimental consequence under water droplet impingements [115,132,133]. Additionally, the high operating temperature for HVOF process is another concern as the properties of the base material can be affected.

iii. PVD TiN coatings

TiN coating has been studied by several researchers for combating WDE [37,134]. Various techniques have been used to apply TiN coatings, such as gas nitriding, laser nitriding and plasma nitriding. Failure due to brittle fracture is reported as the primary damage mechanisms for most of the TiN coatings. PVD multilayer coatings have been investigated for CE applications [124,125]. An increased incubation period was observed in the CrN/CrCN coating system with austenitic steel substrate [124], which was attributed to the enhanced adhesion and stiffness.

iv. Chemical Vapour Deposited (CVD) coatings

CVD coatings have been succefully applied for solid particle erosion protection. However, few studies examine its potential on WDE application. The CVD diamond coating has been applied on a range of IR-transparent substrates for WDE investigation [117]. However, the thermal and intrinsic stresses are a problem and cause extensive coating delamination and catastrophic sample failure.

v. Polymer coatings

In addition to hard coatings, elastomeric coatings (a type of polymer coatings), by the virtue of their elasticity can reduce the magnitude of the impact pressures, perform successfully in low-intensity environments [135,136]. This approach is widely applied on wind turbines and helicopter blades against rain erosion at moderate speeds [137].

2.6 Summary

Until now WDE studies have depended mainly on laboratory testing to determine what might be happening on leading edges of aero-engine blades, while the real world is much more complicated in terms of what these edges experience and indeed what erosive mechanism are actually occurring in operation. Thus, the present research is an invaluable opportunity to validate the results obtained from laboratory tests by comparing with the real-life WDE, which then helps to further elucidate the damage mechanisms behind WDE. Additionally, although the WDE mechanisms of Ti6Al4V in the advanced stages has been well established, the phenomenon occurred during the incubation period still leaves research gap.

Whirling-arm rig test is the standard approach for evaluation of WDE resistance. However, there is limited access with only a few rigs in the world can reach over an impact velocity of 300 m/s. Moreover, the high cost for conducting the whirling-arm rig tests is undesirable. Therefore, vibratory CE test is considered as a more practical and cost-effective screening process for WDE. The WDE and CE process share similar damage mechanisms, still there is a lack of detailed examinations of their correlations.

Many attempts have been made to correlate the WDE resistance to single mechanical property; however no universal agreement has been established. WDE is a complicated process and that a combination of material properties should be considered when combatting such a phenomenon. Additionally, water droplet impingement is a dynamic loading process with a high strain rate, hence, dynamic mechanical properties are applicable.

In the case of the best means to combat WDE, surface treatments might only be beneficial for low intensity WDE with low impact velocity. For high intensity WDE with high impact velocity, the search of solution is more challenging. Various coatings approaches have been investigated under WDE and CE. However, no significant enhancement is found. For coating applications, in addition to the premise of a strong adhesion to the substrate, a hard yet tough surface is desired. The ideal coating surface should not only resist the high impact pressure, but also inhibit stress wave reinforcements at the interface. It is believed that the key to combat WDE with coatings is to prolong the incubation period while maintaining smooth surface finish. This would impede/delay the interaction between surface asperities and lateral outflow jetting, which is the driven force for instant increase of the erosion rate.

Chapter 3.
Experimental methodologies

This chapter describes the experimental metrologies applied in this study. Some techniques have been used for several subjects, therefore, only the general procedure is given. The more specific procedures and parameters employed are demonstrated in the corresponding chapter.

3.1 Sample preparation

3.1.1 Cutting

i. Ti6Al4V turbofan blade

Two ex-service Ti6Al4V turbofan blades from the same aeroengine model were investigated. The length of as-received blades is around 0.95 m. The diameter of the fan is around 2.5 m. They were taken out from significantly different flight cycles, where Blade 1 exhibits less severe damage at the leading edge than Blade 2. Both blades are designed with certain curvature for enhancement of aerodynamic performance. Each blade was received as 4 sections, as shown in Fig. 3.1. Section *a* and *b* were the leading edges of the turbofan blades, which are the main focus of this study; section *c* and *d* were the trailing edges. Specimens were cut from the leading edge sections using a precision cutting saw (Mecatome T210) with a diamond blade under a feed rate of 0.05 $mm \cdot s^{-1}$ at the rotation speed of 3600 rpm. Sufficient coolant was used to minimize the heat generated during cutting. The specific procedures regarding the sample preparation are given in details in Chapter 4.

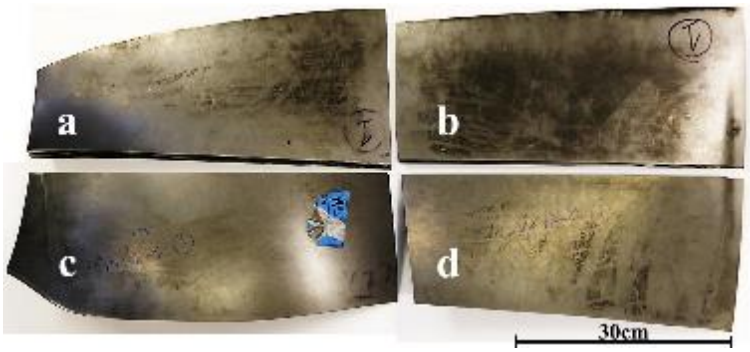

Fig. 3.1 As received ex-service turbofan blade.

ii. Ti6Al4V base material

A Ti6Al4V plate (Grade 5) was provided by Rolls Royce aeroengine UK, which was the base material for manufacturing the turbofan blades. The specimens were cut by water-jet cutting and machining into the dimensions required for CE and WDE tests: 25 mm × 25 mm × 5 mm and 25 mm × 8 mm × 3 mm, respectively. The characterisations of Ti6Al4V base material are presented in Chapter 5.

3.1.2 Mounting

The sectioned small specimens were mounted using KonductoMet (a conductive phenolic mounting compound with good edge retention that will contribute to quality of microscopic observation) and a hydraulic press Buehler Simplimet 2000 for cross-sectional analysis. The process involves heating for 4 minutes at 150° C under 290 bar pressure and cooling for 3 minutes. The diameter of the mounted specimens is 32 mm. The thickness of which is about 2.5 cm.

3.1.3 Grinding and polishing

Grinding and polishing of the mounted specimens was performed with a semi-automatic polishing equipment, SAPHIR 520. The specimens used for metallography observation were polished to a mirror-like, bright surface following the procedure listed in Table 3.1. The procedure was adapted following the consultation from MetPrep Ltd and adjusted for current project. An ultrasonically cleaning process was applied in a solution of distilled water and methanol.

Table 3.1 Metallurgical preparation of Ti6Al-4V specimens

Preparation	Abrasive	Lubricant	Load per sample	RPM	Time (mins)
Grinding	220 500 1200	Water	10-15N	300	5-10
Polishing	9 µm on MD Dac	Diamond	15N	150	5-10
	0.04 µm OP-S on Chemical Cloth				10-60

3.2 Topographical characterisation

The rain erosion morphology of the leading edge specimens were observed using Alicona InfiniteFocus G4 system. The process was conducted using × 20 lens with 75 nm of vertical resolution and 2 µm of lateral resolution. The software captures multiple images of the same object in different distances (Z-position) within a given range (upper/lower) in order to build 3D models of the leading edge profile. The same parameters were applied for constructing surface profiles of the specimens after CE and WDE tests.

The system was also applied for measurements of surface roughness values. For the leading edge specimens, it was used for comparing the surface roughness values of the leading profiles at different impact velocities. A cut-off wavelength (Lc) of 800 µm and a profile length of 5 mm were used for the measurements. The results are shown in Chapter 4. For the coated specimens, the measurement was conducted with × 100 lens using 10 nm vertical resolution.

3.3 Microstructural characterisation

3.3.1 Optical microscope

An optical microscope Olympus BX51P was used for cross-sectional observations of the mounted specimens. The software Stream Essentials was used to measure depths of erosion craters from images taken at different magnifications ranging from x50 to x1000.

3.3.2 Scanning Electron Microscope (SEM)

i. Secondary electron imaging (SEI) / backscattering electron imaging (BEI)

A JEOL 6500F Field Emission Gun (FEG)-SEM was used for microstructural analysis. 15 kV of the voltage and 10 μA of the current at 10 mm working distance was applied for both secondary electron imaging (SEI) and backscatter (BEI) modes, which allows topographical and compositional information to be obtained from the specimens

ii. Energy-Dispersive X-ray Spectroscopy (EDS)

Energy-dispersive X-ray spectroscopy (EDS) was conducted on the cross-section of specimens to identify the coating chemical composition. The technique was used for characterisation of Hardide coatings in Chapter 6 and Chapter 8.

iii. Electron back-scattered diffraction (EBSD)

In order to further understand the orientations of the facets on the as-deposited surface, electron back-scattered diffraction (EBSD) analysis was performed using SEM equipped with a NordlysMax3 detector, a CCD camera, the AZtekHKL data acquisition software and the Channel 5.0 post-processing analysis package. The samples were tilted at 60°, the accelerated voltage was set to 20 kV, the minimum step size was 0.2 μm and the indexing was over 80% for all the mappings. EBSD analysis was applied on the Ti6Al4V turbofan blade in Chapter 4; Ti6Al4V base material in Chapter 5 and Hardide W/WC coatings in Chapter 6. The parameters used for each system are demonstrated in details in the corresponding chapters.

3.3.3 Focused-Ion Beam (FIB)

A FEI QUANTA 3D FEG - SEM was used for milling and imaging the cross-sections of the HIPIMS multilayer coatings at the point of interest. FIB was also used for preparation of TEM specimens. This part of the experimental work was carried out and analysed by the National HIPIMS Centre at Sheffield Hallam University. The results are shown in Chapter 7.

3.3.4 Transmission Electron Microscopy (TEM)

Detailed analysis of the HIPIMS multilayer coating microstructure in terms of the nanoscale multilayer architecture, interfaces, epitaxy and density among the columnar grains was carried out using bright field TEM (Philips STEM 420 equipped with a LaB6 filament) by National HIPIMS Centre at Sheffield Hallam University. The results can be seen in Chapter 7.

3.3.5 X-ray Diffraction (XRD)

i. Phase composition

X-ray diffraction (XRD) analysis was carried out using a Rigaku SmartLab diffraction system (Rigaku Corporation, Japan) with Cu-Kα X-rays to identify the phase composition of Hardide W/WC coatings. The diffractometer was operated at a grazing incidence angle of 1° for phase identification of the top-surface coatings. The results are shown in Chapter 6.

ii. Crystalline texture

The texture of the HIPIMS nanoscale multilayer structure was investigated using Brag-Brentano geometry (20°-130°) X-Ray Diffraction (XRD) technique (PHILIPS XPERT) at Sheffield Hallam University. Texture coefficient (T*) was calculated using the following equation [138,139]:

$$T^* = \frac{I_{hkl}/R_{hkl}}{(1/n)\sum_0^n (I_{hkl}/R_{hkl})} \qquad \textbf{Equation 5}$$

where $I_{(hkl)}$ is the measured peak intensity from the (hkl) reflections, R_{hkl} is the reference standard (random) peak intensity from the (hkl) reflections and n is the number of reflections considered. The JCPDS values of peak intensity were used as the standard reference (R_{hkl}) intensity values since it was not possible to determine R_{hkl} intensity values for a randomly oriented coating material. The corresponding results are discussed in Chapter 7.

Glancing angle geometry XRD technique was used for determining the residual stress in the coatings by Sheffield Hallam University. The angle of incidence to the substrate was fixed at a low angle of 2º where a scan rate of 0.008º per second was employed. Residual Stress (σ) was calculated from the slope of the least-squares fit of the plot of a_Ψ versus $\sin^2\Psi$ and using the following expression

$$\boldsymbol{\sigma = \frac{Slope\ E}{a_\Psi\,(1+\nu)}} \qquad \textbf{Equation 6}$$

where E is the elastic modulus, a_Ψ is the lattice parameter and ν (0.3) is the Poisson's ratio [139]. The elastic modulus E was determined by nanoindentation test. A nano hardness tester (CSEM-Anton Paar) with a Berkovich indenter was used to evaluate E of the coatings. The applied load for all of the elastic modulus measurements was 30 mN. The lattice parameter a_Ψ can be calculated for each diffraction peak where Ψ is the angle between the diffraction vector of

planes (hkl) and the normal to the surface, such that $\Psi = \theta - \gamma$ where θ is the Bragg angle and γ is the angle of incidence of the X-ray beam relative to the specimen surface.

3.4 Mechanical characterisation

3.4.1 Nanoindentation test

Nanoindentation tests were performed using a Micro Materials NanoTest Vantage system equipped with a Berkovich diamond indenter, calibrated by using a standard fused silica sample. All tests were carried out at a stabilized chamber temperature of 25 °C on the polished surface and cross-sections. A depth control mode of 300 nm was applied for measurements of the Ti6Al4V leading edge and Ti6Al4V base material. A load control mode of 30 mN was used for measurements of Hardide W/WC coatings. Thermal drift was measured by adding a dwell period of 60 s during unloading and calculated over 60% of the collected depth vs time data. The nanohardness (H) and reduced Young's Modulus (E_r) were calculated using Oliver-Pharr methodology [140]. The nanohardness (H) can be defined as the maximum indentation load (P_{max}) divided by the projected area of contact (A_p), which is estimated from the projected contact depth (h), as schematically shown in Fig. 3.2, such that,

$$H = \frac{P_{max}}{A_p}; \quad A_p = 24.5h^2 \qquad \textbf{Equation 7}$$

The reduced elastic modulus (E_r) is measured from the slope of unloading curve $(\mathrm{d}P/\mathrm{d}h)$, which is given by,

$$E_r = \frac{1}{2}\frac{\sqrt{\pi}}{\sqrt{A_p}}\frac{dP}{dh} \qquad \textbf{Equation 8}$$

The elastic modulus can be calculated using the equation shown below,

$$\frac{1}{E_r} = \frac{1-\nu_m^2}{E_m} + \frac{1-\nu_i^2}{E_i} \qquad \textbf{Equation 9}$$

Where E_m and ν_m are the modulus and Poisson's ratio of the indented material, and E_i and ν_i are elastic modulus and Poisson's ratio of the indenter, which correspond to 1140 GPa and 0.07 for the Berkovich indenter, respectively.

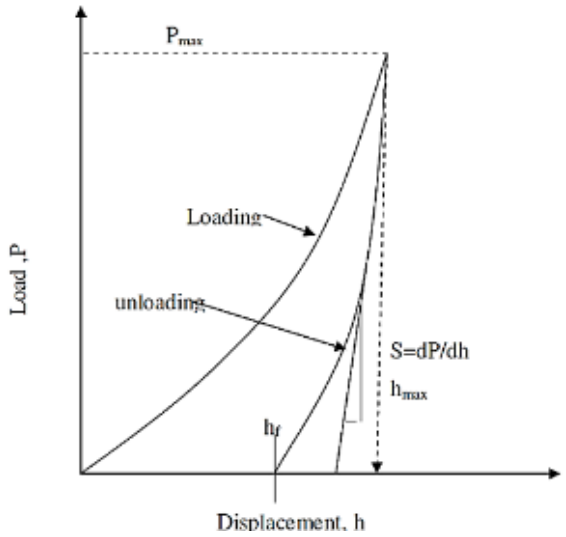

Fig. 3.2 A schematic of the loading and unloading curve obtained from one load cycle during nanoindentation.

3.4.2 Knoop hardness test

The Knoop hardness of the HIPIMS multilayer coatings was investigated with Mitotoyo microhardness tester using a 0.25N load by the National HIPIMS Centre at Sheffield Hallam University. The results are shown in Chapter 7.

3.4.3 Scratch test

The adhesion of HIPIMS multilayer coatings was measured by the Daimler Benz, (DB) Rockwell indentation test, (ISO 26443) as well as a progressive loading scratch test (maximum load: 80 N) conducted on CSEM-Anton Paar REVETEST, (ISO 20502) by the National HIPIMS Centre at Sheffield Hallam University. The results are discussed in Chapter 7.

3.5 Vibratory CE test

An ultrasonic induced cavitation device (UIP 1000 hdT, Hielscher Ultrasound Technology) was used to carry out the CE tests in distilled water bath maintained at laboratory temperature (~ 25 °C) with procedures following ASTM G32-92. The specimen was in the dimension of 25 mm × 25 mm × 5mm and in a location opposite to the vibrating tip of titanium sonotrode. Cavitation was induced by longitudinal oscillation at 20 kHz at a peak-to-peak amplitude of 50 μm. The titanium tip (grade 5) of the vibrating horn was 18 mm in diameter. A stand-off distance between the tip of the sonotrode and surface of the specimen was set to 1 mm using a filler gauge. Fig. 3.3 shows the schematic of the experimental setup. After each test interval, the specimens were rinsed, dried and weighed by an analytical balance with a sensitivity of 0.1 mg to determine mass loss. An average value and standard deviation was obtained from 5 readings taken after each test interval. The results of CE tested on Ti6Al4V base material are

discussed in Chapter 5; while those tested on coating systems are shown in Chapter 6 and Chapter 7.

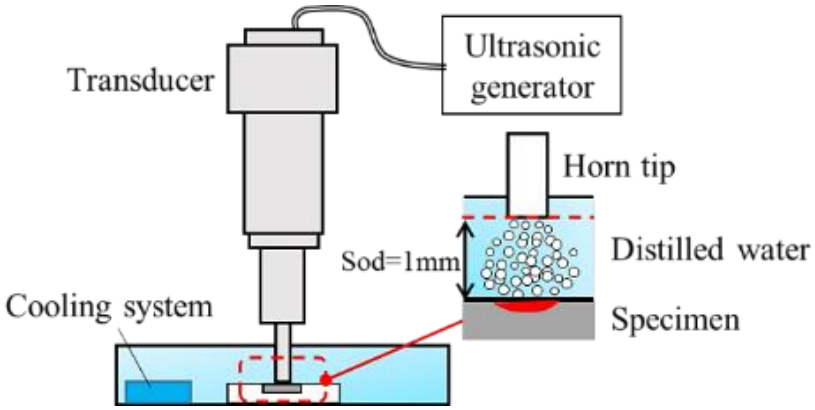

Fig. 3.3 Vibratory cavitation erosion test setup.

3.6 Whirling-arm WDE test

WDE tests were conducted with a whirling arm rig at National Physical Laboratory (NPL) in Teddington, as shown in Fig. 3.4. The chamber was kept under vacuum during the tests. An impact velocity of 300 $m \cdot s^{-1}$ was used and it was the maximum applicable speed of the rig. The droplets were generated using deionised water by a 300 µm film nozzle, which was fixed in a cylinder. The assembly was then installed horizontally into the port inside the chamber prior to the tests. Therefore, the droplets were ejected horizontally inside the chamber during operation, Fig. 3.5 (a). The droplet diameter was characterised with high-speed imaging system and majority of the droplets ranges from 425 to 550 µm in diameter, as shown in Fig. 3.5 (b). The specimens were inserted into the sample holders and fixed with screws, Fig. 3.6. The surface of the specimens were polished up to a Ra of 0.05 µm and 0.16 µm, respectively, for investigation of the initial surface roughness of WDE behaviour of Ti-6Al-4V. The specimens were installed in the sample holders at both sides of the rotating arm and fixed with a torque screwdriver under 1 Nm. The tests were conducted under various time interval following ASTM G73-10 (2017). The mass loss was monitored after each test interval. The specimens were rinsed, dried and weighed by an analytical balance with a sensitivity of 0.1 mg. An average of 5 readings were taken for the tested specimen after each interval. The WDE test results of Ti6Al4V base material are discussed in Chapter 5 and those of the coated specimens are shown in Chapter 8.

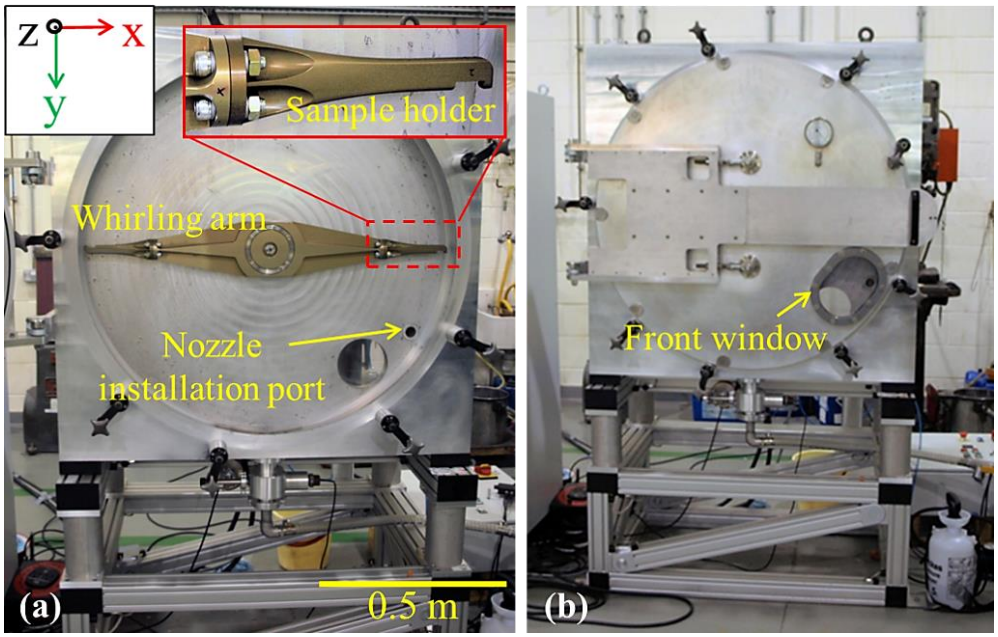

Fig. 3.4 Whirling arm rig at NPL Teddington.

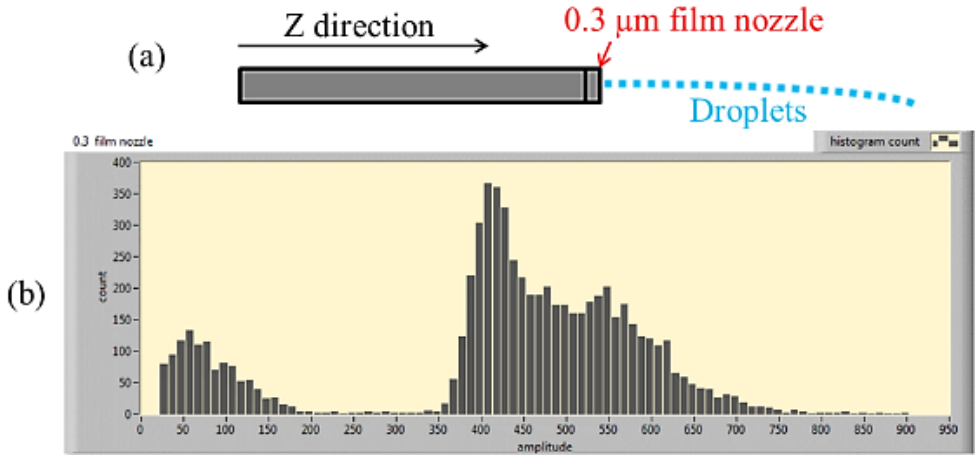

Fig. 3.5 (a) 0.3 μm film nozzle; **(b)** distribution of droplet diameter.

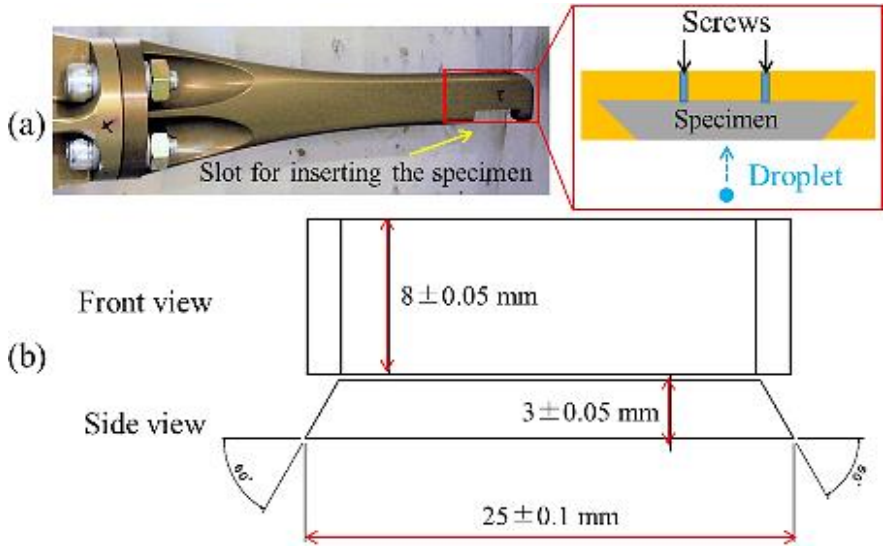

Fig. 3.6 (a) schematic of specimen installation; **(b)** specimen dimension.

Chapter 4.

Characterisation of rain erosion at ex-service turbofan blade leading edges

Past WDE studies have depended mainly on laboratory testing to determine what might be happening on leading edges of aeroengine blades, while the real world is much more complicated in terms of what these edges experience and indeed what erosive mechanism are actually occurring in operation. Therefore, this chapter aims to fill this gap in knowledge by examining the ex-services Ti6Al4V turbofan blades to further elucidate the damage mechanisms behind WDE.

4.1 Material characterisation

Two ex-service Ti6Al4V turbofan blades from the same model of aeroengine were investigated in this study. They were taken out from significantly different flight cycles, where Blade 2 exhibits more severe damage at the leading edge than Blade 1. Both blades are designed with certain curvature for enhancement of aerodynamic performance. The blades were sectioned into 4 parts, as labelled in Fig. 4.1. Section *a* and *b* were the leading edges of the turbofan blades, which are the main focus of this study; section *c* and *d* were the trailing edges. Three zones of interests were selected from the blade leading edges to examine the effect of impact velocity on the rain erosion damage. They were labelled as L (low speed), M (moderate speed) and H (high speed) zones, which correspond to the root, centre and the tip of the blades. For each zone, three specimens were sampled with 1 cm in width and 1 cm in height (distance away from the leading edge toward the blade surface), as marked in Fig. 4.1. While for the H zone, macro inspection shows that the tip of the leading edges (where the impact velocity is known to be approximately 400 $m \cdot s^{-1}$) exhibits notably less damage compared to the section that is about 3 cm away. Therefore, three additional sites were sampled for further investigation. The specimen designations include blade number, section and number in that section, such as 1L1 for the L1 zone of Blade 1, 2L1 for that of Blade 2 and so on. The impact velocity was assumed to be proportional to the blade radius. Hence, the corresponding impact velocity for each site of the leading edges is computed and listed in Table 4.1.

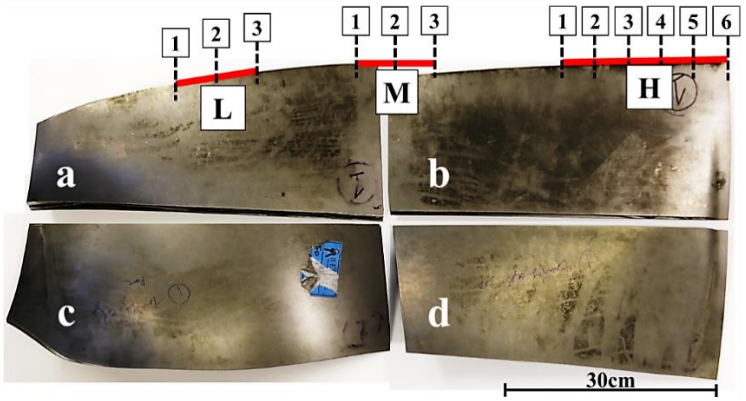

Fig. 4.1 As received ex-service turbofan blade.

Table 4.1 Impact of velocity at each site of the leading edges.

Impact velocity / m·s^{-1}											
Root side			**Centre**			**Tip side**					
L1	L2	L3	M1	M2	M3	H1	H2	H3	H4	H5	H6
144	164	204	226	246	286	308	328	348	368	382	396

Samples were cut in cross-section, polished with 1 µm diamond suspension and 0.04 µm colloidal silica prior to Scanning Electron Microscope (SEM) examination of its microstructure. A duplex microstructure composed of equiaxed primary α-grains (α_p) and a lamella-structured secondary α_s embedded in β matrix is observed in Fig. 4.2 (a). Electron Backscatter Diffraction (EBSD) was also performed on the polished cross-sections for quantitative microstructural analysis of the Ti6Al4V blade material. A step size of 0.85 µm was used. The average grain size was estimated using the linear intercept method, which is 9.73 ± 5.28 µm. Moreover, different grain orientations are given in the form of a colour-map in Fig. 4.2 (b).

Nanohardness measurements using a Micro Materials NanoTest Vantage system equipped with a Berkovich diamond indenter were conducted on the polished blade cross-sections. A depth control mode of 300 nm was applied and nanohardness and reduced Young's Modulus were calculated using Oliver-Pharr methodology [140]. Results are listed in Table 4.2.

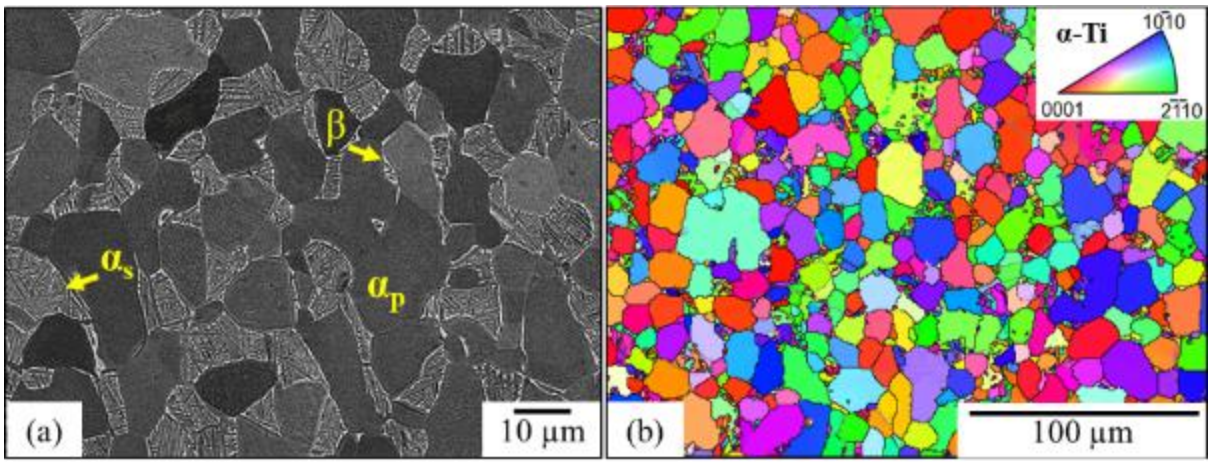

Fig. 4.2 (a) Microstructure of the ex-service Ti6Al4V turbofan blade leading edge; **(b)** Colour-map showing different orientations of α-Ti grains.

Table 4.2 Nanoindentation measurements of ex-service Ti6Al4V fan blade material.

Nanohardness / GPa	4.86 ± 0.97
Reduced Young's Modulus / GPa	145.44 ± 15.10

4.2 Rain erosion metrology at turbofan blade leading edges

Inspection via Alicona profilometer indicates that the rain erosion occurs exclusively at the leading edges. No sign of damage induced by rain droplet impingements was observed at the trailing edges. Results obtained from L1, L3, M2, H1, H3 and H6 zones of both blades are presented for comparison in Fig. 4.3 and Fig. 4.4. From L zone to H zone, rain erosion

morphology evolves with increasing severity along both leading edges. By comparing the two blades, it can be seen that specimen 1L3 exhibits negligible damage, while specimen 2L3 shows roughened surface due to the formation of cavities. Initiation of the rain erosion is found at the highest curvature of the leading edge profile, which can be further confirmed from cross-sectional analysis in the following section. As the rain erosion process develops with increasing impact velocity at M and H zones, 'canyon'-like morphology starts to form on both blades due to significantly increased material loss. However, more prominent 'canyon' feature is observed on Blade 2 leading edge with the angle of the peaks is around 45º, as shown in Fig. 4.4-2H1 and 2H3. The severity of the rain erosion damage decreases after H3 zone towards the tip of the blade (H6 zone) at both leading edges. This is believed to be attributable to the shielding effect of the fan blade casing.

The rain erosion morphology observed on the ex-service blade leading edges presents unique characteristics that are not commonly found on the laboratory tested specimens. This is because in majority of the test rigs, the droplets are generated by nozzles with one orifice to simplify and better control the test conditions. Furthermore, most of the tested specimens consist of flat surfaces perpendicular to the droplet impact. Hence, an erosion line with deep craters is typically formed across the exposure surface, an example shown in Fig. 4.5 (a). Kirols et al. [33] examined WDE morphology from the side of an ex-service steel steam turbine blade after severe steam erosion with 100 µm-droplets at supersonic impact velocity, Fig. 4.5 (b). The magnified damage zone displays homogenously compacted 'canyons' that resemble the 3D profiles of M and H zones at the leading edges. It should be noted that the rain droplet size ranges from 0.5 mm to 2 mm, which is significantly larger than steam droplets. This can contribute to the 'canyons' formed by rain erosion are more scattered.

The rain erosion damage is initiated at the centre of the leading edge surface, where the profile with the highest curvature is found. Continuous rain droplet impacts result in the broadening of the damage region assisted by lateral outflow jetting interacting with surface irregularities. The erosion craters are deepened due to hydraulic penetration, which eventually shapes the surface into such 'canyon' feature. With damage accumulation, repeated impinging droplets can be trapped within the exposed 'canyon walls', leading to stress concentration, which enhances the effect of lateral outflow jetting and hydraulic penetration, thus, further broadening and deepening the valleys that consequently sculptures the large steep 'cliff', as shown in Fig. 4.4-H1.

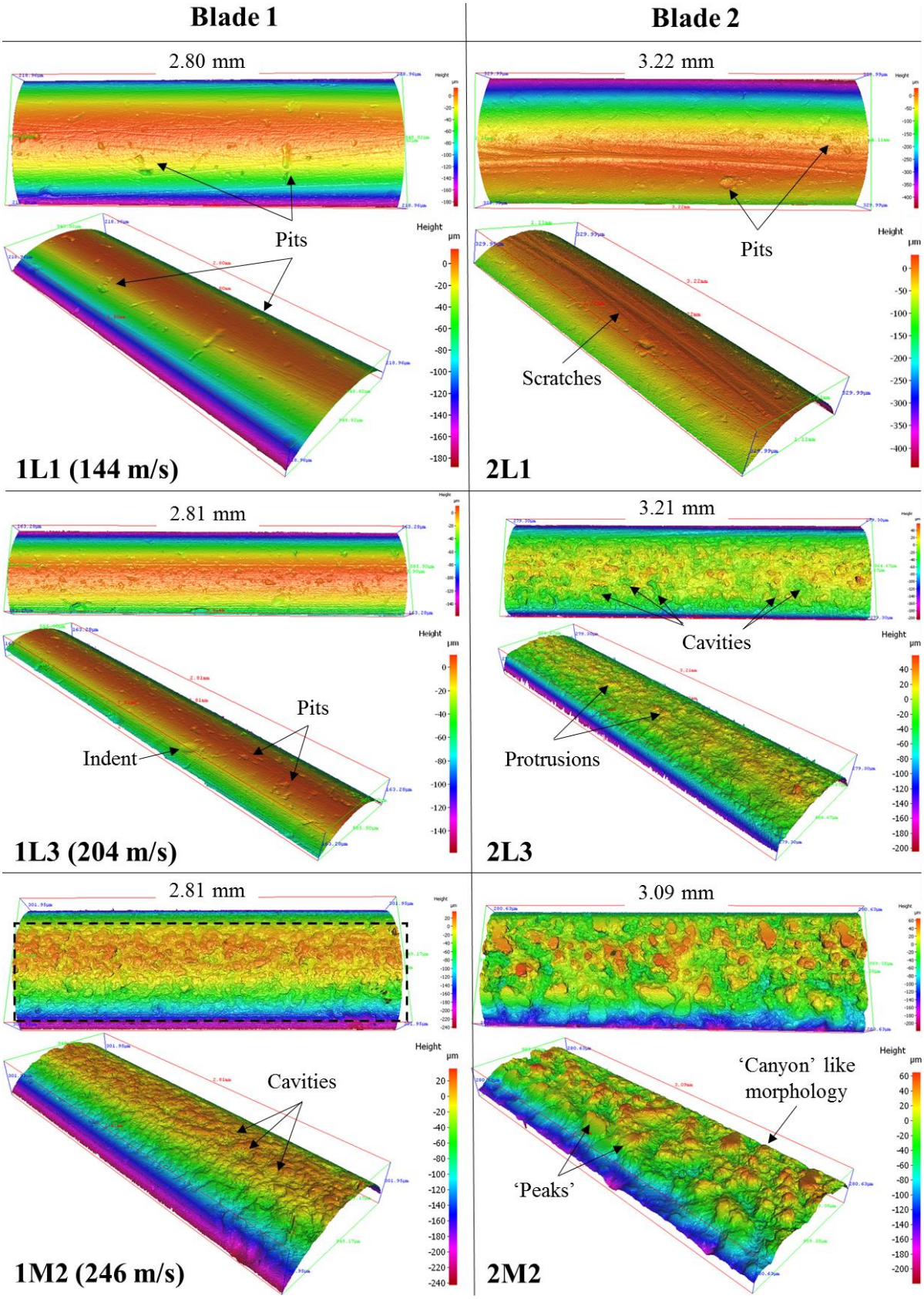

Fig. 4.3 3D profiles of L1, L3 and M2 zones of both leading edges.

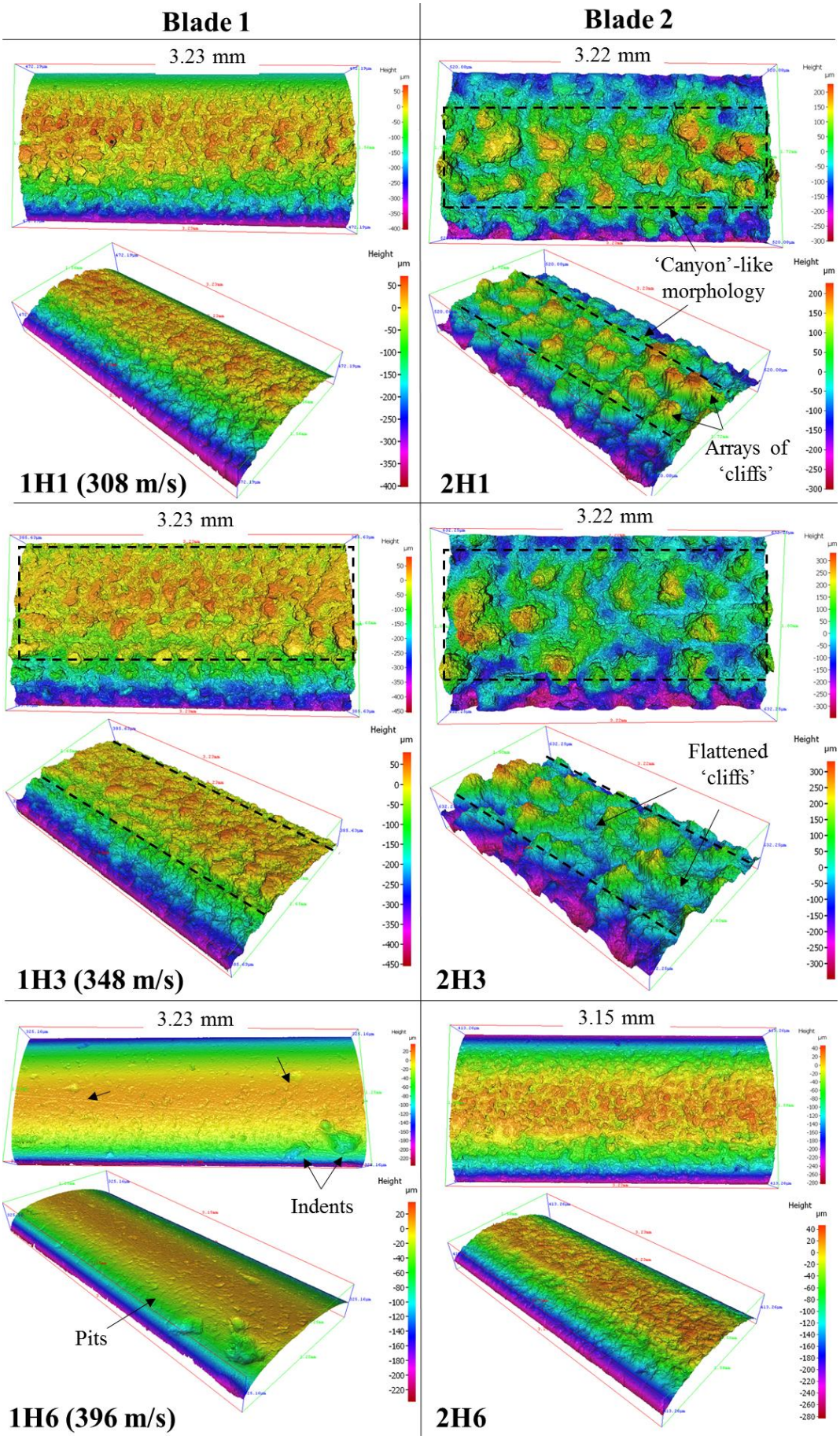

Fig. 4.4 3D profiles of H1, H3 and H6 zones of both leading edges.

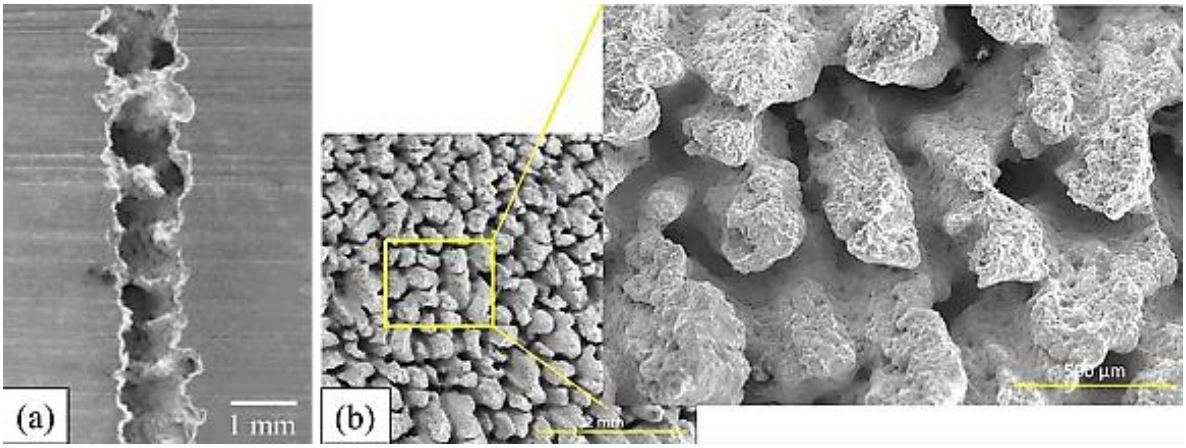

Fig. 4.5 (a) Advanced stage of WDE on flat Ti6Al4V specimen tested with whirling arm rig [71]; **(b)** steam erosion on the side of ex-service steam turbine blade [33].

4.3 Effect of impact velocity of rain erosion at turbofan blade leading edges

Quantitative characterisation of erosion morphology was conducted with line scans (Alicona) on the leading edges. For each 3D profile, 3 line scans with a length of 5 mm were placed along the leading edge. Measurements of width and depth of the five largest erosion craters were collected from each line scan. Examples of the measurements are given in Fig. 4.6. Additionally, 2D (Ra, Rq and Rz) and 3D roughness (Sa, Sq and Sz) data was also obtained from the measurements conducted on the leading edge profiles, which reveals the variations in roughness values along the leading edge. All roughness parameters follow a similar trend, example of Rq is shown in Fig. 4.7. Comparison of Blade 1 and Blade 2 roughness shows that notable increase of roughness values takes place for impact velocities over 204 $m \cdot s^{-1}$. The increment becomes more significant for impact velocities range from 286 to 368 $m \cdot s^{-1}$.

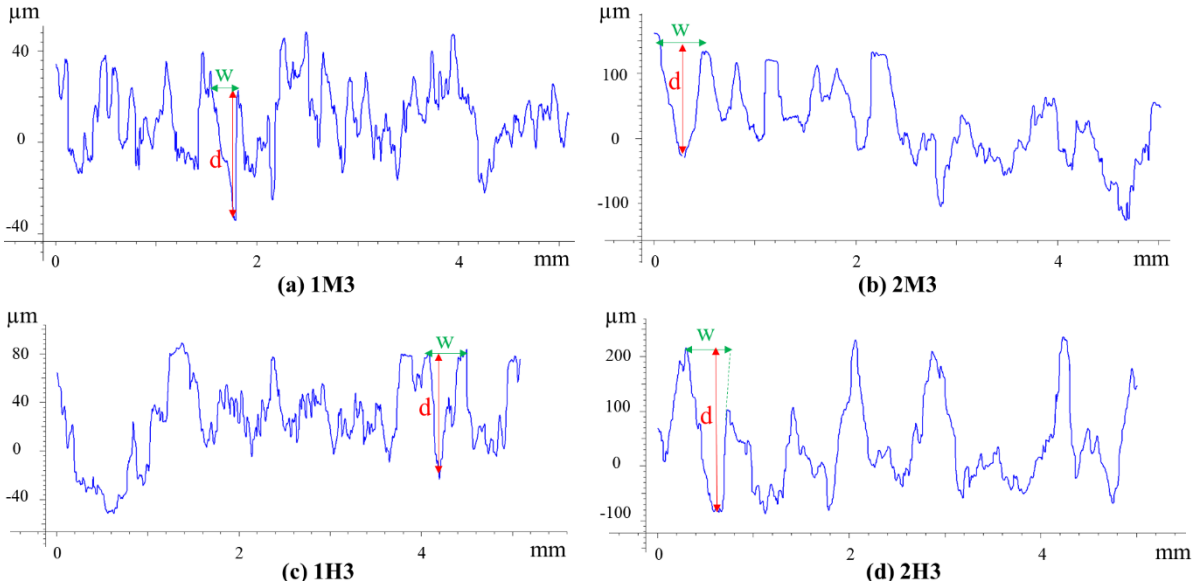

Fig. 4.6 Examples of line scan profiles at H3 zones for measurements of mean crater width and depth.

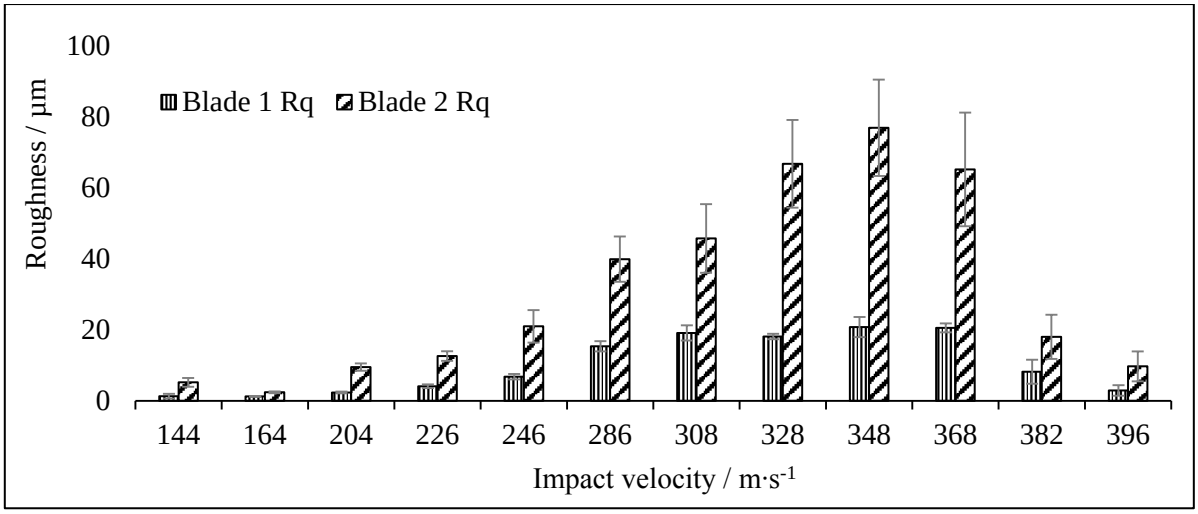

Fig. 4.7 Comparison of Rq values between Blade 1 and Blade 2.

Mass-loss or volume-loss against exposure duration is typically monitored during laboratory WDE studies to determine the erosion rate of a test subject, however, this process cannot be applied in the case of ex-service turbofan blades. Therefore, a cone-shape erosion crater geometry is assumed to further quantify erosion damage (Fig. 4.6). The volume-loss per crater can then be computed using Equation 10 with the mean width and depth measurements. The results shown in Fig. 4.8 reveal a general increasing trend in material loss with impact velocity. The volume loss per crater reaches the maximum at 348 m·s^{-1} (H3 zone) for both blades. The magnitude of increment is more significant in Blade 2. This agrees with the morphological analysis, since Blade 2 exhibits more severe rain erosion damage than Blade 1 (already discussed in the previous section).

$$\upsilon = \frac{d}{3}\pi(\frac{w}{2})^2 \qquad \textbf{Equation 10}$$

where υ is volume loss per crater, d is mean crater depth and w is mean crater width.

The relative material loss between Blade 1 and 2 (plotted as red line in Fig. 4.8) can be considered as the accumulated damage after incubation period at various impact velocities. It reveals that negligible material loss takes place for impact velocities lower than 200 m·s^{-1}. However, a significant increase of material removal behaviour is detected for impact velocities higher than 286 m·s^{-1}. A linear relationship between the relative volume loss and impact velocity is established from 286 to 348 m·s^{-1}, as shown in Equation 11.

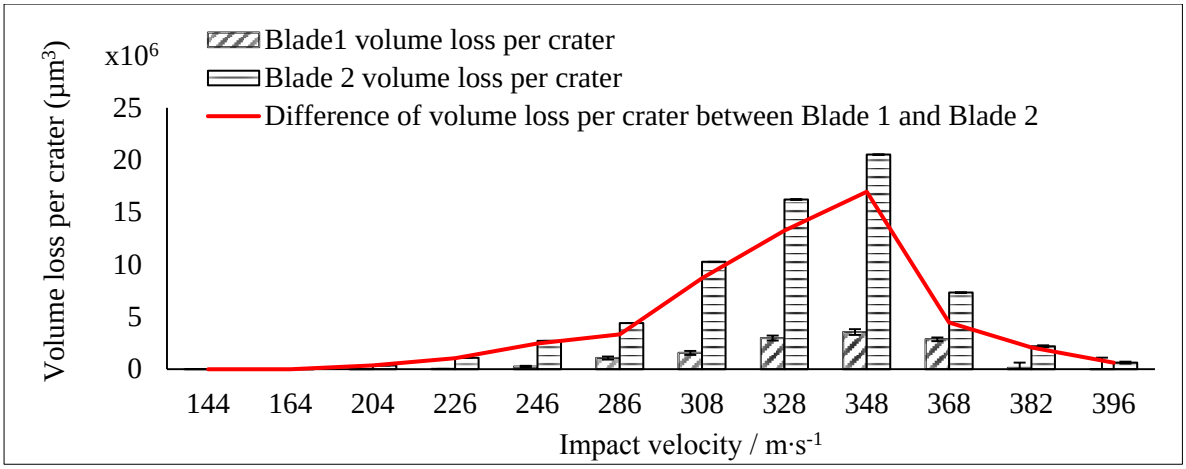

Fig. 4.8 Volume loss per crater along the ex-service turbofan blades leading edges.

$$\frac{v2}{v1} \propto \left(\frac{V2}{V1}\right)^{8.15} \qquad \textbf{Equation 11}$$

Where v is the relative volume loss and V is impact velocity. One should note that the correlation and the exponent might be affected by the assumption of the crater geometry used to calculate v. Nevertheless, Equation 11 suggests that Ti6Al4V turbofan blade is very sensitive to WDE for such range of impact velocities. An experimental study [70] on the effect of the impact velocity on WDE performance of Ti6Al4V using whirling disc rig demonstrates the similar linear trend of the change in the maximum erosion rate from 275 to 350 m·s^{-1}. The maximum erosion rate is related to the impact speed with 8.9 and 7.7 exponents for tests conducted with 464 µm and 603 µm droplets, respectively. The conclusion is also supported by Abdullah [71], who reported that the maximum erosion rate of Ti6Al4V increases significantly over the impact velocity of 250 m·s^{-1}.

Cross-sectional observations on leading edge specimens shown in Fig. 4.9 can further verify the relation shown in Equation 11. Comparison of Blade 1 and Blade 2 cross-sections reveals that the rain erosion damage initiates at the highest curvature of the leading edge profile, as shown in Fig. 4.9 - 2L1. The affected zone is then expanded with increasing impact velocity. The severity of material removal increases significantly for impact velocity over 246 m·s^{-1}. The whole tip of the leading edge was removed in 2M2, 2H1 and 2H3. Microstructural characterisation on the erosion mechanisms will be further discussed in the following section.

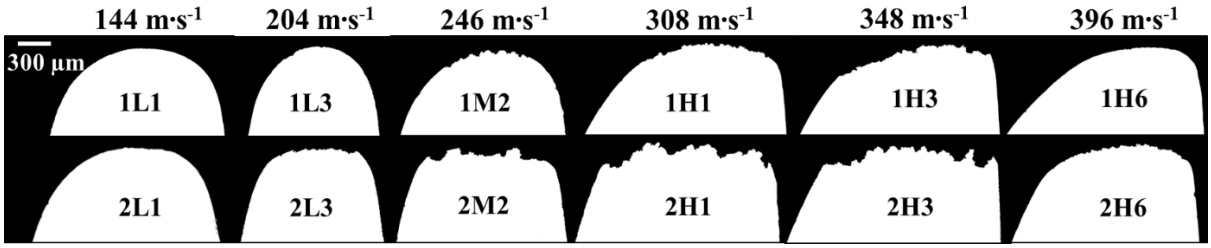

Fig. 4.9 Comparison of cross-sectional profiles of ex-service turbofan leading edges.

4.4 Rain erosion mechanisms at the Ti6Al4V turbofan blade leading edge

The analysis above reveals that the most severe WDE takes place at the H zone of the leading edge with the highest impact velocity, hence, discussions of the damage mechanism will focus on such region. Early stage damage mechanism will be discussed on the results obtained from the tip of the H zone (H5 and H6), where less severe damage was identified. While that of the advance stage will be revealed on results from the rest of the H zones.

4.4.1 Early stage of WDE

The incubation period of the ex-service fan blade at the leading edge cannot be identified, since the material loss is detected (indicating the termination of the incubation period) over the majority parts of the leading edges. The roughened leading edge surface impedes the observation of the features, such as formation of slip lines and grain tilting reported in the literature [39,69,71]. However, SEM observations at H5 zones reveal that the early stage of rain erosion damage is primarily localised at the centre of the leading edge surface, as shown in Fig. 4.10. A higher magnification of the damaged surface, shown in Fig. 4.11, indicates a homogenous pattern of erosion morphology with selective locations of material removal. Cracks are found along the boundaries of grain-like features. The formation of micro-voids at triple junctions that later develop into deep erosion craters due to grain removal are labelled in Fig. 4.11. Additionally, small cavities with diameters smaller than 1 μm are observed inside the un-damaged grain-like features, shown in Fig. 4.12 (a). Signs of plastic deformation are identified adjacent to the cavities, as demonstrated in Fig. 4.12 (b) and (c).

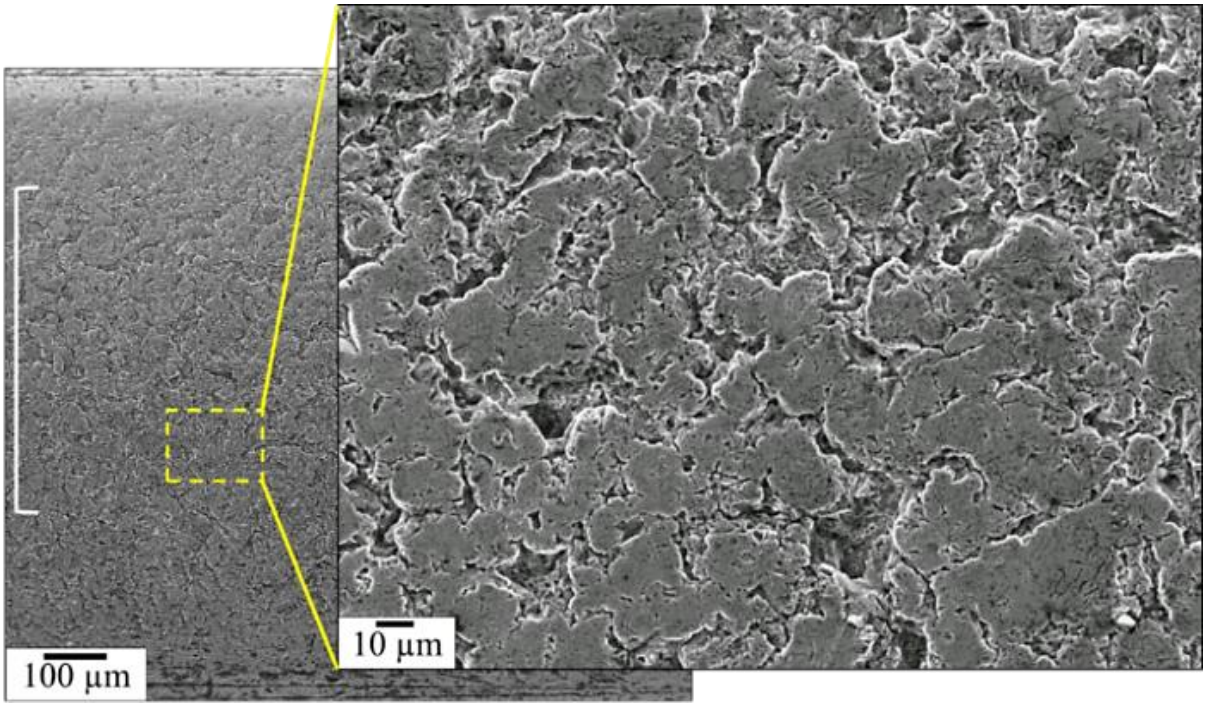

Fig. 4.10 Erosion morphology at the tip of the leading edge (1H5 zone).

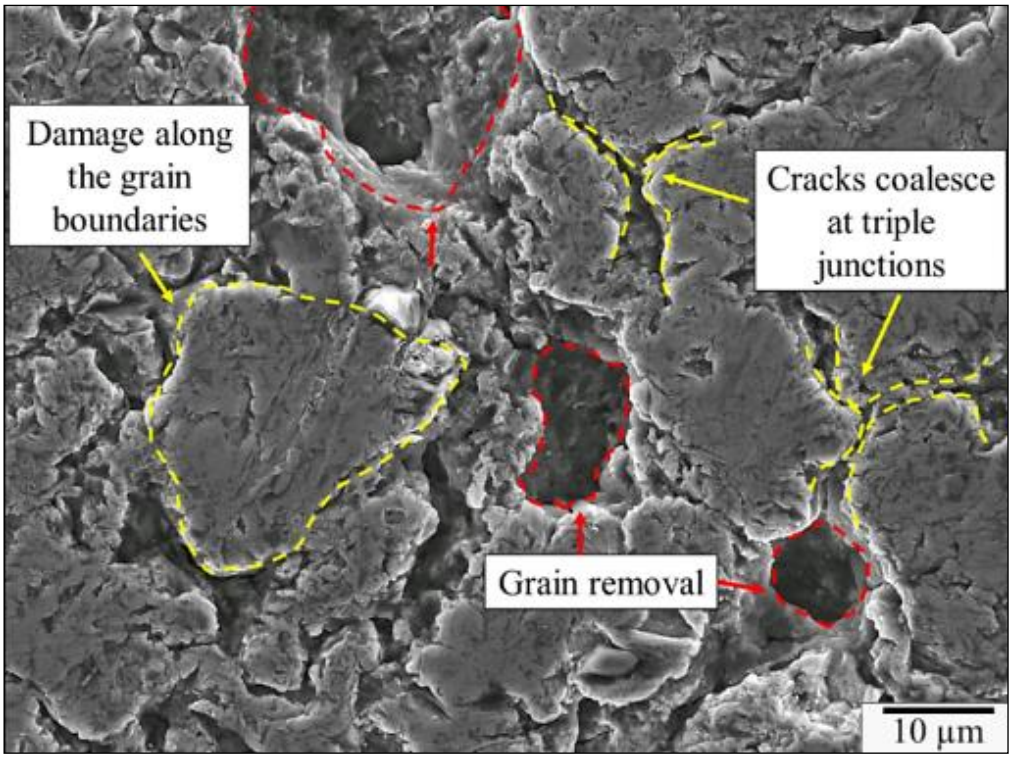

Fig. 4.11 Higher magnification of rosion morphology at the tip of the leading edge (1H5 zone).

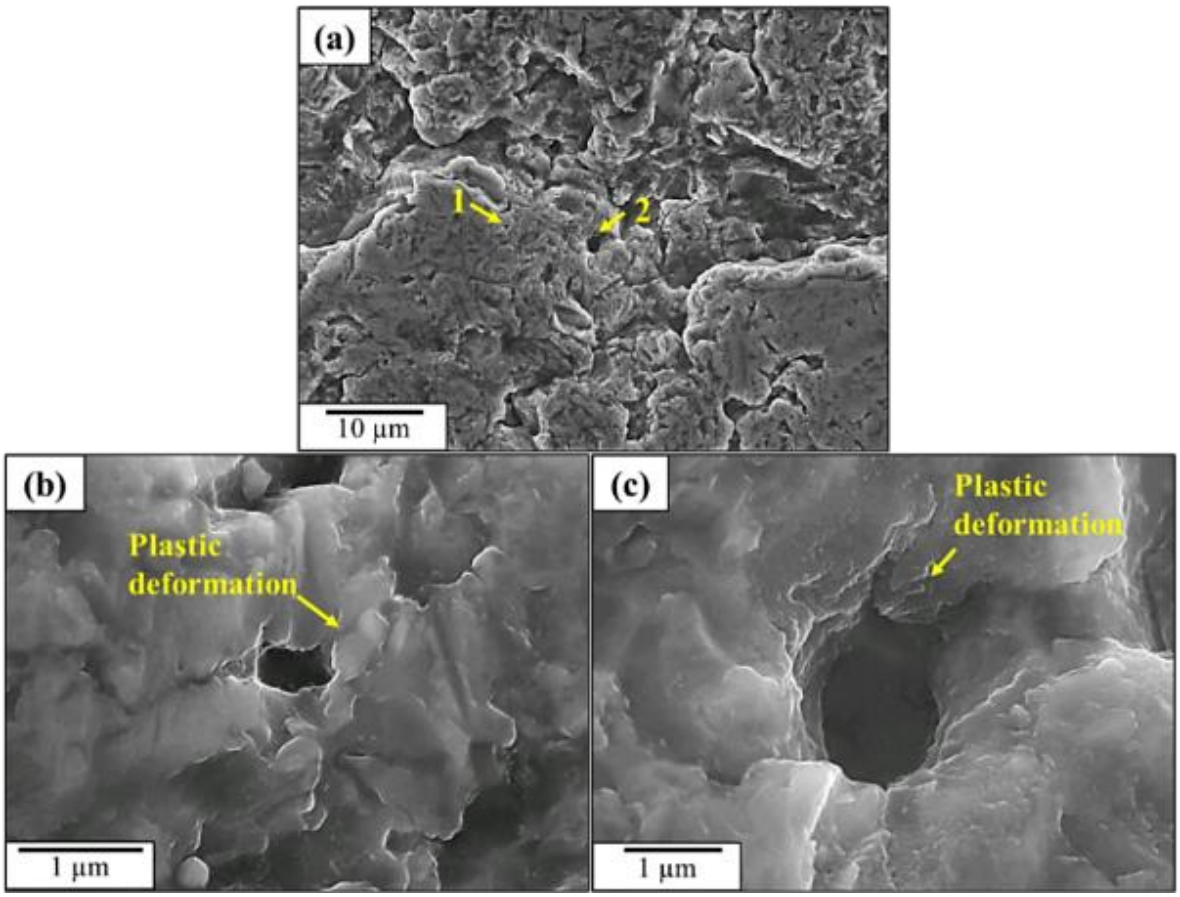

Fig. 4.12 Cavities found at the tip of the leading edges (1H6 zone)

The rain erosion damage shown in Fig. 4.10 and Fig. 4.11 resembles an intergranular-like fracture mechanism, which was also observed on the surface of laboratory tested Ti6Al4V specimen during the early stages of WDE [39,69,71]. It is reported that the initiation of such damage is associated with the grain tilting phenomenon during the incubation period. Hence, it can be suggested that the microstructure of Ti6Al4V fan blade material plays a role on the early stage of rain erosion behaviour. Furthermore, the fluctuation on the nanohardness and reduced Young's Modulus shown in Table 4.2, indicate the effect of crystal orientation on the mechanical properties of the Ti6Al4V fan blade material. Additional evidence is given by a past study [141], which shows the nanohardness of α-phase in Ti6Al4V alloy ranging from 4 to 6 GPa. The same study also shows an increase of nanohardness with the decrease of the declination angle obtained from EBSD analysis. Therefore, a conjecture on the interaction of the water-hammer pressure and α-grain orientation can be raised. As the water-hammer pressure introduces high compressive stress and stress waves to the impact surface during the early stages of WDE [12,32,53,54,60,64], the high anisotropy of α grains in Ti6Al4V blade material can give rise to undesirable hard/soft grain interactions [20,21]. This leads to preferential deformation of grains with certain orientations (soft grains), while hard grains resist the impact pressure and constrain the movement of the soft grains. It then results in the visibility of the grain boundaries on the surface, which act as stress raisers, inducing intergranular cracking due to the interaction with lateral flow jetting.

The hypothesis can be further developed by comparison between the α-grain size of Ti6Al4V blade material with the contact periphery [36], where the latter is the radius of the contact area at which the lateral outflow jetting commences. The contact periphery can be calculated using Equation 3, assuming that the average rain droplet size is 2 mm [3–6], results are shown in Table 4.3. Thus, with comparison to an average α-grain size of 9.73 ± 5.28μm (area of 74.32 ± 21.88 μm^2) mentioned in section 4.1, each rain droplet is interacting with multiple grains for each impingement. Therefore, potential correlation between the crystal orientation of α grains and early-stage WDE behaviour can be established. A similar proposal is discussed in the study by Niederhofer et al. [142], where they studied the influence of crystallographic orientation on cavitation erosion behaviour of austenitic stainless steels. They show that grains with certain orientations present higher resistance to cavitation erosion than other orientations.

Table 4.3 The contact periphery of the water droplet with leading edge surface at L, M and H zones.

Zone	**L**	**M**	**H**
Contact area / μm^2	164.5 – 218.1	236.0 – 281.1	296.3 – 351.2

Microstructural characterisation was conducted with SEM on the leading edge cross-sections in order to further understand the damage mechanism induced by rain droplet impingements. Short cracks in the lengths of 1 - 2 μm are developed at the roughened leading edge, as shown in Fig. 4.13 (a) and (d). However, no preferential path (or location) on the short crack growth with respect to the microstructure of Ti6Al4V (α or β phase) is detected. Formation of micropits with both width and depth of 1 - 2 μm is identified at such zone, as marked in Fig. 4.13 (b) and (c). The cracks are formed due to the shear stress produced by the rapid lateral outflow, exerting pressure against the roughened feature of the exposure surface, as illustrated in Fig. 4.14. Such cracks are then deepened attributable to the hydraulic penetration by forcing a quantity of water

under pressure into a confined space that amplifies the pressure. This eventually leads to the formation of deep cavities following grain removal with repeated impingements (as marked in Fig. 4.11).

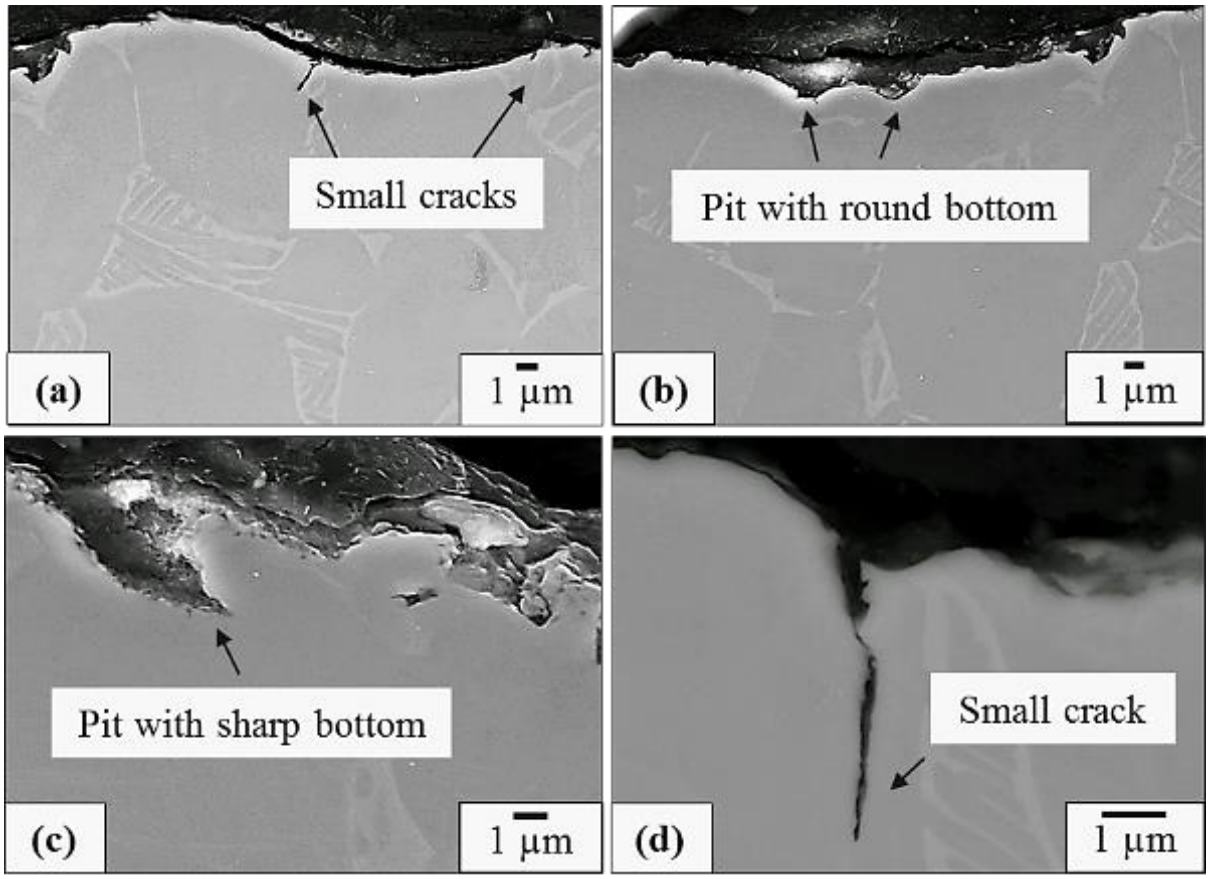

Fig. 4.13 Early stage rain erosion damage: (a) and (b) taken from H5 zone of blade leading edge; (c) and (d) taken from L3 zone of blade leading edge.

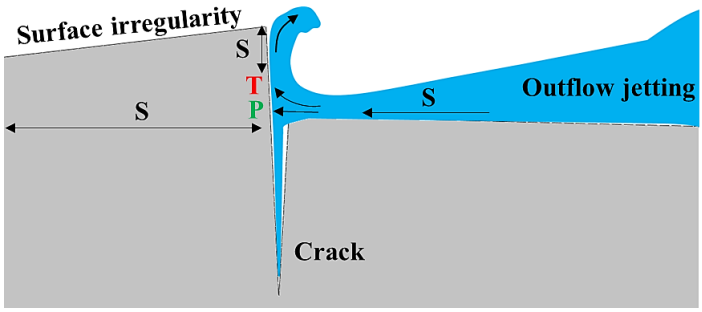

Fig. 4.14 Remade schematic of stress produced at a surface elevation along a crack by the radial flow from a droplet [143].

4.4.2 Advanced stage of rain erosion damage at the leading edge

Although the erosion mechanism of the ex-service turbofan blade leading edge during early stage of WDE is a proposed conjecture, definitive conclusions can be drawn for the advanced stage. SEM examinations of the advanced-stage WDE mechanism are shown in Fig. 4.15. As the impact velocity reaches over 300 $m \cdot s^{-1}$, large craters with depth ranging from 30 to 40 µm are found. Increasing number of longer cracks (≥ 10 µm) becomes a more predominant feature, as they are found mostly on the wall of the erosion craters. It is noteworthy that the majority of

the large-scale cracks, observed on the erosion crater wall, exhibit a tendency of lateral growth, and all cracks grow through both α- and β-phases. Typical advanced-stage WDE craters are presented in Fig. 4.15 (b) and (c) with the formation of lateral cracks tunnelling through the side wall and secondary cracks penetrating from the bottom of the craters. A network of cracks is observed penetrating from one side of the crater to the other shown in Fig. 4.15 (d).

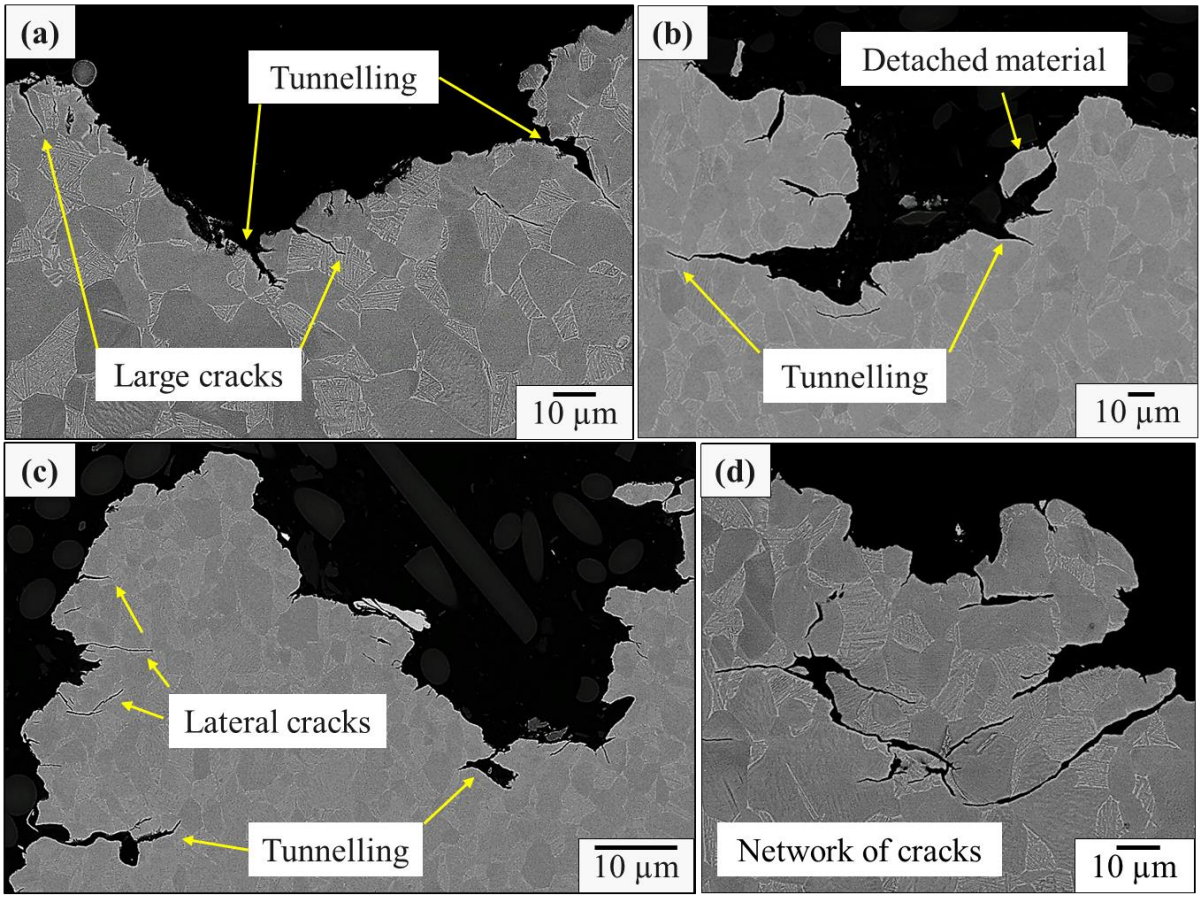

Fig. 4.15 Features of rain erosion damage at advanced stages.

It can be seen that the propagation of the cracks is driven by the stress field developed inside the erosion crater. There is not preferential location or orientation with respect to the microstructure. The same conclusion is reached by whirling arm WDE tests on Ti6Al4V alloy [71,78,79]. A schematic illustration of the damage mechanism for the advanced stage WDE is given in Fig. 4.16. The process is attributed to a joint effect of outflow jetting and hydraulic penetration. The lateral cracks are induced by outflow of the rain droplets jetting on the side walls of the erosion crater. Tensile and shear stresses are then produced when flowing water exerts pressure as it strikes into such cracks on the fractured crater wall. This phenomenon broadens the cracks to form tunnels (labelled as Tunnel 1, 2 and 3). Water is forced into the tunnels for the overlying material to bend upwards due to hydraulic penetration. Material removal would take place when the formed tunnel allows sufficient pressure to be applied to one side of a cantilever (such as cantilever1 and 2 labelled in Fig. 4.16). A number of cracks will eventually develop and grow in an expanding crater. Thus, under the circumstance presented in Fig. 4.16, cantilever 1 with smaller fragment of the material should be removed first once sufficient pressure is applied to Tunnel 2.

Additionally, secondary cracks are formed at the bottom of the erosion craters (labelled in Fig. 4.16) and propagate deeper due to the hydraulic penetration induced by repeated impingements. The same feature was identified on the cross-section of WDE tested Ti6Al4V specimen [71]. The effect of the hydraulic penetration can be further supported by the presence of nanoscale cavities observed inside the erosion crater, as presented in Fig. 4.17. An array of nanoscale cavities are found inside the erosion crater observed in 2H1 zone, coupled with formation of slip lines induced by plastic deformation. It is suggested that the formation of these nanocavities are results of tunnelling effect. The nanocavities seen on the exposed surface (Fig. 4.12) can be originated from the ones formed inside the erosion craters (Fig. 4.17). Such phenomenon was not reported in any laboratory based WDE study.

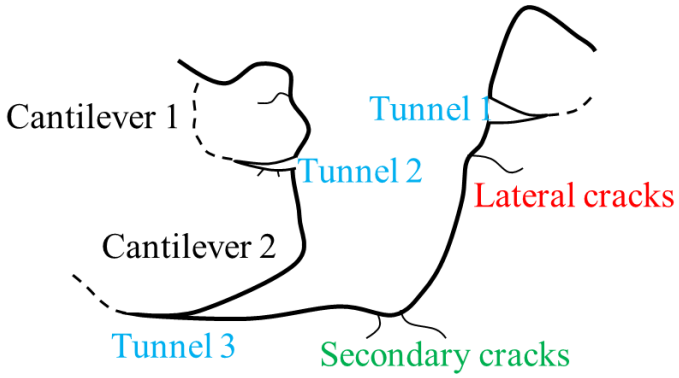

Fig. 4.16 Schematic of damage mechanism at the advance stage of rain erosion.

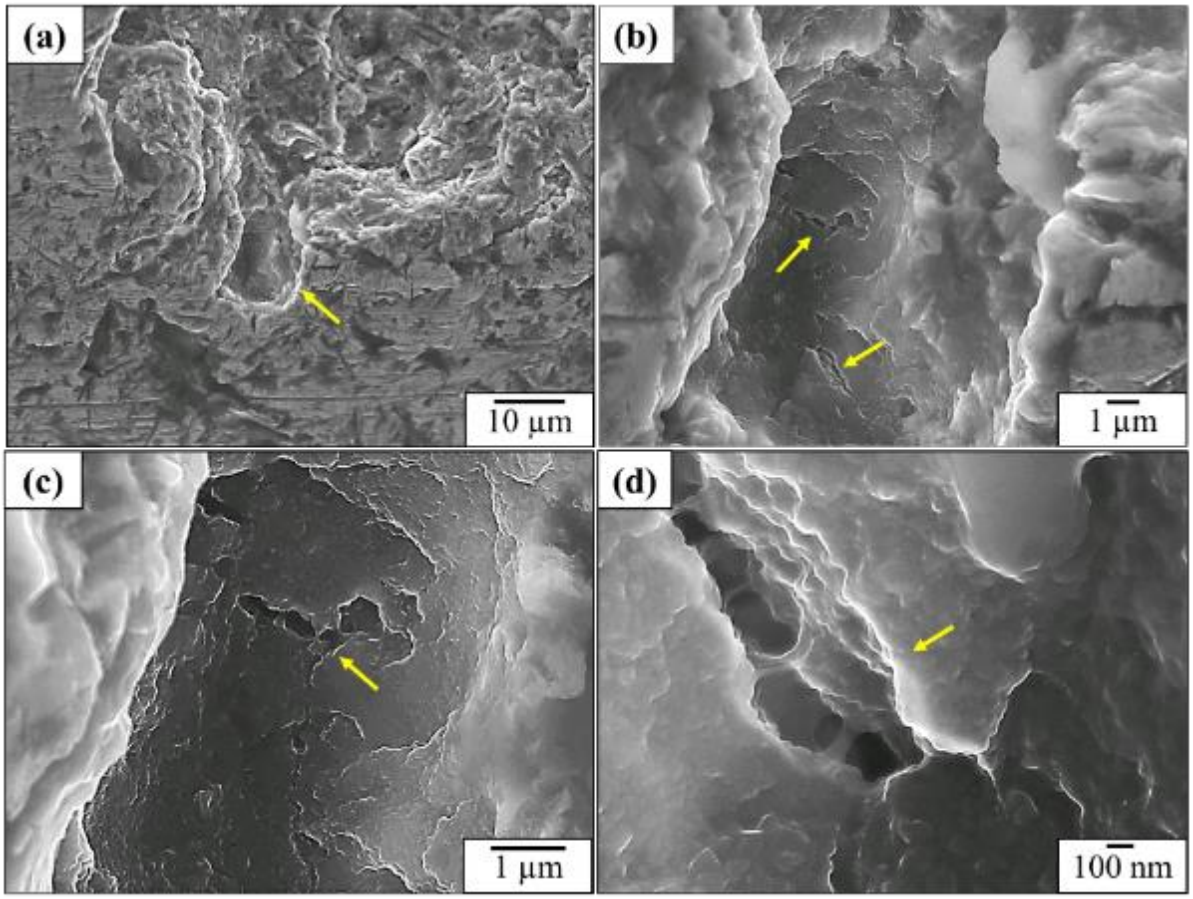

Fig. 4.17 Nano-sized cavities observed on 2H5 zone of the leading edge.

4.5 Summary

The evolution of rain erosion at the leading edge of Ti6Al4V turbofan blades is demonstrated with a series of experimentally determined cross-sectional blade outlines in Fig. 4.18.

a) Initiation of rain erosion takes place at the highest curvature of the leading edge profile. The intergranular fracture observed during early stage of WDE can be due to the high anisotropic behaviour of α-grains in Ti6Al4V blade material under water-hammer pressure.
b) The shear stress generated due to the activation of the lateral flow jetting, leads to the formation of cracks and erosion craters. The area of the WDE damage then expands;
c) Erosion craters are broadened and deepened under the joint effect of lateral outflow jetting and hydraulic penetration, shaping the surface of the leading edge into 'canyon'-like morphology; cracks indicated in red are annotations;
d) Such mechanism is aggravated by the droplets impinging at over 246 $m \cdot s^{-1}$, the increased maximum erosion rate fashions the 'canyon' with steep 'cliffs' and deep 'valleys', presenting a finger-like cross-section;
e) The 'peaks' of the 'canyon' are eventually removed due to the 'cantilever' mechanism.

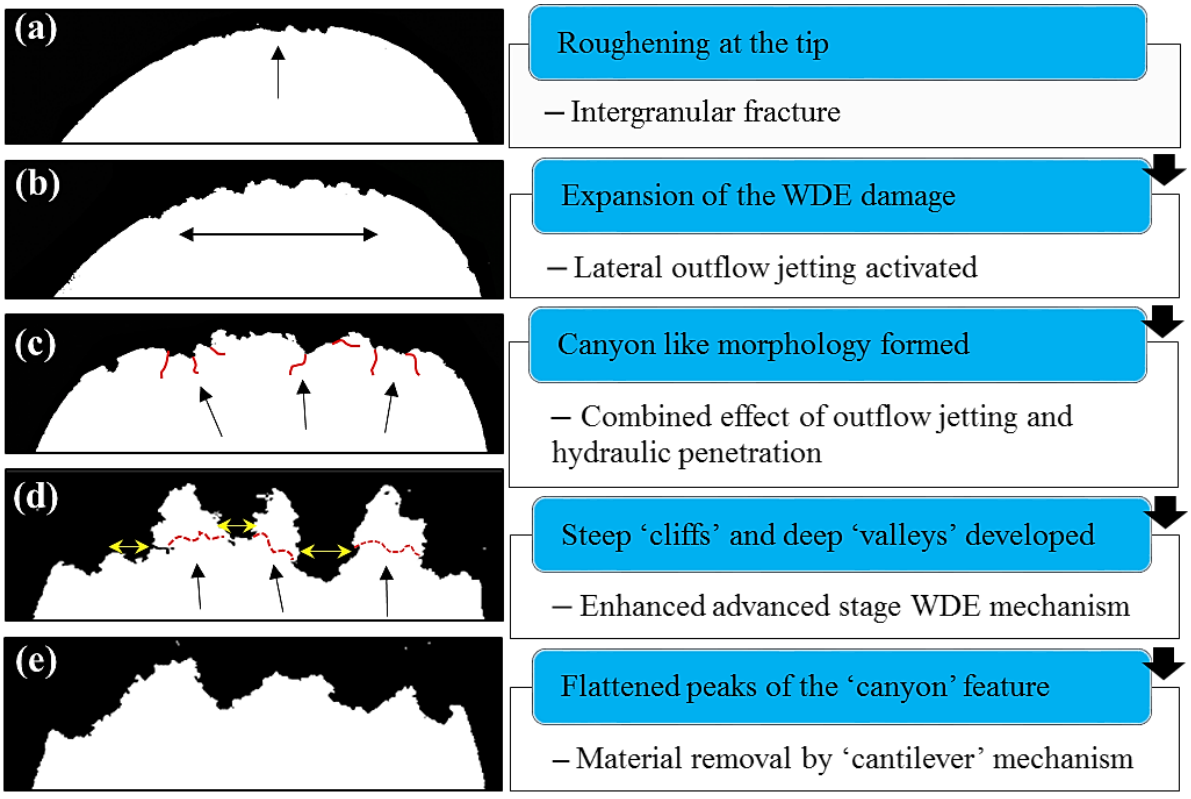

Fig. 4.18 Evolution of rain erosion at the leading edge of Ti6Al4V turbofan blades, cracks indicated in red are annotations.

4.6 Conclusions

Forensic analysis was conducted on two ex-service Ti6Al4V turbofan blades with respect to the microstructure, morphology and impact conditions to examine the WDE damage induced by rain droplets at the leading edges. Damage mechanisms were discussed along with the evolution of WDE.

- Early and advanced stage damage mechanisms identified on the leading edge verified the findings from laboratory-based tests. However, the unique canyon feature of rain erosion morphology was not found on any laboratory-tested flat specimen.

- A hypothesis was raised on the effect of the grain orientation on performance of Ti6Al4V fan blade material during the incubation period of rain droplet erosion.

- Increase of rain erosion severity with increasing impact velocity is confirmed under examination of leading edge morphology and cross-sections along the length of the blades. The reduction of rain erosion damage after H3 zone toward the tip of the leading edge probably caused by the shielding effect of the fan blade casing. More significant increase of WDE damage was observed in the range of 286 ms^{-1} to 348 ms^{-1}.

- The primary mechanism for material removal in the advanced stages of rain droplets erosion at supersonic impact velocity is a process of tunnelling, and upheaval of the overlying materials due to joint effect of lateral outflow jetting and hydraulic penetration induced by repetitive droplet impingements.

- The presence of nano-size cavities observed on the leading edge of the ex-service fan blade suggests the action of hydraulic penetration. Such cavities were not reported in any laboratory based WDE study.

Chapter 5.

Correlation between water droplet erosion (WDE) and cavitation erosion (CE) of Ti6Al4V

As the in-service WDE damage mechanisms are identified through forensic analysis of ex-service turbofan blades, in this chapter, vibratory CE apparatus is employed to replicate the predominant damage induced by rain erosion observed on fan blade leading edge in Chapter 4. A systematic test plan is adopted to cross-check the damage generated by CE with actual damage on the fan blade leading edge, as well as the WDE damage generated with whirling-arm rig to ensure the relevance of the work to the application. The CE testing can then be used as a valid screening process to predict the performance of the coated systems under WDE. The correlation between the damage mechanisms of WDE and CE on Ti6Al4V is discussed.

5.1 Characterisation of Ti6Al4V base material

Characterisation of the Ti6Al4V base material was conducted with respect to the microstructure and mechanical properties. The materials was also used as the substrate for applying the selected coating systems, which will be discussed in the following chapters.

5.1.1 Microstructure

The microstructure of the Ti6Al4V base material was examined with by SEM on transverse sections. Specimens were cut in cross-section, polished with 1 μm diamond suspension and 0.04 μm colloidal silica. The microstructure presented in Fig. 5.1 shows a large proportion of primary α phase (α_p) and lamella structures composed of secondary α plates (α_s) embedded in β matrix. Crystalline orientation map of α grains in Ti6Al4V base material was performed by EBSD. A step size of 0.85 μm was applied. Scattered macrozones (shown as clusters of grains coloured in red, indicating the c-axis of HCP α grains are orientating to [0001] direction) were observed. The average grain size was estimated using the linear intercept method, which is 5.1 ± 3.1 μm.

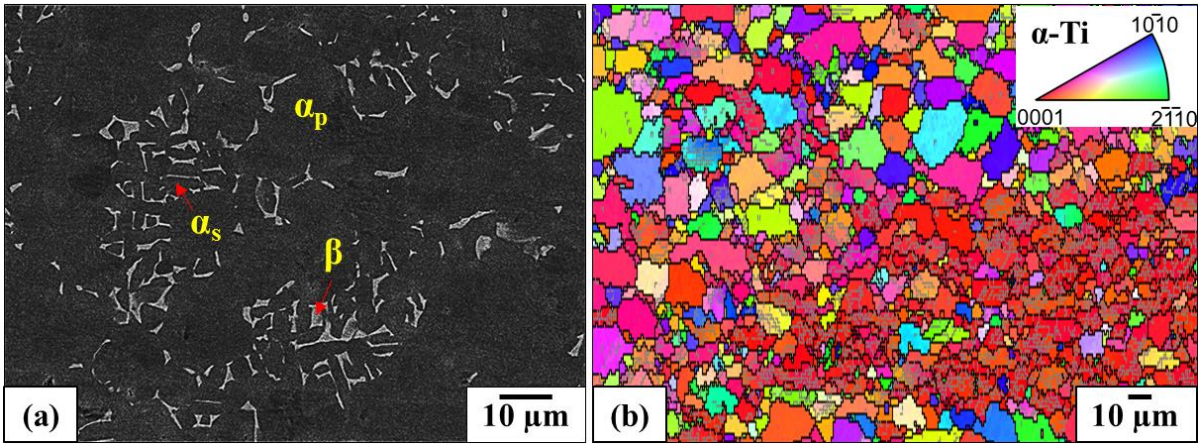

Fig. 5.1 (a) Microstructure of Ti6Al4V base material; (b) EBSD mapping of α grains in Ti6Al4V base material.

5.1.2 Mechanical properties

Nanohardness measurement was conducted on the polished cross-section of Ti6Al4V base material. It utilised a NanoTest Vantage system (Micro Materials Ltd) equipped with a Berkovich diamond indenter. A load control mode of 30 nN was applied and the nanohardness and the reduced Young's Modulus were calculated using Oliver-Pharr methodology [140]. Results are listed in Table 5.1.

Table 5.1 Nanohardness and reduced Young's modulus of Ti6Al4V base material.

Nanohardness / GPa	4.70 ± 0.57
Reduced Young's Modulus / GPa	152.37 ± 7.20

5.2 CE of Ti6Al4V base material

Vibratory CE tests were conducted on two Ti6Al4V base material specimens (1 and 2) with two different surface finishes, 0.05 µm and 0.16 µm, respectively.

5.2.1 CE curves

CE curves of Ti6Al4V base material with different surface finish was presented in Fig. 5.2. The results of CE tests show the two specimen demonstrate very similar performances. The incubation period and the maximum erosion rate were determined following the ASTM G32 standard. Both specimens show an incubation period of around 135 mins and the maximum erosion rate of 0.03 mg/min.

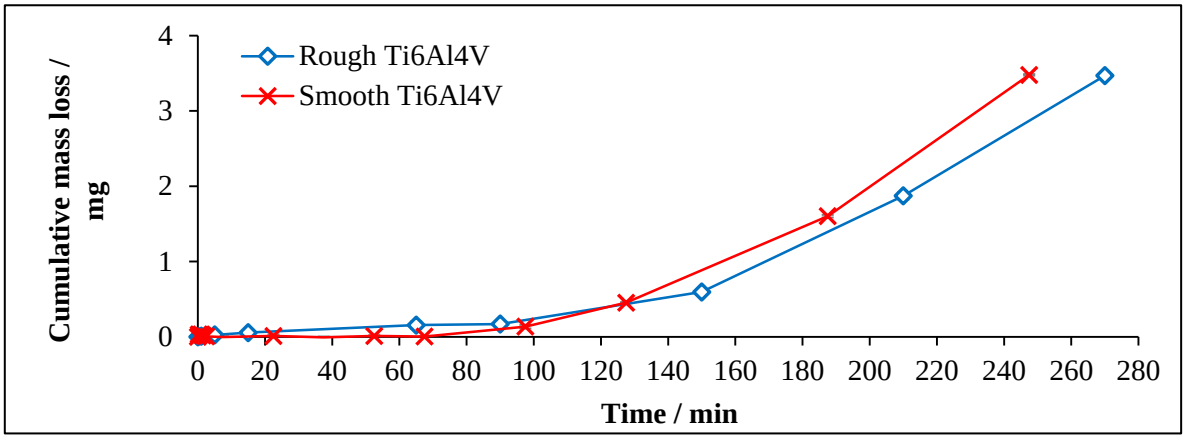

Fig. 5.2 CE curves of Ti6Al4V base material with different surface roughness.

The results of CE tests show no significant difference in the performance between the two Ti6Al4V specimens. Lin's study [131] on the effect of initial surface roughness on the CE behaviour confirms that variation was observed. However, the significant difference in the CE results was only detected between the two specimens with drastically varied surface roughness (80 grit grinding with a roughness of 1.1 mm and 1000 grit grinding with a roughness of 0.03 µm). While the ones with no significant difference in the surface finish (600 grit grinding with a roughness of 0.11 µm and 1000 grit grinding with a roughness of 0.03 µm) show similar CE

performance. Hence, it is believed that the difference of the surface roughness between the two tested Ti6Al4V specimens was not large enough to affect the CE performance.

5.2.2 CE morphology

Morphological examination was conducted with Alicona profilometer on the exposed surface of Ti6Al4V specimen 2 after 270 minutes of CE test. A ring-shape erosion mark was developed on the tested specimen, which agrees with the literature finding [144], as shown in Fig. 5.3 (a). A line scan was conducted across the ring-shape erosion scar and the result shows that the most severe erosion damage was at the outer-ring zone, where the depth was around 9 µm, Fig. 5.3 (b). This was caused by the edge effect of the sonotrode [144]. A more detailed inspection of CE morphology was conducted at the centre zone of the ring erosion scar, as shown in Fig. 5.4.

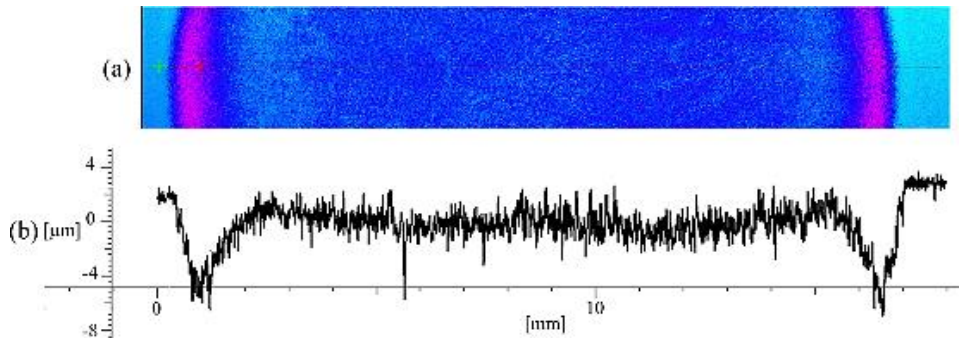

Fig. 5.3 (a) surface profile of Ti6Al4V specimen after 270 minutes of CE test; **(b)** line scan of ring erosion scar.

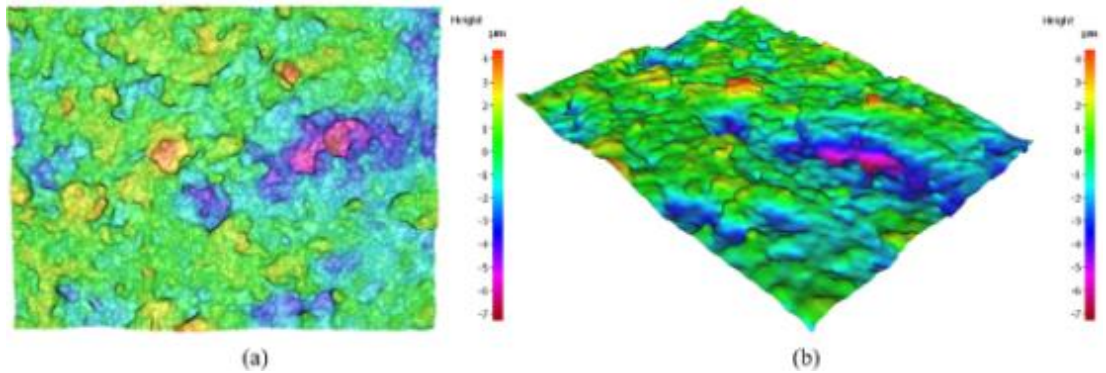

Fig. 5.4 Morphology of CE tested Ti6Al4V.

5.2.3 CE Damage mechanisms

SEM analysis was performed on the Ti6Al4V specimens to further understand the CE damage mechanisms.

5.2.3.1 Incubation period

Fig. 5.5 shows the surface of the Ti6Al4V specimen after 30 seconds of CE exposure. Roughening of the exposed surface was observed. Intergranular cracks and formation of slip

bands was detected on closer inspection, as shown in Fig. 5.5 (c). Additionally, it can be seen that the density of the slip bands are higher in certain grains and lower in others.

Further detailed investigation was conducted on various sites of the exposed surface, shown in Fig. 5.6. Appearance of grain boundaries are seen in Fig. 5.6 (a). Formation of slip lines was found in α phase, as shown in Fig. 5.6 (b). Overlapping of α grain boundaries and formation of cracks at the triple junction of the grains are inspected in Fig. 5.6 (c) and (d). Nano-sized cavities were found on the surface, mostly observed inside α grains adjacent to the grain boundaries, labelled in Fig. 5.6 (c). Intergranular cracks and material removal at the triple junctions were observed in Fig. 5.6 (e) and (f).

The primary damage mechanism of CE is induced by the collapse of cavitation cloud that contains a large number of microjets. The liquid jet that penetrates the bubble can reach a velocity up to several hundred meter per second [99,100]. The implosion of cavitation bubbles induces high impact pressure, stress waves are then generated as the microjets formed and stuck on the solid surface [96,145–147]. The initial microscopic pits are induced by microjets impingements [102,103]. In the case of Ti6Al4V base material, the microstructure of the exposed surface shows strong effect on the response to the microjet impingements. Preferential damage takes place in α grains with favourable shearing orientation. This can be supported by the studies on the effect of crystalline orientation on the CE performance of stainless steel [142,148]. Intergranular fracture was then developed due to displacements of α grains. The damage mechanisms discussed above can be further supported by Fig. 5.7, capturing material chipping at triple junction of α grains. Furthermore, it was suggested that the chip was part of β phases fell off, the size of which was comparable to β phase observed in Fig. 5.7 (b).

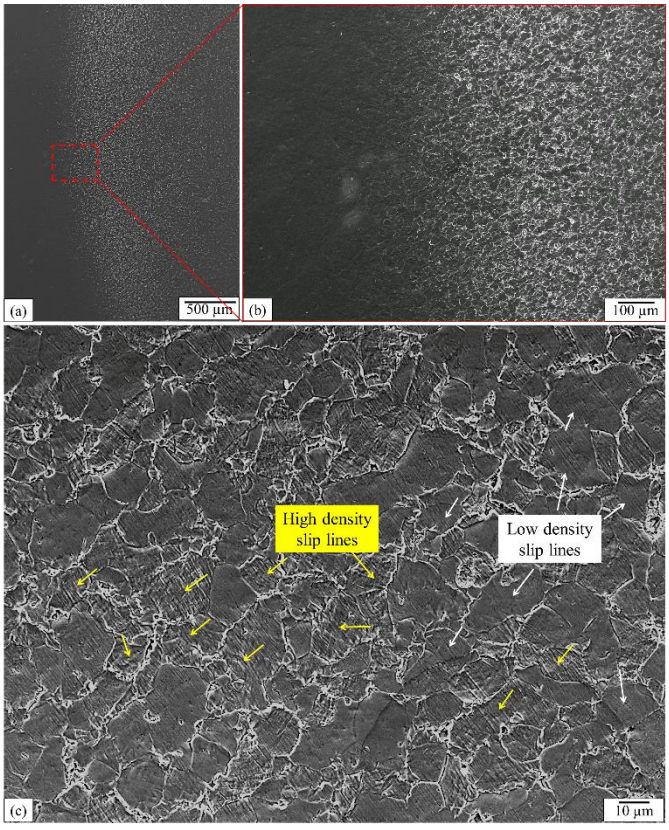

Fig. 5.5 Exposed surface of Ti6Al4V specimen during incubation period.

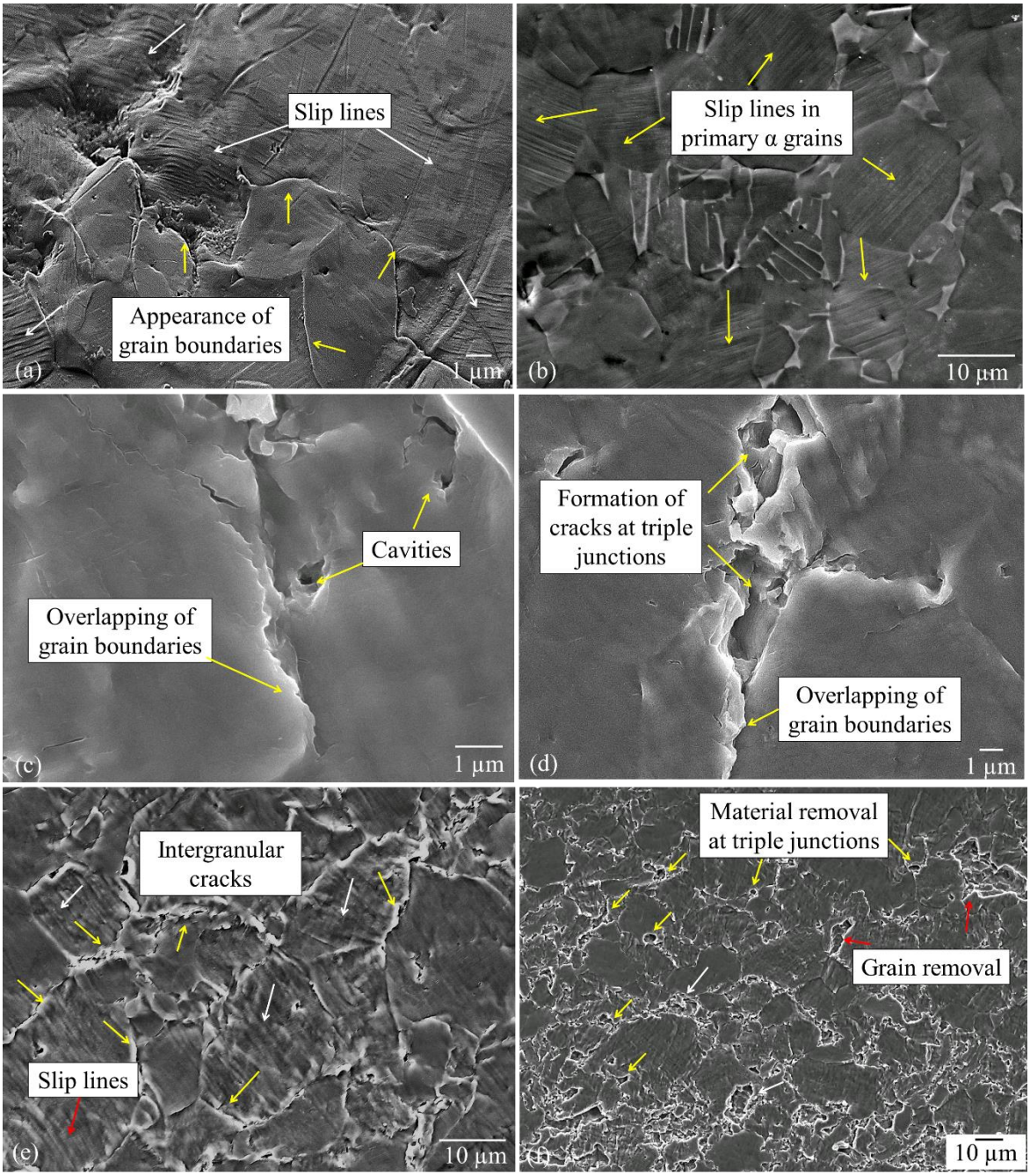

Fig. 5.6 Incubation period of cavitation erosion of Ti6Al4V base material.

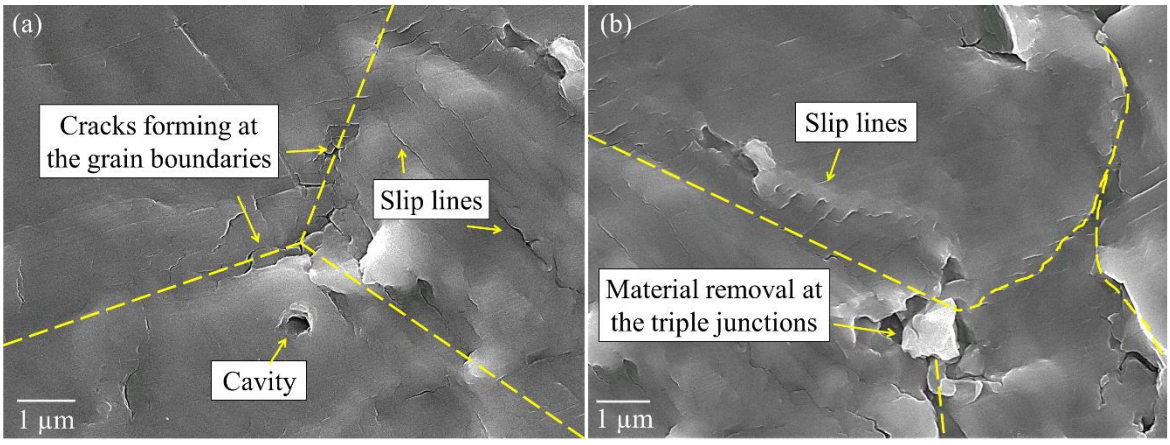

Fig. 5.7 Features observed during incubation period of CE.

5.2.3.2 Advanced stages

As the CE evolves to advanced stages, fracture surfaces are developed due to continuous implosion of cavitation bubbles and repetitive microjet impingements. Damage along the grain boundaries and formation of erosion craters due to grain removal was seen on the exposure surface, as shown in Fig. 5.8 (a) and (b). Preferential sites of material removal were identified as there were certain grains remained unaffected on the exposed surface, labelled in Fig. 5.8 (a). Cavities were found at on the fracture surface in Fig. 5.8 (b). Striation marks were observed inside the erosion craters, shown in Fig. 5.8 (c) and (d). Microcracks were formed on the fracture surface and honeycomb structure was developed with the formation of deep cavities, Fig. 5.8 (e) and (f).

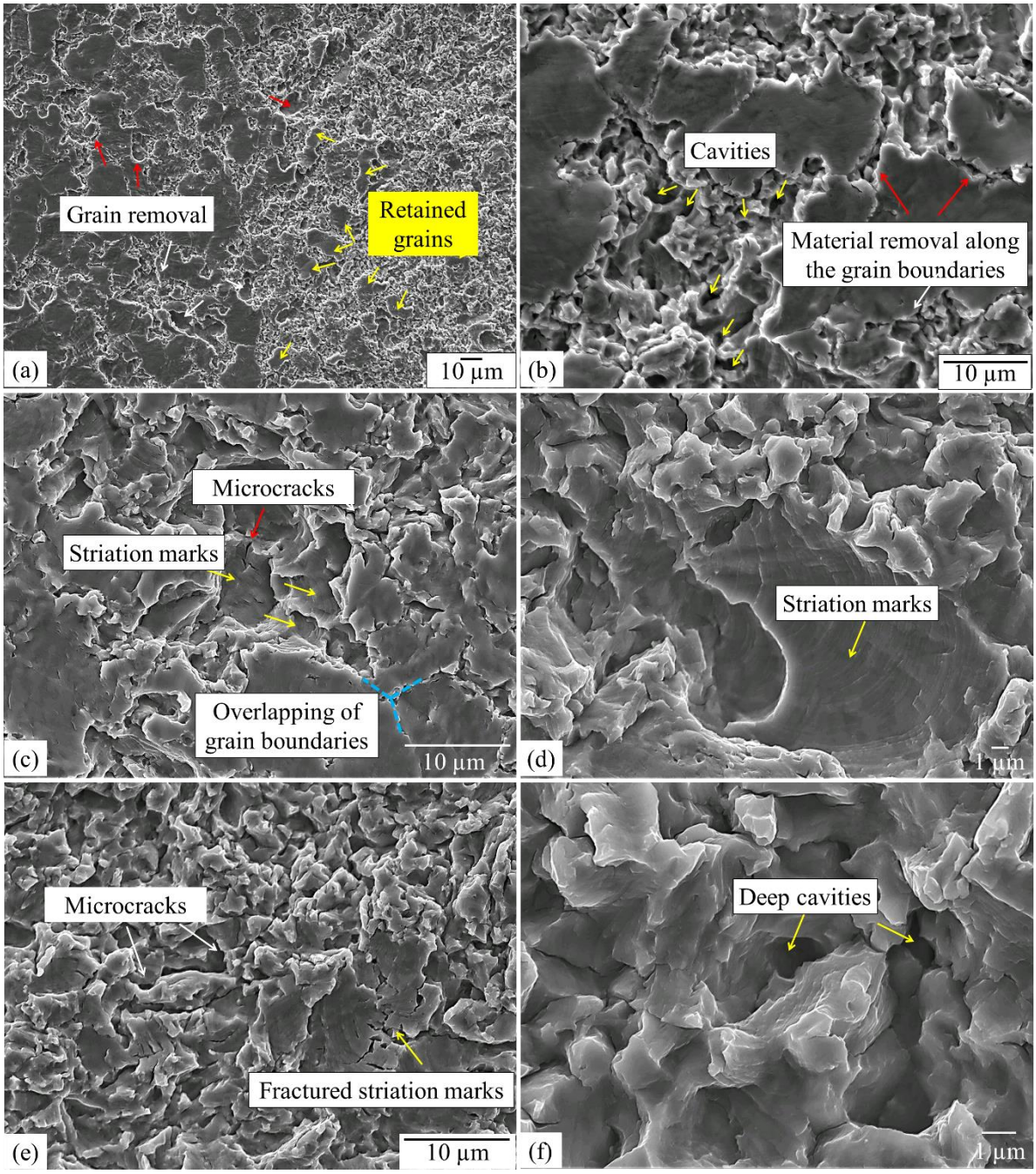

Fig. 5.8 Advanced stage of cavitation erosion of Ti6Al4V base material.

Investigation on the transverse sections show the formation of erosion craters with a depth around 5 µm after 270 mins of cavitation exposure, Fig. 5.9. Cracks were found at the bottom and side of the erosion craters, as shown in Fig. 5.9 (b) and (c). Lateral growth of the crack was seen on the crater wall in Fig. 5.9 (d).

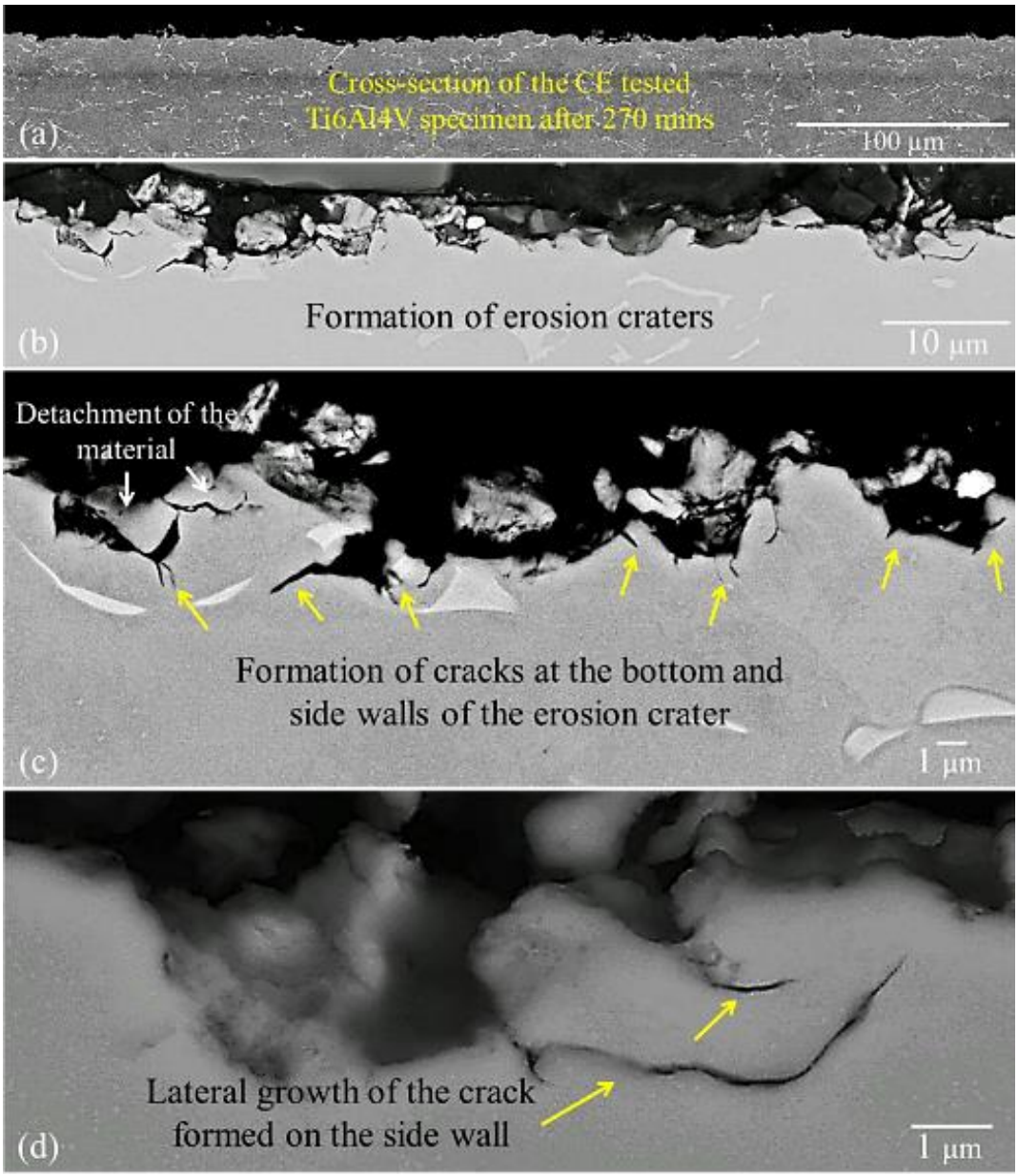

Fig. 5.9 Cross-sectional analysis of the Ti6Al4V specimens during advanced stages.

The initial damage mechanism in the advanced stage CE is induced by the slip lines and cracks formed at α grain boundaries during incubation period. They serve as stress concentrators for the cavitation pulses to initiate material removal by localised fracture. The broadening of the cracks and chipping at triple junctions lead to removal of α grains. While a second damage mechanism is proposed based on a fatigue-like fracture that was induced by the repetitive nature of loading and unloading during CE. This can be supported by the striation marks (Fig. 5.8 c and d) developed with increasing exposure time. However, there was no evidence of the

formation of a single fatigue crack, the striation marks were believed to be the results of large particles had been removed under successive implosion of cavitation bubbles.

5.3 WDE of Ti6Al4V base material

WDE tests were conducted on Ti6Al4V base material specimens with two different surface finishes using a whirling arm rig at National Physical Laboratory (NPL). The mass loss of the Ti6Al4V specimens was monitored during 50 mins of WDE test period, as shown in Fig. 5.10. Negligible mass loss was detected for specimen 1 with a smooth surface finish (0.05 µm) while pitting was observed on the exposed surface. In the case of specimen 2 with rough surface finish (0.16 µm), there was a cumulative mass loss of 0.49 mg after 50 mins of WDE test. Hence, a smooth initial surface roughness had a positive effect on the WDE performance of Ti6Al4V. This is in agreement with past studies [52,77,102] that confirm the pre-existence of surface asperities or irregularities accelerates the initiation of WDE. Kirols et al. [77] reported the effect of initial surface roughness on the WDE behaviour of Ti6Al4V specimens with varied initial surface roughness values (Ra of 0.04, 0.12 and 0.30 µm). The results showed that the specimen with 0.04 µm surface roughness exhibits more than doubled incubation period in comparison to the one with 0.30 µm surface roughness.

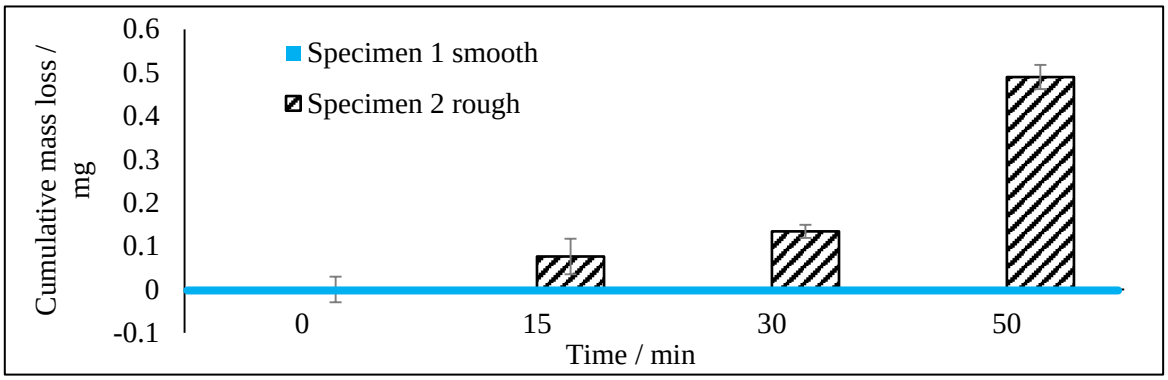

Fig. 5.10 WDE test results of Ti6Al4V specimens with different initial surface roughness.

The WDE test results were further compared to the literature shown in Fig. 5.11. The literature reference was obtained from WDE tests conducted with the whirling arm rig in Concordia University (Montreal, Canada) with 460 µm-droplets on Ti6Al4V specimens at 250, 275 and 300 $m \cdot s^{-1}$. The rotating arm of the Concordia rig is installed horizontally, while that of NPL rig is set vertically. The nozzle is placed differently in the two rigs to reach the maximum erosion rate at a 90º impact angle. Hence, the nozzle is installed vertically in the Concordia rig (Fig. 2.18) and horizontally in the NPL rig (Fig. 3.4). For each revolution, 4 droplets impacted on the specimen, which was the same as for the NPL test. The surface roughness of the specimens was around 0.05 µm, thus, similar to that of the Ti6Al4V specimen 1 (smooth) in this study. It can be seen that the WDE tests conducted at NPL show significant lower erosion rate in comparison to all the tests conducted at Concordia University, even at much lower impact velocity, as listed in Table 5.2. The maximum erosion rate during the 50 mins test period was more than 46 times smaller than that of the Concordia test under the same conditions.

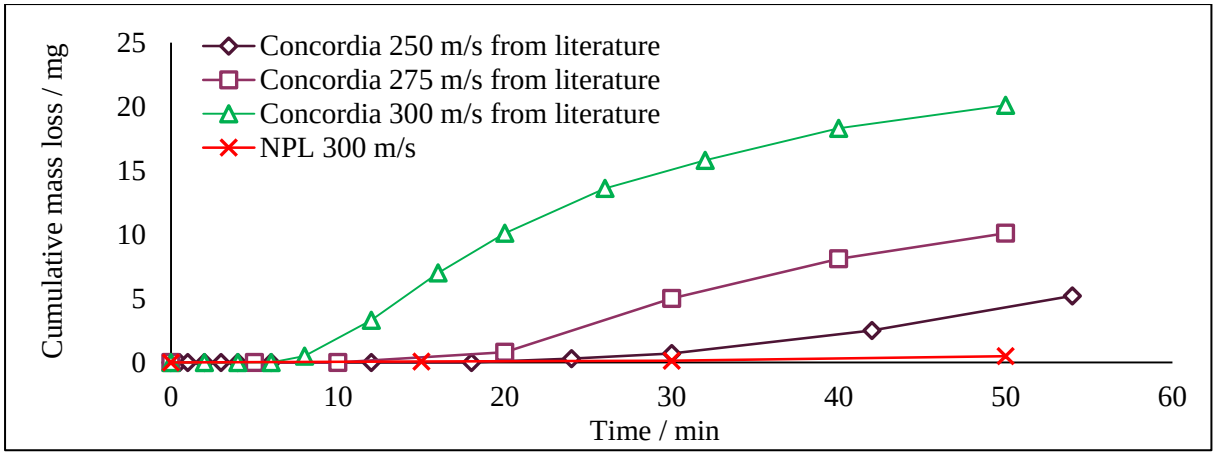

Fig. 5.11 WDE curve of Ti6Al4V base material in comparison to the literature results.

Table 5.2 The maximum erosion rate of various WDE conditions.

WDE test condition	**NPL**	**Concordia University**		
	300 m/s	**250m/s**	**275 m/s**	**300 m/s**
Incubation period	50+ mins	30+ mins	18 mins	8 mins
$ER_{max\ during\ 50min\ test}$	0.02 mg/min	0.34 mg/min	0.42 mg/min	0.93 mg/min

Additionally, solid particles were found during operation of WDE test at the NPL rig. Scattered indents were observed on the tested specimens, as seen in Fig. 5.12. These indents were believed to be introduced by solid particle impacts, hence, the mass loss monitored during the WDE can be affected by such incidents. However, the erosion rate was still much smaller than that of the literature data. The tests cannot proceed further due to safety regulations. We were informed that the rig required maintenance, which is still in progress. Therefore, the study will focus on the investigation of WDE damage mechanisms on Ti6Al4V base material.

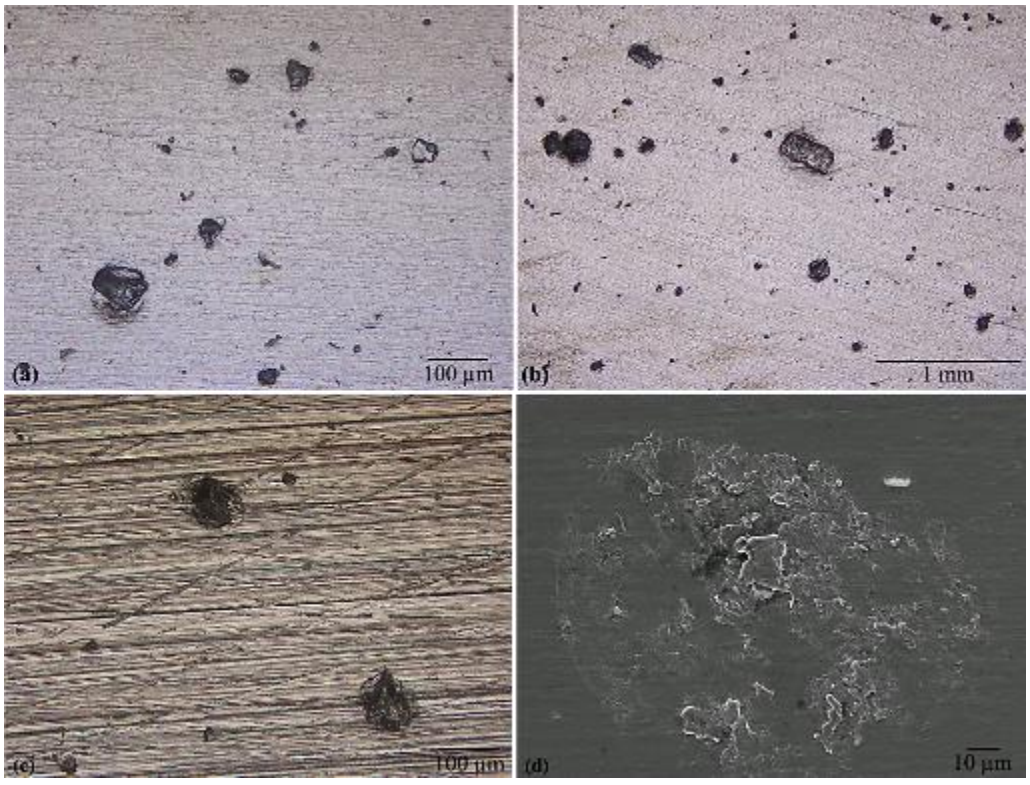

Fig. 5.12 Indents observed on the tested Ti6Al4V specimens.

5.3.1 WDE morphology

The surface profiles of the Ti6Al4V specimens after 50 mins of WDE test were inspected with Alicona profilometer. The two Ti6Al4V specimens (1 and 2) with surface roughness of 0.05 µm and 0.16 µm were tested under the same round of the WDE test, and the post-test surface profiles are shown in Fig. 5.13. Line scans were conducted on both surface profiles to further quantify the erosion damage, as shown in Fig. 5.14 and Fig. 5.15, respectively. It can be seen that Ti6Al4V specimen 2 shows more severe damage in comparison to specimen 1. An erosion line composed of linearly distributed craters was formed across the width of specimen 2. The maximum depth of the erosion craters was around 200 µm. A close inspection of one large erosion crater is shown in Fig. 5.16. While in the case of specimen 1 with smoother surface finish, slight roughening of the impacted area was detected. Small pits were found scattered along the erosion line with a depth of 3 to 40 µm.

The results obtained from morphological analysis of the post-tested Ti6Al4V specimens confirm the effect of initial surface finish on WDE behaviour. Specimen 1 with smooth surface demonstrates superior WDE performance with prolonged incubation period. On the other hand, specimen 2 under the same condition of WDE shows more sever mass loss as the process already evolved into advanced stages with significantly higher erosion rate. The depth of the largest erosion crater formed on specimen 2 was 5 times than that observed on specimen 1. The variation in the WDE performance is attributed to the interaction between the surface irregularity and lateral outflow is delayed on the smoother surface (specimen 1). While for the rough surface (specimen 2), the surface asperity meets the lateral outflow jetting, generating shear stress. Cracks are then formed and coalesced that later lead to crack growth to the surface, eventually resulting in material removal. The same observation was reported in Kirol's study [77] that the initial surface roughness plays an important role on the duration of the incubation period. The damage mechanisms involved during this process will be further discussed in the following section.

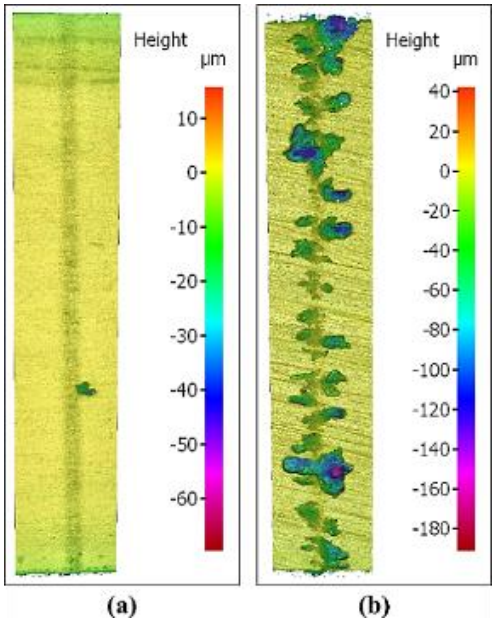

Fig. 5.13 Surface profiles of Ti6Al4V specimens after 50 mins of WDE test: (a) specimen 1 with surface roughness of 0.1 µm; (b) specimen 2 with surface roughness of 0.25 µm.

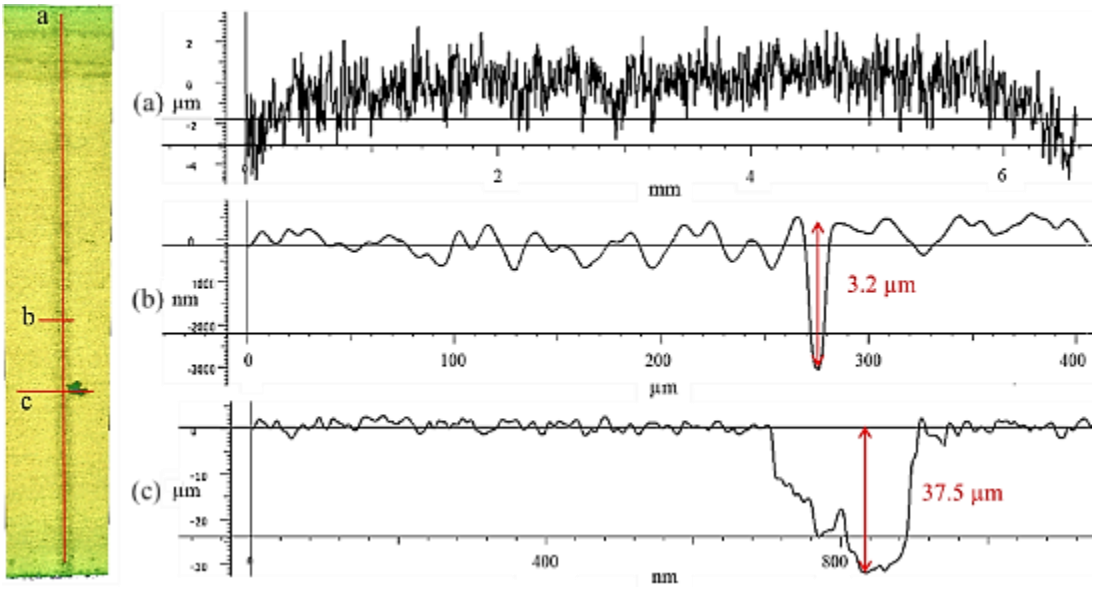

Fig. 5.14 Line scans of Ti6Al4V specimen 1 after 50 mins of WDE test.

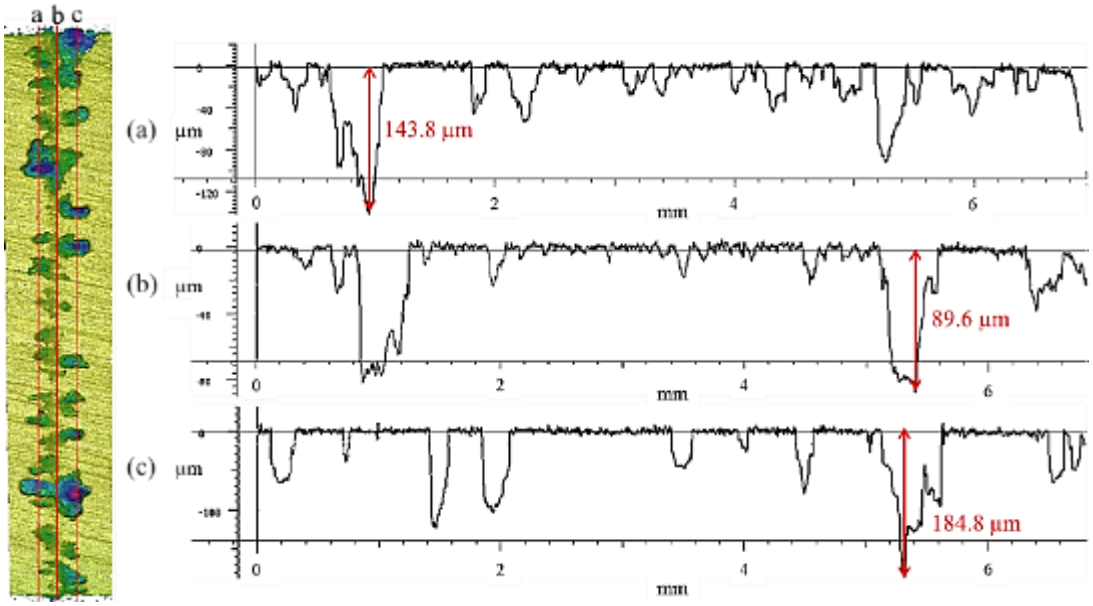

Fig. 5.15 Line scans of Ti6Al4V specimen 2 after 50 mins of WDE test

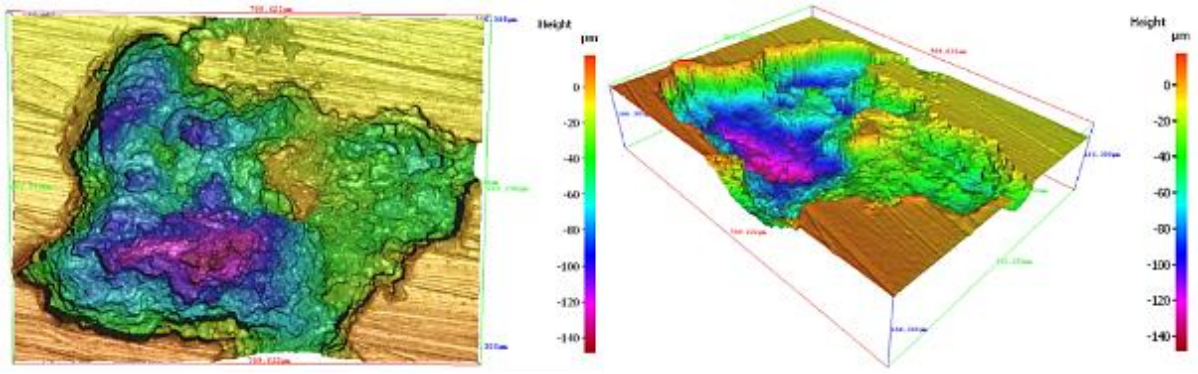

Fig. 5.16 3D profile of an erosion crater on Ti6Al4V specimen 2.

5.3.2 WDE Damage mechanisms

Characterisation of WDE damage was performed with an SEM on the surface and transverse-sections of the tested specimens. Investigation of the damage mechanisms induced during the incubation period was conducted on Ti6Al4V specimen 1 since there was negligible mass loss; while that of the advanced stages was inspected on specimen 2.

5.3.2.1 Incubation period

The exposed surface of specimen 1 during the incubation period is shown in Fig. 5.17. It indicates the changes in the material surface under water droplet impingements even though no mass loss was detected. In comparison to the unaffected zone, the impacted area shows features of roughening and pitting. On closer inspection, appearance of grain boundaries was identified on the exposed surface, shown in Fig. 5.18 (a) and (b). Pitting was found at the boundaries and the triple junctions of α grains, labelled in Fig. 5.18 (c) to (d). Intergranular cracks were inspected. Additionally, formation of erosion craters due to grain removal was observed in Fig. 5.18 (e) and (f). Signs of plastic deformation and dimples were found at the edge of the erosion crater.

The primary damage mechanism during the incubation period of WDE is induced by high impact pressure and stress waves [32,52,54,63]. Thomas and Brunton [73] identified the occurrence of grain tilting (the water droplets impacts change the grain orientation that leads to the grain boundaries become visible on the exposed surface) phenomenon during incubation period. The theory was supported by researchers [39,69] with topographical characterisation of the exposed surface in later studies. However, the action of grain tilting has not be further explained. The features observed on the Ti6Al4V specimens during the incubation period suggest that the microstructure of Ti6Al4V plays a vital role on the response to early stage water droplet impingements. The statement was well supported by the evidence shown in the literature [39,69,71]. The appearance of grain boundaries was seen on the exposed surface of Ti6Al4V base material, which later developed into intergranular fracture. However, the change of the grain orientation cannot be verified. Instead, we believe that the phenomenon can be correlated to the high plastic anisotropy of α phase in Ti6Al4V base material [20,21]. This means that the crystallographic orientations of hard and soft α grains in the hcp structured Ti6Al4V affect the material behaviour under water droplet impacts. Soft oriented grains are those favourably oriented for easy slip whereas hard grains are not. Hence, the impact pressure and stress waves can result in the deformation of the soft grains, even though the stress induced is smaller than the yield strength of the material. The presence of such properties in the Ti6Al4V base material can be supported by the IPF crystal orientation maps shown in Fig. 5.1 (b). The effect of the anisotropic behaviour can be magnified by the presence of macronzones observed in the base Ti6Al4V material since they can potentially act as one large grain despite being much larger than the mean grain size [149–151]. The grain boundaries become surface irregularities, preferential sites of damage were then induced at α grain boundaries due to the interaction with lateral outflow jetting, which results in the increase of the erosion rate. Formation of slip lines in α phase reported in the literature [39,69,71] was not seen due to the rough surface finish of the specimens.

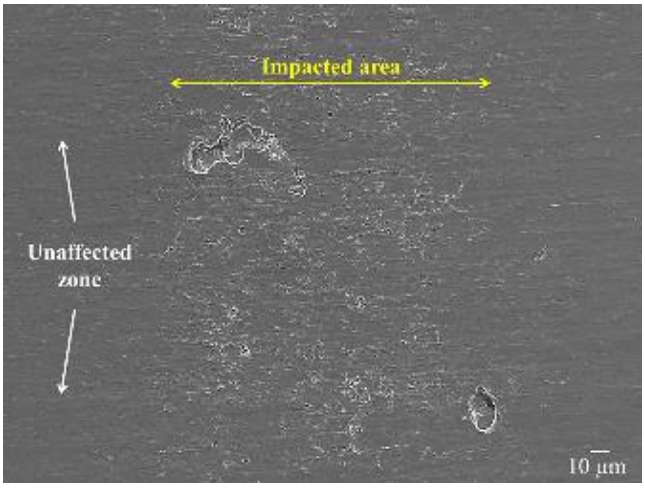

Fig. 5.17 Exposed surface of smooth Ti6Al4V specimen 1 during incubation period.

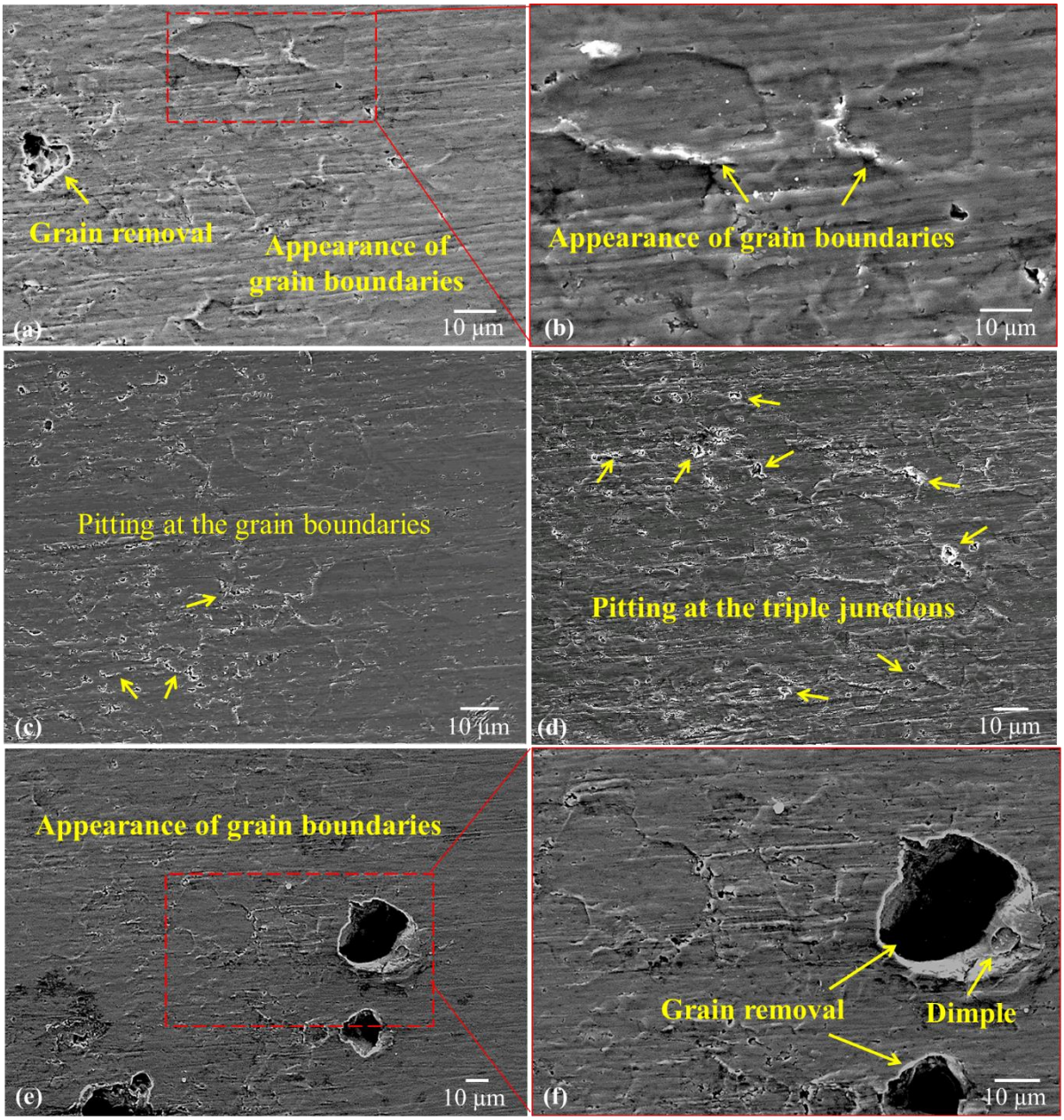

Fig. 5.18 Close inspection of Ti6Al4V specimen 1 surface during incubation period.

Therefore, a proposed damage mechanism of WDE during the incubation period can be schematically demonstrated in Fig. 5.19. The hard/soft grain interactions were initiated under water droplet impacts. The slip systems in soft grains were activated that leads to local deformation in soft grains. While the hard grains remain unaffected, which results in the visibility of the grain boundaries on the exposed surface, as shown in Fig. 5.19 (b). This surface irregularity acts as stress a raiser for lateral outflow jetting [54,152]. Cracks were then formed under the shear stress generated by the rapid lateral outflow (speed of which can be up to ten times of the impact velocity [54]) exerting pressure against the roughened feature. Material removal took place at the triple junctions due to coalescence of cracks, Fig. 5.19 (c). These cracks were then widened and deepened attributable to the hydraulic penetration in the advanced stages of WDE. This action eventually leads to formation of deep cavities following grain removal with repeated impingements, Fig. 5.19 (d).

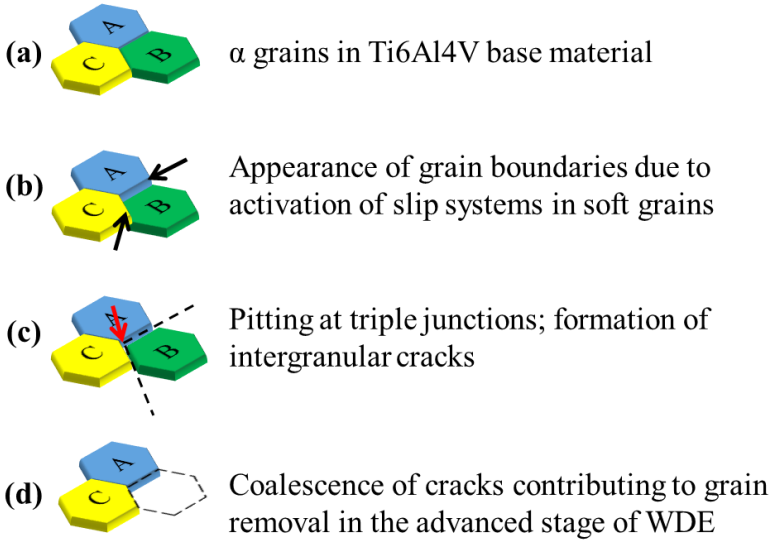

Fig. 5.19 Schematic of damage mechanism of incubation period.

5.3.2.2 Advanced stages

SEM inspection was performed on the surface of specimen 2 in order to study the damage mechanisms in the advanced stages of WDE. An erosion line was developed after 50 mins of WDE test, as shown in Fig. 5.20 (a). Craters of various sizes can be seen scattering along the erosion line and the maximum width was found to be around 1 mm, Fig. 5.20 (b) to (d). More detailed examination was carried out under higher magnification and several dominant features were identified. Firstly, the damage mechanisms observed during the incubation period, such as the appearance of grain boundaries and intergranular fracture, were detected at the region with less severe damage, as shown in Fig. 5.21 (a). Selective locations of material removal took place adjacent to such region, seen in Fig. 5.21 (b). Formation of erosion craters in granular shapes was detected in Fig. 5.21 (c) and (d). Secondly, lipping and folding up of material was observed at the edge of the erosion craters. Features of plastic deformation were identified at the same region. Dimples were found on the folded-up material, as seen in Fig. 5.22. Thirdly, striation marks were detected inside the large erosion craters, shown in Fig. 5.23 (a) and (b).

Cracks were formed on the fractured striation marks. Additionally, deep cavities were found inside the erosion craters, as shown in Fig. 5.23 (c) and (d). Fig. 5.23 (e) and (f) captured the moment that a large piece of material was being removed from the surface.

Further analysis was conducted on the polished transverse-sections, as shown in Fig. 5.24. An erosion crater with a width over 300 μm and depth around 100 μm was seen in Fig. 5.24 (a). Up folding of the material was observed at both edges of the erosion crater, Fig. 5.24 (b) and (g). The tunnelling effect was observed at bottom of the erosion crater in Fig. 5.24 (c) and (d). Fig. 5.24 (d) captures the material removal due to coalescence of microcracks. More microcracks were formed on the fractured crater walls in Fig. 5.24 (f). Secondary cracks were detected at the bottom of the smaller crater formed at the edge, as labelled in Fig. 5.24 (g).

The damage mechanisms in the advanced stages of WDE were well established in the past literature [12,46,60,64,69,71,75,78,79,143]. Lateral outflow jetting and hydraulic penetration induced by repetitive droplet impacts were responsible for the significantly increased erosion rate. The above observations well agreed with the literature findings. The effect of the lateral outflow jetting can be supported by the folded-up material observed at the edge of the erosion craters, which leads to ductile failure with the evidence of dimples shown in Fig. 5.22. Additionally, the direction of stress wave propagation can be indicated by the slip bands formed behind the folded-up material, labelled in Fig. 5.22 (d) and (e). The same observation was reported by Ma et al [79] on bare and surface-treated Ti6Al4V tested at an impact velocity of 350 $m \cdot s^{-1}$ with the whirling arm rig at Concordia University.

In terms of the microstructural response of the Ti6Al4V material, the analysis on transverse section indicates there is no preferential path in which the cracks propagate. This agrees with past studies [69–71,78,79] The stress field in the advanced stages of WDE was complex and the cracks were found propagating trans-granularly within α grains, at the triple junction of α grains, and at the interface of α- and β-phases. Furthermore, the formation of striation marks indicates a fatigue-like mechanism induced by repetitive impingements. However, there is no sign of the formation of a fatigue crack. The loading condition is much more complex in WDE process as it involves high strain rate and stress waves. Hence, it is believed that the formation of the striation marks was attributable to a large piece of material that had been removed under continuous droplet impacts. The theory can be further supported by Fig. 5.23 (e) and (f). With the development of large craters, the exposed surface was more roughened. This enhances the effect of lateral outflow jetting and hydraulic penetration, which leads to formation of large cracks and deep cavities, eventually forming honeycomb structured fracture surface shown in Fig. 5.23 (d). The effect of hydraulic penetration can also be evidenced from the tunnelling phenomenon observed at the bottom of the erosion crater in Fig. 5.24 (c).

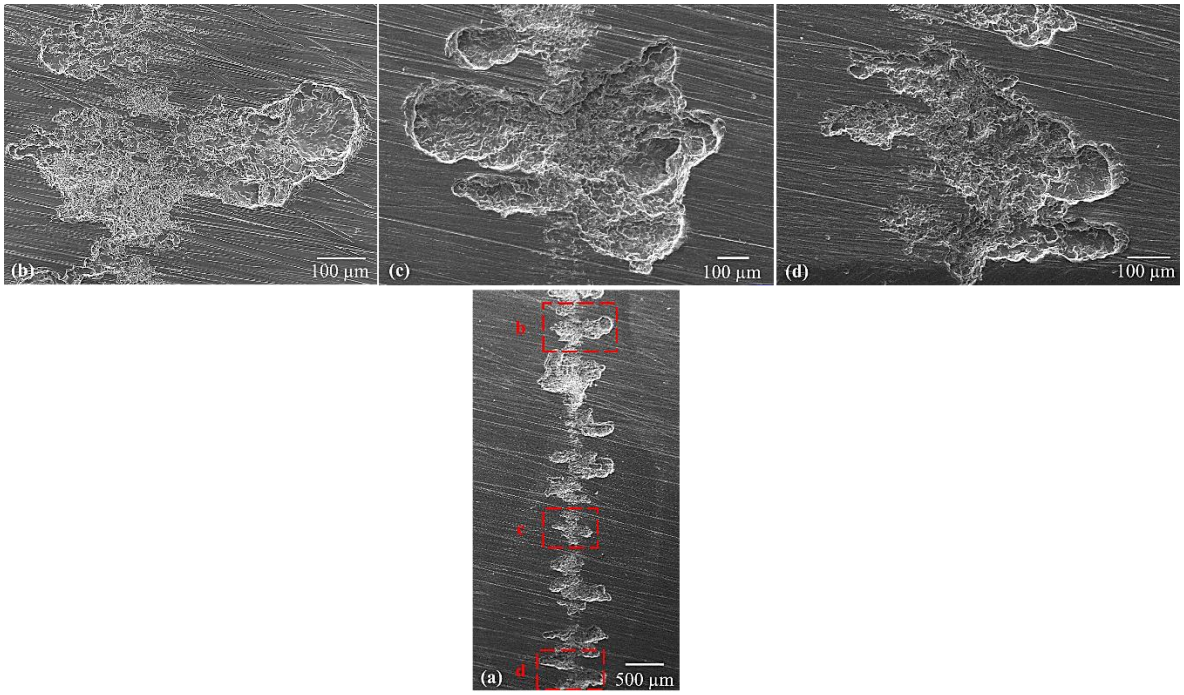

Fig. 5.20 Exposed surface of rough Ti6Al4V specimen 2 during advanced stages.

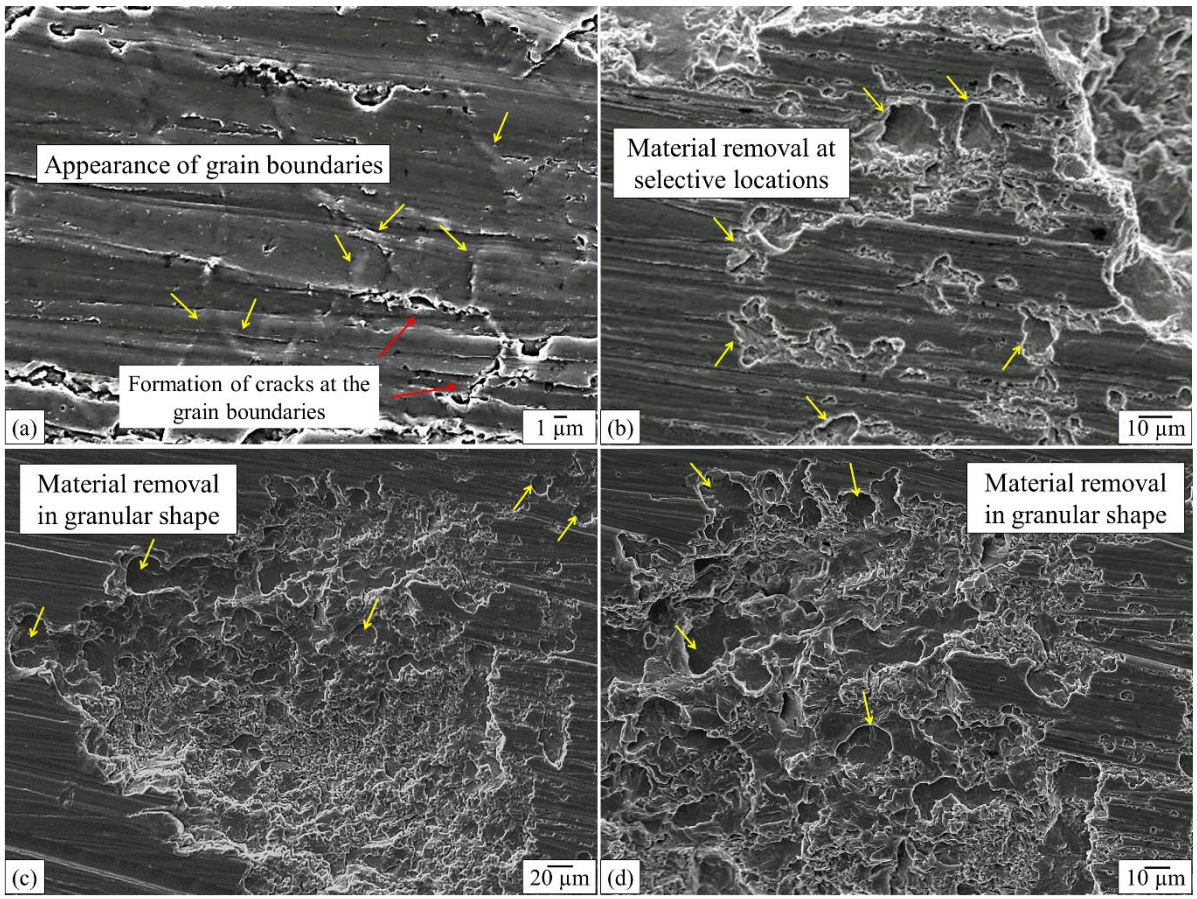

Fig. 5.21 Features of material removal in granular shape.

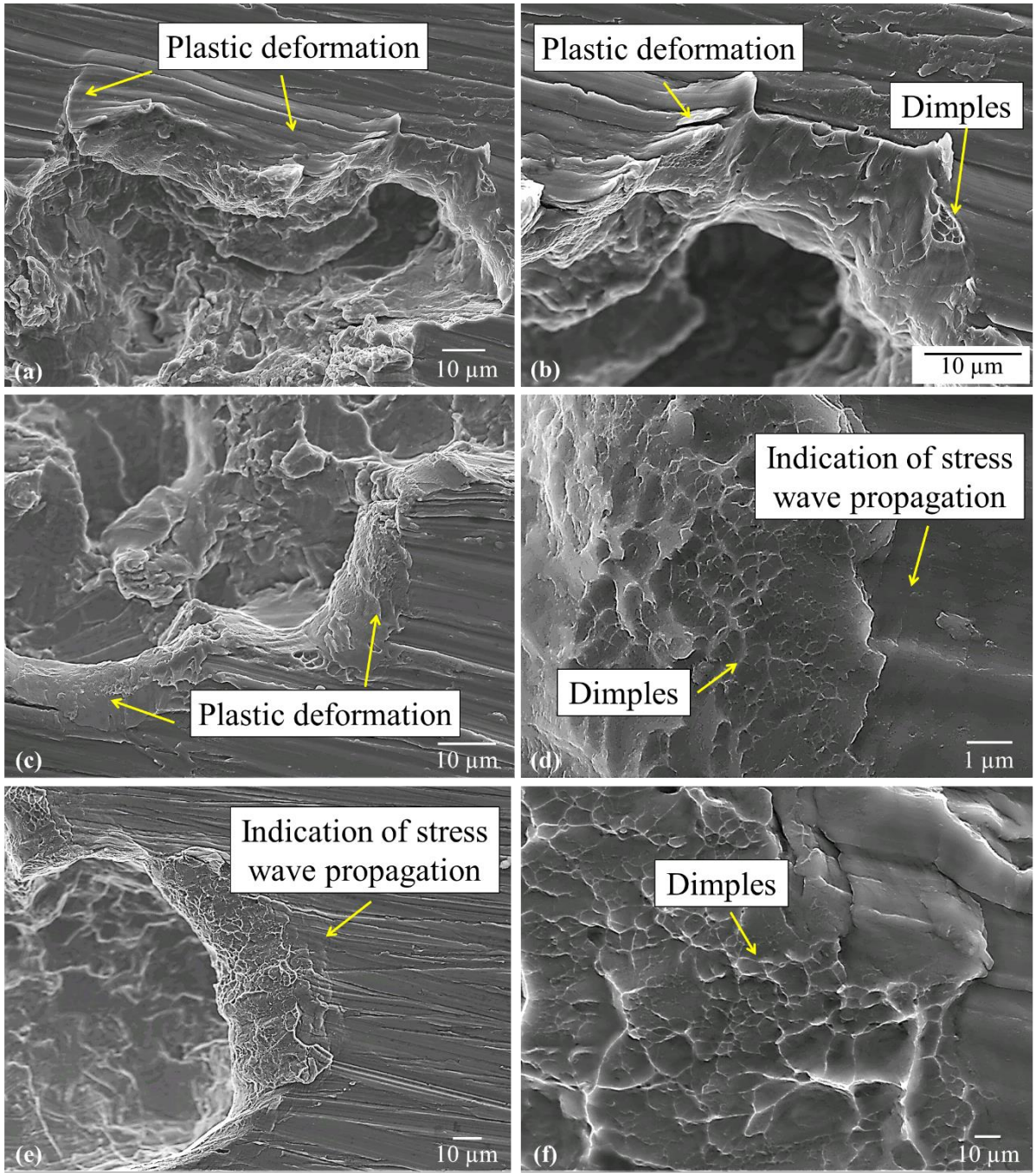

Fig. 5.22 Features of material up folding observed at the edge of the erosion craters.

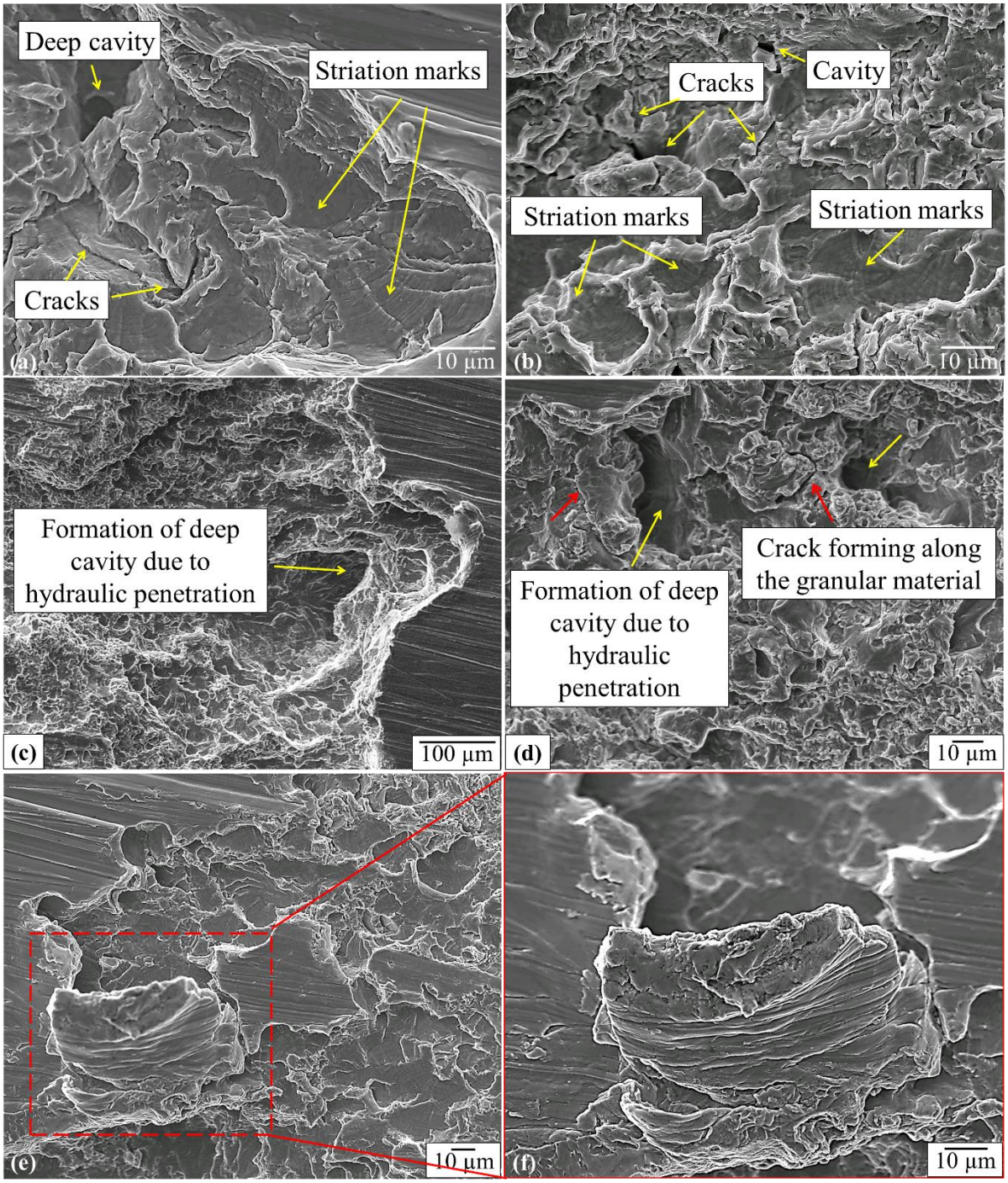

Fig. 5.23 Damage mechanisms in the advanced stages of WDE: (a) and (b) up-lifting of material; (c) and (d) formation of striation marks inside the erosion craters; (e) and (f) formation of deep cavities.

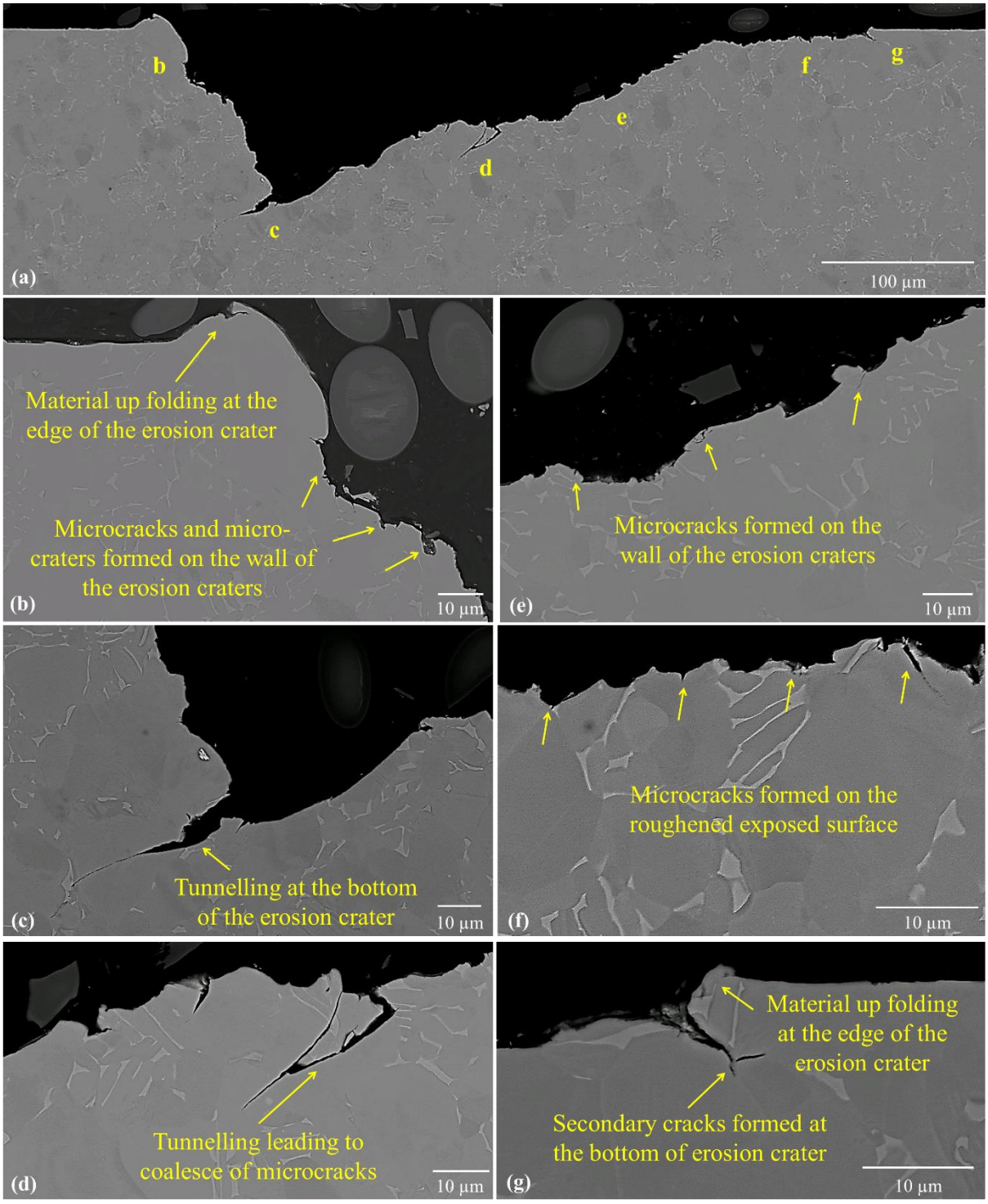

Fig. 5.24 Cross-sections of rough Ti6Al4V specimen 2 during advanced stages.

5.4 Correlation between WDE and CE of Ti6Al4V

Comparison between WDE and CE of Ti6Al4V base material is shown in Fig. 5.25. The maximum erosion rate of CE during 65 mins test period was 0.002 mg/min, while that of WDE was 0.02 mg/min. Hence, the erosion rate was 10 times higher in WDE. The correlation between the two processes has been studied in the past on stainless steel substrate and the maximum erosion rate of WDE was 500 time higher than that of CE [91]. Preece and Brunton [153] reported that although the magnitude and duration of the pressure pulses produced by the two processes are similar, the materials required three to four orders of magnitude more impacts by CE than by WDE for a given amount of erosion. The shearing effects induced by lateral outflow in WDE contributes to greater erosive power in comparison to CE. Moreover, the maximum erosion rate of the WDE test conducted under similar conditions with Concordia rig (Fig. 5.11) was calculated to be 0.58 mg/min, which was around 300 times higher than that of CE in this study. The ratio was more close to the literature data. Therefore, it is believed that the test conditions of WDE at NPL was less severe, which can be attributed to the different rig designs. Additionally, the effect of initial surface roughness was found more significant in WDE than CE. This can be due to the rapid acceleration of erosion rate induced by the interaction between lateral outflowing jetting and surface asperities. Further comparison of the damage mechanisms between the two processes is discussed as follows.

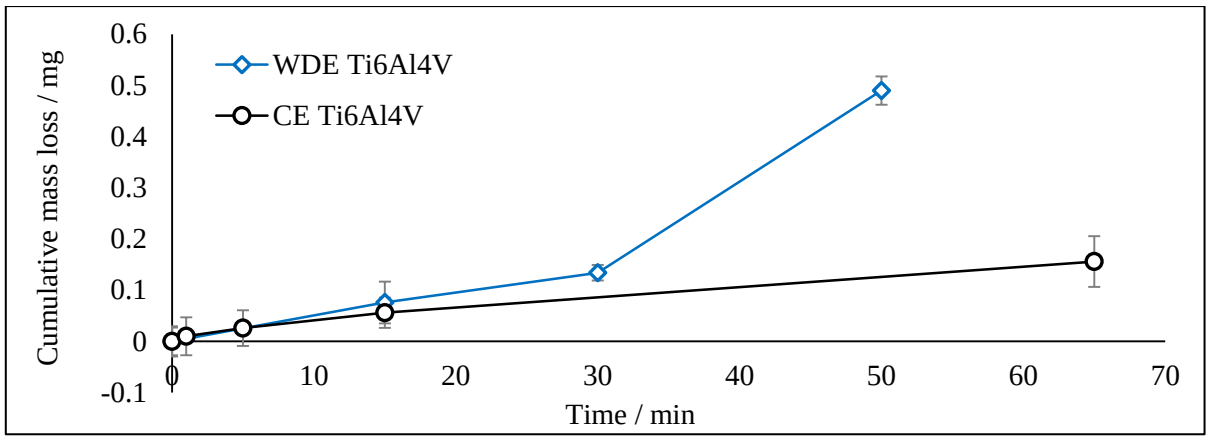

Fig. 5.25 Comparison between WDE and CE of Ti6Al4V base material.

5.4.1 Early stages

Ti6Al4V base material exhibits similar behaviour during early stages of WDE and CE. In both cases, grain boundaries were visible on the exposed surface due to displacements of α grains with favourable shearing orientation, as shown in Fig. 5.26 (a) and (b). Later, damage initiating along the grain boundaries and material chipping at the triple junctions was developed in Fig. 5.26 (c) and (d). These features resemble the rain erosion damage observed on the ex-service Ti6Al4V fan blade leading edge shown in Fig. 5.26 (e) and (f). Slip lines were not seen on Ti6Al4V tested under WDE nor the ex-service leading edge due to the rough surface finish, however, evidence can be provided in past literature [69]. Hence, it can be proposed that the damage mechanisms of WDE and CE of Ti6Al4V during the early stages were similar. They

involve grain displacements under high impact pressure and stress waves, which later leads to the formation of intergranular fracture and material removal at triple junctions. The microstructure and crystal orientation of Ti6Al4V have strong effect on the material response to both processes.

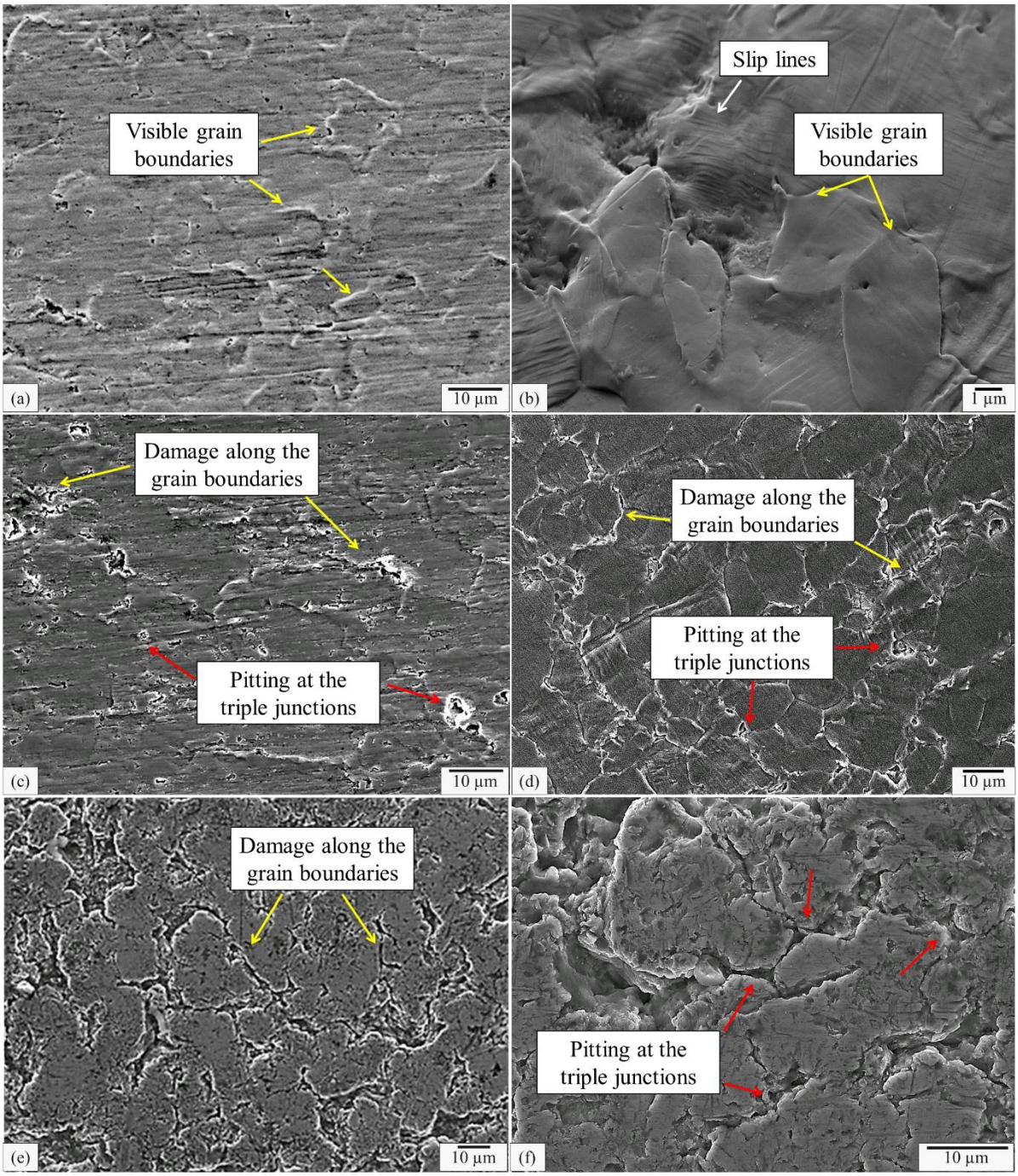

Fig. 5.26 Appearance of grain boundaries on the exposed surface during incubation period of: **(a)** WDE; **(b)** CE on Ti6Al4V base material; formation of damage along the grain boundaries and at the triple junction on exposed surface of **(c)** WDE, **(d)** CE of Ti6Al4V base material and **(e), (f)** on ex-service turbofan blade leading edge.

5.4.2 Advanced stages

In the advanced stages of WDE and CE processes, granular erosion craters were formed due to grain removal, as shown in Fig. 5.27 (a) and (c). The fracture surfaces were developed with selective locations of material removal that verifies the effect of microstructure and crystal orientations during the early stages, as seen in Fig. 5.27 (b) and (d). The rain erosion morphology detected at the leading edge of ex-service turbofan blade, shown in Fig. 5.27 (e) and (f), demonstrating great similarities to the damage mechanisms discussed above. Additionally, with increasing exposure time, striation marks and honeycomb structured fracture surface were formed in both processes, see Fig. 5.28.

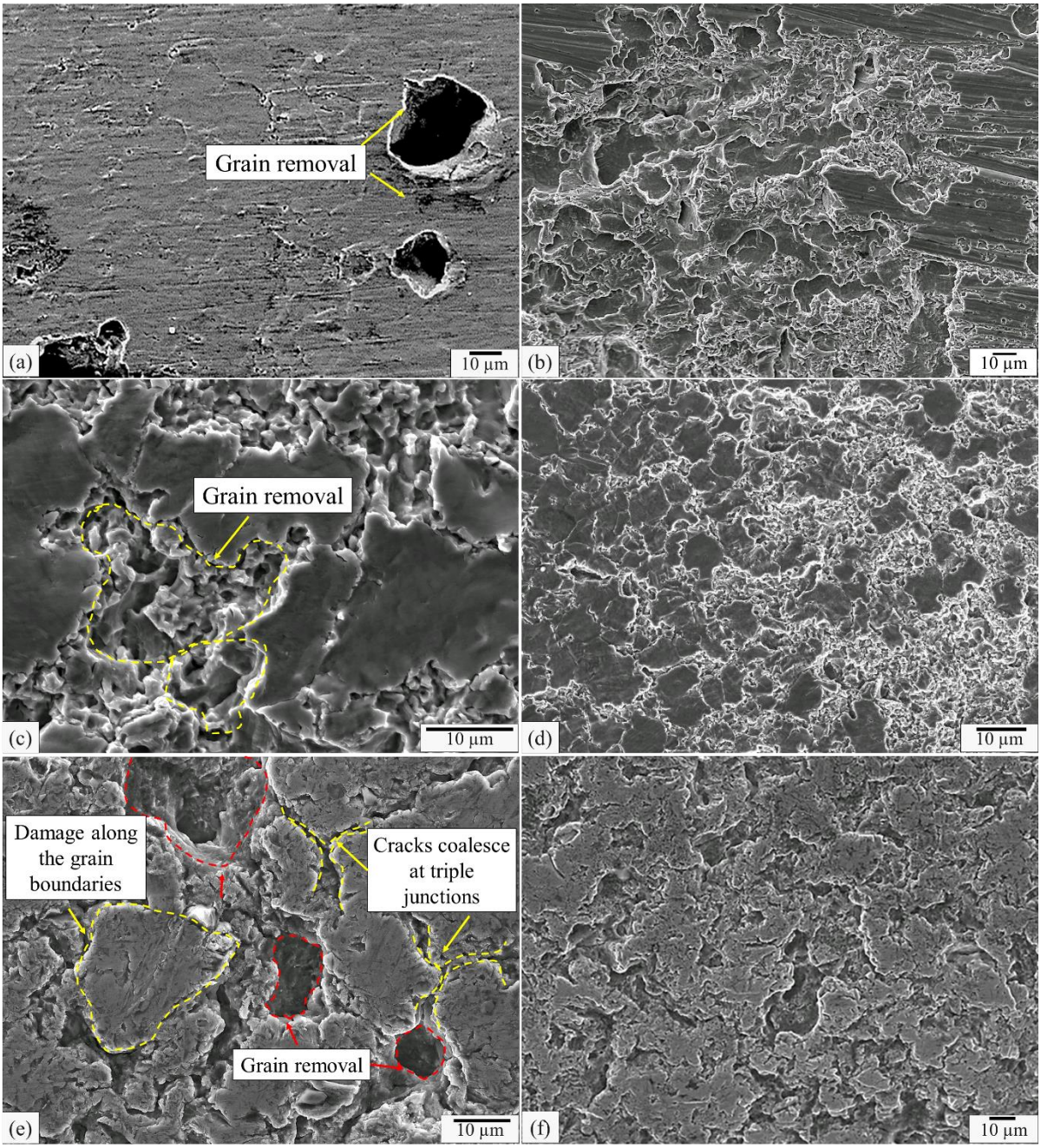

Fig. 5.27 Grain removal features observed in advanced stage of **(a), (b)** WDE on Ti6Al4V base material; **(c), (d)** CE on Ti6Al4V base material; **(e)** and **(f)** ex-service fan blade leading edge.

The cross-sectional analysis of CE and WDE of Ti6Al4V base material, as well as the rain erosion at the blade leading edge is compared in Fig. 5.29. It is revealed that the dimension of the erosion craters was much greater in WDE at high impact velocity ($V > 300$ m·s^{-1}), as seen in Fig. 5.29 (a) and (b). This indicates that the material removal behaviour was more severe in WDE process with high impact velocity due to much higher erosion rate. Moreover, the effect of hydraulic penetration can be demonstrated by the tunnelling phenomenon seen at the bottom of the erosion craters. While in the case of CE of Ti6Al4V, the damage observed in Fig. 5.29 (c) greatly resembles the rain erosion damage at low impact velocity ($V < 200$ m·s^{-1}). This further confirms that the unique effect of lateral outflow jetting in WDE contributes to the drastically increased erosion rate with increasing impact velocities. Therefore, it can be concluded that the damage mechanisms in the advanced stages of both processes show certain similarities, such as fatigue-like fracture and hydraulic penetration. The severity of CE induced damage can be similar to WDE at low impact velocity. However, the effect of lateral outflow jetting is unique in WDE process, which leads to folding-up of the material (Fig. 5.22) and formation of large erosion craters (at high impact velocity). These were not seen in CE process.

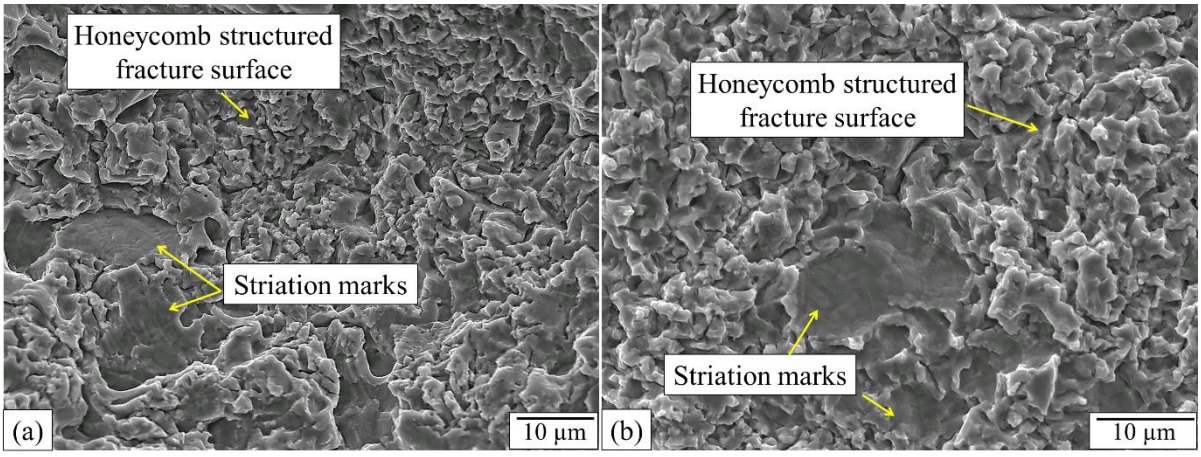

Fig. 5.28 Striation marks and honeycomb structured fracture surface developed on Ti6Al4V base material under **(a)** WDE test and **(b)** CE test.

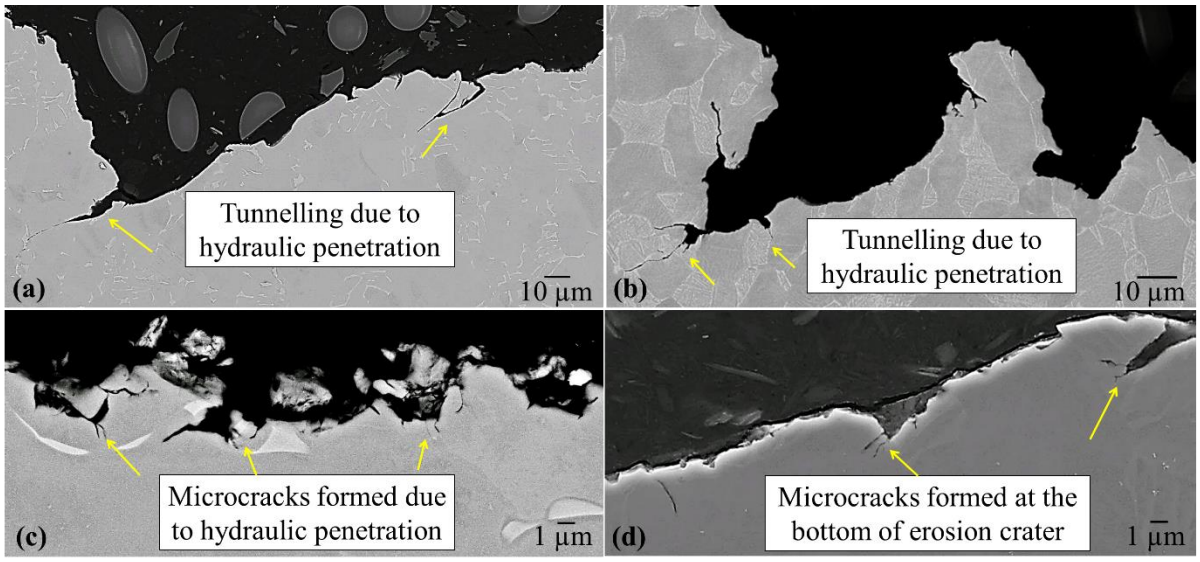

Fig. 5.29 Cross-sectional analysis of **(a)** WDE of Ti6Al4V base material at 300 m·s^{-1}; **(b)** rain erosion at H zone ($V > 300$ m·s^{-1}) of ex-service fan blade leading edge; **(c)** CE of Ti6Al4V base material; **(d)** rain erosion at L zone ($V < 200$ m·s^{-1}) of ex-service turbofan blade leading edge.

5.5 Conclusions

The predominant damage observed at the fan blade leading edge is successfully generated through vibratory CE test on Ti6Al4V base material. Correlation between WDE and CE of Ti6Al4V is established as similarities in the damage mechanisms are identified, especially during the incubation period. Hence, CE testing can be employed as a valid screening process to predict the WDE performance of the coated systems in the following Chapter. The correlation between the two processes is summarised as follows:

- CE and WDE demonstrate similar mechanisms on Ti6Al4V. However, the effect of lateral outflow jetting is unique in WDE process, which contributes to the much higher erosion rate in WDE than CE.

- The effect of initial surface roughness was more significant in WDE than CE. This can be due to the interaction of lateral outflow jetting and surface asperities leads to drastic increase of erosion rate in WDE process

- Microstructure of the impact surface plays a vital role on the response to water droplet impingements during incubation period. Grain displacement leading to formation of intergranular cracks is primarily induced by high impact pressure and stress waves.

- The damage mechanism during the incubation period of both processes was similar: intergranular fracture was induced due to anisotropic behaviour of α grains under high impact pressure and stress waves.

- In the advanced stages of both processes, similarities of the damage mechanisms were identified: erosion craters were formed due to grain removal; striation marks were developed inside the erosion craters due to large particle had been removed and honeycomb structured fracture surface with deep cavities was formed with increasing exposure time.

- The WDE tests conducted at NPL exhibit much lower erosion rate in comparison to the ones reported in the literature under similar testing conditions.

Chapter 6.
CE performance of CVD-W/WC coatings

The correlation between CE and WDE is identified as similar damage mechanisms are involved in both processes, especially during the incubation period. Therefore, for the second stage of this work, a series of coatings are applied on Ti6Al4V base material and tested under CE to evaluate their potentials for WDE application. The process effectively screened 14 coatings with 4 coatings showing good resistance in comparison to Ti6Al4V with extended incubation period. They are nanocrystalline CVD W/WC T1200, LT coatings, HIPIMS deposited nanoscale multilayer CrAlYN/CrN C1 and C2 coatings. The results are summarised in Table 6.1. The common coating failure modes seen under CE are delamination and brittle fracture.

For the 4 down-selected coatings, an in-depth understanding of the coating damage mechanisms is established by correlating the coating performance with microstructure, crystallographic texture, interface design, deposition conditions and mechanical properties for the first time. In this chapter, the CE performance of the best performed Hardide CVD W/WC coatings are further discussed.

Table 6.1 Coatings tested under CE screening test

Coating	Deposition	Thickness	Hardness	Test results
Hardide A1	CVD	55 µm	800 HV	Delamination at the coating/substrate interfaces
Hardide A2		100 µm		
Hardide A3		100 µm	1200 HV	
Hardide T1200		55 µm	1200 HV	Negligible mass loss
Hardide T1600		55 µm	1600 HV	Extended incubation period
Hardide LT		60 µm	1250 HV	Negligible mass loss
CrN/NbN 1	HIPIMS	4 µm	2700 $HK_{0.25}$	Brittle fracture
CrN/NbN 2			3500 $HK_{0.25}$	
TiAlN/VN			3500 $HK_{0.25}$	
CrAlYN/CrN C1			3000 $HK_{0.25}$	Extended incubation period
CrAlYN/CrN C2			2700 $HK_{0.25}$	Negligible mass loss
TiN	PVD		2200 $HK_{0.25}$	Brittle fracture
AeroKret elastomeric coating 1	Flow coat	2 mm	/	Coating penetration, weight gain due to water absorption
AeroKret elastomeric coating 2	Spray coat			

6.1 Coating deposition

The Hardide coating systems are a series of nano-structured coatings composed of Tungsten Carbide (WC) nano-particles embeded in metal Tungsten (W) matrix. The W/WC coating specimens studied in this Chapter were produced with CVD by Hardide Coatings Limited in Oxfordshire UK using the conditions listed in Table 6.2. A copper (Cu) interlayer is applied on the Ti6Al4V base material with electroplating. The coated specimens are polished after the deposition process.

Table 6.2 Information of Hardide coatings.

Coatings	T-1200HV	T-1600HV	LT
Manufacturing temperature (º C)	500	500	350
Thickness (µm)	~55	~55	~60

6.2 Topographical characterisation

The 3D surface profiles of the Hardide coatings are presented in Fig. 6.1. Features of various heights are detected on all Hardide coating surfaces indicating the rough surface profile. The corresponding values of Ra, Sa, Ssk and Sku are listed in Table 6.3, which shows that the Ra and Sa values of LT coating are the smallest. The sign of skewness (Ssk) indicates the predominance of peaks (Ssk > 0) or valley (Ssk < 0) structures comprising the surface [154]. The Ssk values of all coatings are negative, however, that of LT coating is significantly larger than the other two coatings. Hence, it can be suggested that there are more valley structures on LT coating surface. In terms of T1200 and T1600 coating surfaces, there is a tendency of valley structures, however, it is not as significant as that of the LT coating.

The Kurtosis (Sku) is useful for indicating the presence of either peak or valley defects which may occur on a surface. It indicates the presence of extremely high peaks / deep valleys (Sku > 3.00) or lack thereof (Sku < 3.00) making up the texture [154]. The Sku values of T1200 and T1600 coatings are similar and smaller than 3, but that of LT coating is around 4.05 µm. Thus, the topography of the T1200 and T1600 coatings are free of extreme peaks or valley features, whereas that of LT coating exhibits predominant deep valley features.

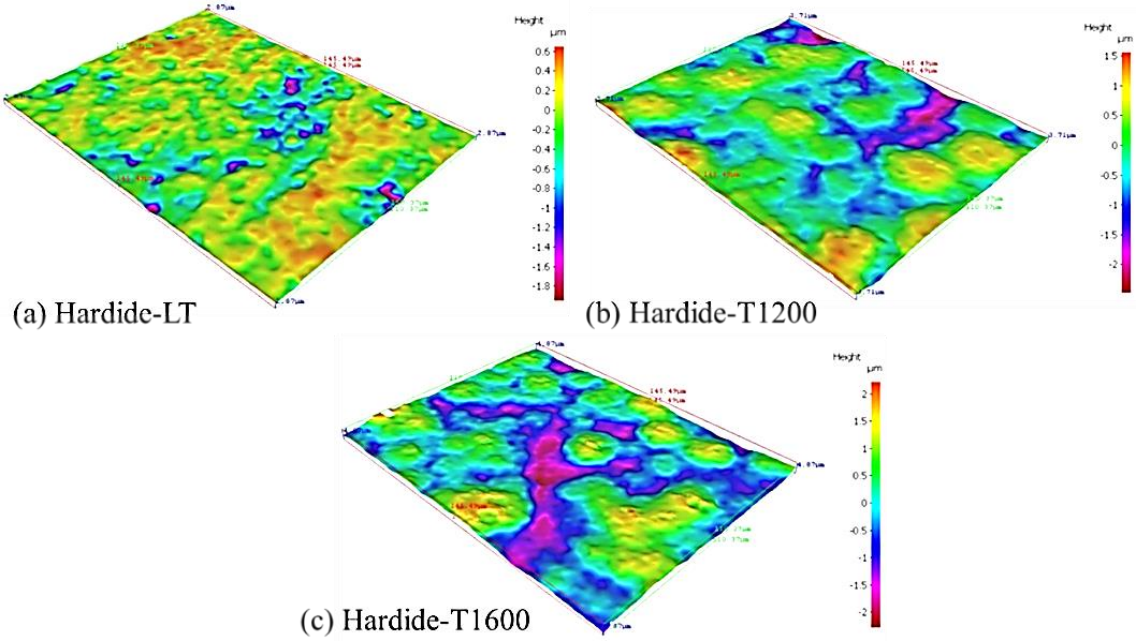

Fig. 6.1 Surface profiles of Hardide coatings: (a) T1200 coating; (b) T1600 coating; and (c) LT coating.

Table 6.3 Roughness values of Hardide coatings

Coatings	Ra / µm	Sa / µm	Ssk/µm	Sku/µm
LT	0.24 ± 0.02	0.25 ± 0.02	- 0.80 ± 0.24	4.05 ± 0.41
T1200	0.28 ± 0.03	0.31 ± 0.03	- 0.18 ± 0.19	2.47 ± 0.25
T1600	0.35 ± 0.01	0.41 ± 0.01	- 0.04 ± 0.09	2.62 ± 0.17

6.3 Microstructural characterisation

6.3.1 Surface characterisation

XRD analysis of three Hardide coatings shown in Fig. 6.2 indicates that there is no variation of the coating composition. All three Hardide coatings are composed of high purity W, the WC cannot be detected due to the nano-sized WC particles inside the coatings. The intensity of the W (200) peak is significantly higher than the rest in the XRD spectrum of LT coating, thus, a different scale was used to show the lower intensity peaks in Fig. 6.2 (c).

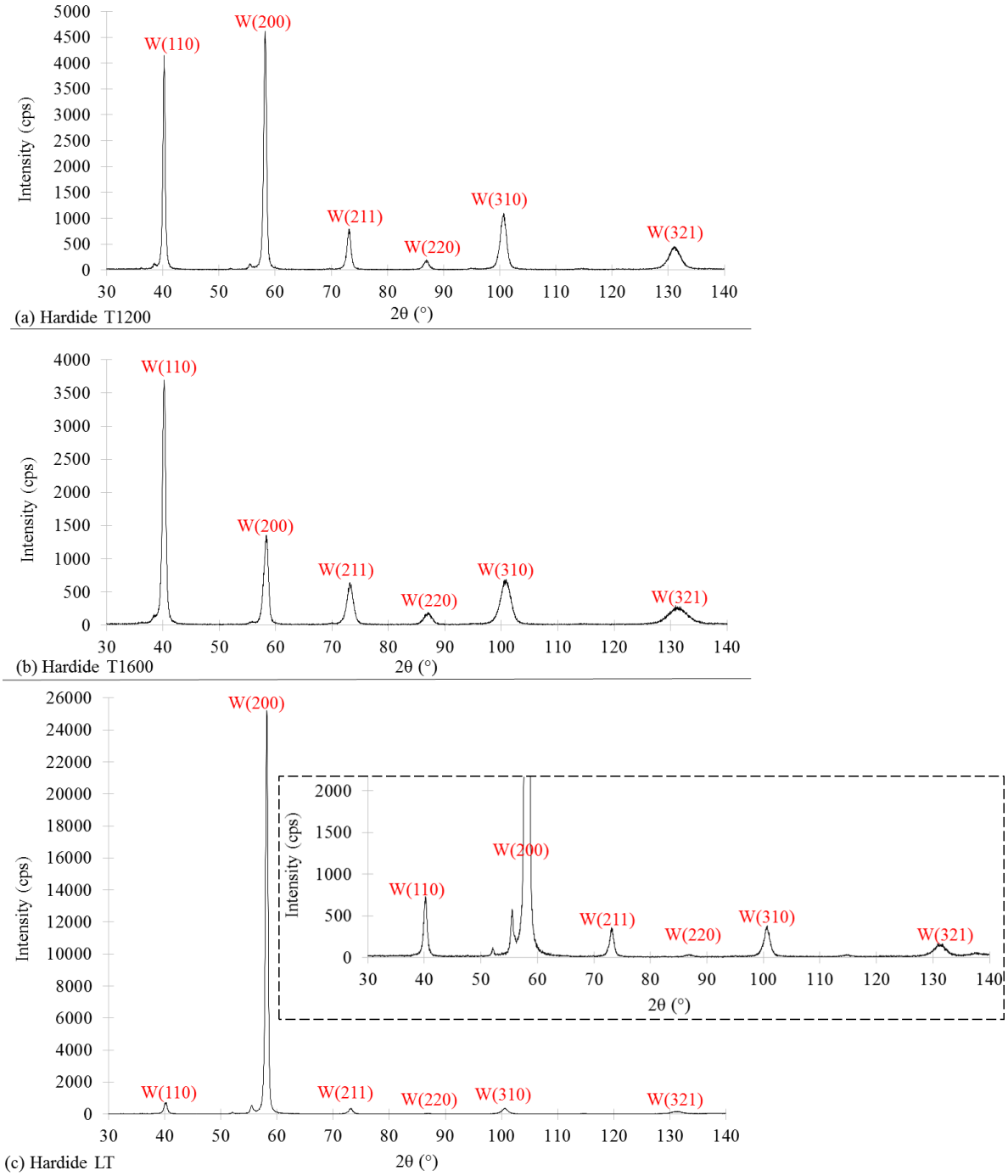

Fig. 6.2 XRD analysis of (a) Hardide T1200; (b) T1600 and (c) LT coatings.

SEM observation was conducted to identify the microstructural features of the three Hardide coatings, as shown in Fig. 6.3. It can be seen from the lower magnification images, Fig. 6.3 (a), (c) and (e), that all coating surfaces are composed of dark and shiny areas. The dark zone of all coatings is shown as flat surfaces with presence of macro scratches, which might be induced by post-polishing process. While for the shiny zones, all three coatings present significantly different features, as magnified in Fig. 6.3 (b), (d) and (f), respectively. The shiny zone of the LT coating surface is covered with clusters of grains-like features, as shown in Fig. 6.3 (b); whereas that of T1200 coating is composed of angular particulates in Fig. 6.3 (d). For T1600 coating surface, the shiny zone shows tangles of stem-like features, as seen in Fig. 6.3 (f).

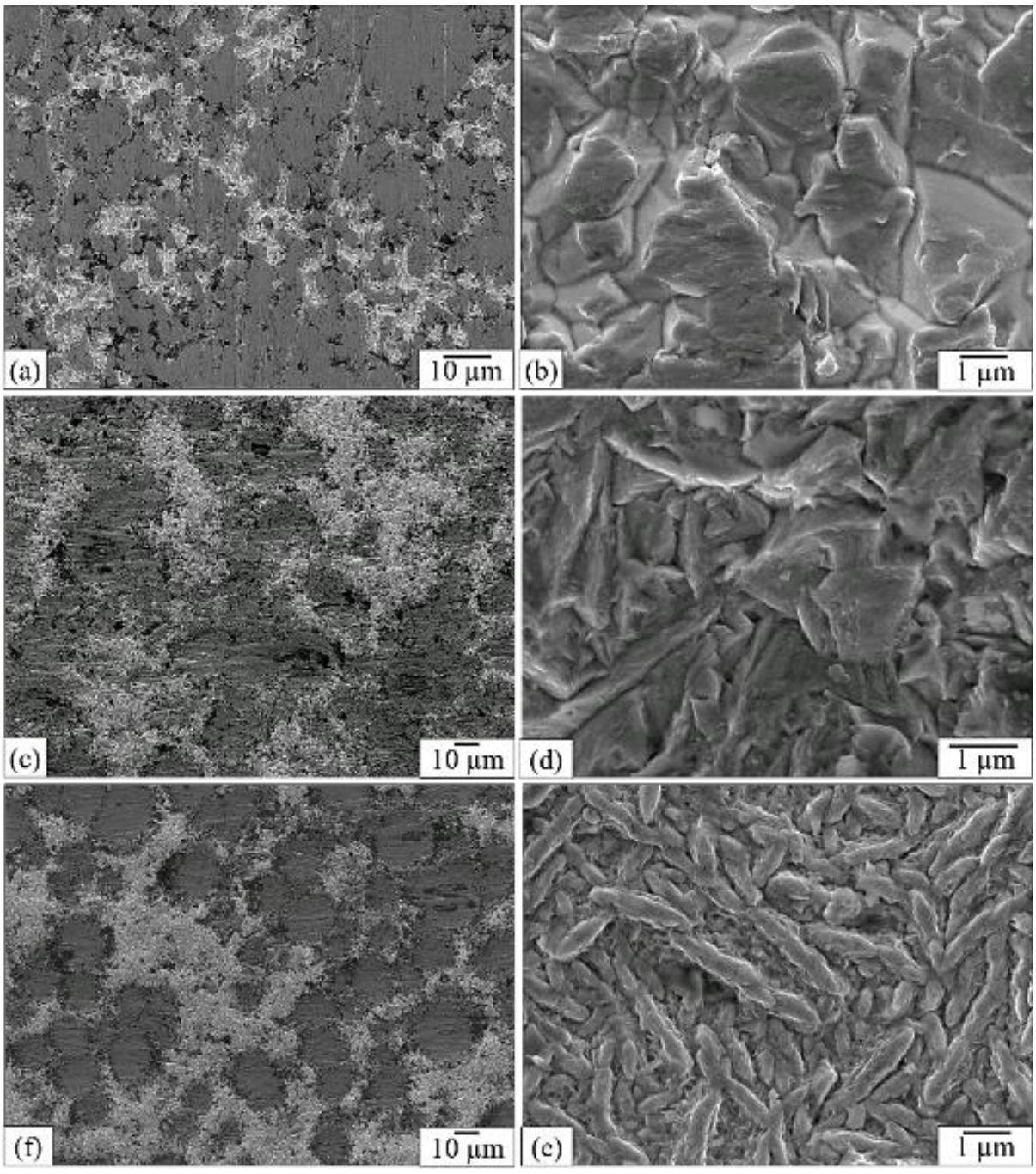

Fig. 6.3 Microstructure of Hardide coating surfaces: (a) and (b) LT; (c) and (d) T1200; (e) and (f) T1600.

6.3.2 Cross-sectional characterisation

The cross-sectional characterisation of the coating microstructure was further conducted with SEM and EBSD. The results are shown in Fig. 6.4. It reveals different structures for all three coatings. LT coating exhibits columnar grain structures with a preferential growth to the ⟨001⟩ orientation. Three growth stages can be identified in EBSD grain orientation map in Fig. 6.4 (a): (1) nucleation and growth of nearly equiaxed grains with random orientations; (2) formation of premature small columnar grains, which is a transitional stage; and (3) stable growth of mature large columnar grains with a preferred orientation normal to the substrate. In this stage, there are a few columnar grains grew as high as the thickness of the CVD-W, but most columnar grain growth is stopped by fine grains nucleated nearby the grain boundaries.

The LT coating presents a textured columnar grain structure manufactured by the CVD process. Similar CVD coating structures have been investigated in the past studies with the textured columnar grain growth [155–159], the formation of which is because of the growth kinetics favour only the grains with a [001] axis oriented to the substrate [155–162]. The process resembles the manufacturing process of nanocrystalline diamond (NCD), which is the thin film diamond grown with a very high initial nucleation density [161,162]. There is little or no re-nucleation, as shown in Fig. 6.4 (a). The grain size and the roughness increase with film thickness.

For T1200 and T1600 coatings, the cross-sectional views present a unique hierarchical coating configuration that are tailored by the Hardide CVD process, as shown in Fig. 6.4 (b) and (c). Three distinct stages of grain growth were observed. Firstly, nucleation of fine equiaxed grains at the interface with the substrate Ti6Al4V material was detected in both coatings, which is the same in LT coating. The second stage is a 20 to 25 µm layer of coarse columnar grains developed over the first layer in both coatings. The EBSD results show that the columnar grains in both coatings demonstrate a preferred ⟨001⟩ orientation. However, those in T1200 show a stronger texture. The third stage in both coatings is composed of fine grains with a thickness of 25 to 30 µm. The top fine layer in T1200 coating extends from the columnar grains in the second growth stage, showing a branch-like feature. Such transitional change of microstructure facilitates the grain growth in the same ⟨001⟩ orientation for the top layer. While in the case of T1600 coating, the top fine layer is formed independently from the coarse columnar grains. Hence, a distinct interface between these two stages of grain growth is identified. The fine grains in the top layer are in the shape of fine stems with random orientations. Additionally, the pre-existence of subsurface vertical cracks in a length up to 15 µm was detected on the cross-section of T1600 coating, as shown in Fig. 6.4 (c). One end of these cracks were located around 10 to 20 µm beneath the coating surface; while the other end stops at the interface of the fine and coarse layer of the T1600 coating.

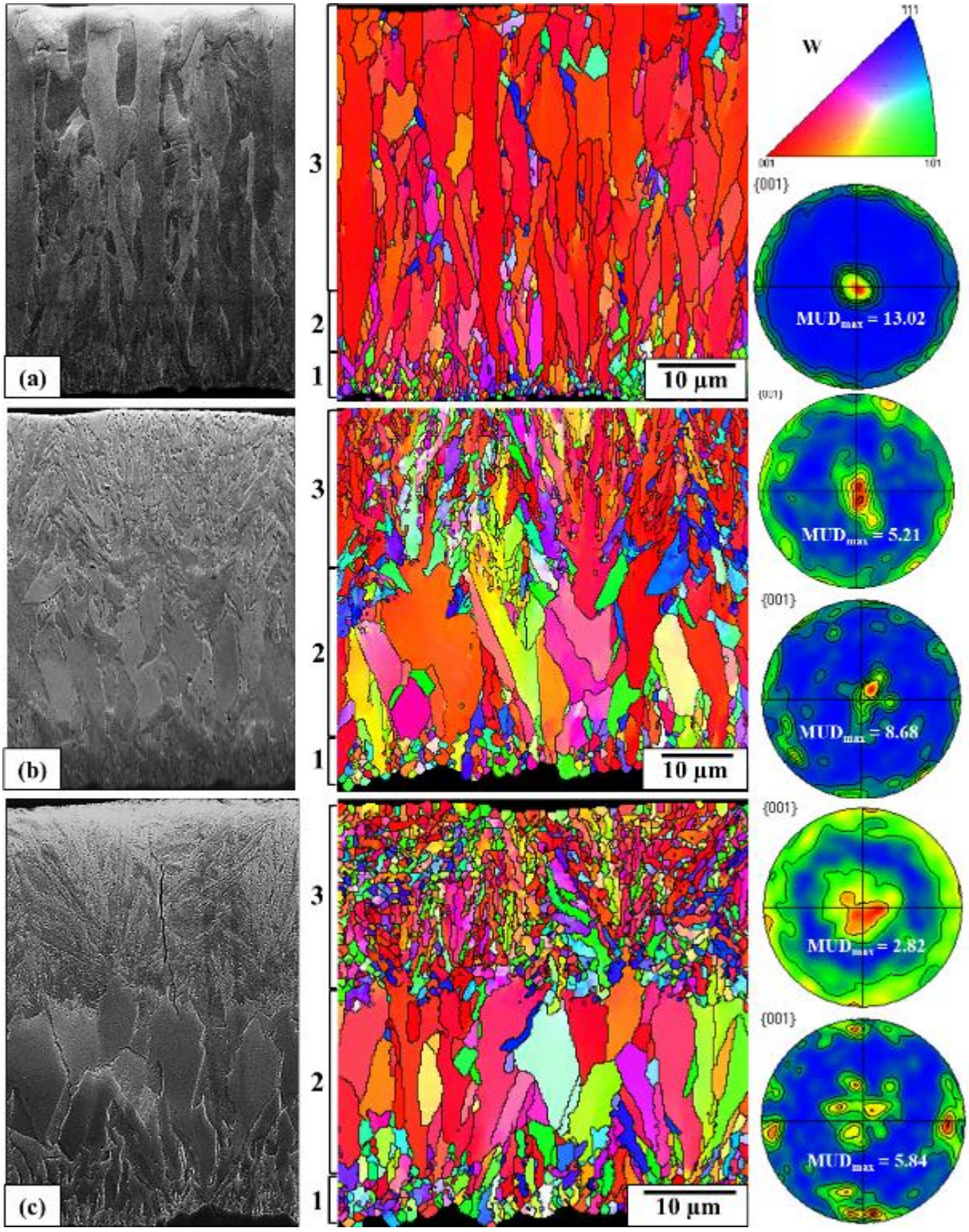

Fig. 6.4 Cross-sectional views of CVD W coatings: (a) Hardide LT; (b) Hardide T1200; and (c) Hardide T1600; where "MUD_{max}" stands for the maximum value of multiples of uniform density.

Further analysis was applied for characterisation of the grain size. However, the resolution of the EBSD analysis (a step size of 0.2 µm was used) cannot precisely identify the grain size of the top fine layers of T1200 and T1600 coatings. Hence, such characterisation was only applied in the growth stage composed of columnar grains in all coatings and the results are presented in Table 6.4. The width of columnar grains in LT coating is 4.89 µm with the largest height

reaches up to the whole thickness of the coating (50 µm). The width of the columnar grains in the second growth stage of Hardide-T1600 is similar to that of LT coating, which is 4.53 µm; while the average height of such stage is about 12.31 µm. The width of the columnar grains is the largest in T1200 coating, which is 6.43 µm, and the average height is around 15.22 µm.

Table 6.4 Grain size measurements of each stage of grain growth in all coatings.

Coatings	Growth stage	Stage 2 (µm)
LT	Height	10 – 50
	Width	4.89
T1200	Height	15.22
	Width	6.43
T1600	Height	12.31
	Width	4.53

6.4 Mechanical properties

6.4.1 Nanoindentation measurement of coating surface

Nanoindentation measurements conducted on the surface of all Hardide coatings. The average values of nanohardness and the reduced Young's modulus are listed in Table 6.5. The T1600 coating shows the highest nanohardness and Young's modulus. While those of LT and T1200 coatings are similar. The fluctuation of the data can be potentially correlated to the surface morphology of the coatings observed in the previous section. Additionally, the hardness of the substrate Ti6Al4V material was measured 10 to 20 µm away from the coating-substrate interface and the results are listed in Table 6.5. It can be seen that the variation in the manufacturing temperature of three coatings has little effect on the substrate hardness.

Table 6.5 Nanohardness and reduced Young's modulus of Hardide coatings.

Coatings	LT	T1200	T1600
Nanohardness (Gpa)	11.5 ± 3.6	12.6 ± 4.5	19.5 ± 7.3
Reduced Young's modulus (GPa)	309.1 ± 62.4	333.8 ± 78.0	393.1 ± 123.8
Substrate hardness (GPa)	4.82 ± 0.37	4.78 ± 0.55	4.99 ± 0.60

6.4.2 Cross-sectional nanoindentation analysis

The cross-sectional nanoindentation measurements were conducted through coating thickness (Fig. 6.5) and the results are shown in Fig. 6.6 and Fig. 6.7. The nanohardness and the reduced Young's modulus show a trend of gradient increase from the bottom to the surface of all three coatings. For the LT coating, the nanohardness increases from 10 GPa at the bottom layer to 25 GPa near the coating surface. The reduced Young's modulus of which remains stable in a range from 300 to 400 GPa and slightly increases to 500 GPa close to the coating surface.

The nanohardness profiles of T1200 and T1600 coatings show similar values over the thickness of 30 µm (top fine layers of both coatings). Where the nanohardness for both coatings increase gradually from 20 to 25 GPa. However, a significant difference between the two was detected

from the measurements taken at 10 and 20 µm thickness. These indentations were located in the layers of coarse columnar grains in both coatings. Hence, the nanohardness of the coarse layer in T1200 coating is around 15 GPa, while that of the T1600 coating is around 7 GPa. Therefore, a significant variation in the nanohardness between the second and the top layer was identified in T1600 coating.

The reduced Young's modulus of the T1200 coating starts at 320 GPa at 10 µm thickness and rises up to 400 GPa at 20 µm, within the columnar grain zone of the coating. The values obtained in the top fine layer (30 to 50 µm) are relatively stable, showing a slight increase from 420 GPa to 470 GPa. While in the case of T1600 coating, the reduced Young's modulus for the columnar grain zone (10 to 20 µm) is 320 GPa. The values then increase from 370 GPa to 450 GPa across the fine top layer.

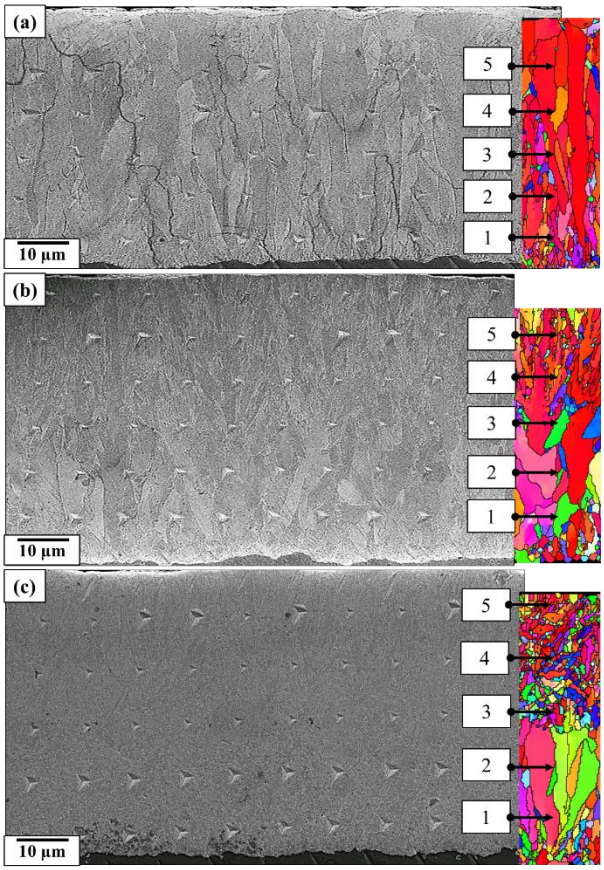

Fig. 6.5 Cross-sectional nanoindentation measurements on three CVD-W coatings: (a) LT; (b) T1200; (c) T1600.

It is noted that the results of E values through coating thickness is abnormal. As E is a material dependant factor that cannot be easily changed. Hence, the variation of E values of all coatings ranging from 300 GPa at the substrate interface to 450 close to the coating surface is strange.

Additionally, the nanohardness results of LT and T1600 coatings at 10 and 20 µm from substrate show different values, where the microstructure of the two coatings is similar. This can be attributed to the variation in the residual stress through coating thickness that was developed under different manufacturing processes.

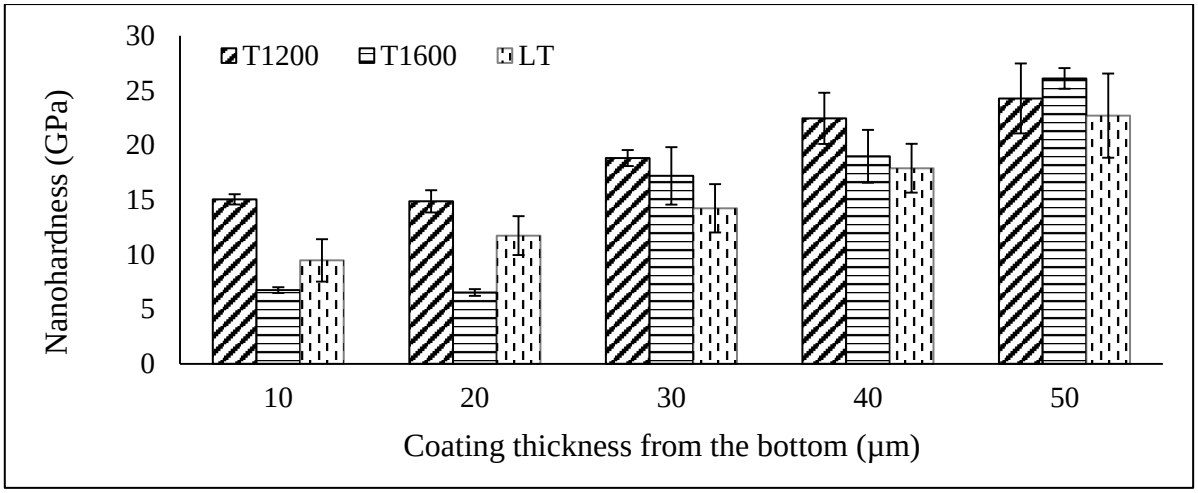

Fig. 6.6 Cross-sectional nanohardness measurements.

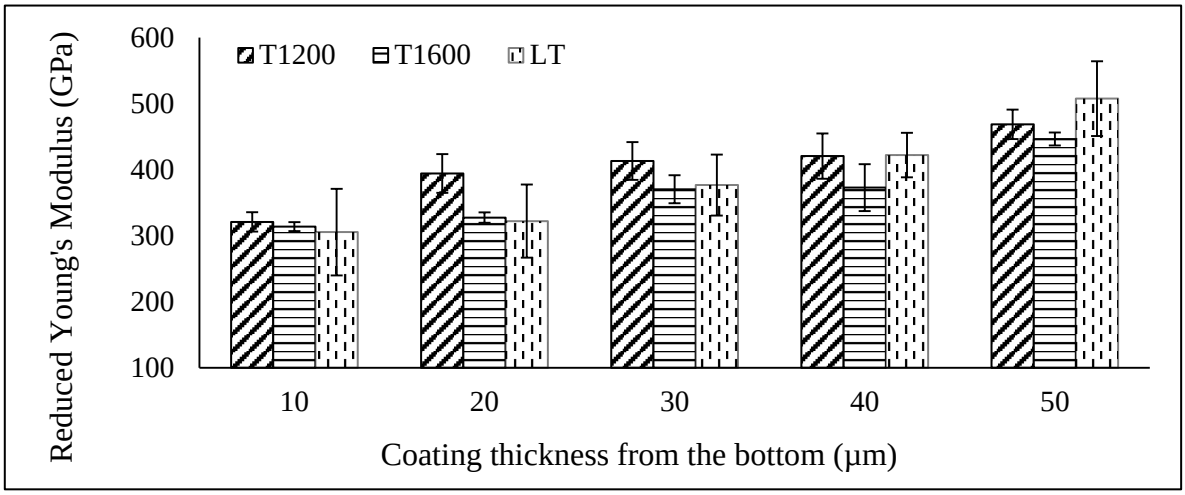

Fig. 6.7 Cross-sectional effective Young's modulus.

6.5 Cavitation erosion performance of Hardide coatings

6.5.1 CE curves

The CE curves of all three Hardide coatings with reference to the un-coated Ti6Al4V specimen are plotted in Fig. 6.8. The cumulative volume loss was converted from the gravimetric measurements and the density used for Ti6Al4V base material and Hardide coatings were 4.5 and 19.4 g/cm^3, respectively. All the coatings outperform the substrate Ti6Al4V with significantly lower erosion rate throughout the test period of 330 mins, as shown in Table 6.6. It can be seen that the Ti6Al4V substrate material reached the maximum erosion rate of 15.6 mg/min after 120 mins of incubation period, while those of the Hardide coatings cannot be identified in Fig. 6.8. Hence, the CE curves of the Hardide coatings are presented separately in Fig. 6.9 to better observe the variation among the coating performances. The T1200 coating shows the best performance among the three coatings with the lowest cumulative volume loss. For the LT coating, a rapid increase of the erosion rate (0.013 mg/min) was detected during the initial 10 mins of exposure to CE. The coating then maintained at an erosion rate of

approximately 0.004 mg/min at the end of the test. In the case of the T1600 coating, the CE curve indicates the worst performance among the three coatings. The erosion rate experienced the first significant increase (0.132 mg/min) after 30 mins of CE exposure, it then demonstrated a gradient increase until 210 mins of test. The erosion rate increased drastically to 0.010 mg/min after 210 mins until the end of the CE test. The mean depth of erosion (MDE) of all tested specimens was calculated using Equation 12, and the results are listed in Table 6.6. The MDE of the un-coated Ti6Al4V substrate is significantly larger (15 to 20 times) than that of Hardide coatings.

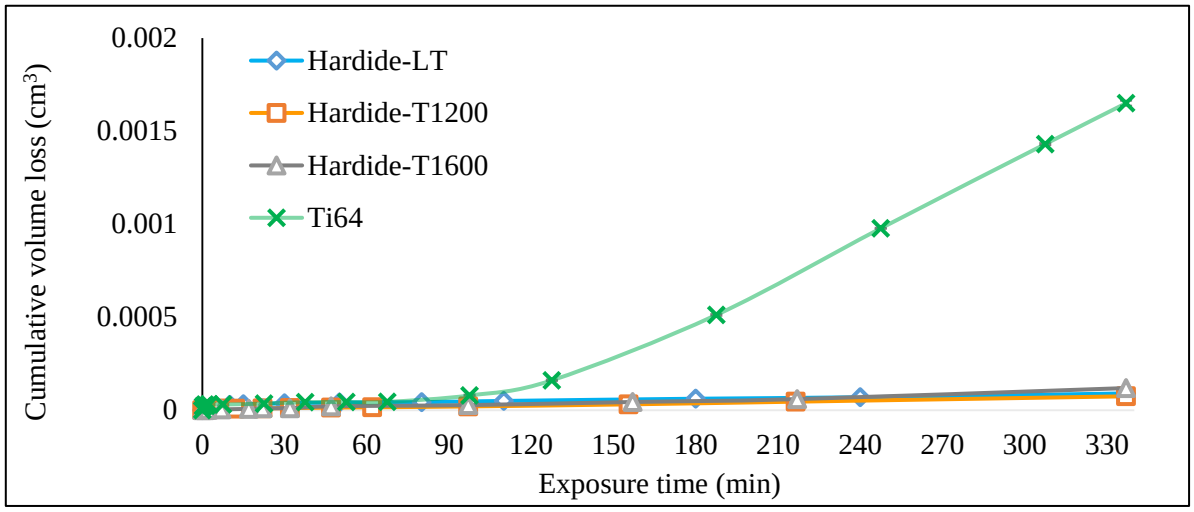

Fig. 6.8 CE results of Hardide coatings with reference to un-coated Ti6Al4V specimen.

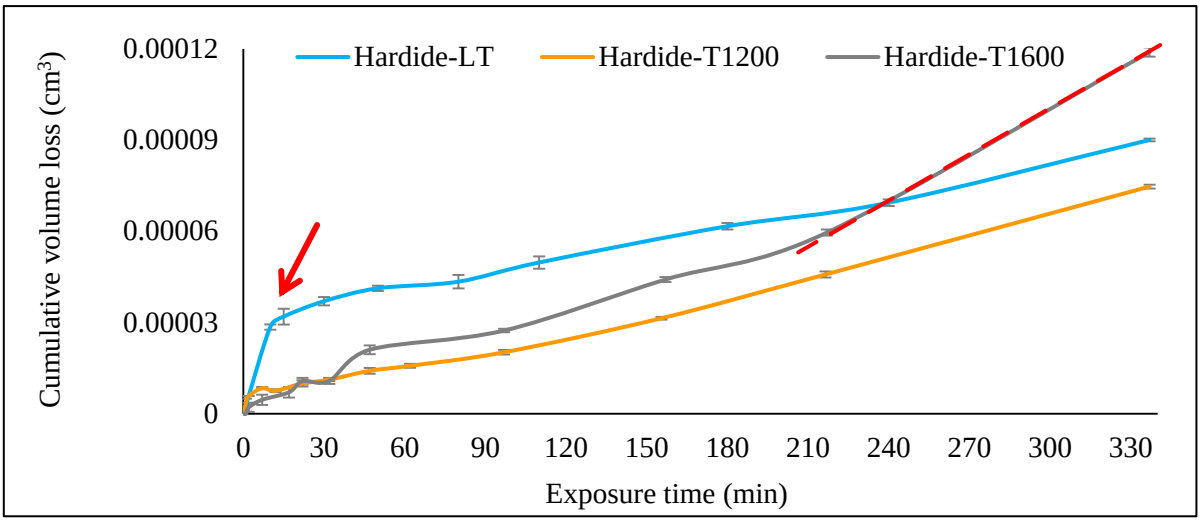

Fig. 6.9 CE results of Hardide coatings in Fig. 6.8 (continued from Fig. 6.8).

$$\text{MDE} = \frac{\text{Accumulated mass loss}}{\text{Density} \times \text{testing area}} \qquad \textbf{Equation 12}$$

Table 6.6 ER_{max} and MDE of Ti6Al4V and three Hardide coatings.

Coatings	Ti6Al4V	LT	T1200	T1600

ER_{max} (mg/min)	15.6	0.004	0.004	0.010
MDE 6.5 hrs (µm)	9.38	0.45	0.37	0.59

6.5.2 Erosion morphology

The surface profiles were obtained from the area-scan across the centre zone of the erosion scars using Alicona 3D profilometer, as shown Fig. 6.10. The exposed surface of uncoated Ti6Al4V substrate indicates more severe damage and an edge effect [144] induced by the sonotrode is observed, as shown in shown Fig. 6.10 (d). While all three Hardide coatings did not show such phenomenon.

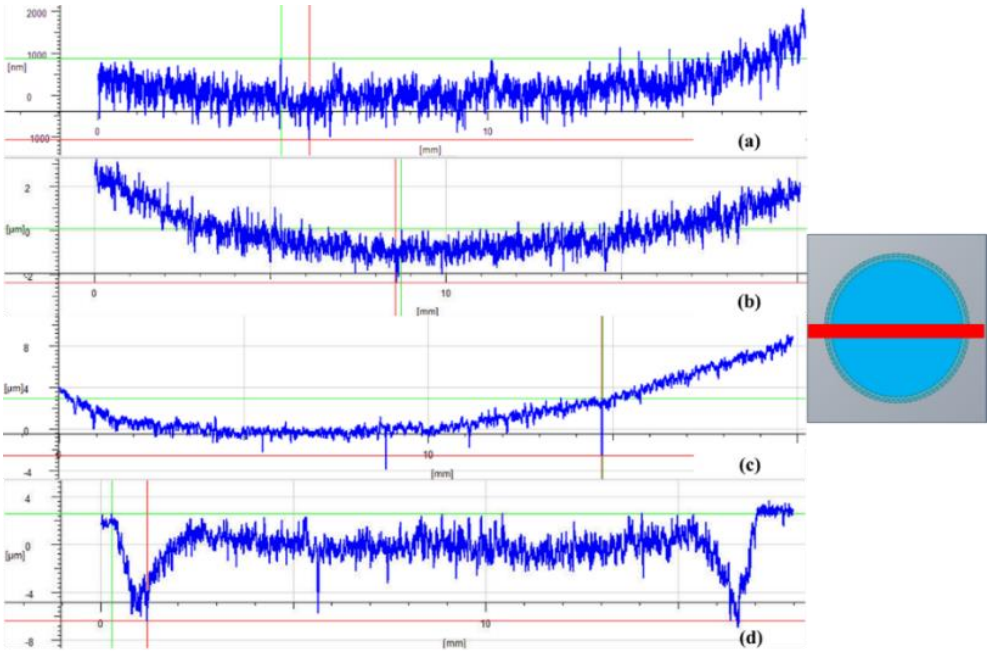

Fig. 6.10 Surface profile of post-test exposure surface: (a) LT; (b) T1200; (c) T1600; and (d) uncoated Ti6Al4V substrate.

Inspection of erosion morphology was conducted through SEM on various sites of the exposed surfaces to understand the material removal behaviour. The exposed surface of the LT coating after CE is shown in Fig. 6.11. Compared to the pre-tested coating surface shown in Fig. 6.3 (a) and (b), the exposed surface undergoes intergranular fracture, as shown in Fig. 6.11 (a) and (b). On closer inspection, cracks were found propagating inside the columnar grains, Fig. 6.11 (c). As the material removed from the coating surface, erosion craters were formed. Striation marks were observed on the wall of the craters, as shown in Fig. 6.11 (d). Moreover, formation of cleavage facets and steps was detected, as marked in Fig. 6.11 (e) and (f). Signs of plastic deformation was found adjacent to the features observed above. It can be seen that the exposure surface of the LT coating indicates a combined brittle and ductile fracture behaviour.

The exposed surface of the T1200 coating is shown in Fig. 6.12. With comparison to the pre-test coating surface in Fig. 6.3 (c) and (d), the dark zone of the coating surface undergoes brittle fracture after CE exposure. Fig. 6.12 (a) captures the fragments that are detached from the

fractured dark zone. Additionally, cracks were formed at the boundaries of the angular particulates in the shiny zone. These angular edges were polished into a smoother curvature in Fig. 6.12 (d). Formation of erosion craters followed by material removal is shown in Fig. 6.12 (e) and (f). Network of small cracks (few microns) were observed inside the erosion craters.

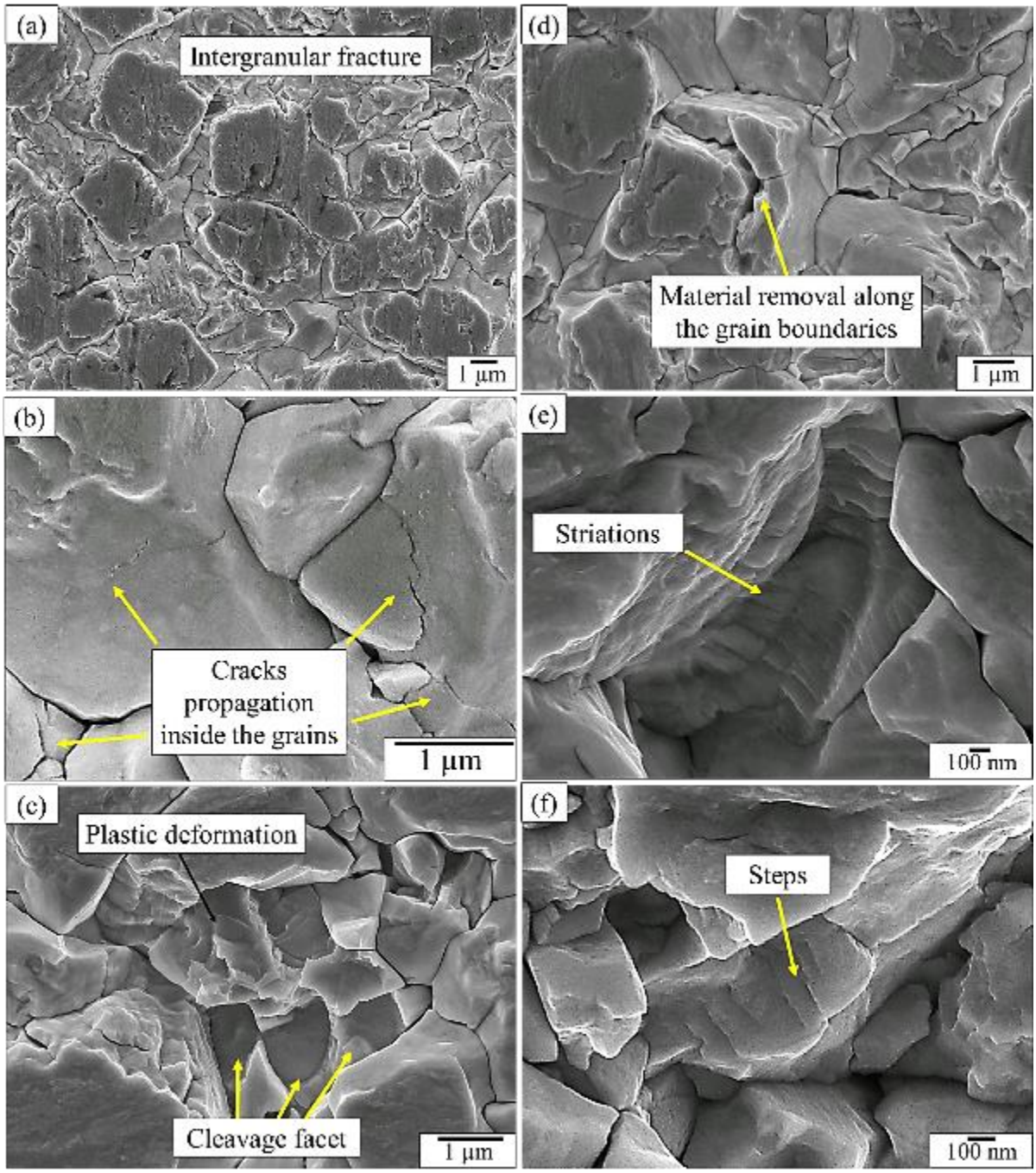

Fig. 6.11 Post-test exposure surface of LT coating.

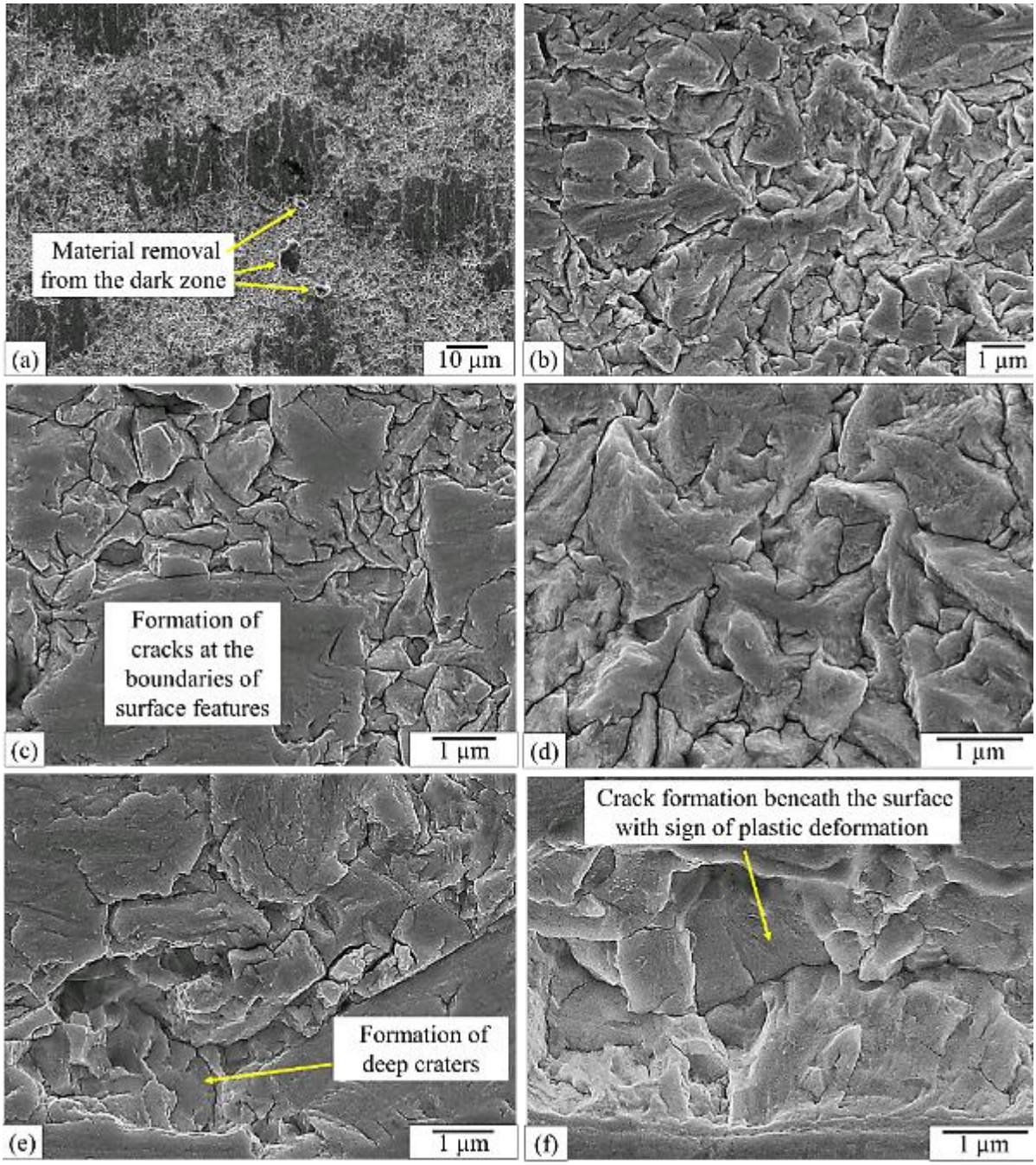

Fig. 6.12 Post-test exposure surface of T1200.

The post-test observation of the T1600 coating surface is shown in Fig. 6.13. Comparing to the original surface presented in Fig. 6.3 (e) and (f), the exposed surface reveals brittle failure evidenced by the dark zone being fragmented in Fig. 6.13 (b). Formation of chevron marks was observed in Fig. 6.13 (c). Fracture along the boundaries of the stem-like surface features in the shiny zone is shown Fig. 6.13 (e). Deep erosion craters were formed, Fig. 6.13 (d). Submicron cavities were found spreading over the exposed surface, as labelled in Fig. 6.13 (e). Additionally, subsurface deep cracks adjacent to arrays of slips lines are observed in Fig. 6.13 (f).

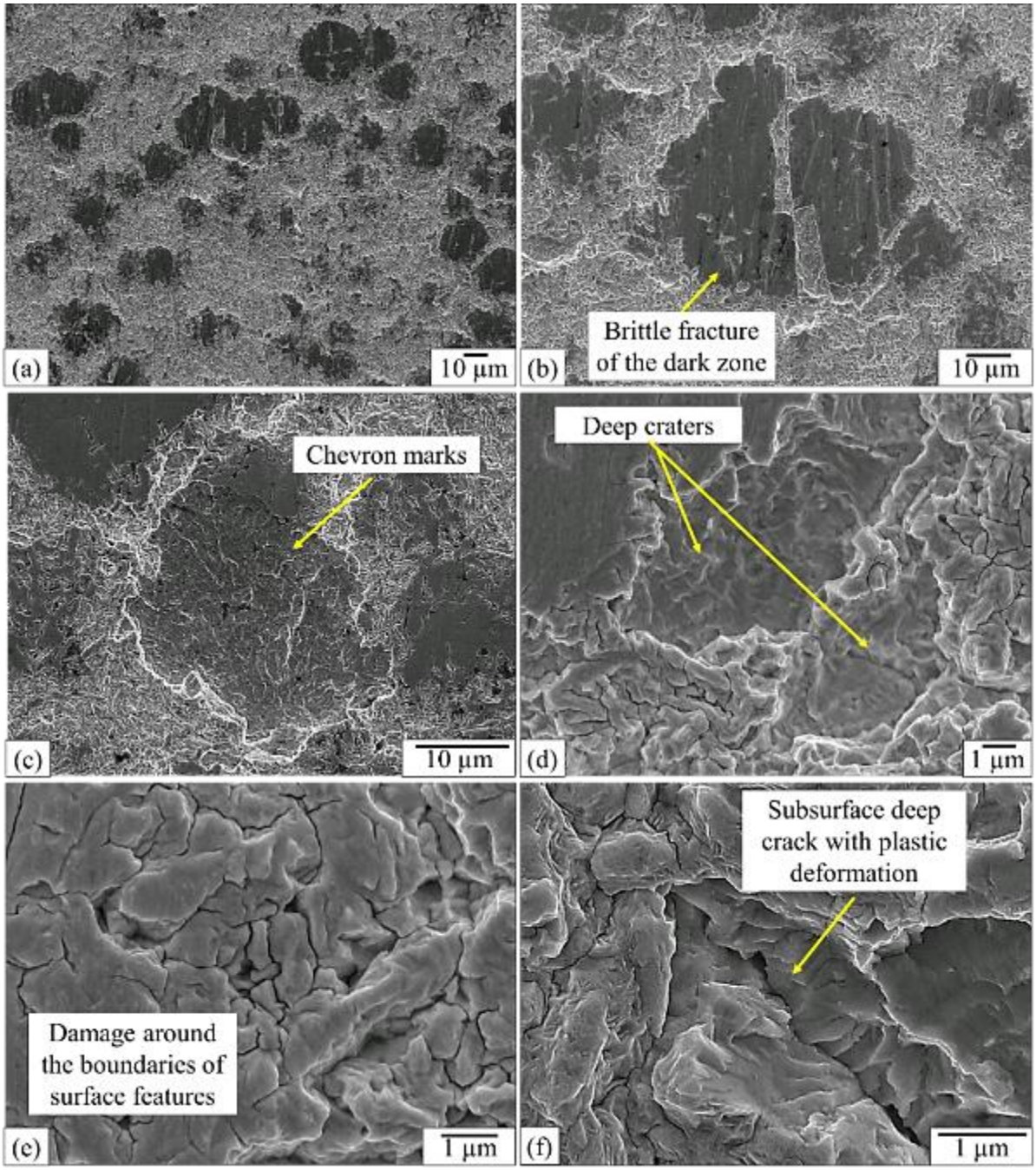

Fig. 6.13 Post-test exposure surface of T1600

6.5.3 Cross-sectional analysis

In order to further facilitate the understanding of the CE damage mechanisms, cross-sectional characterisation was conducted through SEM analysis, as shown in Fig. 6.14 to Fig. 6.16, respectively.

It can be seen that the LT and the T1200 coatings indicate less damage compared to the T1600 coating. Networks of microcracks were formed at the coating surface on both coating cross-sections. For the LT coating, the cracks were found propagating along the boundaries of

columnar grains (as shown in Fig. 6.14). As the cracks reach a depth up to approximately 10 µm, laterals cracks were then initiated, propagated and coalesced, which leads to the removal of coating material, as shown in Fig. 6.14 (e). While for the T1200 coating, the cracks were observed at relative random locations (shown in Fig. 6.15) and they did not penetrate deeply (less than 5 µm) into the coating. Formation of micropits was detected in Fig. 6.15 (e). However, such damage was limited within few microns away from the coating surface.

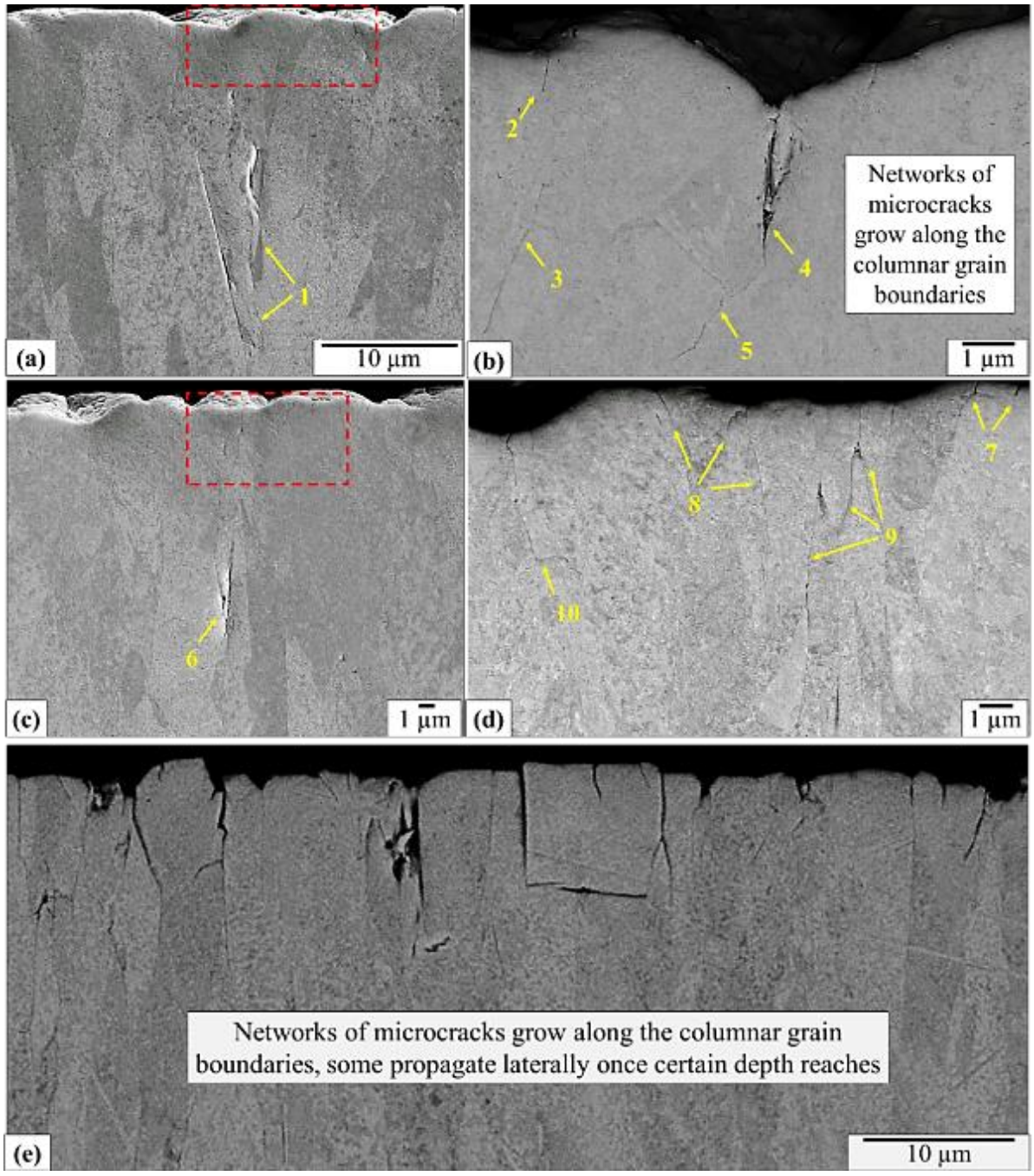

Fig. 6.14 Cross-sectional analysis of post-tested LT coating.

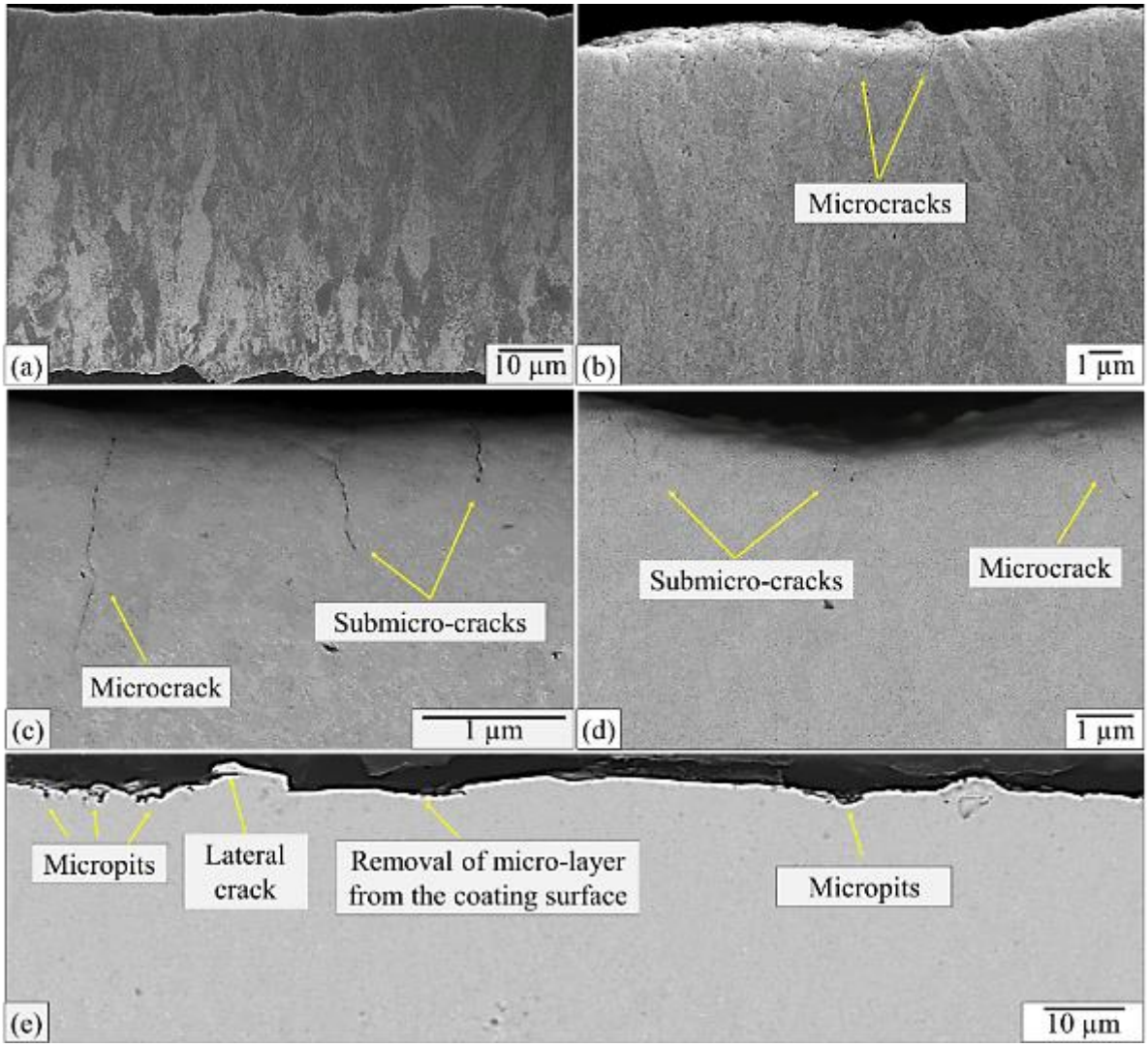

Fig. 6.15 Cross-sectional analysis of post-tested T1200 coating.

In the case of the T1600 coating (as shown in Fig. 6.16), the cross-section indicates a complex stress field generated during the exposure to CE. Small cracks (< 5 µm) were observed at the coating surface, as labelled in Fig. 6.16 (a), (b) and (c). Subsurface lateral cracks range from 10 to 15 µm in length were found 10 µm away from the coating surface, shown in Fig. 6.16 (a) and (b). Thus, these lateral cracks were formed within the top fine layer of the T1600 coating. Formation of a large erosion crater with 30 µm in width and 15 µm in depth was identified due to the detachment of the coating material from the top layer, shown in Fig. 6.16 (c). It can be suggested that the removal of coating surface material contributed to the drastically increased erosion rate after 210 mins of CE test, shown in Fig. 6.9. Additional cracks were detected developing on the side and bottom walls of the erosion crater. Further extended erosion crater with more than 100 µm in width was observed in Fig. 6.16 (d). Additionally, subsurface large vertical cracks (> 20 µm) were found in Fig. 6.16 (a), (b) and (d). It can be seen that one end of these cracks locates around 10 to 20 µm beneath the coating surface; while the other end stops at the interface of the fine and coarse layer of the T1600 coating.

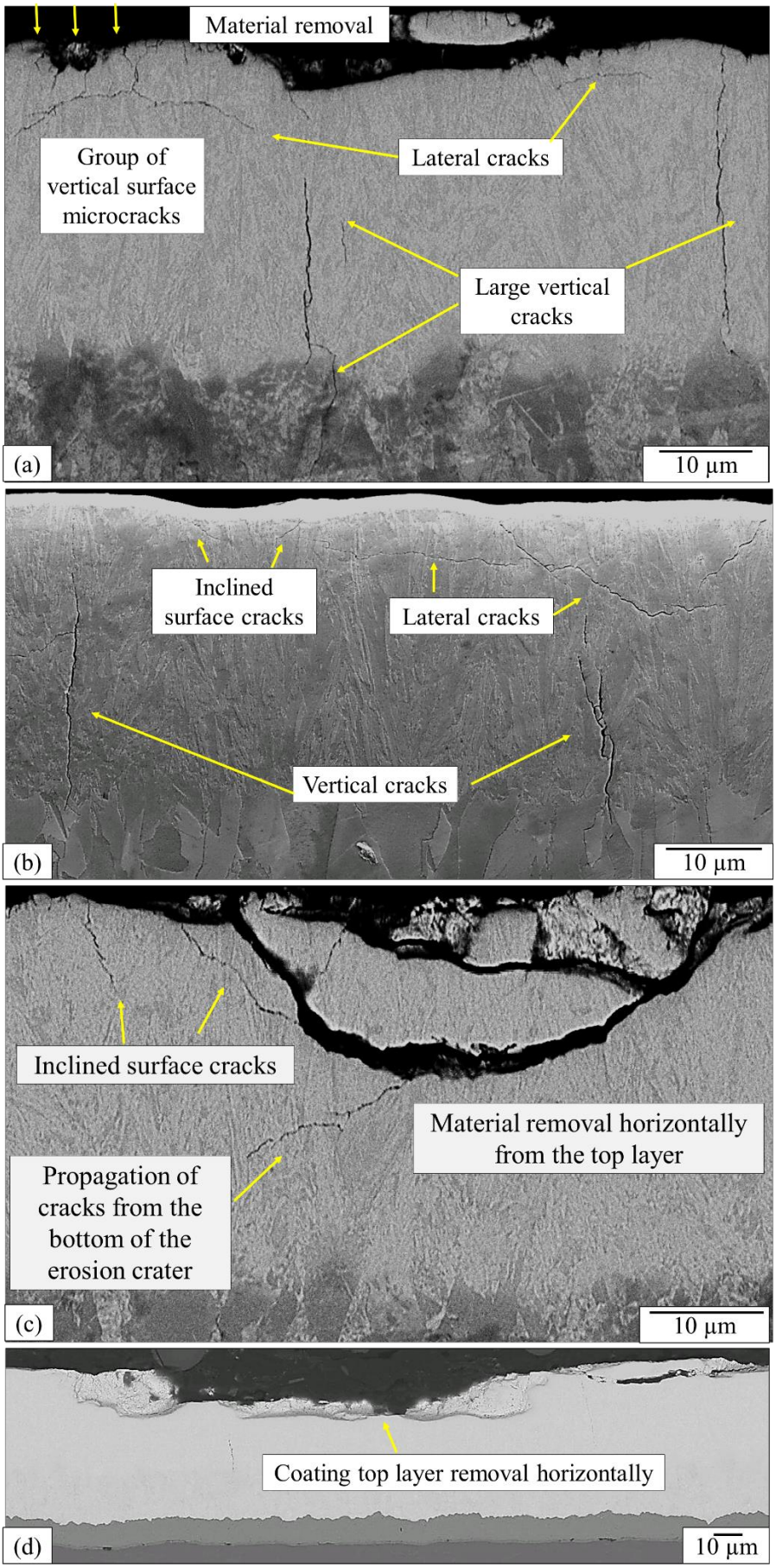

Fig. 6.16 Cross-sectional analysis of post-tested T1600 coating.

6.6 Discussions

A complex stress field is generated during the CE process: compression is induced by implosion of cavitation bubbles on the impact surface; high shear stress is developed within the solid and below the impacted region, thus, shear failure can occur beneath the surface. Furthermore, brittle failure can start at the surface due to the surface tensile stress that is present outside the impacted region [163]. The Hardide CVD W/WC coatings show superior CE resistance with respect to the substrate Ti6Al4V alloy. Such improvement can be attributed to the tailored microstructure and mechanical properties of the Hardide coatings. The following discussion is established on the effects of the three factors: coating topography, microstructure and mechanical properties on the CE behaviour.

6.6.1 Effect of initial coating topography on CE performance

The fracture surfaces of the Hardide coatings show the formation of the striation marks adjacent to a plastic deformation zone with cracks, as shown in Fig. 6.11 (e), Fig. 6.12 (e) and Fig. 6.13 (f). The properties of such eroded surfaces are similar to the characteristics of fatigue fracture [97,98,164]. This indicates a potential correlation of CE to a fatigue-like process, which has been extensively studied in the past [97,98,164–169]. During any fatigue failure, microcracks first formed at stress risers (voids, notches, defects, etc.) or at heterogeneous areas of the material, such as at the interface of difference phases, microstructures and grain boundaries [97,98,164–169]. Therefore, a target surface with potential stress risers, such as topographical features observed on the surface of Hardide coatings, is prone to cavitation wear. It is reported that poor initial surface finish due to the pre-existed defects on thermal sprayed coating surface leads to undesirable CE performance [131,166].

The topographical characterisation (Sa and Sq) of the Hardide coating surfaces (Fig. 6.1) indicate the LT coating exhibits the smoothest surface finish (as listed in Table 6.3). However, the LT coating shows an abrupt increase in the erosion rate after 10 minutes of CE exposure, while the T1200 and T1600 coatings with a worse surface finish outperform the LT coating at the initial stage of CE. Hence, it is suggested that the Sa and Sq cannot effectively characterise the effect of the initial surface topography on CE performance, as these parameters cannot specify the features of the surface profile [170]. On the other hand, surface parameters Ssk (skewness) and Sku (kurtosis) are proposed to better characterise the features of the surface topography, which might affect the CE rate [171]. The Ssk and Sku values shown in Table 6.3 indicate a potential correlation to the coating performance during the early exposure to cavitation. Comparing to the T1200 and T1600 coatings, the LT coating demonstrates a distinct surface feature of deep valleys with a negative sign of Ssk (- 0.80 ± 0.24) and Sku value over 3 (4.05 ± 0.41 μm). It is found on the cross-section of LT coating that cracks usually initiate when the roughness valley meets with the grain boundary of the columnar structure. The deep valley feature can serve as stress riser for implosion of the bubbles and cause shearing. The localisation of plastic strain then leads to high stress concentrations that initiate cracks at the surface, as shown in Fig. 6.17 (a). The cracks will soon be enlarged with water filled inside, preventing its closure, as shown in Fig. 6.17 (b). Once a crack is initiated, the repetitive stress

mode of CE causes it to propagate laterally in a fatigue-like manner, giving rise to the striations. The process is shown schematically in Fig. 6.17 (c) and (d).

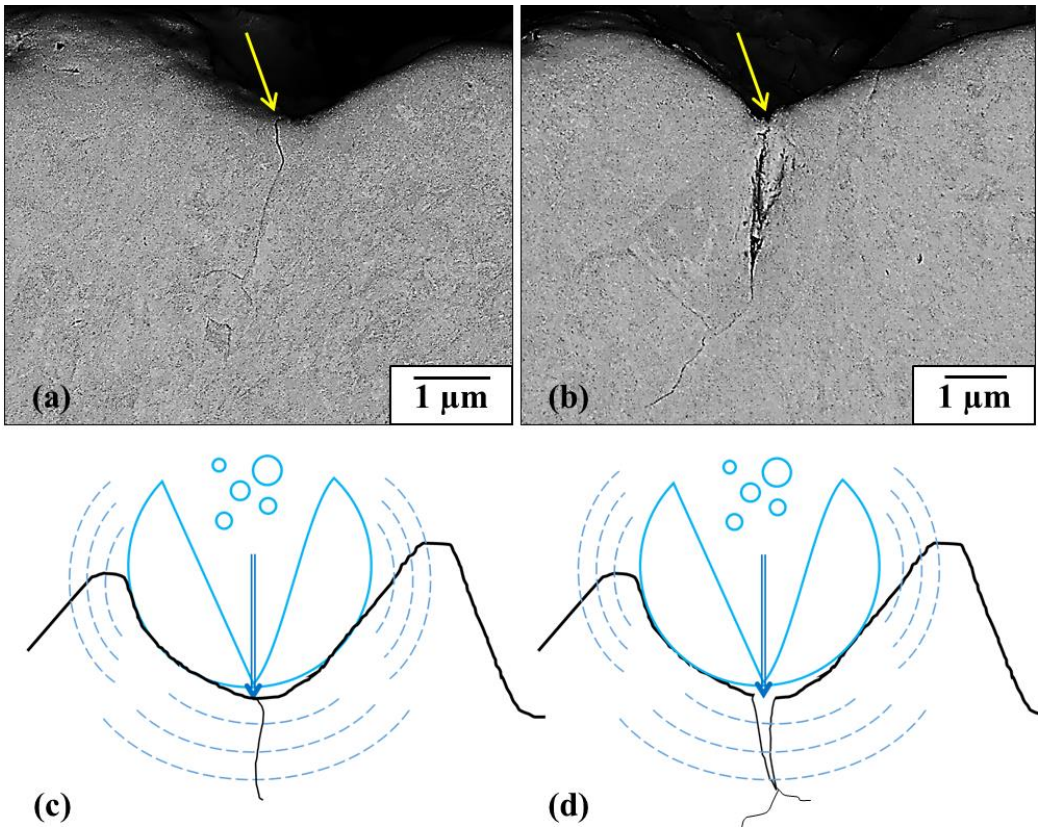

Fig. 6.17 The effect of initial surface topography of the LT coating on CE performance during early stage.

The proposed mechanism can be supported by the post-test cross-sectional views of the LT coating in Fig. 6.14 (b), (d) and (e). As the LT coating has a columnar grain structure, shown in Fig. 6.4 (a), the cracks tend to be initiated within valleys formed among the columnar grains with various heights. Once the vertical cracks propagates along the grain boundaries to a certain depth, lateral cracks are formed and propagate horizontally. Additionally, the fracture surface of the LT coating shown in Fig. 6.11 (b) and (d) suggests the same mechanism. Brittle fracture was found along the grain boundaries and propagating inwards to the grains. Hence, we can conclude that the valley features of the LT coating give rise to the propagation of cracks longitudinally and laterally, which eventually facilitate the material ejection. The same conclusion is reached in the literature [166].

Although the effect of coating surface topography on the CE performance is identified, the phenomenon is only observed at the initial stage of CE process. The LT coating shows similar erosion rate as the T1200 coating after initial 10 mins of cavitation exposure. Hence, the topographical effect is not the sole parameter contributing to the coating CE performance. The effect of which is limited during early stage of CE, which is agreed by the past study [172].

6.6.2 Effect of coating mechanical properties on CE performance

Correlation between the mechanical properties and CE behaviour is extensively studied in the past [167,173–175]. Hardness [173], fatigue strength [167,174] and toughness [175] are proposed to have close correlation to the CE resistance, but there is no consensus on one individual property. In a vibratory cavitation system, the stress which is responsible for erosion is primarily due to the concerted collapse of the aggregated bubbles generated by the pressure changes in the liquid, and this stress pulse has the characteristics of a shock wave [98,165,166,176,177]. The deformation and erosion of metals by cavitation are related to the magnitude of the shock wave emitted by the bubble cloud and the high-velocity impingements of microjets on the surface of the metal [178]. Hence, the CE resistance of a material in general is connected with its ability to absorb energy [15]. The total energy of cavitation clouds is transferred to the solid material and must be either absorbed or dissipated by the solid or reflected as shock waves in the liquid.

Solid material absorbs the impact energy through elastic deformation, plastic deformation or fracture. Hence, the elasticity and toughness of the coatings are considered as important factors for combating the erosive wear induced by cavitation. Toughness measurement with a nanoindenter [179] cannot be applied in the current study as the coating surfaces does not crack but deform in a ductile fashion during indentation. It is reported that the hardness H of these hard, tough and well resilient coatings ranges between 15 to 25 GPa [180]. The cross-sectional hardness of the best performed T1200 coating falls in such range. For the other two Hardide coatings (LT and T1600), the hardness ranges between 15 to 25 GPa at the top 30 µm of the coating surfaces. This suggests the top layers of the two coatings demonstrate higher toughness than the bottom layers.

The elasticity and toughness can be correlated to the measured hardness (H) and effective elastic modulus (E) [181]. The H over E ratio (H/E), a description of ‘elastic strain to failure’ has shown some merit in the past studies [181–183]. The H^3/E^2 ratio is proportional to the load that defines the transition between elastic to plastic contact in a ball-on-plane system, which can be a strong indicator of a material's toughness [181]. The H/E and the H^3/E^2 ratios across the coating thickness are plotted in Fig. 6.18 and Fig. 6.19 based on the measured H and E values by nanoindentation tests. The variation in the H/E and H^3/E^2 ratios are found to correlate well to the CE performance of the Hardide coatings. Coatings with higher H/E and H^3/E^2 ratios perform better under CE. Hence, the T1200 coating exhibits the best CE resistance, while the T1600 coating shows the worst among the three. Such correlation is supported by the literature findings on the CE of various coating systems [129,184–187]. The incubation period and the erosion rate are found to correlate well with the H/E ratio in the study on CE of HVOF ceramic coatings [129]. The H^3/E^2 ratio correlates well to the toughness that promotes the CE behaviour of the plasms-sprayed YSZ coatings [185].

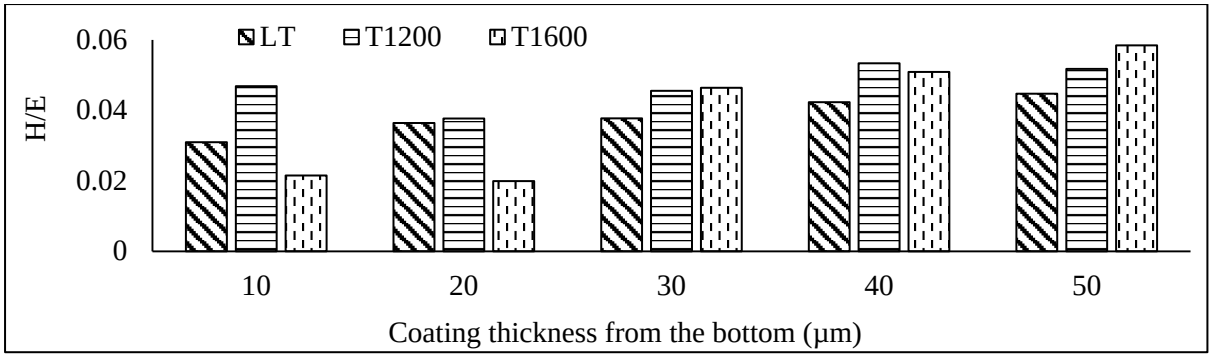

Fig. 6.18 H /E ratios through all coating thickness.

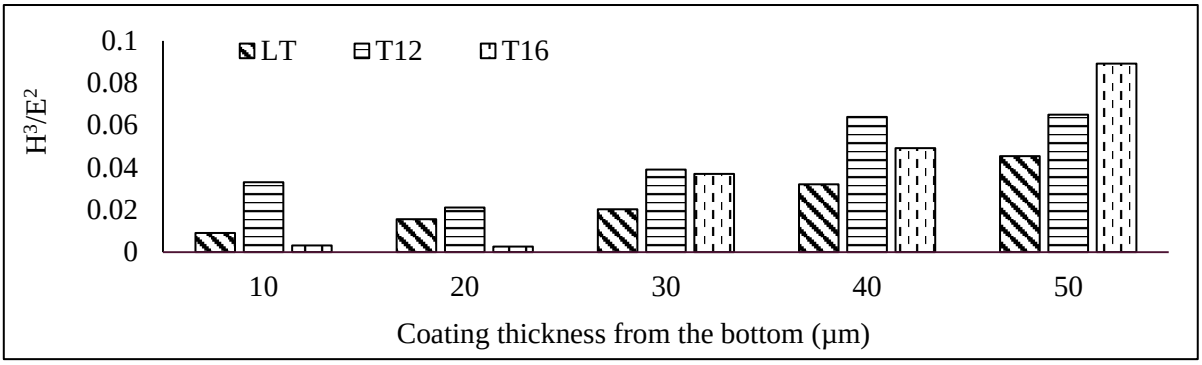

Fig. 6.19 H^3/E^2 ratios through all coating thickness.

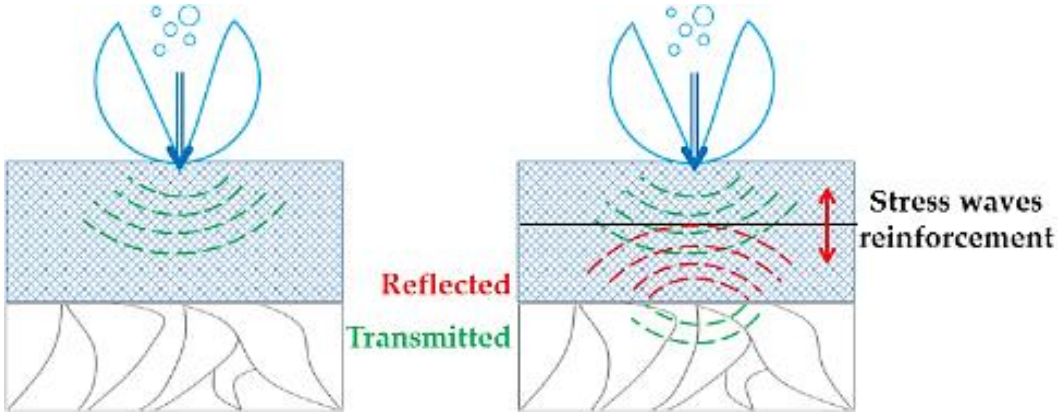

Fig. 6.20 Schematic of stress wave reinforcements in the T1600 coating.

It is proposed that the poor CE performance of the T1600 coating attributed to the bottom columnar grain zone (10 and 20 μm), where the H/E and H^3/E^2 ratios show significantly smaller values. The unique configuration of the Hardide-T (T1200 and T1600) coating structures are designed to demonstrate the following potential benefits: the fine top layers are aimed to improve the resistance to the high impact pressure induced by bubble implosion; while the coarse columnar grains at the bottom layers are to support the top layer with better ductility to dissipate the impact energy as well as the transmitted stress waves. However, in the case of the T1600 coating, the bottom layer of columnar grains indicates significantly reduced elasticity and toughness. Thus, the transmitted stress waves cannot be absorbed nor dissipated effectively when reaching such a zone of the coating, but reflected, as illustrated in Fig. 6.20. The reflected stress waves meet the newly generated ones under the repeated motions of bubble implosion, leading to stress wave reinforcements. This results in the formation of the tensile stress close

to the coating surface. The phenomenon will be further discussed in the following section as the microstructural interface can enhance the effect mentioned above.

6.6.3 Microstructural effect on CE mechanism

The main advantage of applying hard and tough coatings is their enhanced resistance to crack growth. However, a high hardness is unlikely to be beneficial for coating fracture toughness. Therefore, the microstructural characteristics of the coating material is important as it is likely to affect the crack propagation mechanisms in the coating [36]. The following section will address the discussion on the potential interaction between the coating microstructures and the high-strain-rate impact loading induced by the CE process.

A critical aspect of the cavitation wear process is surface destruction and material displacement caused by implosion of cavitation bubbles. During the CE process, small local plastic strains initiate the formation of cracks similar to fatigue cracks. The repeated action of bubble collapse then causes crack propagation, which leads to the removal of material particles. The path of the crack propagation can be affected by different microstructures of the exposed surface.

The post-test SEM analysis shown in Fig. 6.11 to Fig. 6.13 indicates an intergranular brittle facture behaviour on all coating surfaces. However, the cross-sectional investigation reveals different damage mechanisms for each coating system due to the variation in the microstructure. The effect of which will be discussed in two main aspects: microstructural configurations and crystallographic orientations of the coatings.

6.6.3.1 Microstructural configuration of the coatings

There are two main microstructural configurations of Hardide coatings: the LT coating demonstrates a monotonic columnar grain structure; while the Hardide-T coatings (T1200 and T1600) show hierarchical microstructures with a layer of coarse columnar grains at the bottom, and a layer of submicron grains at the top. The difference between the T1200 and T1600 coatings configuration is mainly at the transition stage from the coarse to fine layer. In the T1200 coating, the fine grains nucleate at the bottom coarse columnar grains, forming a gradient change of microstructure through the coating thickness. While in the case of T1600 coating, the top fine grains are grown independently from the coarse columnar grain structure at the bottom, hence, a distinct interface between the two layers is formed. Furthermore, the results of the EBSD analysis shown in Fig. 6.4 reveals the grain size of the three coating surfaces. Compared to the LT coating, both T1200 and T1600 coatings are constructed with a submicron top layer.

The post-test SEM observation on of all coating surfaces (Fig. 6.11 to Fig. 6.13) indicate a mixture of brittle and ductile fracture behaviour. Intergranular brittle fracture was found on all the coating surfaces irrespective of the variation in the grain size of the exposed surface. This

is in agreement with the literature that CE at the initial stages involves delineation of the grain boundaries regardless of the grain sizes [188]. One of the factors determines the amount of the brittle or ductile fracture that occurs in a material is the dislocation density. Increase in dislocation density can be introduced by CE process [176]. When the dislocations reach the grain boundaries, they pile into each other, the intergranular fracture takes place. Literature [148,189] suggests that the grain refinement contributes to better CE resistance as the smaller grains restrain dislocation movements with increased surface grain boundary density. This is partially agreed with the results obtained in this study. The enhancement in CE performance is only observed in the T1200 coating. The fine grains of the top coating layer provides more grain boundaries to better resist to plastic deformation due to highly localised strain induced by cavitation bubbles. On the other hand, the T1600 coating surface also composed of fine grains shows inferior CE performance. The coating surface was removed due to the formation and nucleation of lateral cracks after CE exposure. This can be due to the significant change in mechanical properties at two layers of the coating microstructure discussed in section 6.6.2.

One other factor that should be considered is the effect of the microstructural characteristics on the crack propagation mechanisms. It is reported that the cracks formed under CE usually develop perpendicular to the surface and in parallel direction when a certain depth is obtained [165]. This agrees with the cross-sectional views of the LT coating shown in Fig. 6.14. The cracks were found initiating and propagating along the columnar grain boundaries. Lateral cracks were then developed at a depth around 7 to 8 μm. While for Hardide-T coatings (T1200 and T1600), the bush-like and the stem-like fine grains at the top layers play a role in the crack propagation during CE process. The cracks tend to grow horizontally at the coating surface, as the grain boundaries of the fine grains act as obstacles. The cracks deflect and nucleate laterally, instead of growing vertically in depth. Such mechanism can potentially reduce the mass loss rate, leading to less severe damage of the coating.

6.6.3.2 Crystalline texture of the coatings.

The EBSD analysis, shown in Fig. 6.4 (a) and (b), reveals that the T1200 and LT coatings demonstrate a distinct crystal texture at <001> orientation. The LT coating presents a higher texture intensity with monotonic columnar grain structure. The results of the CE test indicate that these two coatings perform better than the T1600 coating, in which no crystalline texture was observed. Studies on the CE of titanium alloy [165] and stainless steel show that grains with certain orientations resist to cavitation condition better than others. It is argued that although the magnitude of most of the pressure pulses induced by CE is insufficient to indent the rigid surface, the magnitude is sufficient to induce shearing in favourably oriented grains. Hence, it is proposed that the CVD W/WC coatings with <001> crystalline texture are likely to better resist to CE. The conjecture can be supported by the study on the wear performance of the textured CVD α-Al_2O_3 coatings. It reveals that the coating with <001> texture demonstrates improved wear resistance [190].

Furthermore, although all coating fracture surfaces demonstrate brittle intergranular failure, once the material is removed, signs of plastic deformation were detected. It is revealed in the study that CVD-W coatings with <001> texture show a strong strain rate sensitivity [191,192]. These coatings show large ductility at all strain rates and significant strain softening during high strain rate deformation, as shown in Fig. 6.21. On the other hand, the coatings deposited with random orientation exhibit brittle failure. Hence, it can be suggested that the superior CE performance of <001> textured specimens (LT and T1200) can be attributed to the enhanced ductility compared to the random oriented grains (T1600). As the shock wave induce plastic deformation during the CE process [98,165,166,176,177], specimens with better ductility can delay the formation of microcracks. The fact that the T1200 coating demonstrates better performance than the LT coating is due to a combined effect of the functionally graded microstructure and mechanical properties that have been discussed in the previous sections.

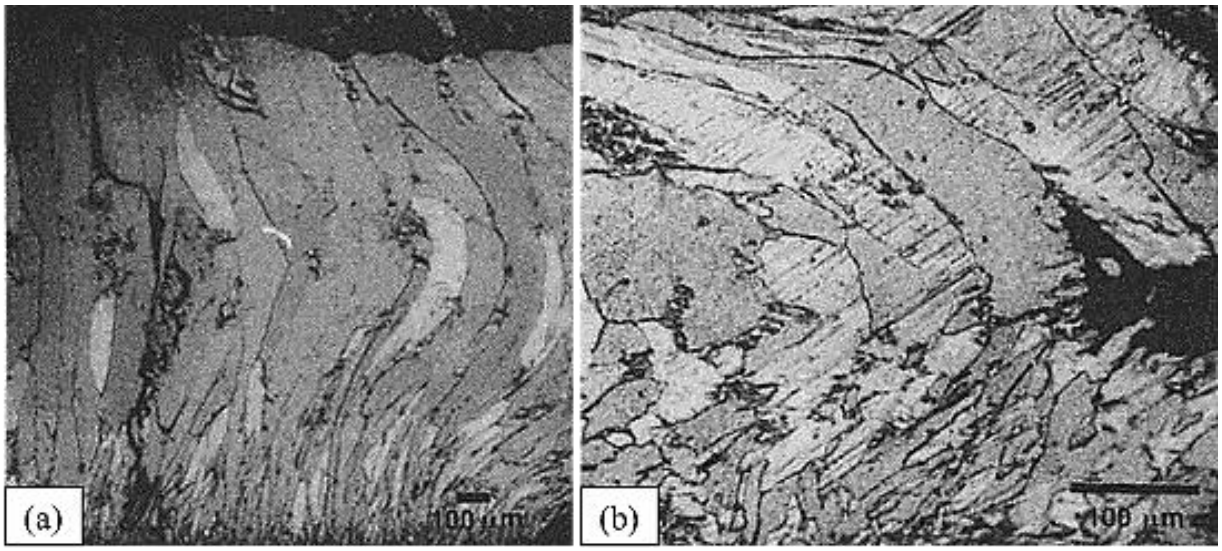

Fig. 6.21 The cross section of <001 > specimens deformed: (a) to a strain of 0.8 under quasistatic loading at a strain rate of 0.0003 s^{-1} ; (b) a strain of 0.87 at a strain rate of 9500 s^{-1} [191].

6.7 Conclusions

Investigation on the CE performance of three CVD W/WC coatings deposited on Ti6Al4V substrate is conducted in this chapter. Correlation between the coating performance and the coating topography, mechanical properties and microstructure is discussed. The following conclusions are drawn:

- All three CVD-W coatings show improvement in the CE resistance with respect to Ti6Al4V substrate, which can be attributed to a combined factors of mechanical properties and microstructures.

- Among the three CVD-W coatings, T1200 and LT coatings demonstrate better resistance to cavitation. T1600 undergoes premature spallation of the coating surface during the CE test.

- The effect of the initial coating topography on the CE performance is more effectively characterised by the surface parameters Ssk and Sku.

- The H/E and H^3/E^2 ratios correlate well with the CE performance of the coatings, which suggest a hard yet tough coating is targeted for the CE application.

- Correlation between the superior CE performance of the T1200 and LT coatings and the crystal orientation is identified. Both coatings are textured with <001> orientation, which show better resistance to CE.

- The hierarchical microstructure of T1200 coating demonstrate enhancement in CE performance compared to the LT coating with the monotonic columnar grain structure.

- The T1600 coating with a distinct interface between the coarse and fine layer failed under the premature spallation of the coating surface. The damage mechanism is proposed to be correlated to the overlapping of the stress waves.

Chapter 7.

CE performance of CrAlYN/CrN nanoscale multilayer coatings deposited by HIPIMS

Employment of various hard coatings for WDE resistance has been tried in the past studies, however, their failure caused by brittle fracture and delamination due to poor adhesion have been reported. Improvement of toughness while maintaining the hardness is the challenge for such application. Deposition of nanoscale multilayer microstructure is one of the most advantageous approaches to improve toughness of thin films and is achieved via the following three main mechanisms: crack deflection at interfaces between layers, ductile interlayer ligament bridging and crack tip blunting due to nanoplasticity at the interface [193]. Furthermore, it was shown that in superlattice structured coatings a significant fracture toughness enhancement can be achieved (e.g. by factor of two for the TiN/CrN system) in a way similar to the superhardening effect reported for these structures [194]. With the introduction of the novel High Power Impulse Magnetron Sputtering (HIPIMS) technique, very dense and defect free nanoscale multilayer coatings with high adhesion can be deposited. The unique properties of the layered structures deposited by HIPIMS technique, such as crack deflection at the sharp and flat interfaces and their role as sites for elastic energy dissipation, also add to the established mechanisms responsible for the enhancement of the mechanical properties. HIPIMS utilises transient impulse (short pulses) glow discharge with a very high power and current density which translates to high plasma densities and ionised metal particles [195]. The utilisation of highly ionised metal fluxes during the surface pre-treatment and coating deposition stages allow fine-tuning of the metallurgical reactions at the coating substrate interface as well as precise control over the coating structure, crystallographic orientation, and surface morphology.

This chapter will investigate the potential usage of HIPIMS deposited nanoscale multilayer CrAlYN/CrN coatings to protect Ti6Al4V substrate against WDE with CE screening test. The results will be compared with monolayer TiN coating, which is one of the most established and popular coatings due to its high hardness and wear resistance [196].

7.1 Coating deposition

Nanoscale multilayer CrAlYN/CrN coatings were deposited in an industrial size HTC 1000-4, coating system, (Hauzer Techno Coatings, Europe B.V., Venlo, The Netherlands) equipped with four unbalanced magnetron sources, which can be operated in HIPIMS mode. The HIPIMS plasma was generated using dedicated High-pulse 4008 power supplies (Hüttinger Elektronik Sp. z o.o., Warsaw, Poland). Prior to coating deposition, adhesion enhancing pre-treatment of substrates was carried out with the help of HIPIMS plasma sustained on a Cr target [197]. Coating deposition was carried out using CrAlY, CrAl and Cr targets in a mixed reactive $Ar+N_2$ atmosphere at 400 °C. The coating architecture comprises of CrAlYN base layer followed by alternating nanoscale CrAlYN and CrN multilayers. In this chapter, 2 sets of

multilayer coatings were deposited by manipulating the ion energies available from the depositing flux; one with high and one with low ion bombarding energies and henceforth will be referred to as coating C1 and coating C2, respectively. The substrates were subjected to three-fold rotation to assist uniform distribution of depositing flux over the surface of substrates. The Ti6Al4V substrate was polished up to a Ra of 0.05 µm prior to coating deposition and the coated specimens maintained the same surface finish.

7.2 Coating mechanical properties

The adhesion strength of CrAlYN/CrN coatings was measured by Rockwell C indentation and scratch tests, as shown in Fig. 7.1. For both coatings deposited with low and high ion bombarding energies (C1 and C2 coating, respectively), optical microscopic observation shows no cracks, delamination or spallation of the coatings around the Rockwell indents. This confirms the superior adhesion between the coating and the substrate, which can be rated as grade Class 0 (ISO 26443) equivalent to HF1 (Daimler-Benz test). Likewise, no spallation of the coatings was evident under scratch tests even though the normal load progressively reached 80N leading to through thickness perforation (Fig. 7.1c). This excellent adhesion behaviour is mainly attributed to the well-defined crystal structure at the coating-substrate interface provided by the HIPIMS metal ion etching, which promotes the localized epitaxial growth of the coating. Both C1 and C2 coatings had a similar thickness of around 4 µm. The hardness of C1 coating was in the range of 3000 $HK_{0.25N}$ whereas the Young's modulus value (E) was calculated to be around 300 GPa. The C2 coating was found to have a hardness value in the range of 2700 $HK_{0.25N}$ as well as reduced Young's modulus (E) value of 275 GPa. Both coatings had a near similar compressive residual stress values in the range of – 4.0 ± 0.5 GPa. The commercially sourced TiN coatings had a hardness of 2200 $HK_{0.25N}$, and compressive residual stress value of -2.0 ± 0.5 GPa. The thickness of the TiN coating was 2.7 µm.

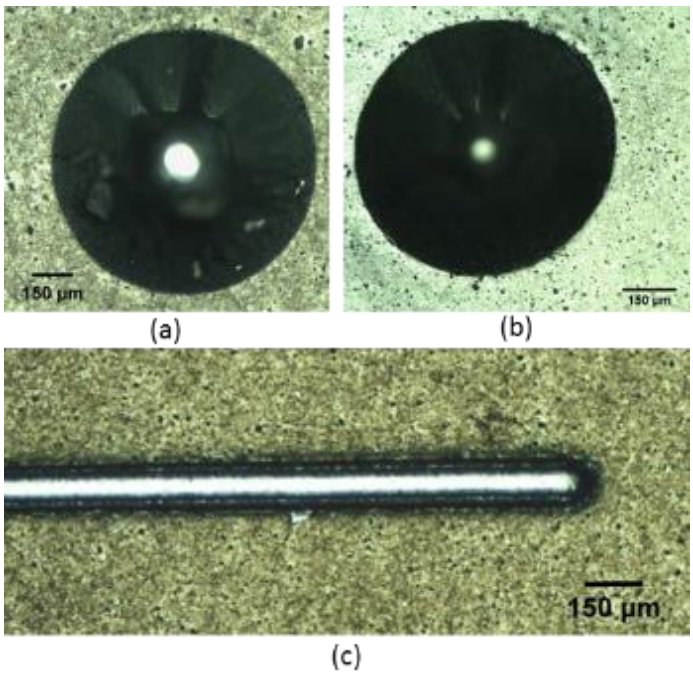

Fig. 7.1 Rockwell C adhesion tests: (a) C1 coating (b) C2 coating, (c) Scratch test C2 coating.

7.3 Coating microstructure

Fig. 7.2 (a) shows the low magnification TEM image of the whole CrAlYN/CrN coating (C2) obtained in a bright field imaging mode. As observed, the image shows a surface of the substrate which has been pre-treated (etched) with a metal ion enriched HIPIMS plasma followed by the deposition of a dense CrN base layer (around 250 nm thick). The interface between the substrate and the base layer is smooth, sharp and without any defects (neither droplets nor any voids in the interface region often observed in arc and Argon ion etching respectively). This is a typical feature of HIPIMS etching [198]. On top of the base layer, alternating layers of CrAlYN and CrN (bi-layer thickness of approximately 3 nm) have been deposited, Fig. 7.2 (b), to form the nanoscale multilayer coating. The implantation of metal ions during the etching step leads to the formation of a superior epitaxial coating microstructure that not only is limited to the adjacent base layer but also extends to the top of the coating, [198]. In this case, the epitaxy is evident in Fig. 7.2 (a), wherein the wide portions of coating columnar microstructure with a similar colour contrast can be seen extending right from the bottom of the base layer to the top of the coating as the coating synthesises uninterruptedly. The epitaxial microstructure along with smooth, defect free substrate-coating interface leads to superior adhesion bonding. The effect of the high metal ion irradiation during coating synthesis is also visible from the growth of dense and wide columns with flat tops in Fig. 7.2 (a), as well as the presence of flat and sharp interfaces within the nanoscale multilayers in Fig. 7.2 (b). This superior dense microstructure along with high adhesion imparts superior barrier and mechanical properties to the coating. The microstructure of the C1 coating also has similar multilayer architecture, but with anticipated minute changes in the bi-layer thickness, columnar width and texture of the coating due to the different intensity of the ion bombardment during the growth. The monolithic TiN coatings in general had smooth surfaces without any macro-particle defects. FIB cross-sectional studies confirmed the microstructure to be composed of dome shaped columnar grains, which are typical for sputtered coatings (see Fig. 7.9) but without the nanoscale multilayer stacking as observed in the C1 and C2 coatings.

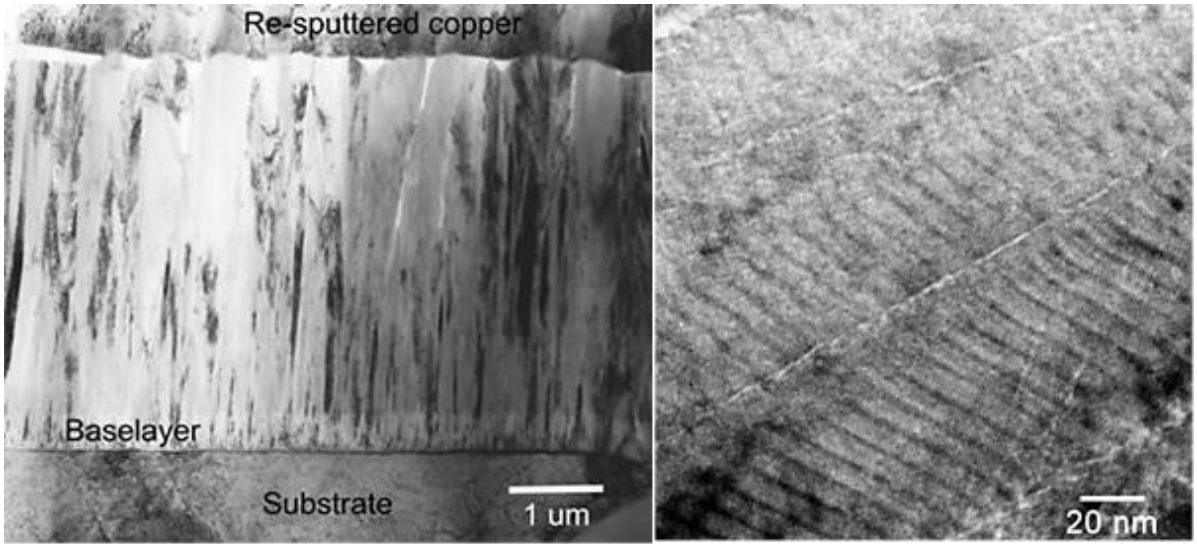

Fig. 7.2 (a) Bright field TEM image of the whole C2 coating; (b) High magnification bright field TEM image of the multilayer structure consisting of alternating CrAlYN (light contrast) and CrN (dark contrast) nanoscale layers.

7.4 Coating texture

The texture evolution in CrAlYN/CrN coatings was analysed using X - ray diffraction (θ-2θ, BB geometry) technique and the details of the technique is given in Chapter 3. Fig. 7.3 shows BB XRD patterns of the C1 and C2 coatings deposited with high and low ion bombarding energies. The CrAlYN/CrN coating deposited with low ion bombarding energy exhibited a strong {111} preferred orientation, as shown in Fig. 7.3 (a); in contrast to {200}, shown in Fig. 7.3 (b), for the coating deposited with high ion bombarding energy. It was reported in the literature that the texture in HIPIMS deposited TiN coatings transformed from {111} to {200} while increasing the ion bombardment energy [199]. The increased ion energy influenced the texture of the coatings by enhancing the ad-atom mobility and increasing the flux of atomic nitrogen created by a kinetically-induced dissociation of nitrogen molecules at the substrate surface. The {200} orientation was found to be dominant in the presence of atomic nitrogen and ionized metal flux due to the trapping of Ti on {200} sites through the formation of TiN clusters. It was also reported that {111} orientation was promoted under deposition conditions in which the incident particles are mainly metal atoms and N_2 molecules (non-ionised flux) and Ti is trapped predominantly on {111} sites [199]. Thus, even though, compositionally similar, C1 and C2 coatings show difference in texture owing to the difference in ion bombardment levels during the coating growth stage.

In turn, the crystalline texture plays a significant role in CE behaviour [142,148,165]. Grains with {111} orientations resist CE better. The effect of the texture of HIPIMS coating on the CE performance will be further discussed later. The commercially sourced monolithic TiN coating had a strong {111} texture, as can be seen in Fig. 7.3 (c).

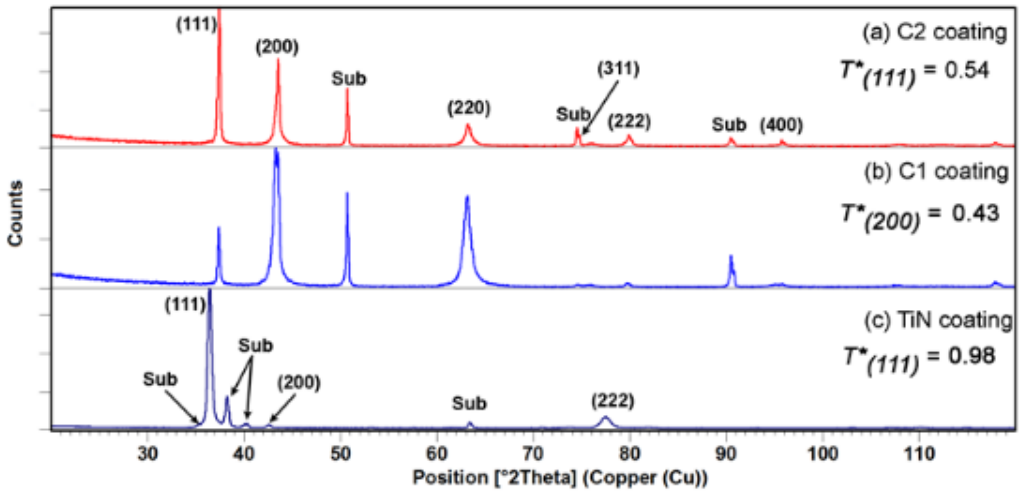

Fig. 7.3 XRD results used for texture analysis of different coatings in this study.

7.5 Cavitation erosion performance of HIPIMS coatings

Results of the CE tests show that both HIPIMS coated specimens outperform the bare Ti6Al4V substrate, Fig. 7.4. The C2 coating demonstrates a significant improvement of CE performance with reduced maximum erosion rate of 0.002 mg/min, comparing to 0.024 mg/min for the

substrate material. Furthermore, the incubation period is prolonged more than twice (>240 min) with comparison to that of the substrate Ti6Al4V (120 min), as listed in Table 7.1. In the case of C1 coating, the incubation period also indicates an improvement of 60 minutes (180 min); however, the erosion rate starts to increase after 150 mins of CE exposure and reaches up to the maximum value of 0.030 mg/min by the end of the test. Both HIPIMS coatings present excellent CE behaviour comparing to the multilayer coatings manufactured by traditional PVD process [124,125]. This can be attributed to the synergy between superhardness and a special crack propagation mechanism that enhances the toughness. Additionally, the thin HIPIMS coatings (about 4 microns) outperform thick coating systems reported in the literature, such as CVD [128] and High Velocity Oxy-Fuel (HVOF) [129,200]. It is revealed that the thick but porous HVOF coatings demonstrate almost no incubation period under CE. Surface and cross-sectional analysis was conducted to further understand the coating behaviour under CE.

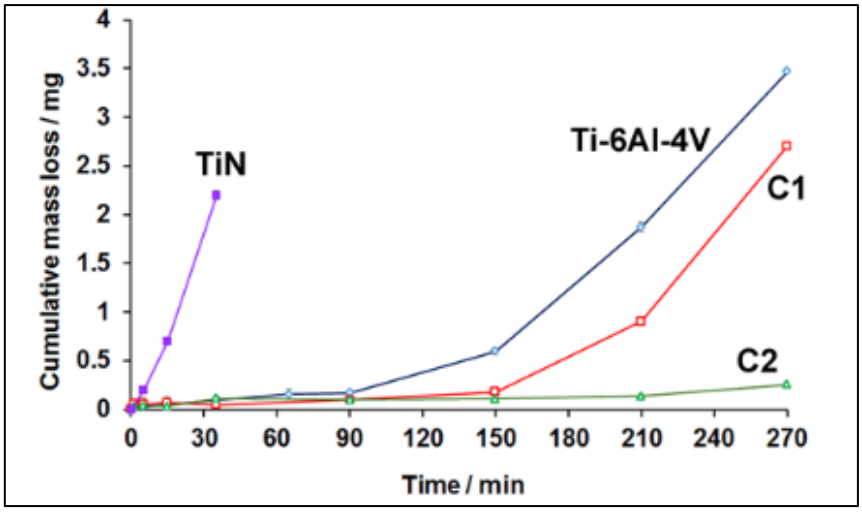

Fig. 7.4 CE results of HIPIMS coatings versus Ti6Al4V substrate and TiN coating.

Table 7.1 Comparison of CE performance of HIPIMS coatings with those reported in literatures.

Coatings	Incubation period (min)	Maximum erosion rate (mg/min)	Manufacturing process	Thickness (μm)	Test period (hour)
Ti6Al4V	120	0.027	/	/	4.5
C1	180	0.013	HIPIMS	4	
C2	240+	0.002			
CrN/CrCN [124]	30	0.020	PVD	4.3	10
Ti/TiN-4 [125]	60	0.004		3.7	
(NiTi/TiCN)0.5 [126]	60	0.004		3.32	12
Nanocrystalline diamond [128]	30	0.011	HF-CVD	1	2.5
M6-HV [128]	15.6	0.027	HVOF	134 ± 6	8
WC-CoCr [128]	61.8	0.041		107 ± 12	8
Cr_3C_2-NiCr [129]	0	0.050		30 - 40	8
CoMoCrSi [130]	0	0.125	Plasma spray	/	2
FeNiCrBSiNbW [131]	0	0.150	Arc spray	230	2

7.6 Cavitation mechanisms

7.6.1 Incubation period

The CE behaviour of both HIPIMS coatings during incubation period was investigated with FIB/SEM analysis. Fig. 7.5 (a) to (c) show areas of the C1 coating which were subjected to erosion tests for 90 mins (incubation period) and then subsequently chosen for FIB milling. As observed in Fig. 7.5 (a), the C1 coating surface was found to be intact without any evidence of intergranular cracking or cohesive fracture or similar coating removal mechanisms. Formation of pits due to localised removal of deposition chamber related nodular, open void and cone shape coating defects [201] can be seen. On closer inspection at the cross-sectional view, cracks were found at the substrate, as labelled in Fig. 7.5 (b), and propagating into both the substrate and the coating, Fig. 7.5 (c). In the case of C2 coating, shown in Fig. 7.5 (d) to (f), no cracks were found on the surface nor on the cross-sections during incubation period.

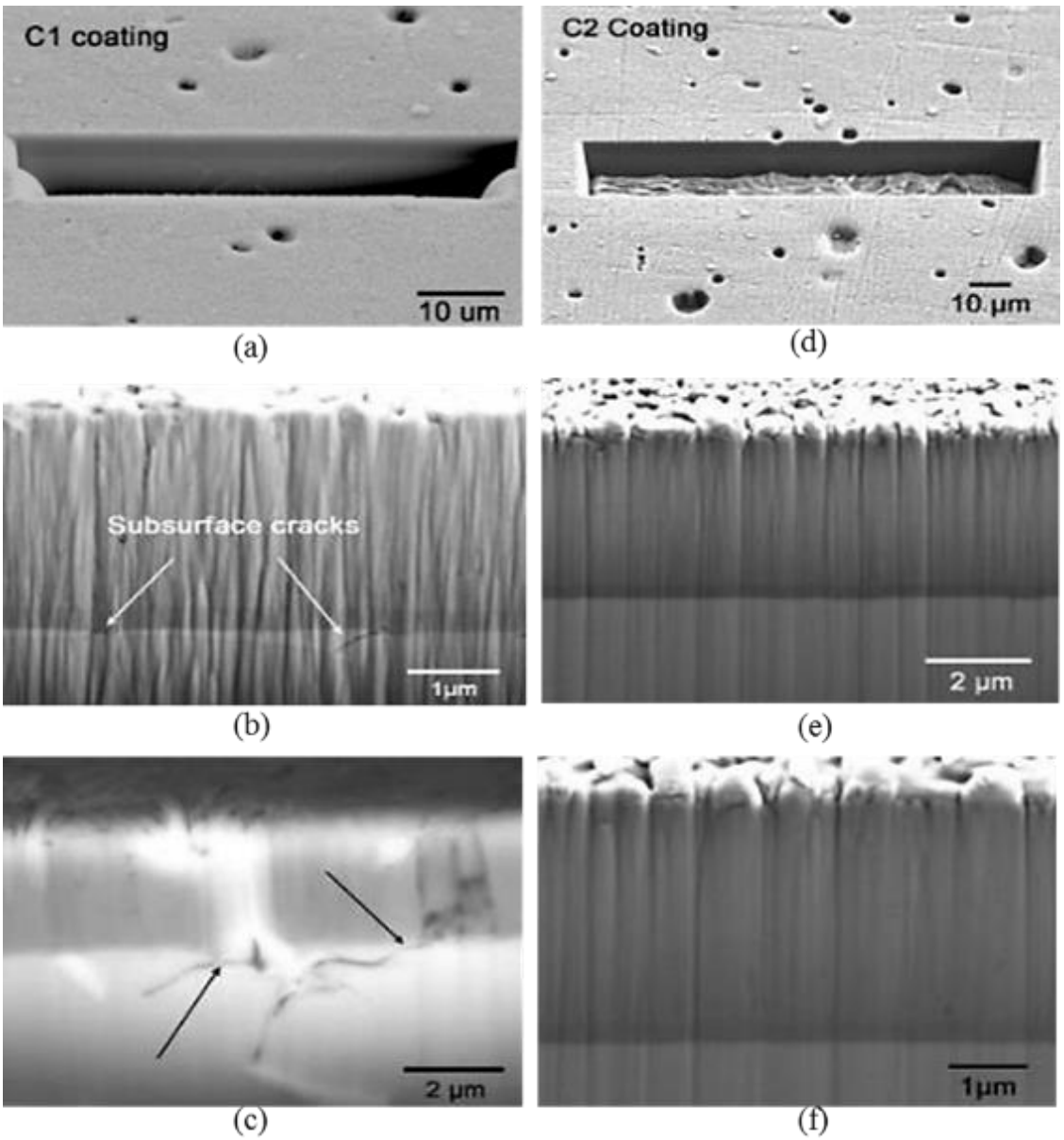

Fig. 7.5 (a), (b) and (c): FIB cross-sections of C1 coating during incubation period; arrows indicate cracks (d), (e) and (f): cross-sections of C2 coating during incubation period.

The coated specimens construct a system with a hard and tough coating applied on a compliant substrate. The hardness and Young's modulus of the coatings are up to 10 times higher than those of the substrate. The high impact pressure and stress waves induced by implosion of cavitation bubbles cause deformation in the target material [176,202,203]. The dislocation density is increased during this process [176]. The nanoscale multilayer structure restrains the mobility of the dislocations, hence, limited plastic deformation occurs. Additionally, the enhanced toughness of the superlattice structured coatings can also contribute to better resistance to cavitation impulse. As the stress waves propagate through the coatings and reach the interface, they would be partially transmitted and partially reflected. The magnitude of the stress waves reaching the interface can vary due to the different coating textures, which will be further discussed in the following section. The transmitted stress waves then interact with the substrate material. The Ti6Al4V substrate demonstrates more compliance with larger grain size (5µm), which can promote the dislocations with more space to move and lead to plastic deformation. The repetition of the process of loading and unloading induced by clouds of microjet impingements leads to a fatigue-like phenomenon, eventually forming cracks in the Ti6Al4V substrate. The fact that we observed subsurface cracks on the C1 coating cross-sections indicates that more stress waves transmitted to the substrate material. While for C2 coating, the crack initiation is delayed. More detailed discussion shown in the following section.

7.6.2 Advanced stage

The surface profile of the two coatings tested under CE for 270 mins are shown in Fig. 7.6. Material removal was detected at the edge and the centre of the exposed surface of C1 coating, Fig. 7.6 (a); whereas for C2 coating, the surface profile shown in Fig. 7.6 (b) indicates that the damage was localised. These observations were further confirmed by SEM analysis presented in Fig. 7.7. It can be seen that the substrate surface of C1 coating was exposed due to large areas of coating erosion in Fig. 7.7 (a); whereas in the case of C2 coating, removal was much localised and in general very limited damage was observed in Fig. 7.7 (b).

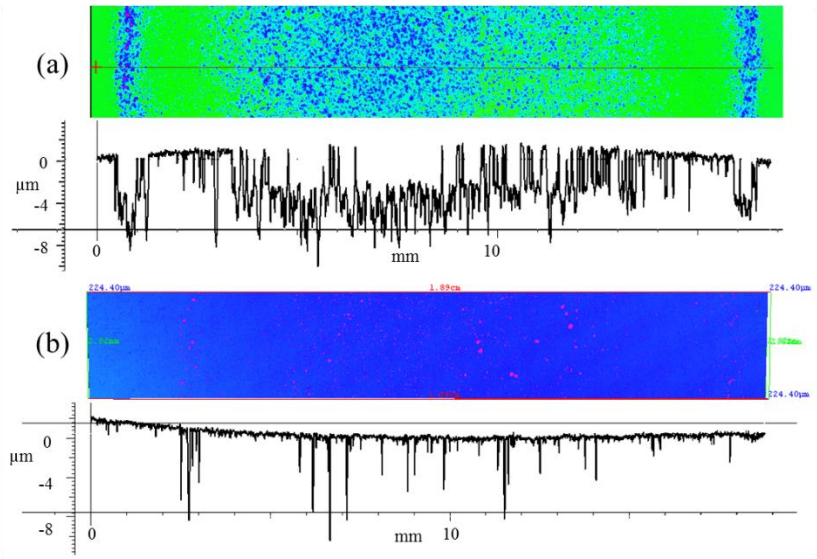

Fig. 7.6 Surface profiles of 270 mins of CE tests: (a) C1 coating; (b) C2 coating.

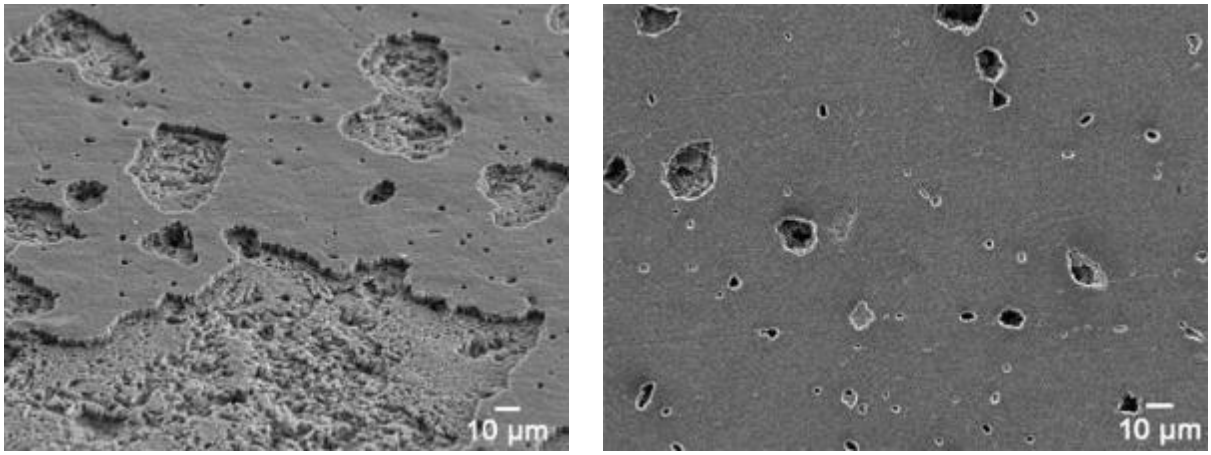

(a) (b)

Fig. 7.7 Exposure surface of 270 mins of CE tests: (a) C1 coating; (b) C2 coating.

Cross-sectional investigation through FIB/SEM was conducted to further understand the CE mechanisms of both nanoscale multilayer coatings, as shown in Fig. 7.8. It shows a variation in the level of protection offered by the two coatings in the advanced stages of CE. In the case of C1 coating, lateral growth of the subsurface cracks (near the coating-substrate interface) into the Ti6Al4V substrate was prominently observed, as shown in Fig. 7.8 (a) and (b). Some of these cracks were also found to traverse into the coating, as labelled in Fig. 7.8 (a). An erosion crater was formed inside the substrate due to the removal of the substrate material together with the coating, Fig. 7.8 (c). It can be seen that the coating at the surrounding area was still attached to the substrate surface which clearly indicates that the damage is not adhesion related. In the case of C2 coating, initiation of subsurface cracks (initially absent in the incubation period) was also observed. However, compared to the C1 case the subsurface cracks were much smaller in size and their number density lower. As expected for a nanoscale multilayer structured coatings crack propagation in a lateral manner was observed due to deflection at the interfaces between the individual nanolayers, see Fig. 7.8 (d).

It was widely reported that the most common failure mode with coated substrates under CE is through coating delamination, [124,125,204]. This is due to the high impact pressure and stress wave reinforcement induced by repeated implosion of the cavitation bubbles at the coating-substrate interface. The same damage mechanism is also reported in the multilayer coating systems, such as CrN/CrCN [124] and Ti/TiN [125]. It should be noted that the coating-substrate interface of the referenced coatings was not engineered by metal ion implantation. In contrast, both C1 and C2 nanoscale multilayer coatings deposited by HIPIMS demonstrated excellent bonding strength with no coating delamination from the substrate due to the metal ion surface pre-treatment, [197,198].

It can be further proposed that one of the damage mechanisms in both coatings can be induced by the surface defects formed during the deposition process. These nodular, open void and cone shape coating defects [201] can act as stress raisers for implosion of cavitation bubbles. Then, the continuous actions of shearing and tearing at these sites lead to subsequent material removal, eventually contributing to enhanced local erosion rates. However, this is not

considered as the main failure mechanism, since both coatings have similar surface defects but exhibit different CE performance.

It is believed that the formation of cracks in the sub-surface region in the incubation period and the way these cracks propagate, both into the substrate and coating during the advanced stage, seems to be the key to understanding the wear mechanism in such system in CE conditions.

As discussed, after a test period of 270 mins, prolonged plastic deformation and crack formation in the substrate of C1 coating was observed, as shown in Fig. 7.8 (a). This could be attributed to the less effective dissipation of the exerted impact pressure and the stress waves on the {200} oriented crystallographic structure. As the cracks developed in the substrate and coalesce at the subsurface, shown in Fig. 7.8 (b), material removal can then take place that leads to the formation of erosion craters inside the Ti6Al4V substrate, as seen in Fig. 7.8 (c). On the other hand, the results indicate that the C2 coating appears to be better equipped to dissipate the stress waves. This can be correlated to the denser atomic packing of the {111}crystallographic planes, which delay crack initiation in the substrate more effectively as compared to the lower atomic density {200} planes of the C1 coating. This phenomenon has been observed in the past studies on CE applications suggesting that materials with certain crystal orientation demonstrate better resistance to wear and CE [142,148,165]. The experiments further revealed that the efficiency of the elastic energy transport through the material, which depends on its elastic properties, also needs to be considered. In our case, the Young's modulus value (E) of the C1 coating, (E_{C1}= 300 GPa) is greater than that of the C2 coating, (E_{C2}= 275 GPa) therefore we observe more effective elastic energy transport through the C1 coating, resulting in more damage to the underlying substrate material.

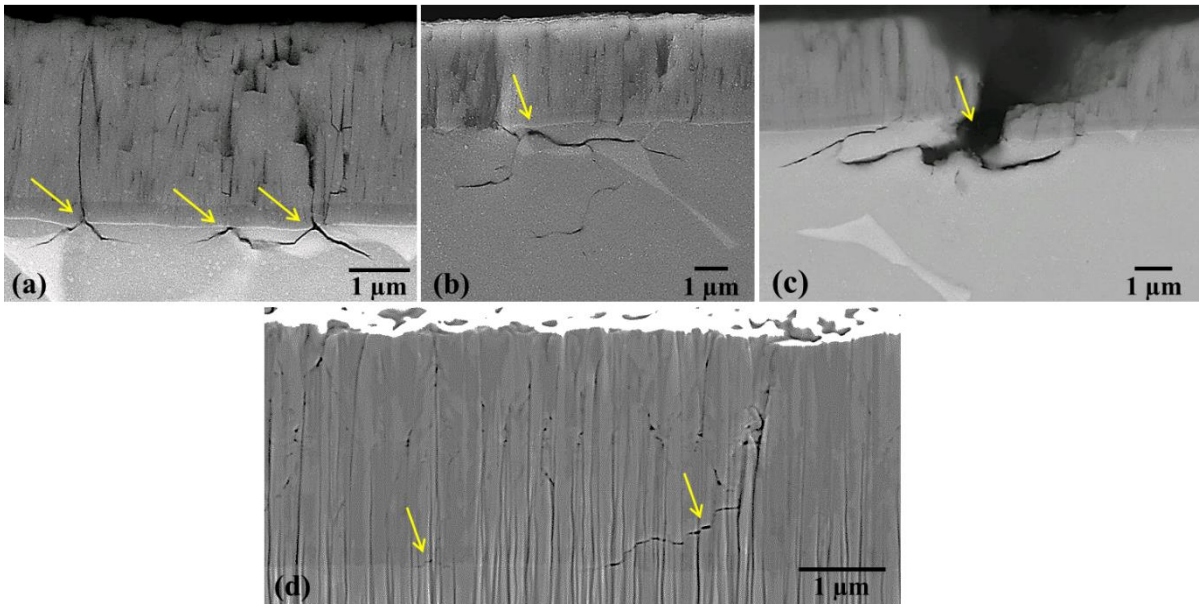

Fig. 7.8 Cross-sectional FIB SEM analysis after 270 mins of CE tests, white arrows indicate the cracks observed in: (a,b,c) C1 coating; (d) C2 coating.

Thus superior coating microstructure, along with the engineered coating texture ({111} dominant) and lower Young's modulus, (E) value seems to define the superior CE resistance of the C2 coating as compared to C1 coating.

7.7 Comparison with monolithic coating

For comparison and analysis of wear mechanisms, CE experiments were also carried out on commercially deposited monolithic TiN coatings deposited on Ti6Al4V substrates. The beneficial effect of nanoscale multilayer structure can be further demonstrated when comparing the CE performance with a monolithic magnetron sputtered TiN coating on the same Ti6Al4V substrate. The investigated TiN coating exhibits a strong {111} texture. Fig. 7.9 shows SEM image of the eroded areas of the coating after subjecting it to similar testing conditions as those employed for C1 and C2 coating. The TiN coating failed after 5 mins of CE exposure and the erosion rate exceeded that of the Ti6Al4V substrate after 270 mins of CE tests. As seen in Fig. 7.9 (a), the TiN coated specimen shows severe damage and loss of coating on large areas of the surface. Formation of inter-columnar cracks as shown in Fig. 7.9 (b) and eventual coating delamination seems to be the dominant mode of failure. However, unlike the C1 and C2 coating, these cracks appear to originate at the top and propagate vertically along the columnar boundary towards the substrate without any deflection or hindrance. Despite its more favourable {111} texture, owing to the weak bonding between columnar grains, which is an inherited problem of the standard magnetron sputtering deposition renders the coating weak. The results clearly demonstrate that monolithically grown PVD coatings do not prevent the crack initiation due to the shearing forces encountered in CE as effectively as compared to the nanoscale multilayer structures.

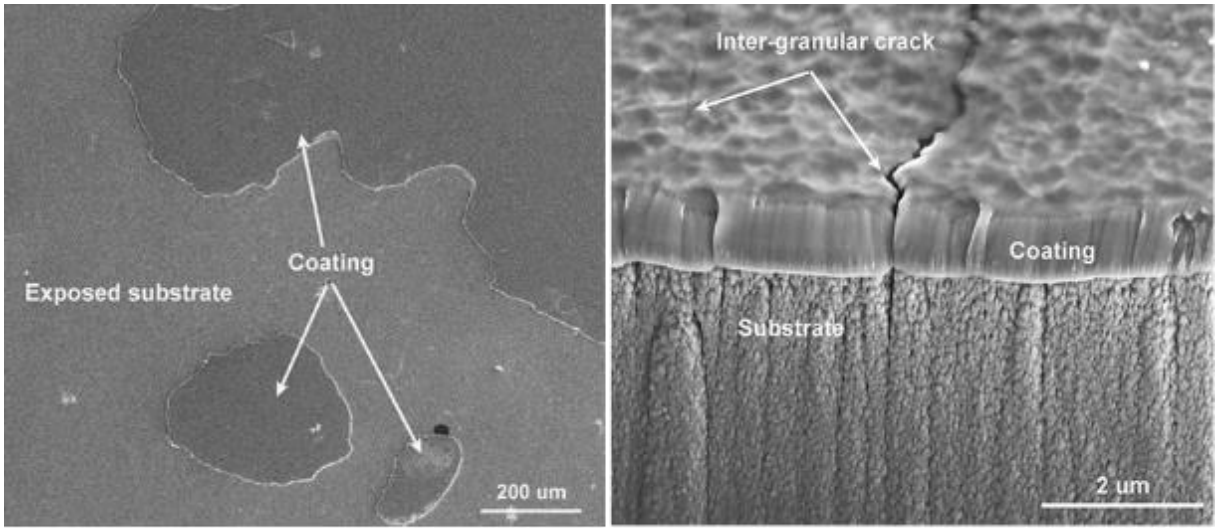

Fig. 7.9 Cavitation erosion studies on TiN coating (a) SEM image of the eroded coating in plan view (b) FIB cross-sectional analysis showing vertical cracking in the coating indicated by white arrows.

7.8 Conclusions

1. High Power Impulse Magnetron Sputtering (HIPIMS) technology was successfully used to deposit CrAlYN/ CrN coatings utilising nanoscale multilayer structure with high hardness, $HK_{0.25N}$ = 2750, enhanced adhesion (scratch adhesion critical load, L_C= 80 N) and high coating density as shown by FIB/SEM and TEM analyses. In Cavitation Erosion (CE) tests the novel coatings show a factor of 14 lower erosion rates than the base Ti6Al4V substrate and outperformed a range of coatings reported in the literature deposited by PVD, CVD, Plasma spray, HVOF and Arc spray techniques.

2. The research shows that in CE conditions there are significant differences in the coating failure mechanisms between monolithically grown and nanoscale multilayer structured coatings:
   – Monolithically grown TiN coatings with {111} texture deposited by standard magnetron sputtering exhibited severe damage after only a few minutes in the CE test where the main failure mechanism was coating delamination due to the weak adhesion bonding and opening of tensile stress inter-columnar cracks due to the sub-dense columnar coating structure.
   – The HIPIMS-deposited CrAlYN/CrN nanoscale multilayer structured coatings show no signs of delamination due to the strong metallurgical bonding between the coating and the substrate. Crack initiation was significantly delayed with a 240 minute incubation period achieved in CE tests. FIB/ SEM analyses show clear evidence that the crack propagation mechanism involved crack deflection at the interfaces between the nanolayers, which was highly beneficial for the coating lifetime.

3. HIPIMS-deposited CrAlYN/CrN coatings with {111} texture grown in conditions of low ion bombardment shows better protection of the substrate material against sub-coating substrate deformation and crack formation as compared to coatings with {200} crystallographic orientation deposited in conditions of higher ion bombardment. It is suggested that the denser atomic packing of the (111) crystallographic planes better dissipate the propagation of the elastic stress waves produced in the CE through the coating material.

4. CE tests revealed that CrAlYN/CrN coatings with lower Young's modulus, (E_{C2} = 275 GPa) provide better protection of the substrate material against crack formation as compared to coatings with higher Young's modulus, (E_{C2} = 300 GPa) due to the less effective elastic energy transport through such materials.

Chapter 8.
Coating performance under WDE

The results of the CE screening tests indicate that Hardide T1200, Hardide LT, HIPIMS multilayer C1 and HIPIMS multilayer C2 coatings were the best performing coatings. Hence, validation of the coating performance under WDE was further investigated in this chapter.

8.1 WDE test results

WDE tests were conducted on Hardide T1200 and LT coatings under the same conditions as applied to the Ti6Al4V base material: 500 µm droplets at 300 $m \cdot s^{-1}$ impact velocity using the NPL whirling arm rig. The results are shown in Fig. 8.1. The cumulative volume loss is converted from gravimetric analysis and the densities of Hardide coatings and Ti6Al4V base material are 19.3 g/cm^3 and 4.4 g/cm^3, respectively. The T1200 coating showed negligible material loss after 30 mins of test, the erosion rate then increased and reached the maximum value after 80 mins. In comparison to the Ti6Al4V base material, the T1200 coating exhibits slightly higher erosion rate during 50 mins of test duration. While for the LT coating, it failed due to delamination after 30 mins exposure to WDE. The WDE test results of the Hardide coatings suggest similar ranking in coating performance as in CE tests. The T1200 coating outperformed LT coating in both tests.

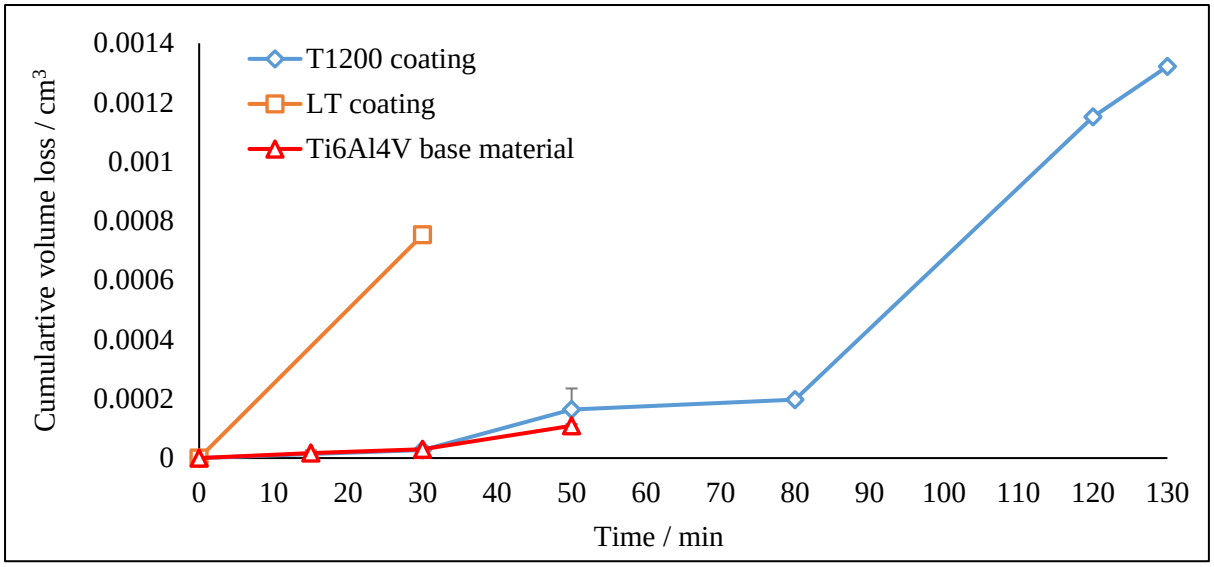

Fig. 8.1 WDE test results of Hardide coatings in comparison to Ti6Al4V base material.

The second run of WDE tests were conducted on the HIPIMS nanoscale multilayer CrAlYN/CrN coatings with different crystalline textures: C1 coating with (200) texture and C2 coating with (111) texture. Negligible mass loss was detected after 160 mins of WDE test for both coatings. Post-test characterisation was conducted to further investigate the coating performance.

8.1.1 WDE metrology

The post-test surface profiles of the coated specimens were examined with the G4 Alicona profilometer. Fig. 8.2 and Fig. 8.3 show the plan views of Hardide T1200 and LT coating, respectively. A horizontal crack was formed across the width of the exposed surface of T1200 coating after 130 mins of WDE test. Chipping was observed at the top of the specimen and the depth of the crater was found to be 74.4 µm. While for LT coating, delamination of the coating was observed after 30 mins of WDE exposure in Fig. 8.3. The depth of the material removed was around 55 to 57 µm. The surface profile of HIPIMS multilayer C2 coating after 160 mins of WDE test is shown in Fig. 8.4. No signs of significant material removal was seen, small cavities with a maximum depth of 2.5 µm was detected.

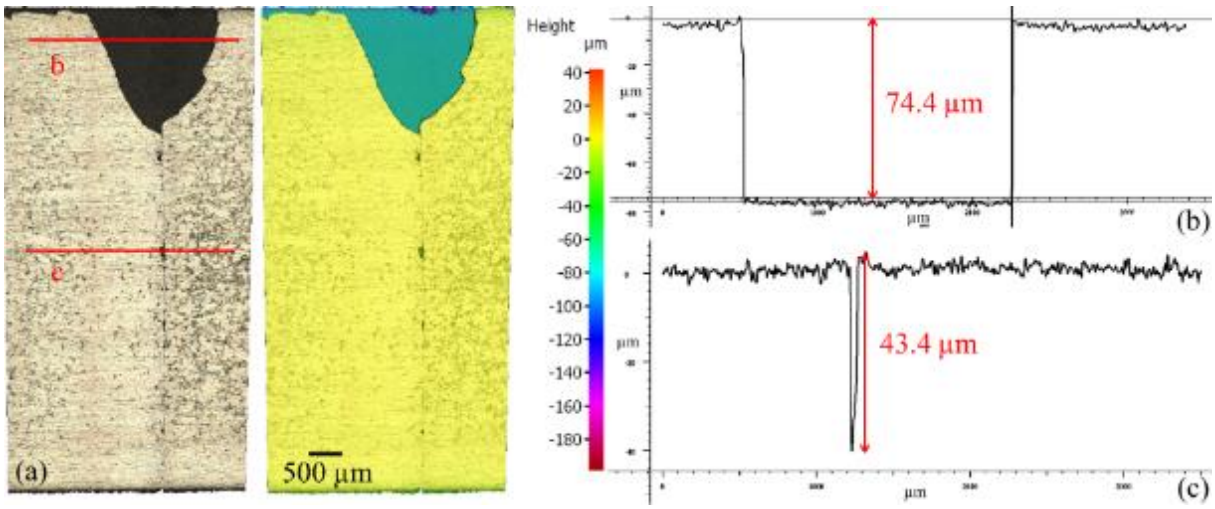

Fig. 8.2 Surface profile of T1200 coating after 130 mins of WDE test.

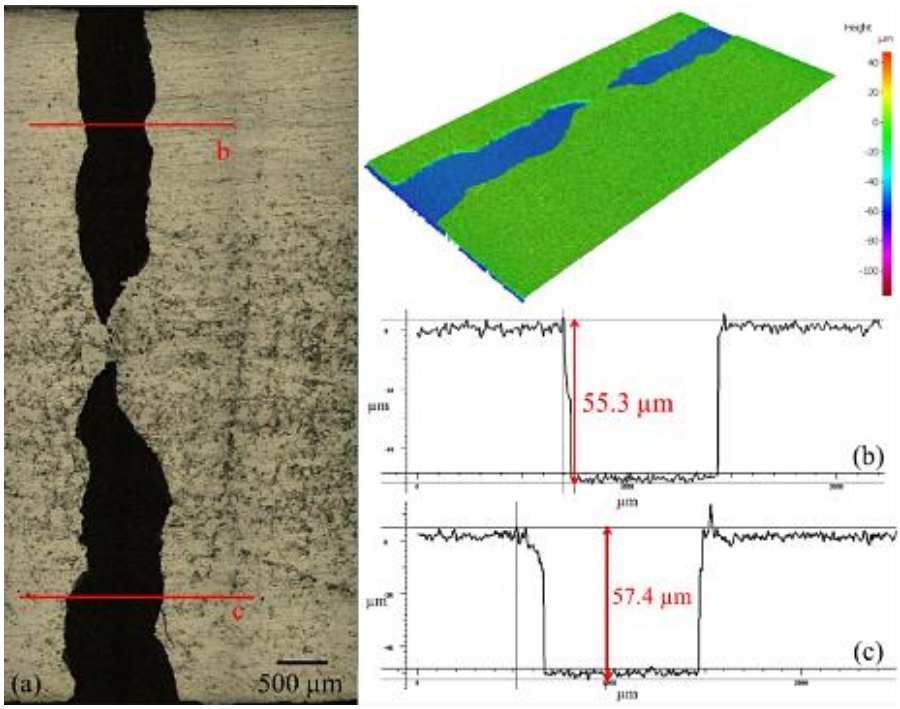

Fig. 8.3 Surface profile of T1200 coating after 30 mins of WDE test.

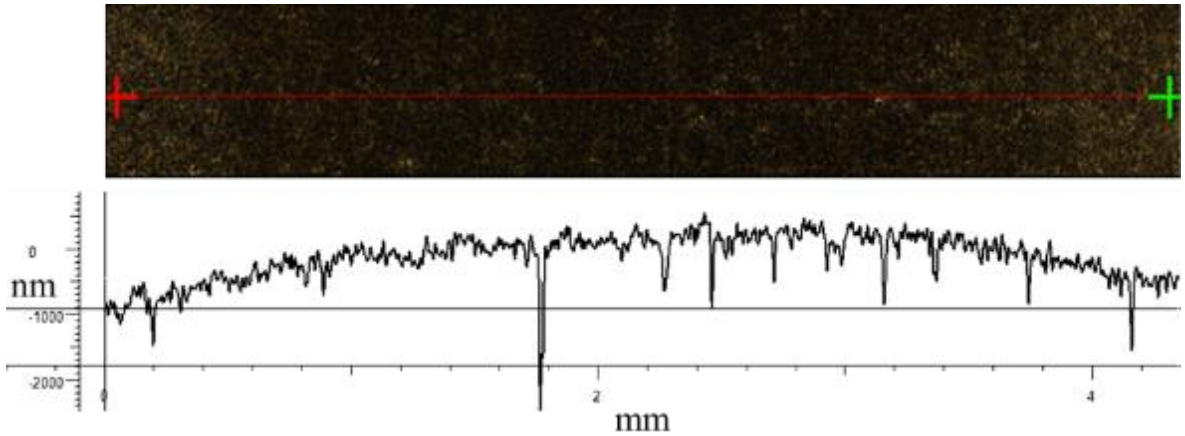

Fig. 8.4 Surface profile of C2 coating after 160 mins WDE test.

8.1.2 Microstructural analysis

8.1.2.1 Hardide coatings

SEM and EDS analysis was conducted in order to understand the damage mechanisms induced by WDE. Fig. 8.5 shows the EDS results conducted on the crater formed at the top of T1200 coating specimen. Ti6Al4V base material was exposed due to the removal of T1200 coating. Small percentage of copper (Cu) interlayer was also detected inside the crater.

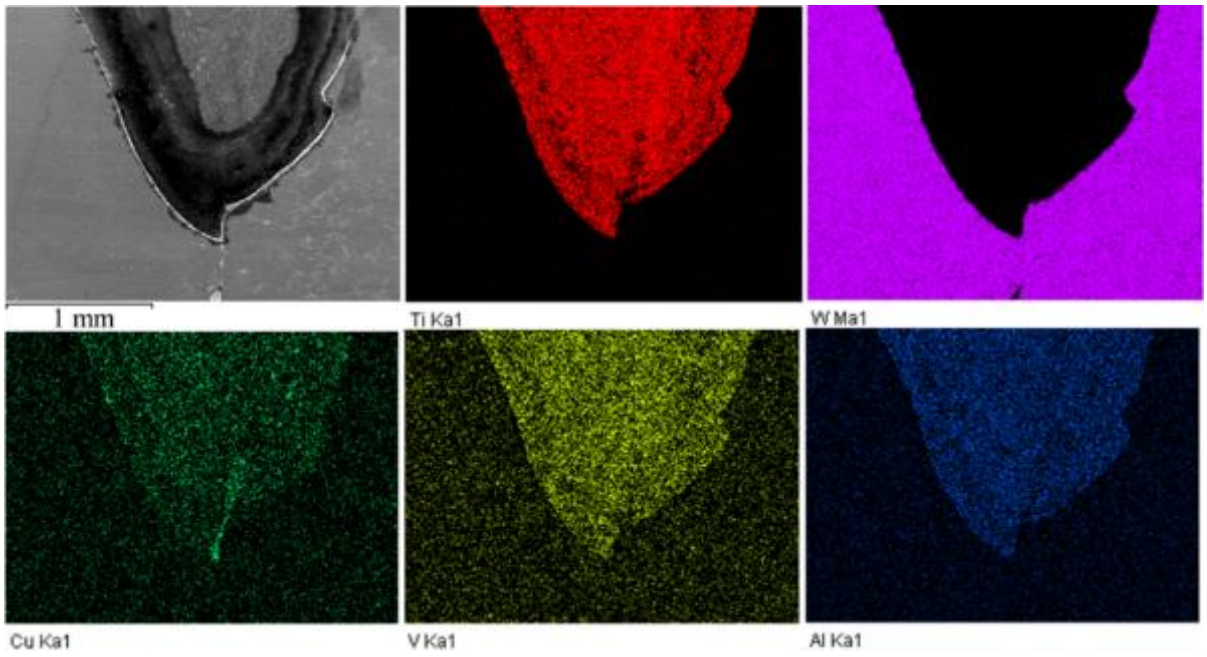

Fig. 8.5 EDS analysis of the material removal at the top of the T1200 specimen.

Material removal was observed at various sites along the horizontal crack formed across the T1200 coating surface, as shown in Fig. 8.6. All the damage was developed on one side of the crack. Higher magnification of the fracture surface is presented in Fig. 8.7. In addition, scattered regions of material removal was seen away from the crack. Cracks and craters were formed on the coating surface in Fig. 8.8.

Cross-sectional analysis of the T1200 coating is shown in Fig. 8.9. A vertical cracks was found propagating through the coating thickness. Formation of cracks was observed between the Ti6Al4V substrate and the Cu interlayer, which can be confirmed by EDS analysis shown in Fig. 8.9 (d).

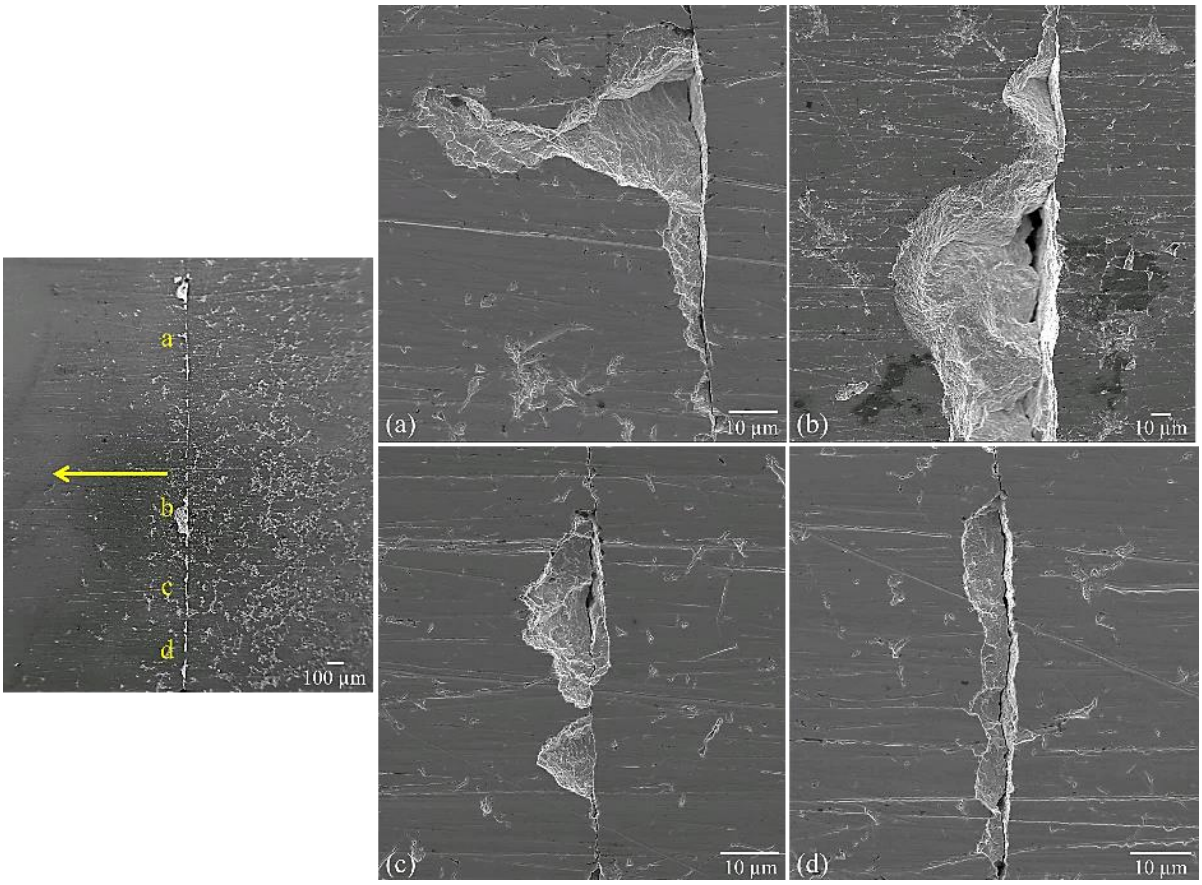

Fig. 8.6 Exposed surface of T1200 coating surface after 50 mins WDE test.

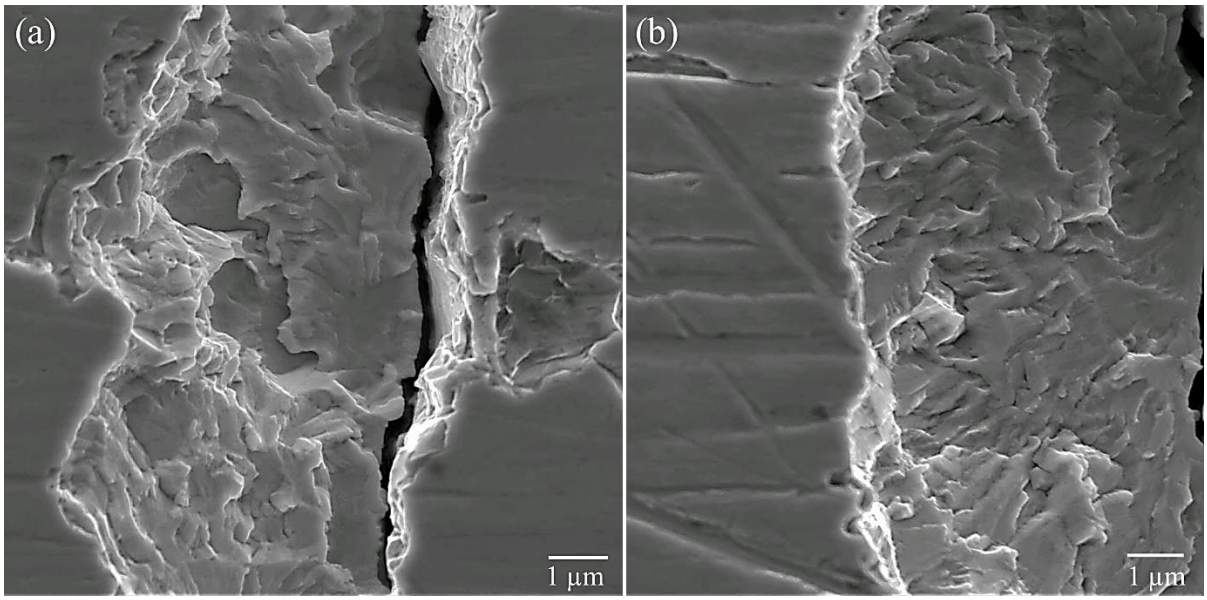

Fig. 8.7 Exposed surface of T1200 coating surface after 50 mins WDE test.

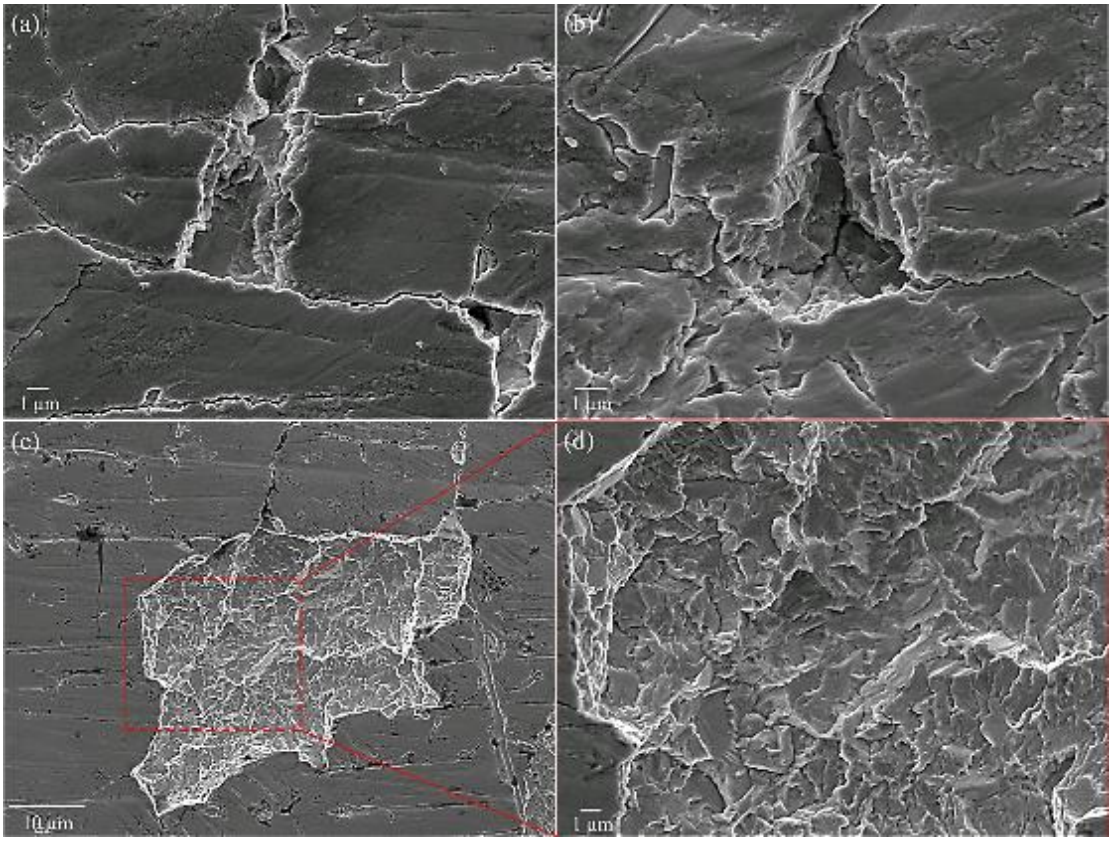

Fig. 8.8 Exposed surface of T1200 coating surface after 50 mins WDE test.

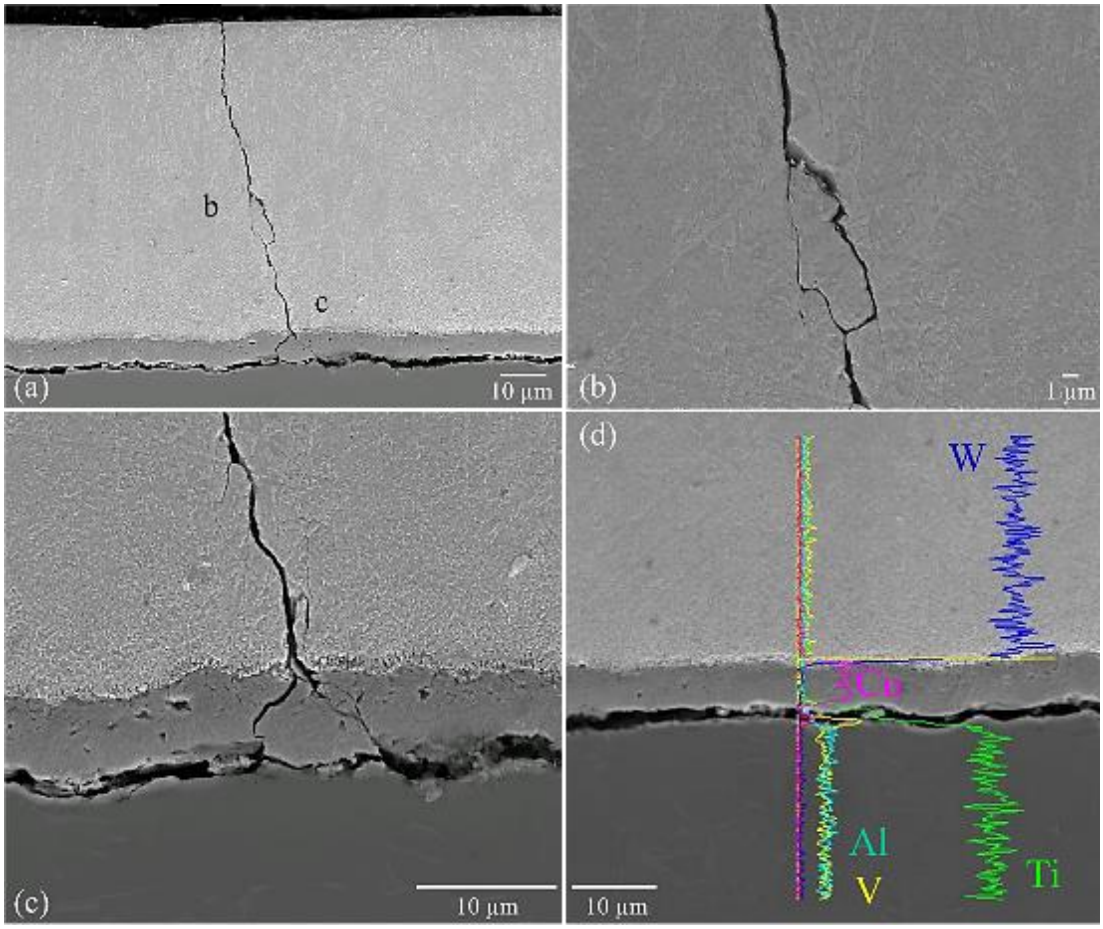

Fig. 8.9 Cross-section of T1200 coating after 50 mins WDE test.

In the case of the Hardide LT coating, delamination was observed on the surface, buckling was detected on the side of the specimen, as shown in Fig. 8.10. The substrate material Ti6Al4V was exposed, which can be confirmed by the EDS analysis shown in Fig. 8.10 (c). Formation of cavities was found at the centre of the specimen, Fig. 8.10 (c). On closer inspection, intergranular fracture was formed adjacent to the cavities, as shown in Fig. 8.10 (d). Cross-sectional analysis shown in Fig. 8.10 (f) indicates the formation of a crack formed at the interface between the Ti6Al4V substrate and Cu interlayer. Moreover, large impact scars and indents were observed over the coating surface in Fig. 8.11.

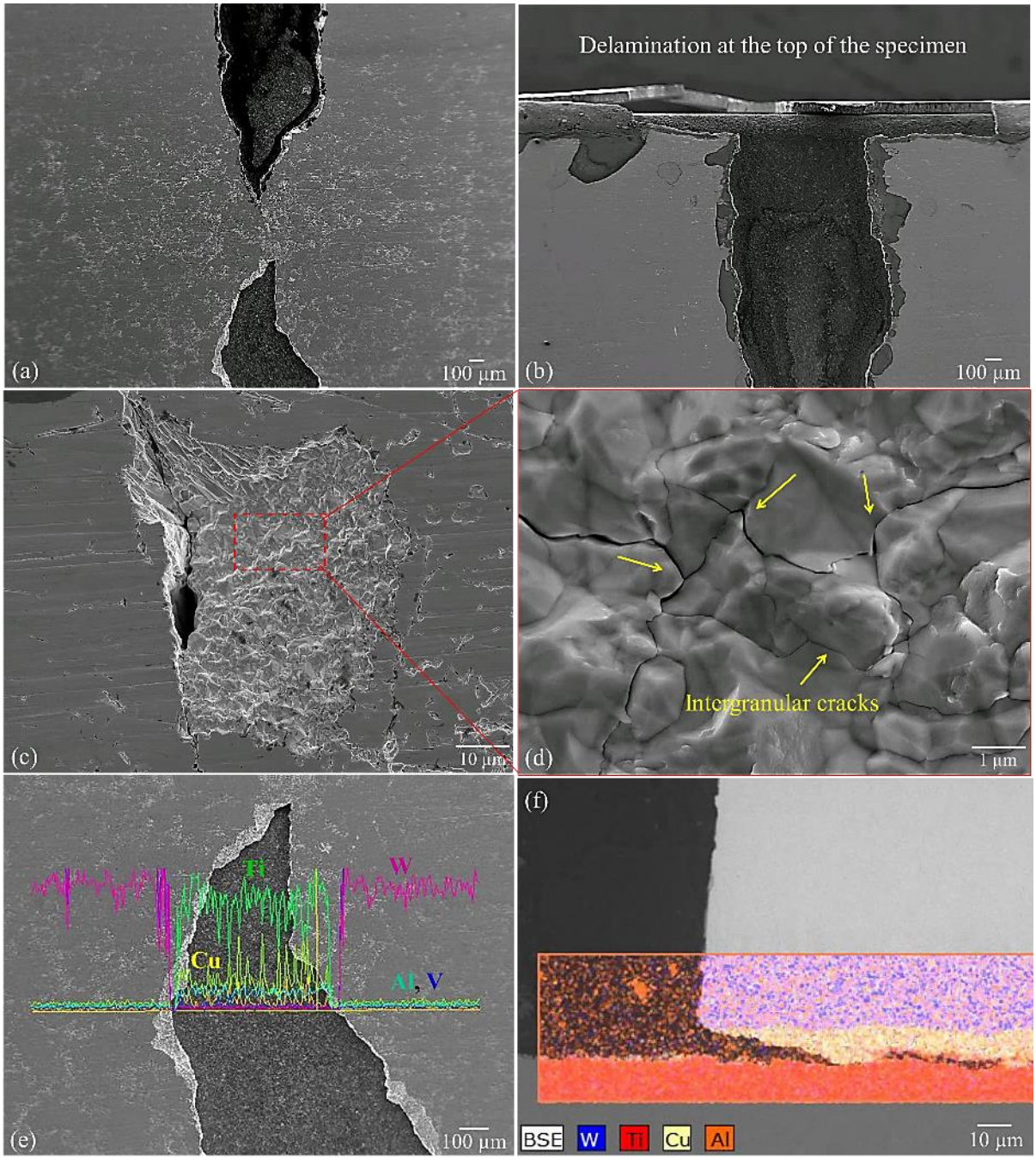

Fig. 8.10 LT coating after 30 mins WDE test.

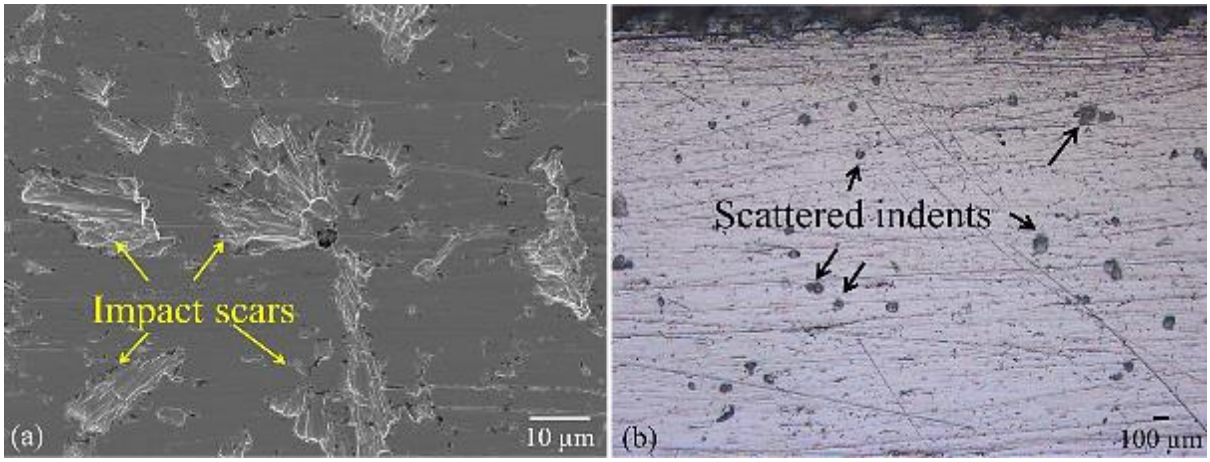

Fig. 8.11 Scattered indents and impact scars over the surface of Hardide coatings.

8.1.2.2 HIPIMS nanoscale multilayer coatings

The exposed surface of the C1 and C2 coatings were investigated with optical microscope and SEM, as shown in Fig. 8.12 and Fig. 8.13. Arrays of cracks were observed across the exposed surface on both coatings. Surface defects induced during the manufacturing process [201] were seen on both coating surfaces. Additionally, triangular indents in the size of 80 to 100 μm and large impact mark up to 1 mm were found scattering over the coating surface, as shown in Fig. 8.14 and Fig. 8.15.

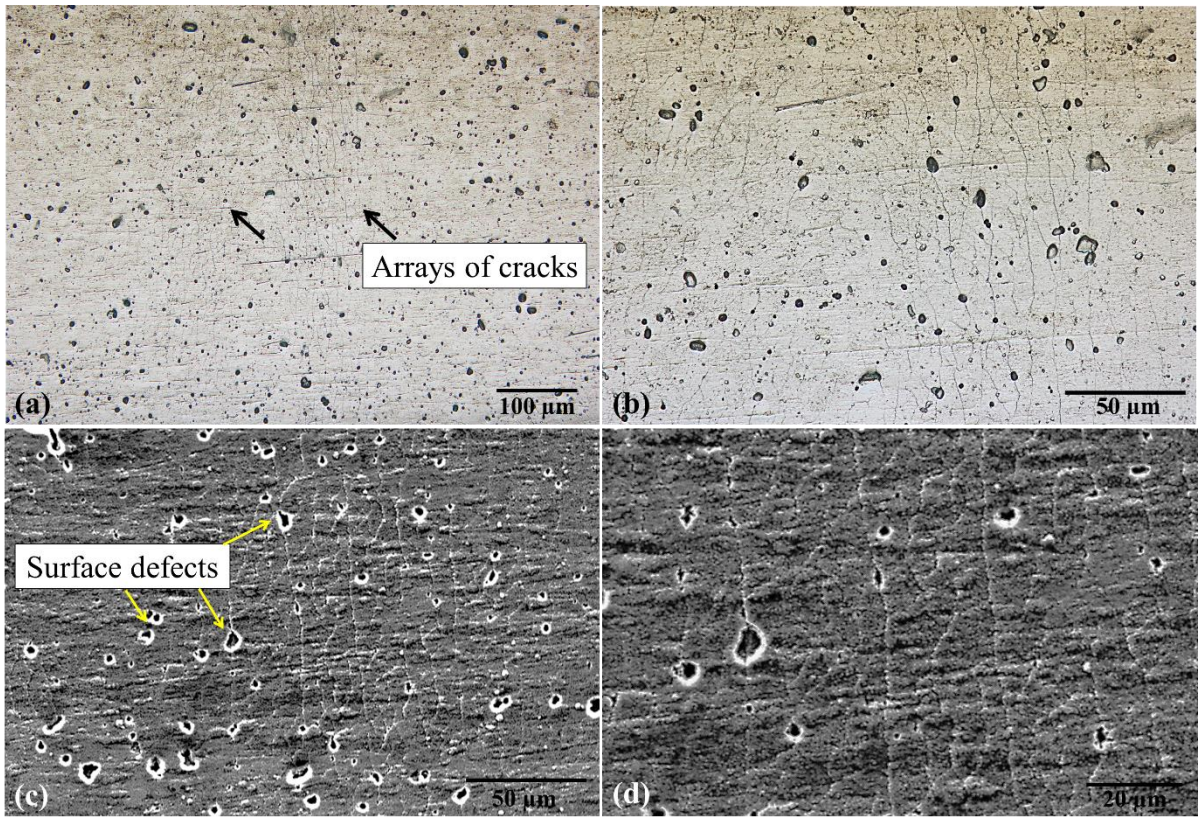

Fig. 8.12 Exposed surface of C1coating after 160 mins WDE test.

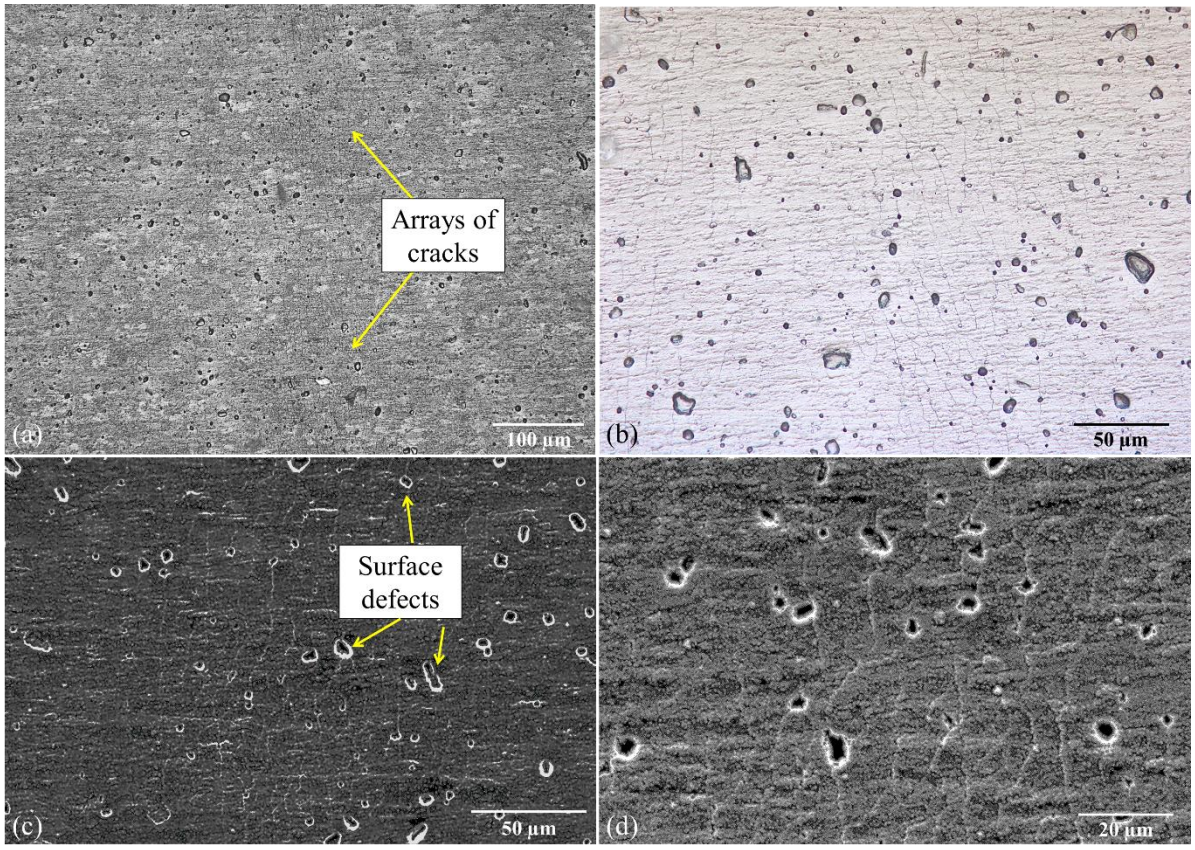

Fig. 8.13 Exposed surface of C2coating after 160 mins WDE test.

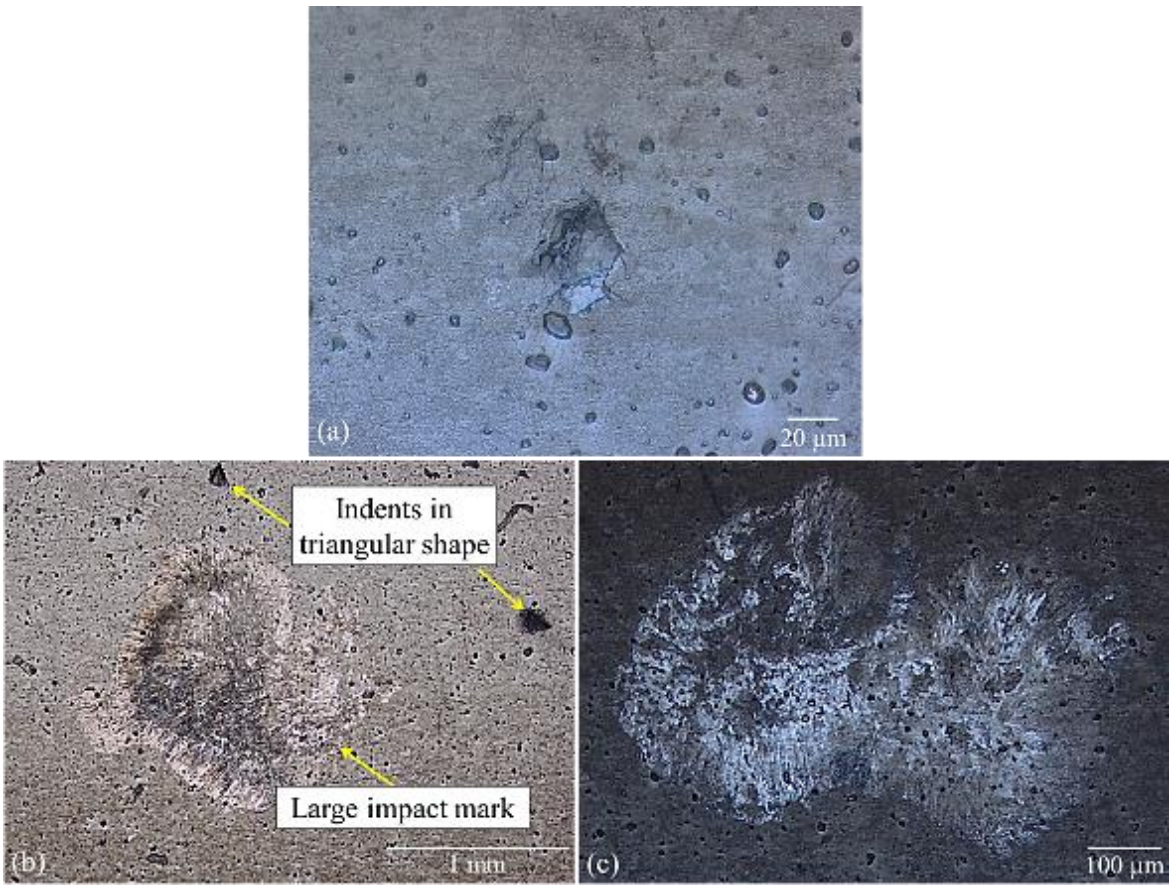

Fig. 8.14 Indents and large impact marks observed on C1 multilayer coating.

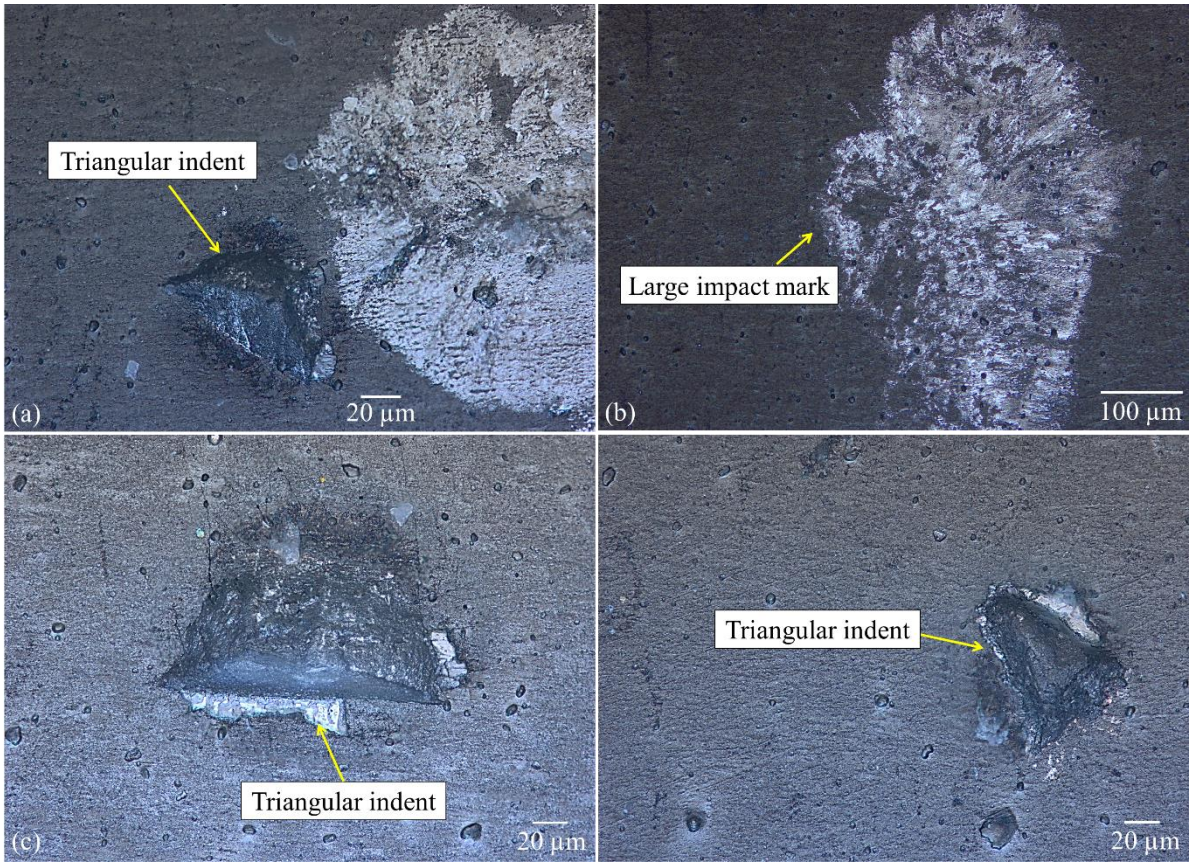

Fig. 8.15 Indents and large impact marks observed on C2 multilayer coating.

8.2 Damage mechanisms

The results shown above do not particularly demonstrate the damage mechanisms induced by WDE when compared to past studies [46,76,83,116,122,133,134]. Formation of a single horizontal crack (s) across the specimen surface was not considered as one of the typical failure modes under WDE. On closer inspection of the specimen holder, as illustrated in Fig. 8.16, it was suspected of applying four-point bend to the target sample. The results therefore represent the damage mechanisms of the coated system under bending [205–207], as shown in Fig. 8.17.

Fig. 8.16 Means of the specimen installed in the sample holder of WDE rig at NPL.

Additionally, the NPL rig had previously undergone an accident in which the sample holders became detached from the whirling arm leading to them flying off inside the chamber during

operation. This led to damage inside the chamber, which can subsequently affect the vacuum conditions. Moreover, the horizontal set-up of the nozzle can also be affected due to the poor vacuum condition. A new pair of sample holder was designed and rebuilt, which were used in the current study. However, the installation of the specimens is believed to improper as it can induce 4-point bending.

Therefore, the crack based damage mechanism observed in the coating systems was more likely induced by four-point bending. The water droplet impacts can potentially aggravate the bending stress. For both Hardide T1200 and LT coatings, it is believed that the damage can be initiated by the surface defects formed by coating features. A crack was formed due to high surface tension developed under four-point bending at defect sites. The crack then propagates through the coating and the soft copper interlayer, it eventually arrests and grows along the interface between the substrate and the copper interlayer. The fact that the LT coating failed much earlier than T1200 coating can be attributable to its full columnar structure. The crack can propagate easily along the grain boundaries and lead to delamination of the coating. It is speculated that the fracture surface formed along the horizontal crack can be resulted from WDE, however, it is believed that the damage was more likely developed after the formation of the crack. Hence, WDE might not be the primary damage mechanism.

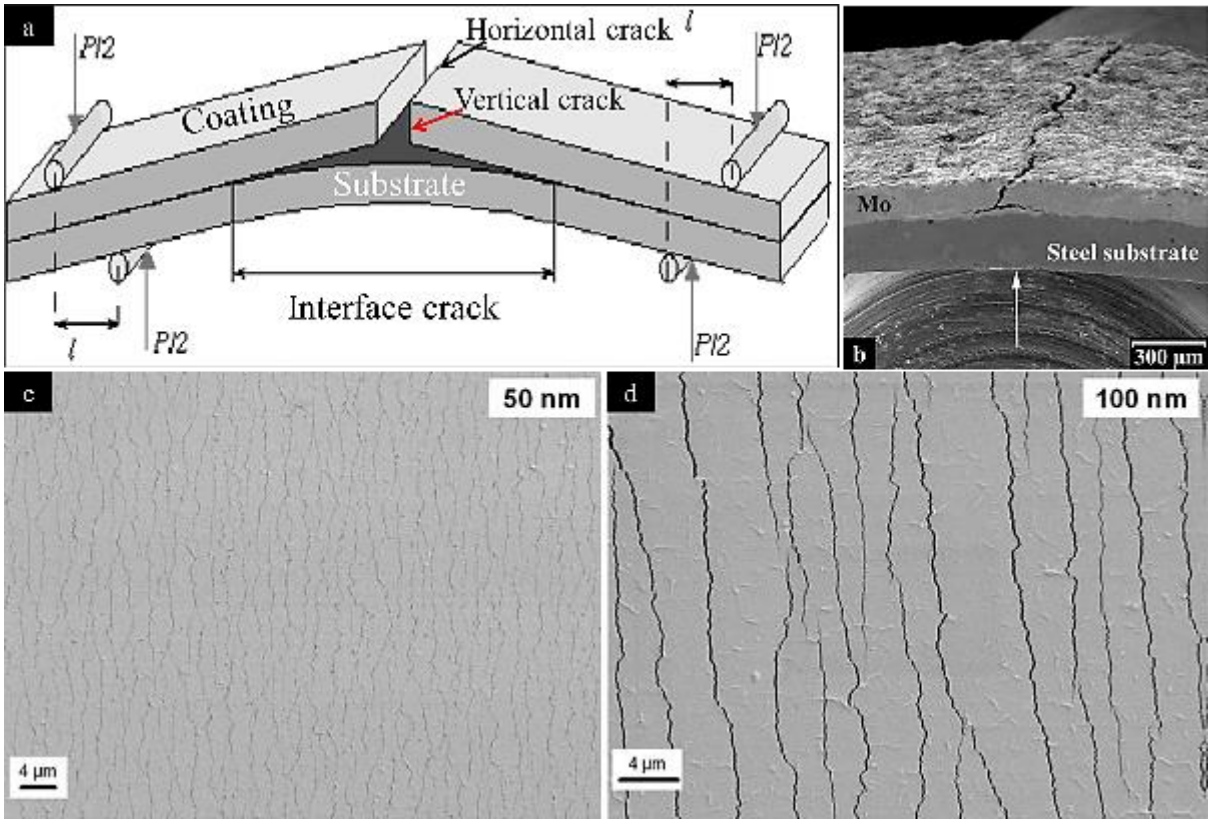

Fig. 8.17 Damage mechanisms of coated systems under bending tests reported in the literature: (a) schematic of four-point bending test [205]; (b) cross-section of bent Mo coating on steel substrate [206]; (c) and (d) formation of multiple cracks on Cr thin film [207].

In the case of the HIPIMS deposited nanoscale multilayer coating systems, strong adhesion can be confirmed since no significant coating removal was observed. The initiation of the cracks can be caused by the coating surface defects, shown in Fig. 8.12 and Fig. 8.13, formed during

the manufacturing process [201]. These defects can act as stress concentrator and lead to formation of cracks under four-point bending. Additionally, residual stress can be developed in the coatings due to the deposition conditions. They can be tailored to be beneficial for coating properties. The distribution of residual stress can impact the adhesion and the fracture toughness of thin films and coatings. However, in certain circumstances, the coatings can suffer from cracking under tensile residual stress [208,209], or peeling off, buckling, or blistering under compressive residual stress [210,211]. These residual stresses can interact with the stresses induced by CE, leading to coating damage. The measurements of these stresses is still a challenging task, especially in the case of strongly textured, nanocrystalline and multilayer structured coatings [212].

Moreover, the formation of the multiple horizontal cracks in comparison to the single crack observed on the Hardide coating systems can be correlated to the coating thickness [213,214]. A critical coating thickness is reported to determine the fracture modes under bending, which depends on the intrinsic properties of coatings and the interfaces between the coatings and the substrates. For coatings thicker than the critical thickness, the interface crack between the coatings and the substrates was likely to be the main fracture mode. While for the thinner coatings, the multiple cracks would be formed in the coatings and propagate into the substrate with increasing deformation. Fig. 8.18 presents the simulated results on the thickness dependence of the coating fracture modes under bending, which agrees with the experimental findings. Nevertheless, the topic is beyond the scope of current study.

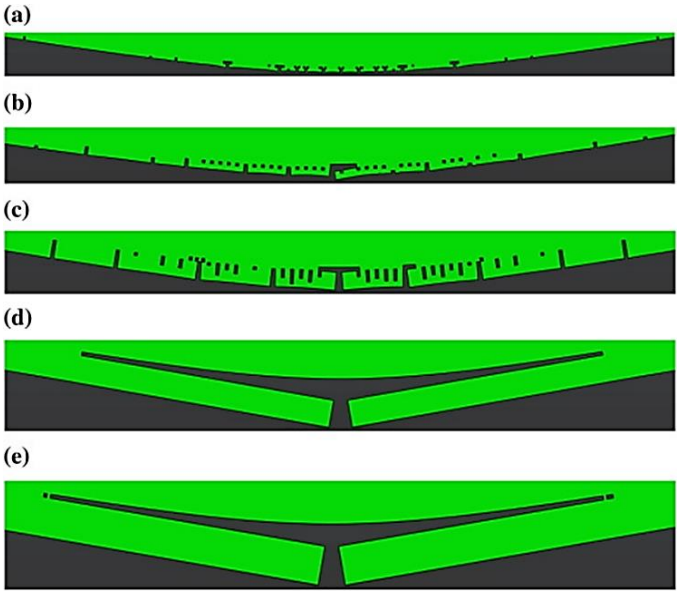

Fig. 8.18 Variation of fracture modes in different coating thicknesses [213].

Furthermore, formation of large indents and impact scar was seen scattered over the tested specimens. Investigation was carried out after the tests and metallic solid particles were found in the rig system with a maximum size up to 2 mm. The large indents, triangular erosion craters and impact scars suggest damage mechanisms under SPE [215,216] Hence, it is believed that they were induced by the solid particle impacts during the operation of WDE tests. There was potentially a synergistic damage mechanism induced by WDE, SPE and four-point bending

during the tests run with NPL rig. However, we cannot verify how they were interacting with each other at this stage.

8.3 Comparison of WDE and CE on coated specimens

The coatings show different performance under CE and WDE, as seen in Fig. 6.9 and Fig. 8.1. This can be due to the four-point bend discussed in the previous section, which can potentially leading to adhesion failure in Hardide coating systems. As the torque used for installation of the specimen is 1 Nm and the nominal diameter of the screw is around 4mm, the applied force on each screw is therefore calculated to be 1250 N. Assuming a simply supported beam with two points loads, a rough estimation can be made on the maximum bending stress using Equation 13 to 15, which is around 885 MPa. This bending stress can lead to adhesion failure in coated systems. However, the variation of the coating performance under CE and WDE can also be caused by the different loading in the two processes. The loading in WDE process is believed to be greater than that of CE process, as shown in Fig. 5.11. Hence, the poor coating performance under WDE can be caused by high impact loading induced by water droplets. However, it is difficult to decouple the failure mechanisms due to the complexity of the test conditions and malfunction of the test rig.

$$\sigma_{b,max} = \frac{Mc}{I_c} \qquad \textbf{Equation 13}$$

$$I_c = \frac{bh^3}{12} \qquad \textbf{Equation 14}$$

$$M = Fa \qquad \textbf{Equation 15}$$

where $\sigma_{b,max}$ is the maximum bending stress, M is the bending moment, c is the centroidal distance of the cross section (1.5 mm), I_c is the centroidal moment of inertia of the beam's cross section, b is the width of the beam (8 mm), h is the thickness of the beam (3 mm), F is the load applied to the beam (1250 N) and a the distance to the applied load (8.5 mm).

Additionally, although similar damage mechanisms of CE and WDE on Ti6Al4V substrate were identified, we cannot quantitatively correlate the two processes in terms of the threshold value for damage. As for coated systems, a more complex stress field can be developed due to stress wave reinforcement induced by the mismatch of acoustic impedance. Moreover, the impact loading in CE process can be not sufficient to induce considerable damage on the coated systems with improved hardness and toughness. While in the case of WDE, the coated system can perform differently under much greater loading. Further validation is required.

8.4 Conclusions

The HIPIMS deposited nanoscale multilayer coatings indicate the best performance under the WDE tests conducted at NPL compared to nanocrystalline Hardide W/WC coatings. However, the primary damage mechanism was believed to be induced by four-point bending for all the tested specimens. Features of WDE might be seen on the Hardide coating surfaces. An unintended synergy between WDE, SPE and four-point bending might be present during the

operation of the tests. The large indents and impact scars scattered over the coating surfaces were caused by the solid particles found inside the rig system. They are thought to be wear particles or fragments of previous test material.

Therefore, the results shown in the chapter are not representative of WDE as the specimen holder induced unintended 4-point bend stress and the test rig induced SPE and WDE accidentally. Further tests need to be conducted under WDE condition only.

Chapter 9.
Conclusions

This work is the first to showcase the real-life rain erosion damage of aeroengine fan blades, which offers valuable information to the field of WDE study. A cost-effective laboratory testing, vibratory CE apparatus, is successfully employed to generate the predominant damage mechanisms observed at the leading edge of aeroengine fan blade. A systematic test plan is adopted to cross-check the damage induced by CE with actual damage on the fan blade leading edge to ensure the relevance of the work to the application. The CE test is then consequently used as a screening process for WDE application.

For the second stage of the work, a series of coatings are applied on Ti6Al4V base material and tested under CE in order to evaluate their potentials for WDE application. The process effectively screened 14 coatings with 4 coatings showing good resistance, including nanocrystalline CVD W/WC coatings and HIPIMS deposited nanoscale multilayer CrAlYN/CrN coatings. In-depth understanding on the coating damage mechanisms are established by correlating the coating performance with microstructure, crystallographic texture, interface design, deposition conditions and mechanical properties for the first time. It is suggested that simple H/E approaches that are widely used in past studies to predict CE performance do not hold or indeed the ultimate resilience ($UTS^2/2E$). However, it is more plausible when taking consideration the H/E ratios together with the factors of microstructure, crystal orientations and nano-layered systems into the understanding of the stress wave dissipation / absorption and attenuation under dynamic compressive stress loading.

The achievements of the work are shown in further details below:

9.1 Rain erosion degradation mechanisms at Ti6Al4V turbofan blade leading edge

The rain erosion mechanism is identified through forensic analysis of ex-service turbofan blades. The process initiates from intergranular fracture induced due to anisotropic behaviour of α grains under high impact pressure and stress waves during early stages. The roughened surface features then interact with lateral outflow jetting, forming cracks. Material removal then takes place in the forms of tunnelling and upheaval of the overlying materials under joint effect of hydraulic penetration. The severity of rain erosion at the leading edge is found increasing with impact velocity. However, at the tip of the leading edge, mild rain erosion damage is detected, which might be caused by the shielding effect of the fan blade casing.

The results of the forensic analysis can alternatively offer design suggestions of fan blades. As it is found that the Ti6Al4V fan blade leading edge can well resist WDE under 200 m·s-1 impact velocity. Hence, the protective coating can be applied on the regions with an impact velocity higher than 200 m·s-1, which can be economically beneficial. Additionally, a drastic increase of rain erosion severity was found within the impact velocity ranging from 286 m·s-1 to 348 m·s-1. Thus, the maximum operating tip velocity is suggested to be below 300 m·s-1.

9.2 Replication of predominant rain erosion damage using vibratory CE testing on Ti6Al4V base material

The predominant damage observed at the fan blade leading edge is successfully generated through vibratory CE test on Ti6Al4V base material. Correlation between WDE and CE of Ti6Al4V is established as similarities in the damage mechanisms are identified, especially during the incubation period. Microstructure plays a vital role on the material behaviour in incubation period. Grain displacement leading to formation of intergranular cracks is primarily induced by high impact pressure and stress waves. In the advanced stages, the two processes show similar damage mechanisms, such as formation of erosion craters due to grain removal, striation marks and honeycomb structured fracture surface with deep cavities. However, effect of lateral outflow jetting is found unique in WDE process, which contributes to the much higher erosion rate in WDE than CE.

9.3 Potential coating solutions screened from CE testing

As the correlation between WDE and CE is verified, CE testing is consequently employed as a valid screening process to predict the WDE performance of the coated systems. For coating applications, incubation period is the most concerned stage, thus, the coatings are screened based on the extension of the incubation period in comparison to the substrate Ti6Al4V. Ultimately, the Hardide CVD-W/WC coatings and HIPIMS deposited CrAlYN/CrN nanoscale multilayer coatings are selected through CE screening test as potential coating solutions for WDE. The improvement in the CE resistance can be attributed to a combined factors of adhesion, mechanical properties, microstructure and coating configuration.

For Hardide CVD-W/WC coating systems, the T1200 coating demonstrate the best resistance to CE. The enhancement credits to the hierarchical coating configuration with nanocrystalline top layer and columnar base layer; consistent through-thickness mechanical properties and a {001} coating texture that is better resist to CE. Additionally, the H/E and H3/E2 ratios obtained from coating mechanical properties correlate well with the CE performance. It suggests a hard yet tough coating can be beneficial for CE applications. Furthermore, the hierarchical microstructure of Hardide T1200 coating demonstrates enhancement in CE performance compared to the Hardide LT coating with the monotonic columnar grain structure. The Hardide T1600 coating with a distinct interface between the coarse and fine layer failed due to stress wave reinforcements. Hardide T1600 undergoes premature spallation of the coating surface during the CE test. Although improvement had been made by Hardide coatings, yet the surface finish of the Hardide coatings cannot be improved less than 0.2 µm. Thus, the rough surface feature can function as stress raisers under CE. The effect of the initial coating topography on the CE performance is effectively characterised by the surface parameters Ssk and Sku.

In the case of the nanoscale multilayer CrAlYN/ CrN coating systems, a high hardness, HK0.25N = 2750, enhanced metallurgical adhesion and high coating density is achieved with the HIPIMS deposition technique. In CE tests, the novel coatings show a factor of 14 lower

erosion rates than the base Ti6Al4V substrate. The CrAlYN/CrN C2 coating with {111} texture grown in conditions of low ion bombardment shows better protection of the substrate material against sub-coating/substrate deformation and crack formation as compared to the C2 coating with {200} crystallographic orientation deposited in conditions of higher ion bombardment. It is suggested that the denser atomic packing of the (111) crystallographic planes better dissipate the propagation of the elastic stress waves generated during CE. Additionally, the coating lifetime is highly beneficial from the crack propagation mechanism involved crack deflection at the interfaces between the nanolayers. The HIPIMS deposition technology remains the original surface finish of the substrate, nevertheless, the surface defects formed during the manufacturing process can act as preferential sites of damage under CE exposure.

Therefore, the following factors are suggested to be taken into consideration when designing an ideal surface that is resist to CE and WDE: strong adhesion, homogenous fine microstructure (nanostructure), high density, hard yet tough properties, beneficial crystalline texture, coating configuration and smooth surface finish with no defects.

9.4 Attempted WDE testing of coatings using whirling-arm rig at NPL

The best-performed coatings screened from the CE tests are Hardide T1200, Hardide LT, HIPIMS multilayer C1 and HIPIMS C2 coatings. Ultimately, these coatings are tested with the whirling arm rig at NPL using 500 μm droplets at 300 m·s-1 impact velocity to validate their potentials for rain erosion protection of fan blade leading edge. The HIPIMS nanoscale multilayer C1 and C2 coatings demonstrate the best performance under the WDE tests compared to the nanocrystalline Hardide W/WC coatings. However, the primary damage mechanism was believed to be induced by four-point bending for all the tested specimens. An unintended synergy between WDE, SPE and four-point bending might be present during the operation of the tests. The large indents and impact scars scattered over the coating surfaces were caused by the solid particles found inside the rig system. They are thought to be wear particles or fragments of previous test material. Therefore, the results are not representative of WDE as the specimen holder induced unintended 4-point bend stress and the test rig induced SPE and WDE accidentally. Further testing needs to be conducted with WDE only.

Chapter 10. Future work

The suggestions for future work as listed as follows:

10.1 WDE testing of CE screened coatings

As there were faulty mechanisms involved in the WDE testing at NPL, the down-selected coatings from CE screening tests need to be tested under WDE condition only in order to further confirm their performance.

10.2 Effect of intrinsic residual stress in coatings on CE and WDE performance

The residual stress developed in the coating during the manufacturing process can potentially interact with the stress waves generated under CE and WDE. Therefore, this information can be beneficial for further understanding of coating performance. However, evaluation of residual stress in coatings and thin films has been a challenging task, especially for functionally graded and nanoscale multilayer coating structures.

10.3 Examination of the evolution of dislocation formation during early incubation period of WDE

Examination of the evolution of dislocation formation during early incubation period of WDE can potentially aid the further understanding of the damage mechanisms. The early incubation period of WDE is analogous to a dynamic work hardening process [52,54], such as metallic shot peening (MSP) or laser shock peening (LSP). Laine et al. [151] presented the correlation between the deformation structure of Ti6Al4V and estimated strain rates of various loading procedures. The deformation mechanisms of Ti6Al4V under very high strain rate ($> 10^6$ s^{-1}) impact loading during LSP exhibit differently to what is expected under conventional high strain rate deformation (10^4 s^{-1}). Long wavy tangles dislocation structures and shear band are observe under the MSP treated Ti6Al4V surface, whereas LSP produces more directional planar dislocations and networks of dislocation cells and sub-grains, as shown in the TEM images in Fig. 10.1. Since the strain rate induced by water-hammer pressure has not yet been well defined, the approximate value can be obtained by applying the same methodology on the specimen tested within early incubation period of WDE. This approach not only can provide experimental evidence for the theoretical calculation of the water-hammer pressure, but also can further contribute to the information needed for the modelling of the WDE process.

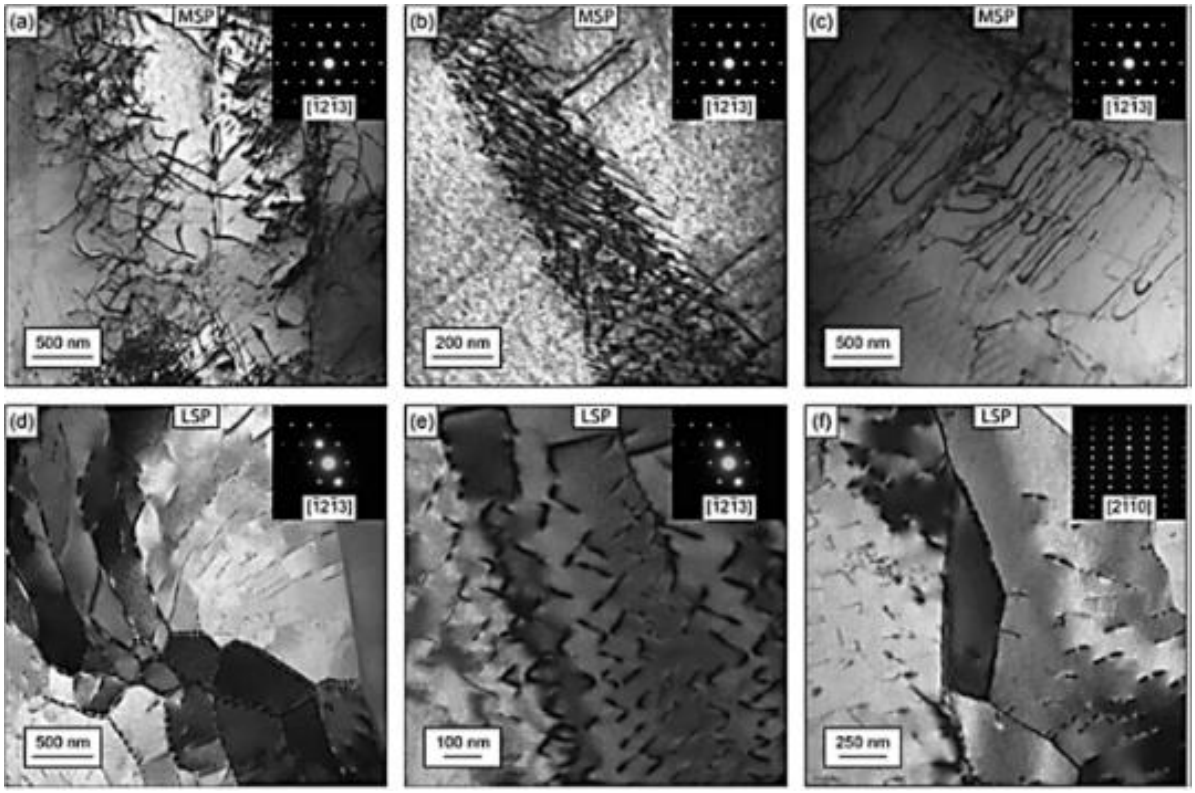

Fig. 10.1 Bright field TEM micrographs from 100 μm below the processed surfaces with corresponding selected area diffraction patterns. (a) to (c) Dislocation structures in the MSP sample. (d) to (f) Dislocation structures in the LSP sample [151].

10.4 Mechanical properties under shock impact loading

Under high strain rate loading, such as WDE and CE, the flow stress is higher than that under quasi-static loading [217,218]. Since the flow stress is higher, many slip systems other than the slip system which has the maximum resolved shear stress can be activated regardless of the crystal symmetry [218]. This can subsequently affect the mechanical properties of a material. Hence, further understanding on the mechanical properties under shock impact load is required.

10.5 Microstructural effect on propagation of stress waves induced by CE and WDE

The microstructural features in the deforming solids are considered as important factors to the stress wave and flow process [219]. Hence, the microstructural effect on stress wave propagation during CE and WDE should be further investigated. It is reported that the pre-existing microstructure dominates the details of nonlinear stress waves, which can load the material beyond the level of plastic yield or fracture [219]. Grain structure, such as grain size and anisotropy, affects the onset of plastic flow or brittle failure [219]. Hence, investigating the effect of substrate and coating microstructure on the stress wave propagation behaviour would be helpful to further understand the material response under CE and WDE.

References

[1] A.A. Fyall, R.B. King, R.N.C. Strain, Rain erosion aspects of aircraft and guided missiles, Journal of the Royal Aeronautical Society. 66 (1962).

[2] E. Honegger, Tests on Erosion Caused by Jets, The Brown Boveri Review, Vol. 14, No. 4, April 1927, pp. 95-10.

[3] J.H. Brunton, J.E. Field, G.P. Thomas, Deformation of solids by the impact of liquids, and its relation to rain damage in aircraft and missiles, to blade erosion in steam turbines, and to cavitation erosion, Nature. 207 (1965) 925–926.

[4] C.J. Hurley, G.F. Schmitt, Development and calibration of a Mach 1.2 rain erosion test apparatus. Technical Report AFML-TR-70-240, Air Force Materials Laboratory, Air Force Systems Command, WrightPatterson Air Force Base, Ohio, 1970.

[5] T.J. Methven, B. Fairhead, A correlation between rain erosion of perspex specimens in flight and on ground rig', Aeronaut.Research Council, Gt. Brit., CP 496, 1960.

[6] A.A. Fyall, Practical aspects of rain erosion of aircraft and missiles, Philosophical Transactions of the Royal Society of London. Series A, Mathematical and Physical Sciences. 260 (1966) 161–167.

[7] F.P. Bowden, J.H. Brunton, Damage to solid by liquid impact at supersonic speeds, Nature. 181 (1958) 873–875. doi:10.1038/022246.

[8] A.B. Thompson, D.W. Woods, Erosion of surfaces by liquid drops, Nature. 176 (1955) 303–304. doi:10.1038/175642b0.

[9] G.P. Thomas, J.H. Brunton, Drop impingement erosion of metals, Proceedings of the Royal Society A: Mathematical, Physical and Engineering Sciences. 314 (1970) 549–565. doi:10.1098/rspa.1970.0022.

[10] O.G. Engel, Mechanism of rain erosion. Part 2. A critical review of erosion by water drop impact, WADC Technical Report. (1953) 53–192.

[11] D.C. Jenkins, A discussion on deformation of solids by the impact of liquids, and its relation to rain damage in aircraft and missiles, to blade erosion in steam turbines, and to cavitation erosion - Disintegration of raindrops by shockwaves ahead of conical bodies, Philosophical Transactions of the Royal Society of London. Series A, Mathematical and Physical Sciences. (1966) 153–160.

[12] O.G. Engel, Waterdrop collisions with solid surfaces, Journal of Research of the National Bureau of Standards. 54 (1955) 281. doi:10.6028/jres.054.033.

[13] Rolls-Royce plc, The Jet Engine, 1986.

[14] National Aeronautics and Space Administration, Turbofan engine, (2018). https://www.grc.nasa.gov/www/k-12/airplane/Animation/turbtyp/etfh.html.

[15] M.G. Dunn, C. Padova, J.E. Moller, R.M. Adams, Performance Deterioration of a Turbofan and a Turbojet Engine Upon Exposure to a Dust Environment, Journal of Engineering for Gas Turbines and Power. 109 (1987) 336. doi:10.1115/1.3240045.

[16] H. De Ryck, Turbofan design for the commercial aircraft, Warsaw University of Technology, Warsaw, Poland, 1-98, 2008.

[17] J.O. Peters, R.O. Ritchie, Foreign-object damage and high-cycle fatigue: role of microstructure in Ti-6Al-4V, International Journal of Fatigue. 23 (2001) 413–421. doi:10.1016/S0142-1123(01)00168-2.

[18] J.C. Williams, Titanium and titanium alloys: scientific and technological aspects volume 3, 1982.

[19] K. Moussaoui, M. Mousseigne, J. Senatore, R. Chieragatti, P. Lamesle, Influence of milling on the fatigue lifetime of a Ti6Al4V titanium alloy, Metals. 5 (2015) 1148–1162. doi:10.3390/met5031148.

[20] P. Road, E. Road, A systematic study of hcp crystal orientation and morphology effects in polycrystal deformation and fatigue, (2007) 1467–1489. doi:10.1098/rspa.2007.1833.

[21] J.C. Williams, R.G. Baggerly, N.E. Paton, Deformation Behavior of HCP Ti-Al Alloy Single Crystals, 33 (2002) 837–850.

[22] E. Brandl, B. Baufeld, C. Leyens, R. Gault, Additive manufactured Ti-6A1-4V using welding wire: Comparison of laser and arc beam deposition and evaluation with respect to aerospace material specifications, Physics Procedia. 5 (2010) 595–606. doi:10.1016/j.phpro.2010.08.087.

[23] S. Viswanathan, D. Apelian, R. J. Donahue, B. DasGupta, M. Gywn, J. L. Jorstad, R. W. Monroe, M. Sahoo, T. E. Prucha, D. Twarog., Remelting Variations Under Vacuum, ASM Handbook, Vol. 15, 2008.

[24] J. Meng, L.F. Liao, D. Li, Y. Cao, L.Y. Yang, Y.Y. Chen, Topology optimization method research on hollow wide-chord fan blade of a high-bypass turbofan engine, Procedia Engineering. 99 (2015) 1228–1233. doi:10.1016/j.proeng.2014.12.652.

[25] P. Spittle, Gas turbine technology, Physics Education. 38 (2003) 504–511. doi:10.1088/0031-9120/38/6/002.

[26] A. Ghenaiet, Study of Sand Particle Trajectories and Erosion Into the First Compression Stage of a Turbofan, J. Turbomach 134, 2012; doi:10.1115/1.4004750

[27] T. Nicholas, J.P. Barber, R.S. Bertke, Impact damage on titanium leading edges from small hard objects, Experimental Mechanics. 20 (1980) 357–364. doi:10.1007/bf02321123.

[28] S.J. Hudak, K.S. Chan, R.C. McClung, G.G. Chell, Y.-D. Lee, D.L. Davidson, High Cycle Fatigue of Turbine Blade Materials, Final Technical Report UDRI Subcontract No. RI 40098X SwRI Project No. 18-8653, 1999.

[29] J.O. Peters, B.L. Boyce, a. W. Thompson, R.O. Ritchie, O. Roder, Role of foreign-object damage on thresholds for high-cycle fatigue in Ti-6Al-4V, Metallurgical and Materials Transactions A. 31 (2000) 1571–1583. doi:10.1007/s11661-000-0167-2.

[30] M. Shinozaki, K.A. Roberts, B. van der Goor, T.W. Clyne, Deposition of ingested ash on surfaces in teh turbine of a small jet engine, Advanced Engineering Materials. 15 (2013) 986–994. doi:10.1002/adem.201200357.

[31] O. Gohardani, Impact of erosion testing aspects on current and future flight conditions, Progress in Aerospace Sciences. 47 (2011) 280–303. doi:10.1016/j.paerosci.2011.04.001.

[32] F.J. Heymann, Liquid impingement erosion, ASM Handbook. 18 (1992) 221–231.

[33] H.S. Kirols, D. Kevorkov, A. Uihlein, M. Medraj, Water droplet erosion of stainless steel steam turbine blades, Materials Research Express. 4 (2017).

[34] M.H. Keegan, D.H. Nash, M.M. Stack, On erosion issues associated with the leading edge of wind turbine blades, Journal of Physics D: Applied Physics. (2013). doi:10.1088/0022-3727/46/38/383001.

[35] ASTM G73-10 (2017), Standard test method for liquid impingement erosion using rotating apparatus, 2017. www.astm.org.

[36] W.F. Adler, The mechanics of liquid impact, in: C.M. Preece (Ed.), Treatise on Materials Science and Technology, Erosion, New York: Academic Press, 1979: pp. 127–183.

[37] C. Gerdes, A. Karimi, H.W. Bieler, Water droplet erosion and microstructure of laser-nitrided Ti6A14V, Wear. 186–187 (1995) 368–374. doi:10.1016/0043-1648(95)07153-9.

[38] A. Déom, R. Gouyon, C. Berne, Rain erosion resistance characterizations link between on-ground experiments and in-flight specifications, Wear. 258 (2005) 545–551. doi:10.1016/j.wear.2004.09.053.

[39] L. Huang, J. Folkes, P. Kinnell, P.H. Shipway, Mechanisms of damage initiation in a titanium alloy subjected to water droplet impact during ultra-high pressure plain waterjet erosion, Journal of Materials Processing Technology. 212 (2012) 1906–1915. doi:10.1016/j.jmatprotec.2012.04.013.

[40] V.N. Varavka, O. V. Kudryakov, Regularities of steel wear under the impact of discrete water-droplet stream. Part II: stage of the developed droplet-impingement erosion, Journal of Friction and Wear. 36 (2015) 153–162. doi:10.3103/S1068366615020166.

[41] W.F. Adler, Waterdrop impact modeling, Wear. 186–187 (1995) 341–351. doi:10.1016/0043-1648(95)07176-8.

[42] B. Soediono, Erosion by liquid and solid impact, in: Proceedings of Fifth International Conferene on Erosion by Liquid and Solid Impact, 1989: p. 160. doi:10.1017/CBO9781107415324.004.

[43] G.F. Schmidtt, Liquid and solid particle impact erosion, Ohio, USA, 1979.

[44] G.E. Cossali, a. Coghe, M. Marengo, The impact of a single drop on a wetted solid surface, Experiments in Fluids. 22 (1997) 463–472. doi:10.1007/s003480050073.

[45] J. Liersch, J. Michael, Investigation of the impact of rain and particle erosion on rotor blade aerodynamics with an erosion test facility to enhancing the rotor blade performance and durability, Journal of Physics: Conference Series. 524 (2014) 012023. doi:10.1088/1742-6596/524/1/012023.

[46] M.C. Kong, D. Axinte, W. Voice, Aspects of material removal mechanism in plain waterjet milling on gamma titanium aluminide, Journal of Materials Processing Technology. 210 (2010) 573–584. doi:10.1016/j.jmatprotec.2009.11.009.

[47] R.M. Blowers, On the response of an elastic solid to droplet impact, IMA Journal of Applied Mathematics (Institute of Mathematics and Its Applications). 5 (1969) 167–193. doi:10.1093/imamat/5.2.167.

[48] N.I. Fox, TECHNICAL NOTE: The representation of rainfall drop-size distribution and kinetic energy, Hydrology and Earth System Sciences. 8 (2004) 1001–1007. doi:10.5194/hess-8-1001-2004.

[49] A.C. Plondke, Droplet characterization in the wake of steam turbine cascades, University of Tennessee, Knoxville, 2012.

[50] N.E. Wahl, Investigation of the phenomena of rain erosion at subsonic and supersonic speeds, AFML-TR-65-330. Air Force Materials Laboratory, Wright-Patterson Air Force Base, Dayton, Ohio, Oct. 1965.

[51] K.K. Haller, D. Poulikakos, Y. Ventikos, P. Monkewitz, Shock wave formation in droplet impact on a rigid surface: lateral liquid motion and multiple wave structure in the contact line region, Journal of Fluid Mechanics. 490 (2003) 1–14. doi:10.1017/S0022112003005093.

[52] F.J. Heymann, On the time dependence of the rate of erosion due to impingement or cavitation, ASTM International. 408 (1967) 70–82.

[53] F.J. Heymann, On the shock wave velocity and impact pressure in high -speed liquid-solid impact, Trans ASME. (1969) 400–402.

[54] F.J. Heymann, High-speed impact between a liquid drop and a solid surface, Journal of Applied Physics. 40 (1969) 5113–5122. doi:10.1063/1.1657361.

[55] F.J. Heymann, A survey of clues to the relationship between erosion rate and impact parameters., in: Second Meersburg Conference on Rain Erosion and Allied Phenomena, Bondensee, Fedreal German Republic, 1967.

[56] S.S. Cook, Erosion by water-hammer, Proceedings of the Royal Society of London. Series A, Containing Papers of a Mathematical and Physical Character, 1928. 119(783): p. 481-488.

[57] F.P. Bowden, J.E. Field, The brittle fracture of solids by liquid impact, by solid impact, and by shock, Proceedings of the Royal Society A: Mathematical, Physical and Engineering Sciences. 282 (1964) 331–352. doi:10.1098/rspa.1964.0236.

[58] J.H. Brunton, M.C. Rochester, Erosion of solid surfaces by the impact of liquid drops, in: Treatise On Materials Science and Technology, Erosion, 1979: pp. 185–248.

[59] J.J. Camus, High-speed flow in impact and its effect on solid surface, PhD thesis, University of Cambridge, 1971.

[60] Y.C. Huang, F.G. Hammitt, W.-J. Yang, Spherical droplet impingement on flat rigid surface non-slip bondary condition, in: Fourth Conference on Fluid Mechanics and Fluid Machinery, Budapest, Hungary, 1971.

[61] J.H. Brunton, Theinfluence of the physical properties of the liquid on the erosion of solids: To be Presented at the, in: 76th Annual Meeting of the American Society for Testing and Materials, University of Cambridge. Engineering Department, Philadelphia, USA, 1973.

[62] S.A.L. Salem, S.T.S. AI-Hassani, W. Johnson, Measurements of surface pressure distribution during jet impingement by a pressure pin transducer, Department of Mechanical. Engineering, UMIST, Manchester, 1979.

[63] J.E. Field, ELSI conference: Invited lecture liquid impact: theory, experiment, applications, Wear. 233–235 (1999) 1–12. doi:10.1016/S0043-1648(99)00189-1.

[64] J.E. Field, J.P. Dear, J.E. Ogren, The effects of target compliance on liquid drop impact, Journal of Applied Physics. 65 (1989) 533–540. doi:10.1063/1.343136.

[65] K.M. Hwang, H.K. Seo, C.K. Lee, W.C. Nam, Development of a LDIE prediction theory in the condition of magnetite formation on secondary side piping in nuclear power plants, World Journal of Nuclear Science and Technology. 07 (2017) 1–14. doi:10.4236/wjnst.2017.71001.

[66] K.F. Graff, Wave Motion in Elastic Solids, Dover Publications, New York, 1975.

[67] K. Yasui, Acoustic Cavitation and Bubble Dynamics, Springer US, 2018. doi:10.1007/978-3-319-68237-2.

[68] N.K. Bourne, T. Obara, J.E. Field, High-speed photography and stress gauge studies of jet impact upon surfaces, Philosophical Transactions of the Royal Society A: Mathematical, Physical and Engineering Sciences. (1997). doi:10.1098/rsta.1997.0028.

[69] N. Kamkar, F. Bridier, P. Jedrzejowski, P. Bocher, Water droplet impact erosion damage initiation in forged Ti-6Al-4V, Wear. 322–323 (2015) 192–202. doi:10.1016/j.wear.2014.10.020.

[70] M.S. Mahdipoor, H.S. Kirols, D. Kevorkov, P. Jedrzejowski, M. Medraj, Influence of impact speed on water droplet erosion of TiAl compared with Ti6Al4V, Scientific Reports. 5 (2015) 14182. doi:10.1038/srep14182.

[71] A.K. Gujba, L. Hackel, D. Kevorkov, M. Medraj, Water droplet erosion behaviour of Ti – 6Al – 4V and mechanisms of material damage at the early and advanced stages, Wear. 358–359 (2016) 109–122. doi:10.1016/j.wear.2016.04.008.

[72] B. Luiset, F. Sanchette, A. Billard, D. Schuster, Mechanisms of stainless steels erosion by water droplets, Wear. 303 (2013) 459–464. doi:10.1016/j.wear.2013.03.045.

[73] G.P. Thomas, J.. Brunton, Drop impingement erosion of metals, Proceedings of Royal Society London. 314 (1970) 549–565. doi:10.1098/rspa.1983.0054.

[74] W.F. Adler, T.W. James, Localized deformation and fracture of fracture of transparent ceramics, Effects Technology, Inc. Technical Report CR80-758, Contract N00014-76-C-0744, March, 1980.

[75] W.F. Adler, A.G. Evans, Erosion damage in carbon-carbon composites at hypersonic impact velocties, Erosion Prevention and Useful Application. ASTM STP 664. (1979) 493–511.

[76] M.S. Mahdipoor, D. Kevorkov, P. Jedrzejowski, M. Medraj, Water droplet erosion behaviour of gas nitrided Ti6Al4V, Surface & Coatings Technology. 292 (2016) 78–89. doi:10.1016/j.surfcoat.2016.03.032.

[77] H.S. Kirols, D. Kevorkov, A. Uihlein, M. Medraj, The effect of initial surface roughness on water droplet erosion behaviour, Wear. 342–343 (2015) 198–209. doi:10.1016/j.wear.2015.08.019.

[78] N. Kamkar, F. Bridier, P. Bocher, P. Jedrzejowski, Water droplet erosion mechanisms in rolled Ti-6Al-4V, Wear. 301 (2013) 442–448. doi:10.1016/j.wear.2013.01.005.

[79] D. Ma, A. Mostafa, D. Kevorkov, P. Jedrzejowski, M. Pugh, M. Medraj, Water Impingement Erosion of Deep-Rolled Ti64, Metals. 5 (2015) 1462–1486. doi:10.3390/met5031462.

[80] G.S. Springer, C.B. Baxi, A model for rain erosion of homogeneneous materials, Erosion, Wear and Interfaces with Corrosion, ASTM STP 567, Socirty for Testing and Materials. (1974) 106–122.

[81] A.W. Momber, Y.C. Wong, R. Ij, E. Budidharma, Hydrodynamic profiling and grit blasting of low-carbon steel surfaces, Tribology International. (2002). doi:10.1016/S0301-679X(02)00009-9.

[82] A. Thirzcuengudam, S.L. Rudy, M. Gunusekarun, Experimental and analytical investigations on multiple liquid impact erosion, Moffett Field, CA, USA, 1969.

[83] Y.I. Oka, H. Miyata, Erosion behaviour of ceramic bulk and coating materials caused by water droplet impingement, Wear. 267 (2009) 1804–1810. doi:10.1016/j.wear.2009.02.009.

[84] M. Ahmad, M. Casey, N. Sürken, Experimental assessment of droplet impact erosion resistance of steam turbine blade materials, Wear. 267 (2009) 1605–1618. doi:10.1016/j.wear.2009.06.012.

[85] J. V. Hackworth, Damage Of infrared-transparent materials exposed to rain environments at high velocities, Proceedings of SPIE. (1983) 123–136. doi:10.1117/12.934142.

[86] M. Ahmad, M. Schatz, M.V. Casey, Experimental investigation of droplet size influence on low pressure steam turbine blade erosion, Wear. 303 (2013) 83–86. doi:10.1016/j.wear.2013.03.013.

[87] D. Ma, Liquid impingement erosion performance of deep-rolled Ti-6Al-4V alloy, MASc Thesis, Concordia University, 2014.

[88] R. Burson-Thomas, Charles B; Wellman, T.J. Harvey, R.J.K. Wood, Importance of surface curvature in modelling droplet, Journal of Engineering for Gas Turbines and Power. (2018). doi:10.1115/1.4041149.

[89] A. Gujba, Water droplet erosion performance of laser shock peened Ti6Al4V, Metals. (2016). doi:10.3390/met6110262.

[90] A. Gujba, M. Medraj, Laser peening process and its impact on materials properties in comparison with shot peening and ultrasonic impact peening, 2014. doi:10.3390/ma7127925.

[91] T. Keil, P.F. Pelz, J. Kadavelil, J. Necker, W. Moser, D. Christ, Droplet impact vs . cavitation erosion, in: Warwick Innovative Manufacturing Research Centre (WIMRC) 3rd International Cavitation Forum, University of Warwick, UK, 2011: pp. 1–8.

[92] C.M. Preece, J.H. Brunton, A comparison of liquid impact erosion and cavitation erosion, Wear. (1980). doi:10.1016/0043-1648(80)90227-6.

[93] H.X. Hu, Y.G. Zheng, C.P. Qin, Comparison of Inconel 625 and Inconel 600 in resistance to cavitation erosion and jet impingement erosion, in: Nuclear Engineering and Design, 2010. doi:10.1016/j.nucengdes.2010.07.021.

[94] S. Hattori, M. Takinami, Comparison of cavitation erosion rate with liquid impingement erosion rate, Wear. 269 (2010) 310–316. doi:10.1016/j.wear.2010.04.020.

[95] G.L. Chahine, C.T. Hsiao, Modelling cavitation erosion using fluid–material interaction simulations, Interface Focus. (2015). doi:10.1098/rsfs.2015.0016.

[96] P. Zhong, C.J. Chuong, G.M. Preminger, Propagation of shock waves in elastic solids caused by cavitation microjet impact II: application in extracorporeal shock wave lithotripsy, The Journal of the Acoustical Society of America. (1993). doi:10.1121/1.407088.

[97] K.M. Emara, S.M. Ahmed, Characterizing cavitation erosion particles by analysis of SEM images, Tribology International. 42 (2009) 130–136. doi:10.1016/j.triboint.2008.05.008.

[98] S.M. Ahmed, K. Hokkirigawab, R. Oba, Fatigue failure of SUS 304 caused by vibratory cavitation erosion, 177 (1994) 129–137.

[99] J. Blake, Cavitation bubbles near boundaries, Annual Review of Fluid Mechanics. (1987). doi:10.1146/annurev.fluid.19.1.99.

[100] W. Lauterborn, C.D. Ohl, Cavitation bubble dynamics, Ultrasonics Sonochemistry. (1997). doi:10.1016/S1350-4177(97)00009-6.

[101] F.G. Hammitt, Damage to solids caused by cavitation, Philosophical Transactions of the Royal Society of London, Series A, Mathematical and Physical Sciences. 260 (1966) 245–255. doi:http://dx.doi.org/10.1016/j.bbr.2003.09.040.

[102] N. Fujisawa, S. Takano, K. Fujisawa, T. Yamagata, Experiments on liquid droplet impingement erosion on a rough surface, Wear. 398–399 (2018) 158–164. doi:10.1016/j.wear.2017.12.003.

[103] W. Lauterborn, H. Bolle, Experimental investigations of cavitation-bubble collapse in the neighbourhood of a solid boundary, Journal of Fluid Mechanics. (1975). doi:10.1017/S0022112075003448.

[104] G.L. Chahine, Modeling of cavitation dynamics and interaction with material, Fluid Mechanics and Its Applications. (2014). doi:10.1007/978-94-017-8539-6_6.

[105] G.F. Miller, H. Pursey, On the partition of energy between elastic waves in a semi-infinite solid, Proceedings of the Royal Society A: Mathematical, Physical and Engineering Sciences. (1955). doi:10.1098/rspa.1955.0245.

[106] C. Haosheng, L. Shihan, Inelastic damages by stress wave on steel surface at the incubation stage of vibration cavitation erosion, Wear. (2009). doi:10.5958/0974-0112.2016.00078.5.

[107] A. Thiruvengadam, W. S., Mechanical properties of metals and their cavitation damage resistance., Journal of Ship Research. 10 (1966) 1–9.

[108] F.J. Heymann, Toward quantitative prediction of liquid impact erosion, ASTM Special Technical Publication. (1970) 212–248.

[109] M.J. Jackson, J.E. Field, Liquid impact erosion of single-crystal magnesium oxide, Wear. 233–235 (1999) 39–50. doi:10.1016/S0043-1648(99)00193-3.

[110] C.F. Kennedy, R.H. Telling, J.E. Field, Liquid impact and fracture of free-standing CVD diamond, in: SPIE Conference on Window and Dome TechnologIand Materials VI, 1999: pp. 290–296.

[111] W.F. Adler, Inestigation of Liquid Drop Impacts On Ceramics, 1982.

[112] J.M.I. Robinson, R.C. Reed, Water droplet erosion of laser surface treated Ti-6A14V, 187 (1995) 360–367.

[113] D.E. Grady, Constitutive features of solids at shock-wave loading rates, in: Transactions of the Army Conference on Applied Mathematics and Computing (2nd), Washington, USA, 1984.

[114] M.K. Lee, W.W. Kim, C.K. Rhee, W.J. Lee, Liquid impact erosion mechanism and theoretical impact stress analysis in TiN-coated steam turbine blade materials, Metallurgical and Materials Transactions A. 30 (1999) 961–968. doi:10.1007/s11661-999-0149-y.

[115] M.S. Mahdipoor, F. Tarasi, C. Moreau, A. Dolatabadi, M. Medraj, HVOF sprayed coatings of nano-agglomerated tungsten-carbide / cobalt powders for water droplet erosion application, Wear. 331 (2015) 338–347. doi:10.1016/j.wear.2015.02.034.

[116] P. Lammel, L.D. Rafailovic, M. Kolb, K. Pohl, A.H. Whitehead, G. Grundmeier, B. Gollas, Analysis of rain erosion resistance of electroplated nickel-tungsten alloy coatings, Surface and Coatings Technology. 206 (2012) 2545–2551. doi:10.1016/j.surfcoat.2011.11.009.

[117] E.J. Coad, C.S.J. Pickles, G.H. Jilbert, J.E. Field, Aerospace erosion of diamond and diamond coatings, Diamond & Related Materials. 5 (1996) 640–643. doi:10.1016/0925-9635(95)00403-3.

[118] M. Duraiselvam, R. Galun, S. Siegmann, V. Wesling, B.L. Mordike, Liquid impact erosion characteristics of martensitic stainless steel laser clad with Ni-based intermetallic composites and matrix composites, Wear. 261 (2006) 1140–1149. doi:10.1016/j.wear.2006.03.024.

[119] O. Gohardani, D.M. Williamson, D.W. Hammond, Multiple liquid impacts on polymeric matrix composites reinforced with carbon nanotubes, Wear. 294–295 (2012) 336–346. doi:10.1016/j.wear.2012.07.007.

[120] M. Duraiselvam, R. Galun, S. Siegmann, V. Wesling, B.L. Mordike, Study of liquid impact erosion in B2-NiTi and Ti3Al based intermetallic matrix composites on laser alloyed Ti-6Al-4V, Advanced Engineering Materials. 9 (2007) 171–176. doi:10.1002/adem.200600227.

[121] E.M. Waddell, B.C. Monachan, Rain erosion protection of IR materials using boron phosphide coatings, Window and Dome Technologies and Materials. 1326 (1990) 144–156.

[122] A.H. Whitehead, H. Simunkova, P. Lammel, J. Wosik, N. Zhang, B. Gollas, Rain erosion characteristics of electrodeposited Ni-SiC metal-matrix composite layers, Wear. 270 (2011) 695–702. doi:10.1016/j.wear.2011.02.001.

[123] A. Krella, Cavitation erosion of TiN and CrN coatings deposited on different substrates, Wear. 297 (2013) 992–997. doi:10.1016/j.wear.2012.11.049.

[124] A.K. Krella, A. Czyżniewski, A. Gilewicz, A. Krupa, Cavitation erosion of CrN/CrCN multilayer coating, Wear. 386–387 (2017) 80–89. doi:10.1016/j.wear.2017.06.007.

[125] A.K. Krella, Cavitation erosion resistance of Ti/TiN multilayer coatings, Surface and Coatings Technology. 228 (2013) 115–123. doi:10.1016/j.surfcoat.2013.04.016.

[126] S. Momeni, W. Tillmann, M. Pohl, Composite cavitation resistant PVD coatings based on NiTi thin films, Materials and Design. 110 (2016) 830–838. doi:10.1016/j.matdes.2016.08.054.

[127] C.J. Lin, K.C. Chen, J.L. He, The cavitation erosion behavior of electroless Ni-P-SiC composite coating, Wear. 261 (2006) 1390–1396. doi:10.1016/j.wear.2006.03.054.

[128] G. Bregliozzi, W. Haenni, H. Haefke, Cavitation erosion behavior of nanocrystalline diamond

thin films on silicon substrates, Journal of Materials Science. 39 (2004) 6603–6606.

[129] G. Taillon, F. Pougoum, S. Lavigne, L. Ton-that, R. Schulz, E. Bousser, S. Savoie, L. Martinu, J. Klemberg-sapieha, Cavitation erosion mechanisms in stainless steels and in composite metal – ceramic HVOF coatings, Wear. 364–365 (2016) 201–210. doi:10.1016/j.wear.2016.07.015.

[130] Y. Wang, J. Liu, N. Kang, G. Darut, T. Poirier, J. Stella, H. Liao, M. Planche, Cavitation erosion of plasma-sprayed CoMoCrSi coatings, Tribiology International. 102 (2016) 429–435. doi:10.1016/j.triboint.2016.06.014.

[131] J. Lin, Z. Wang, J. Cheng, M. Kang, X. Fu, Effect of initial surface roughness on cavitation erosion resistance of arc-sprayed Fe-based amorphous / nanocrystalline coatings, Coatings. 7 (2017). doi:10.3390/coatings7110200.

[132] B.S. Mann, V. Arya, HVOF coating and surface treatment for enhancing droplet erosion resistance of steam turbine blades, 254 (2003) 652–667. doi:10.1016/S0043-1648(03)00253-9.

[133] P.H. Shipway, K. Gupta, The potential of WC-Co hardmetals and HVOF sprayed coatings to combat water-droplet erosion, Wear. 271 (2011) 1418–1425. doi:10.1016/j.wear.2010.12.058.

[134] D. Batory, W. Szymanski, M. Panjan, O. Zabeida, J.E. Klemberg-sapieha, Plasma nitriding of Ti6Al4V alloy for improved water erosion resistance, Wear. 374–375 (2017) 120–127. doi:10.1016/j.wear.2017.01.041.

[135] S. Zhang, K. Dam-Johansen, S. Norkjaer, P.L. Bernad, S. Kill, Erosion of wind turbine blade coatings - design and analysis of jet-based laboratory equipment for performance evaluation, Progress in Organic Coatings. 78 (2015) 103–115. doi:10.1016/j.porgcoat.2014.09.016.

[136] S. Zhang, Accelerated rain erosion of wind turbine blade coatings, Kgs. Lyngby: Danmarks Tekniske Universitet (DTU), 2014.

[137] H.M. Slot, E.R.M. Gelinck, C. Rentrop, E. van der Heide, Leading edge erosion of coated wind turbine blades: review of coating life models, Renewable Energy. 80 (2015) 837–848. doi:10.1016/j.renene.2015.02.036.

[138] D.S. Rickerby, A.M. Jones, B.A. Bellamy, X-ray diffraction studies of physically vapour-deposited coatings, Surface and Coatings Technology. 37 (1989) 111–137. doi:10.1016/0257-8972(89)90124-2.

[139] D.B. Lewis, L.A. Donohue, M. Lembke, W.D. Münz, R. Kuzel, V. Valvoda, C.J. Blomfield, The influence of the yttrium content on the structure and properties of Ti1-x-y-zAlxCryYzN PVD hard coatings, Surface and Coatings Technology. 114 (1999) 187–199. doi:10.1016/S0257-8972(99)00047-X.

[140] W.C. Oliver, G.M. Pharr, An improved technique for determining hardness and elastic modulus using load and displacement sensing indentation experiments, Journal of Materials Research. 7 (1992) 1564–1583.

[141] D. Rugg, T.B. Britton, J. Gong, A.J. Wilkinson, P.A.J. Bagot, In-service materials support for safety critical applications – a case study of a high strength Ti-alloy using advanced experimental and modelling techniques, Materials Science & Engineering A. 599 (2014) 166–173. doi:10.1016/j.msea.2014.01.031.

[142] P. Niederhofer, F. Pöhl, K. Geenen, S. Huth, W. Theisen, Influence of crystallographic orientation on cavitation erosion resistance of high interstitial CrMnCN austenitic stainless

steels, Tribiology International. 95 (2016) 66–75. doi:10.1016/j.triboint.2015.11.002.

[143] O.G. Engel, Impact of liquid drops, in: Symposium on Erosion and Cavitation, American Society for Testing and Materials, Atlantic City, 1961: pp. 3–16.

[144] H. Chen, Iridescent rings around cavitation erosion pits on surface of mild carbon steel, Wear. 269 (2010) 602–606. doi:10.1016/j.wear.2010.06.007.

[145] G.L. Chahine, R. Duraiswami, Dynamical interactions in a multi-bubble cloud, Journal of Fluids Engineering. (1992). doi:10.1115/1.2910085.

[146] N.K. Bourne, On the collapse of cavities, Shock Waves. (2002). doi:10.1007/s001930200128.

[147] U. Rasthofer, F. Wermelinger, P. Hadijdoukas, P. Koumoutsakos, Large scale simulation of cloud cavitation collapse, Procedia Computer Science. 108 (2017) 1763–1772. doi:10.1016/j.procs.2017.05.158.

[148] M. Hajian, a. Abdollah-zadeh, S.S. Rezaei-Nejad, H. Assadi, S.M.M. Hadavi, K. Chung, M. Shokouhimehr, Improvement in cavitation erosion resistance of AISI 316L stainless steel by friction stir processing, Applied Surface Science. 308 (2014) 184–192. doi:10.1016/j.apsusc.2014.04.132.

[149] D. Lunt, J.Q. Fonseca, D. Rugg, M. Preuss, M.S. Centre, Microscopic strain localisation in Ti-6Al-4V during uniaxial tensile loading, Materials Science & Engineering A. 680 (2017) 444–453. doi:10.1016/j.msea.2016.10.099.

[150] F. Bridier, P. Villechaise, J. Mendez, Slip and fatigue crack formation processes in an a/b titanium alloy in relation to crystallographic texture on different scales, Acta Materialia. 56 (2008) 3951–3962. doi:10.1016/j.actamat.2008.04.036.

[151] S.J. Lain, K.M. Knowles, P.J. Doorbar, R.D. Cutts, D. Rugg, Microstructural characterisation of metallic shot peened and laser shock peened Ti-6Al-4V, 123 (2017) 350–361. doi:10.1016/j.actamat.2016.10.044.

[152] J.E. Field, The physics of liquid impact, shock wave interactions with cavities, and the implications to shock wave lithotripsy., Physics in Medicine and Biology. 36 (1991) 1475–1484. doi:10.1088/0031-9155/36/11/007.

[153] C.M. Preece, J.H. Brunton, A comparison of liquid impact erosion and cavitation erosion, Wear. 60 (1980) 269–284.

[154] G.M. Krolczyk, J.B. Krolczyk, R.W. Maruda, S. Legutko, M. Tomaszewski, Metrological changes in surface morphology of high-strength steels in manufacturing processes, Measurement. 88 (2016) 176–185. doi:10.1016/j.measurement.2016.03.055.

[155] Y. Lian, X. Liu, J. Wang, F. Feng, Y. Lv, J. Song, J. Chen, Applied Surface Science Influence of surface morphology and microstructure on performance of CVD tungsten coating under fusion transient thermal loads, Applied Surface Science. 390 (2016) 167–174. doi:10.1016/j.apsusc.2016.08.060.

[156] J.Q. Shi, S.Y. Yao, F. Wang, X.D. Yu, H.T. Huang, C.W. Tan, Z.H. Nie, H.L. Ma, H.N. Cai, Materials Characterization Microstructures of chemical vapor deposited high-purity tungsten achieved by two di ff erent precursors, 134 (2017) 1–8. doi:10.1016/j.matchar.2017.10.007.

[157] Y. Lv, J. Song, Y. Lian, Y. Yu, X. Liu, Z. Zhuang, The thermal properties of high purity and

fully dense tungsten produced by chemical vapor deposition, JOURNAL OF NUCLEAR MATERIALS. 457 (2015) 317–323. doi:10.1016/j.jnucmat.2014.11.095.

[158] K.K. Lai, H.H. Lamb, Tungsten chemical vapor deposition using tungsten hexacarbonyl : microstructure of as-deposited and annealed ® lms, 370 (2000) 114–121.

[159] D. Li, A. Goullet, M. Carette, A. Granier, Y. Zhang, J.P. Landesman, Structural and optical properties of RF-biased PECVD TiO2 thin fi lms deposited in an O2 / TTIP helicon reactor, Vaccum. 131 (2016). doi:10.1016/j.vacuum.2016.07.004.

[160] S.K. Chen, J.H. Du, G.R. Gao, Z.X. Li, Microstructure study of CVD W coating on Mo single crystal rods with 1 1 1 axial orientation by EBSD, 434 (2006) 95–98. doi:10.1016/j.msea.2006.07.010.

[161] E.M.A. Fuentes-fernandez, J.J. Alcantar-peña, G. Lee, A. Boulom, H. Phan, B. Smith, T. Nguyen, S. Sahoo, F. Ruiz-zepeda, M.J. Arellano-jimenez, P. Gurman, C.A. Martinez-perez, M.J. Yacaman, R.S. Katiyar, O. Auciello, Synthesis and characterization of microcrystalline diamond to ultrananocrystalline diamond films via hot filament chemical vapor deposition for scaling to large area applications, Thin Solid Films. 603 (2016) 62–68. doi:10.1016/j.tsf.2015.11.088.

[162] O. Auciello, A. V Sumant, Status review of the science and technology of ultrananocrystalline diamond (UNCD^{TM}) films and application to multifunctional devices, Diamond & Related Materials. 19 (2010) 699–718. doi:10.1016/j.diamond.2010.03.015.

[163] M. Mathias, A. Gocke, M. Pohl, The residual stress, texture induced by cavitation and surface changes in steel, Wear. 150 (1991) 11–20.

[164] S. Kocanda, Fatigue failure of metals, Sijthoff & Noordhoff International Publishers, 1978.

[165] T. Okada, Y. Iwai, Cavitation erosion, JSME International Journal. 33 (1990) 128.

[166] S.M. Ahmed, K. Hokkirigawab, R. Oba, Kikuchi K, SEM observation of the vibratory cavitation-fracture mode during the incubation period and the small roughness effect, JSME International Journal. 34 (1991) 298–303.

[167] W. Be, G. Gasiak, C. Lachowicz, A. Lichtarowicz, T. Łagoda, E. Macha, Relations between cavitation erosion resistance of materials and their fatigue strength under random loading, (1999) 201–209.

[168] R. Fortes, T. Choffat, J. Reboud, A. Archer, Mass loss simulation in cavitation erosion : fatigue criterion approach, Wear. 300 (2013) 205–215. doi:10.1016/j.wear.2013.01.118.

[169] R.H. Richman, W.P. Mcnaughton, A metallurgical approach to improved cavitation-erosion resistance, Journal of Materials Engineering and Performance. 6 (1997) 633–641.

[170] M.N. Goodhand, K. Walton, L. Blunt, R.J. Miller, R. Marsden, The limitations of esing “Ra” to describe surface roughness, Journal of Turbomachinery. 138 (2016) 1–8. doi:10.1115/1.4032280.

[171] S.M. Ahmed, K. Hokkirigawab, R. Oba, Y. Matsudaira, Developing stages of ulrtasonically produced cavitation erosion and corresponding surface roughness, JSME International Journal. 33 (1990) 11–16.

[172] Y. Zhu, J. Zou, W.L. Zhao, X.B. Chen, H.Y. Yang, A study on surface topography in

cavitation erosion tests of AlSi10Mg, Tribiology International. 102 (2016) 419–428. doi:10.1016/j.triboint.2016.06.007.

[173] F.T. Cheng, P. Shi, H.C. Man, Correlation of cavitation erosion resistance with indentation-derived properties for a NiTi alloy, 45 (2001).

[174] R.H. Richman, W.P. Mcnaughton, Correlation of cavitation properties of metals erosion behavior with mechanical, 140 (1990) 63–82.

[175] J.-J.L. Ju-Wan Lima H. Ahn, K.-T. Rie, Mechanical properties of TiNyTiB2 multilayers deposited by plasma enhanced chemical vapor deposition, Surface and Coatings Technology. 174–175 (2003) 720–724. doi:10.1016/S0257-8972.

[176] B. Vyas, C.M. Preece, B. Vyas, C.M. Preece, Stress produced in a solid by cavitation, Journal of Applied Physics. 47 (1976). doi:10.1063/1.322584.

[177] R. Lewis, J. V Me, A study of cavitation erosion on engineering materials, 301 (2013) 467–476. doi:10.1016/j.wear.2012.11.026.

[178] L. Van Wijngaarden, Mechanics of collapsing cavitation bubbles, Ultrasonics - Sonochemistry. 29 (2016) 524–527. doi:10.1016/j.ultsonch.2015.04.006.

[179] M. Sebastiani, K.E. Johanns, E.G. Herbert, G.M. Pharr, Measurement of fracture toughness by nanoindentation methods : Recent advances and future challenges, Current Opinion in Solid State and Materials Science. 19 (2015) 324–333. doi:10.1016/j.cossms.2015.04.003.

[180] J. Musil, Hard nanocomposite coatings : thermal stability , oxidation resistance and toughness, Surface & Coatings Technology. 207 (2012) 50–65. doi:10.1016/j.surfcoat.2012.05.073.

[181] A. Leyland, A. Matthews, Design criteria for wear-resistant nanostructured and glassy-metal coatings, 178 (2004) 317–324. doi:10.1016/j.surfcoat.2003.09.011.

[182] A. Leyland, A. Matthews, On the significance of the H/E ratio in wear control : a nanocomposite coating approach to optimised tribological behaviour, Wear. 246 (2000) 1–11.

[183] C. Wang, K. Shi, C. Gross, J. Miranda, M. De Mesquita, Y. Chung, Toughness enhancement of nanostructured hard coatings : design strategies and toughness measurement techniques, Surface & Coatings Technology. 257 (2014) 206–212. doi:10.1016/j.surfcoat.2014.08.018.

[184] L.A. Espitia, H. Dong, X. Li, C.E. Pinedo, A.P. Tschiptschin, Cavitation erosion resistance and wear mechanisms of active screen low temperature plasma nitrided AISI 410 martensitic stainless steel, Wear. 333 (2015) 1070–1079. doi:10.1016/j.wear.2014.12.009.

[185] W. Deng, Y. An, G. Hou, S. Li, H. Zhou, J. Chen, Effect of substrate preheating treatment on the microstructure and ultrasonic cavitation erosion behavior of plasma-sprayed YSZ coatings, Ultrasonics Sonochemistry. 46 (2018) 1–9.

[186] A. Krella, A. Czyzniewski, Cavitation erosion resistance of Cr-N coating deposited on stainless steel, Wear. 260 (2006) 1324–1332. doi:10.1016/j.wear.2005.09.018.

[187] A. Krella, The influence of TiN coatings properties on cavitation erosion resistance, Surface & Coatings Technology. 204 (2009) 263–270. doi:10.1016/j.surfcoat.2009.07.014.

[188] C.J. Lin, J.L. He, Cavitation erosion behavior of electroless nickel-plating on AISI 1045 steel, Wear. 259 (2005) 154–159. doi:10.1016/j.wear.2005.02.099.

[189] G. Bregliozzi, A. Di Schino, S.I. Ahmed, J.M. Kenny, H. Haefke, Cavitation wear behaviour of austenitic stainless steels with different grain sizes, 258 (2007) 503–510. doi:10.1016/j.wear.2004.03.024.

[190] R. M'Saoubi, O. Alm, J.M. Andresson, H. Engstrom, T. Larsson, M.P. Johansson-Joesaar, M. Schwind, Microstructure and wear mechanisms of texture-controlled CVD α-Al2O3 coatings, Wear. 376 (2017) 1766–1778.

[191] G. Subhash, Plastic deformation of cvd textured tungsten-ii. characterization, Acta Materialia. 42 (1994) 331–340.

[192] G. Subhash, Y.J. Leer, G. Ravichandran, Plastic deformation of cvd textured tungsten -- i. constitutive response, Acta Materialia. 42 (1994) 319–330.

[193] J.W. Hutchinson, Stresses and failure modes in thin films and multilayers, Division of Engineering and Applied Sciences, Harvard University, Cambridge, MA, USA, 1996. doi:10.1.1.366.4011.

[194] R. Hahn, M. Bartosik, R. Soler, C. Kirchlechner, G. Dehm, P.H. Mayrhofer, Superlattice effect for enhanced fracture toughness of hard coatings, Scripta Materialia. 124 (2016) 67–70. doi:10.1016/j.scriptamat.2016.06.030.

[195] A.P. Ehiasarian, Fundamentals and applications of HIPIMS, in: R. Wei (Ed.), Plasma Surface Engineering Research and Its Practical Applications, Research Signpost, Trivandrum, India, 2007: p. 35.

[196] S. Zhang, W. Zhu, TiN coating of tool steels: a review, Journal of Materials Processing Tech. (1993). doi:10.1016/0924-0136(93)90016-Y.

[197] P.E. Hovsepian, W. Munz, L. Vide, A. Conference, P. Examiner, R.G. Mcdonald, A combined process comprising magnetic field-assisted, high-power, pulsed cathode Sputtering and an unbalanced magnetron, US 7,081,186 B2, 2006.

[198] A.P. Ehiasarian, J.G. Wen, I. Petrov, Interface microstructure engineering by high power impulse magnetron sputtering for the enhancement of adhesion, Journal of Applied Physics. 101 (2007). doi:10.1063/1.2697052.

[199] A.P. Ehiasarian, A. Vetushka, Y.A. Gonzalvo, G. Sfrn, L. Székely, P.B. Barna, Influence of high power impulse magnetron sputtering plasma ionization on the microstructure of TiN thin films, Journal of Applied Physics. 109 (2011). doi:10.1063/1.3579443.

[200] S. Lavigne, F. Pougoum, S. Savoie, L. Martinu, J.E. Klemberg-sapieha, R. Schulz, Cavitation erosion behavior of HVOF CaviTec coatings, Wear. 386–387 (2017) 90–98. doi:10.1016/j.wear.2017.06.003.

[201] B. Biswas, Y. Purandare, A. Sugumaran, I. Khan, P. Eh, Effect of chamber pressure on defect generation and their in fl uence on corrosion and tribological properties of HIPIMS deposited CrN / NbN coatings, Surface & Coatings Technology. 336 (2018) 84–91. doi:10.1016/j.surfcoat.2017.08.021.

[202] Y. Zhou, F.G. Hammitt, Cavitation erosion incubation period, Wear. 86 (1983) 299–313.

[203] T.B. Benjamin, A.T. Ellis, The collapse of cavitation bubbles and the pressures thereby produced against solid boundaries, Philosophical Transactions of the Royal Society A: Mathematical, Physical and Engineering Sciences. 260 (1966) 221–240.

[204] F. Cheng, S. Jiang, Cavitation erosion resistance of diamond-like carbon coating on stainless steel, Applied Surface Science. (2014). doi:10.1016/j.apsusc.2013.11.044.

[205] C.W. Kang, H. Huang, Deformation, failure and removal mechanisms of thin film structures in abrasive machining, Advances in Manufacturing. 5 (2017) 1–19. doi:10.1007/s40436-016-0165-2.

[206] J. Siegl, I. Nedbal, J. Kunz, Influence of surface technologies on fracture processes, in: 7th European Conference on Advanced Materials and Processes, 2001.

[207] M.J. Cordill, A. Taylor, J. Schalko, G. Dehm, Fracture and delamination of chromium thin films on polymer substrates, Metallurgical and Materials Transactions A: Physical Metallurgy and Materials Science. 41 (2010) 870–875. doi:10.1007/s11661-009-9988-9.

[208] M. George, C. Coupeau, J. Colin, J. Grilhé, Mechanical behaviour of metallic thin films on polymeric substrates and the effect of ion beam assistance on crack propagation, Acta Materialia. (2005). doi:10.1016/j.actamat.2004.09.036.

[209] V.M. Marx, F. Toth, A. Wiesinger, J. Berger, C. Kirchlechner, M.J. Cordill, F.D. Fischer, F.G. Rammerstorfer, G. Dehm, The influence of a brittle Cr interlayer on the deformation behavior of thin Cu films on flexible substrates: experiment and model, Acta Materialia. 89 (2015) 278–289. doi:10.1016/j.actamat.2015.01.047.

[210] S.J. Yu, M.G. Chen, Y.J. Zhang, H. Zhou, P.Z. Si, An experimental study of the influence of film edges and imperfections on buckling morphologies of quenched iron films, Thin Solid Films. (2011). doi:10.1016/j.tsf.2011.07.024.

[211] J.W. Hutchinson, M.Y. He, A.G. Evans, Influence of imperfections on the nucleation and propagation of buckling driven delaminations, Journal of the Mechanics and Physics of Solids. (2000). doi:10.1016/S0022-5096(99)00050-2.

[212] G. Abadias, E. Chason, J. Keckes, M. Sebastiani, G.B. Thompson, E. Barthel, G.L. Doll, C.E. Murray, C.H. Stoessel, L. Martinu, Review article: stress in thin films and coatings: current status, challenges, and prospects, Journal of Vacuum Science & Technology A. 36 (2018). doi:10.1116/1.5011790.

[213] X.N. Li, L.H. Liang, J.J. Xie, L. Chen, Y.G. Wei, Thickness-dependent fracture characteristics of ceramic coatings bonded on the alloy substrates, Surface and Coatings Technology. 258 (2014) 1039–1047. doi:10.1016/j.surfcoat.2014.07.031.

[214] L.H. Liang, X.N. Li, H.Y. Liu, Y.B. Wang, Y.G. Wei, Power-law characteristics of damage and failure of ceramic coating systems under three-point bending, Surface and Coatings Technology. 285 (2016) 113–119. doi:10.1016/j.surfcoat.2015.11.044.

[215] E. Bousser, L. Martinu, J.E. Klemberg-Sapieha, Solid particle erosion mechanisms of protective coatings for aerospace applications, Surface and Coatings Technology. (2014). doi:10.1016/j.surfcoat.2014.08.037.

[216] E. Avcu, S. Fidan, Y. Yıldıran, T. Sınmazçelik, Solid particle erosion behaviour of Ti6Al4V alloy, Tribology - Materials, Surfaces & Interfaces. 7 (2013) 201–210. doi:10.1179/1751584X13Y.0000000043.

[217] J.A. Zukas, Chapter 3 Shock waves in solids, Studies in Applied Mechanics. 49 (2004) 75–102. doi:10.1016/S0922-5382(04)80004-7.

[218] J.J. Burke, Shock waves and the mechnical properties of solids, in: Segamore Army Materials Research Conference, Raquette Lake, N.Y., USA, 1971.

[219] D.E. Grady, Microstructural effects on wave propagation in solids, International Journal of Engineering Science. 22 (1984) 1181–1186. doi:10.1016/0020-7225(84)90120-4.